**UNIVERSIDAD COMPLUTENSE DE MADRID**
FACULTAD DE CIENCIAS FÍSICAS

# TESIS DOCTORAL

Dinámica de galaxias con simulaciones cosmológicas de la Vía Láctea:
La espiral de fase y perturbaciones verticales

Galactic dynamics with cosmological simulations of Milky Way-sized galaxies:
The phase spiral and vertical perturbations

MEMORIA PARA OPTAR AL GRADO DE DOCTORA

PRESENTADA POR

Begoña García-Conde Navarro

Directores y directoras

Santi Roca Fàbrega
Teresa Antoja Castelltort
Mª de los Ángeles Gómez Flechoso

Madrid

© Begoña García-Conde Navarro, 2024

UNIVERSIDAD COMPLUTENSE DE MADRID

FACULTAD DE CC. FÍSICAS

TESIS DOCTORAL

---

# Dinámica de galaxias con simulaciones cosmológicas de la Vía Láctea

La espiral de fase y perturbaciones verticales

---

# Galactic dynamics with cosmological simulations of Milky Way-sized galaxies

The phase spiral and vertical perturbations

---

*Autor:*
Begoña GARCÍA-CONDE NAVARRO

*Directores:*
Dr. Santi ROCA FÀBREGA
Dr. Teresa ANTOJA CASTELLTORT
Dr. Mª de los Ángeles GÓMEZ FLECHOSO

*MEMORIA PARA OPTAR AL GRADO DE DOCTORA EN ASTROFÍSICA*

Madrid, 2023

"*The quiet shade*
*Across old bark*
*In the ancient glade*
*It's always dark.*"

Outer Wilds

# *Abstract*

Understanding the complex dynamics of galaxies, especially in the context of the Milky Way, remains a challenging and fascinating effort. The discovery of the phase spiral phenomenon in the vertical plane $Z - V_Z$ in the Solar Neighborhood has shown that the Milky Way is in a perturbed state. The origin of such perturbation has been studied via different N-body models but is still not fully understood. In this thesis, we present a comprehensive research on the dynamics of galactic disks through high-resolution cosmological simulations named GARROTXA and observational data from the *Gaia* space observatory. The primary focus of this work lies on, firstly, the study of the phase spirals; secondly, the detailed analysis of the vertical behaviour of the simulated galactic disk; and finally, the determination of the diverse mechanisms that can contribute to the observed perturbations.

We explore the Milky Way-sized model of the GARROTXA simulation over the last 6 Gyr of evolution to detect the presence and origin of vertical perturbations that can resemble those observed in the Milky Way. We identify phase spirals in the vertical projection $(Z - V_Z)$ of the disk's stellar particles. This is the first time that such structures are observed in a hydrodynamical cosmological simulation. We explore the vertical phase space in different azimuths, radii and age populations. We observe that the phase spirals are more pronounced among younger-intermediate star particles. These spirals are present for a prolonged period of time, and their appearance correlates with the passage of satellite galaxies which are, however, less massive than those in previous N-Body models that required or used massive perturbers.

In a second stage of this thesis we explore the bending modes in the galactic disk model via Fourier decomposition, and find intricate patterns of this kind of modes at different radii and times. To quantify the possible causes of perturbation, we calculate the accelerations applied on the galactic plane by all the dark matter particles (from satellites and from the halo general structure) and gas and find that all of them contribute to the vertical deformations. For example, we find evidence of a satellite leading to a tilting of the disk. This tilting results in a misalignment between the disk and the inner dark matter triaxial structure formed in an ancient major merger. All these induce significant vertical accelerations on the galactic plane, and the disk ends up with a distinct warp shape. We highlight that the ancient merger history, which in our case led to a triaxial shape of the halo, can play an important role in the vertical deformations. The anisotropic gas accretion and subsequent star-forming processes may also contribute to further vertical acceleration that the disk suffers. All these phenomena coexist and influence each other, sometimes making it challenging to establish direct causality.

Lastly, we focus on the phase spiral in the observational data of the Milky Way disk using *Gaia* DR3. We apply an edge detection algorithm, to determine the shape of the phase spiral at different positions and selections. The phase spiral exhibits complex variations with angular momentum and azimuth, suggesting multiple perturbations and/or intricate phase mixing processes. We also estimate the time of the perturbation that led to the start of the phase mixing process by using different models of the Milky Way's potential, which on average results in 0.5 Gyr. We find systematic differences when estimating this impact time at different angular momentum and $Z$ which may be due to the assumption of the potential of the Milky Way, or not considering other processes such as multiple perturbations or self-gravity.

In this thesis, we provide a holistic understanding of the galactic disk vertical dynamics. We conclude that the origin of the perturbations affecting a disk galaxy is not unique and thus, the various mechanisms cannot be studied in isolation. Therefore, it is necessary to use these realistic models to study a more complete picture of a Universe in which disk galaxies are often out of equilibrium.

# *Resumen*

Entender la complejidad de la dinámica de galaxias, especialmente en el contexto de la Vía Láctea, sigue siendo un reto fascinante. El descubrimiento del fenómeno de las espirales de fase en el plano vertical $Z - V_Z$ de la Vecindad Solar ha demostrado que la Vía Láctea ha sido perturbada. El origen de esta perturbación ha sido estudiada con diferentes modelos de N-cuerpos, pero todavía no está del todo comprendida. En esta tesis, presentamos un amplio estudio de la dinámica galáctica a través de simulaciones cosmológicas con hidrodinámica de alta resolución junto con datos observacionales del observatorio espacial *Gaia*. El foco principal de este estudio es, primero, las espirales de fase, segundo, el análisis detallado del comportamiento vertical del disco galáctico simulado y, por último, la determinación de los diferentes mecanismos que contribuyen a estas perturbaciones observadas.

En este trabajo exploramos un modelo similar a la Vía Láctea de la simulación GARROTXA a lo largo de los últimos 6 giga-años de evolución. Con este modelo estudiamos la presencia y el origen de las perturbaciones verticales similares a las encontradas en la Vía Láctea. Identificamos las espirales de fase en la proyección vertical ($Z - V_Z$) del disco de partículas estelares. Esta es la primera vez que se observan este tipo de estructuras en una simulación cosmológica hidrodinámica. Exploramos el espacio de fases vertical en diferentes azimuts, radios y en varias poblaciones de edad. Observamos que las espirales de fase son más pronunciadas en las partículas estelares de edades jóvenes e intermedias. La intensidad de estas espirales se mantiene a lo largo de un amplio periodo de tiempo. Además, su aparición está correlacionada con el paso de galaxias satélite que, sin embargo, son menos masivas que los perturbadores usados en estudios previos con N-cuerpos, que requerían o usaban perturbadores más masivos.

En la segunda fase de esta tesis exploramos los modos *bending* del modelo de disco galáctico por medio de descomposición de Fourier, y encontramos complejos patrones de este tipo de modos a diferentes radios y tiempos. Para cuantificar las posibles causas de las perturbaciones, calculamos la aceleración aplicada sobre el plano galáctico por parte de todas las partículas de materia oscura y gas. Por ejemplo, encontramos que la caída de uno de los satélites conduce a una inclinación del disco. Esta inclinación provoca un desalineado entre el disco y la estructura triaxial interna de materia oscura formada en una antigua fusión mayor. Todos estos procesos inducen aceleraciones verticales significativas, y el disco desarrolla un notable alabeo. Destacamos que la historia antigua de la galaxia, que en nuestro modelo ha causado la forma triaxial del halo interno, puede desempeñar un papel importante en las deformaciones observadas. La acreción anisótropa de gas y los subsecuentes procesos de formación estelar también pueden contribuir a una mayor aceleración vertical que sufre el disco. Todos estos fenómenos coexisten y se influyen mutuamente, por lo que resulta difícil establecer una causalidad directa.

Por último, nos centramos en la espiral de fase del disco de la Vía Láctea usando los datos de *Gaia* DR3. Aplicamos el algoritmo de *edge detector* para determinar la forma de la espiral de fase en diferentes posiciones y selecciones. La espiral de fase exhibe variaciones complejas a diferentes momentos angulares y azimut, lo que sugiere múltiples perturbaciones o procesos de mezcla de fase enrevesados. También estimamos el tiempo de la perturbación que inicia el proceso de mezcla de fases con diferentes modelos de potencial de la Vía Láctea, y obtenemos que en media es de 0.5 giga-años. Encontramos diferencias sistemáticas al estimar este tiempo de impacto para diferentes momentos angulares y $Z$, posiblemente debido a asumir el potencial de la Vía Láctea, o a no considerar otros procesos como múltiples perturbadores o auto-gravitación.

Esta tesis aporta un enfoque *holístico* para entender la dinámica vertical de los discos galácticos. Concluimos que el origen de las perturbaciones que afectan a una galaxia de disco no es único y, en consecuencia, los diversos mecanismos no pueden estudiarse de forma aislada. Por lo tanto, es necesario utilizar estos modelos realistas para estudiar un escenario más completo de un Universo en el que las galaxias de disco se encuentran a menudo fuera de equilibrio.

# *Agradecimientos*

Me gustaría agradecer a todas esas personas que me han acompañado durante este periodo de mi vida y sin los cuales, esta tesis no hubiera sido posible. En primer lugar, me gustaría agradecer a mis directores de tesis. A Santi, por tus consejos, tu orientación, y tu disponibilidad. Gracias por darme la libertad de elegir, de explorar ideas y por enseñarme hasta qué punto uno puede tener un mini-universo en un ordenador. A nivel personal, gracias, sobre todo, por enseñarme el lado más humano de la ciencia y por contagiarme tu optimismo. A Teresa, por todos tus conocimientos, por tu ética, rigurosidad y por atenderme en tiempos difíciles. Te considero un modelo a seguir. A Mariángeles, por tu ayuda y consejo en el último (y más frenético) año de la tesis. También quiero agradecerte como coordinadora del Programa de Doctorado de Astrofísica, ya que tu amabilidad y empatía conmigo (y con el resto de los estudiantes), hace más llevadero un viaje que ya de por sí es difícil. Quiero agradecer también a todos los colaboradores que han aportado sus ideas y comentarios para mejorar la interpretación de los resultados. En particular, quiero agradecer a Pau Ramos, por tu tiempo y tus aportaciones, que indudablemente han añadido un gran valor al contenido de esta tesis. Gracias también a mi mentora del programa de mentoría de la SEA, ya que me has ayudado con tus consejos en los últimos dos años de esta tesis.

Me gustaría también agradecer a todo el departamento de Física de la Tierra y Astrofísica. A todos los que os habéis preocupado por mi y habéis estado pendientes de alguna u otra forma, en especial a Ainhoa, Armando y Afri, entre muchos otros, que me habéis ayudado y habéis sido cercanos conmigo. A los compañeros que me habéis hecho el viaje más liviano. A Artemi por tus consejos, y las largas conversaciones, además de los stickers tan geniales, y su buen gusto para llevarnos a sitios de comida durante los congresos. A Pablo por tu simpatía y tus constantes preguntas de "Pero, ¿esto es una simulación?". A los nuevos doctores, Mario por recordarme para qué sirve el código de conducta, y Ángela, que siempre te has ofrecido a ayudarme, y por tus sabias palabras: "No descarto pequeña potita". Gracias también a Ramón, por tu buen rollo y todas las risas que traes al departamento.

En especial, quiero agradecer a mis compañeros del mejor despacho del mundo: Enrique y Christian. No puedo imaginar una tesis sin las paradas para el té, sin la búsqueda de Shreks chiquitos por el despacho (tradición que debéis continuar), sin los memes, y, en general, sin el sentido del humor que traéis al despacho. Gracias por aguantar mis penas.

Quiero agradecer también a los que me acogieron durante mi estancia en Barcelona. En especial, gracias a Marcel y Óscar por ser tan majos conmigo y por llevarme de calçotada. También, gracias a todos los compañeros de doctorado que he ido conociendo a lo largo de estos años. Gracias a Rosi por lo bien que nos lo hemos pasado en los congresos.

A todos mis compañeros que también me acompañaron durante la carrera y que la hicieron más llevadera: Javi, Bárbara, Magdalena, entre muchísimos otros. En particular, me gustaría agradecer a mi amigo Quique. No puedo agradecerte lo suficiente todos estos años de amistad, los cafés y las eternas conversaciones. Como dijo el gran maestro Terry Pratchett: *There is no doubt that being human is incredibly difficult and cannot be mastered in one lifetime*.

Quiero agradecerle también a Raúl, que ha sido mi apoyo todos estos años. Gracias por darme la confianza y la tranquilidad que muchas veces he necesitado. Me has visto en lo peor y en lo mejor. Me siento muy afortunada de tenerte a mi lado.

Una mención especial también a Marcos y a Juanan, que son maravillosas personas ~~(más o menos)~~. Gracias por todas las tardes de juegos de mesa (¡y las que quedan!). También quería mencionar a la gente

que me ha acompañado desde el instituto: Ana, Andrea, Gonzalo, Jose y Álex. Por todos estos años y los que queden.

A toda mi familia, los que están y los que no. A mi abuela. A todos mis tíos, y en especial a mi tía Mari, que siempre te preocupas por mí. A mi tía Asun, que siempre estás interesada por la astronomía. A mis primos.

A mi Ori.

Por último a mi familia más cercana. Quiero agradecer a mi hermano, Josemi, que siempre estás bromeando, pero quieres a todo el mundo de manera incondicional. Tienes un corazón de oro. A mis padres, no sólo quiero agradeceros por vuestro apoyo durante mi tesis, sino todo lo que he recibido de vosotros a lo largo de mi vida. Me habéis dado la libertad de elegir siempre mi camino, y me habéis enseñado valores que forman parte de lo que soy como persona. Gracias por haber celebrado conmigo los buenos momentos. Pero aún más importante, gracias por haberme acompañado durante los malos. Gracias por escucharme con empatía, y por recordarme que puedo confiar en mí misma. Os quiero.

# Contents

**Abstract** **vii**

**Resumen** **ix**

**Agradecimientos** **xi**

**1 Introduction** **1**
1.1 From early astronomy to the current paradigm of galactic formation . . . 1
1.2 Galaxies in the context of ΛCDM . . . 2
1.3 Numerical simulations as a tool to study disk galaxies . . . 3
1.4 N-body algorithms and hydrodynamics for simulations of galaxy evolution . . . 5
1.5 Galactic disk's perturbations . . . 8
1.6 The Milky Way . . . 10
1.7 The *Gaia* era and the Phase Spiral . . . 11
1.8 Aims and scope of this thesis . . . 12

**2 The GARROTXA simulation and methods** **15**
2.1 General properties . . . 15
2.2 Centering and alignment . . . 17
2.3 Properties of the MW-sized model . . . 19
2.3.1 Ancient merger history . . . 19
2.3.2 Stellar structures . . . 20
2.3.3 Rotation curve . . . 22
2.3.4 Satellites . . . 25
Gas in satellites . . . 28
2.4 Star formation . . . 28
2.5 Fourier decomposition of stellar structures . . . 31

**3 Phase spirals in cosmological simulations** **35**
3.1 Introduction . . . 35
3.2 Phase spirals through space and time . . . 36
3.3 Satellites and Star Formation . . . 41
3.4 Discussion and conclusions . . . 43

**4 Vertical perturbations by dark matter, satellite galaxies and gas** **47**
4.1 Introduction . . . 47

4.2 Vertical bending modes of the disk . . . 49
4.3 Perturbation agents: Dark matter, satellite galaxies and gas . . . 51
4.3.1 Accelerations by dark matter . . . 54
4.3.2 Accelerations by satellite dwarf galaxies and dark subhalos . . . 54
4.3.3 Acceleration by gas . . . 57
4.4 Triggering agents of bending deformation . . . 61
4.4.1 Multiple dark and luminous satellites and bending waves . . . 61
4.4.2 Distant interaction triggering bending modes via disk misalignment . . . 63
4.5 Discussion and conclusions . . . 65
4.5.1 Summary . . . 65
4.5.2 Discussion . . . 66

**5 The phase spiral in *Gaia* DR3 69**
5.1 Introduction . . . 69
5.2 Data . . . 70
5.3 The phase spiral in DR3 . . . 71
5.3.1 The local phase spiral . . . 71
5.3.2 Detection of the phase spiral . . . 71
5.3.3 The phase spiral with radius and angular momentum . . . 74
5.3.4 Crossing points of the phase spirals with $L_Z$ . . . 78
5.3.5 The phase spiral with azimuth . . . 79
5.4 Inferring the impact time . . . 79
5.4.1 Method . . . 79
5.4.2 Time results . . . 83
5.4.3 Results for different models and data . . . 85
5.5 Summary and conclusions . . . 89

**6 Conclusions 93**
6.1 Summary . . . 93
6.2 Discussion . . . 94
6.3 Caveats . . . 97
6.4 Future work . . . 100
6.5 Final conclusions . . . 101

**A Alignment: Change of basis 103**

**B Rockstar: Sub-halos and dwarf galaxies as satellites 109**

**C Phase spirals in other cosmological models 117**
C.1 Phase spirals in GARROTXA RAMSES . . . 117

**D Density and breathing 121**

**E Correlations 125**

**F Bending populations 131**

**G Arania's streams** **133**

**H Complete Fourierograms** **135**

**I List of publications** **141**
I.1 Articles in refereed journals (First author) . . . . . 141
I.2 Articles in refereed journals (Co-author) . . . . . 141
I.3 Non-Refereed conferences contributions (First author only) . . . . . 141

**Bibliography** **143**

# List of Abbreviations

| | |
|---|---|
| **MW** | **M**ilky **W**ay |
| **$\Lambda$CDM** | $\Lambda$ **C**old **D**ark **M**atter |
| **dSph** | **D**warf **S**pheroidal |
| **AMR** | **A**daptive **M**esh **R**efinement |
| **SPH** | **S**moothed **P**article **H**ydrodynamics |
| **LMC** | **L**arge **M**agellanic **C**loud |
| **SMC** | **S**mall **M**agellanic **C**loud |
| Gaia **DR2** | Gaia **D**ata **R**elease 2 |
| Gaia **DR3** | Gaia **D**ata **R**elease 3 |
| **SNe** | **S**uper **N**ovae |
| **SFH** | **S**tar **F**ormation **H**istory |

CHAPTER 1

# Introduction

## 1.1 From early astronomy to the current paradigm of galactic formation

The Milky Way appears as a luminous band on the celestial sphere. For thousands of years, people have looked up at the night sky and marveled at the bright band of light that stretches across the sky, and many cultures have created myths and legends to explain its origin. The Milky Way was central to Mayan cosmology, who believed it was the road to *Xibalba*. Abd Al-Rahman Al Sufi (903-986 d.C.) observed the galaxy Andromeda (which was described as a "little cloud") and the Magellanic system. It wasn't until Immanuel Kant that the Milky Way was proposed as a system with a structure similar to the Solar System, where the objects (stars) rotate around a centre with similar orbits. He suggested the existence of other Island Universes which were observed as nebulae.

The last half of the XIX and XX centuries were marked by the discoveries of these nebulae and in this same century, spectroscopy was first used to study astronomic objects. The Great Debate of Shapley and Curtis (Washington, Smithsonian, April 26th 1920) inspired new questions about the nature of galaxies and marked the moment the astrophysics of galaxies was born. In 1936, Hubble published a morphologic classification of the observed galaxies, where different characteristics were taken into account, like the dominance of the bulge over the disk, spiral structures, etc. The "early types" galaxies were elliptical and "later types" were spiral galaxies. Later that century, de Vaucouleurs updated this classification system by including the presence of the bar and more pronounced spiral arms.

The decades of the 1960s and 1970s were key to establishing the modern paradigms of cosmology, with two main discoveries of vital importance in understanding galaxies' formation and evolution. Firstly, the discovery of the Cosmic Microwave Background (CMB) in 1965 by Penzias and Wilson provided strong evidence for the Big Bang theory, which describes the origin of the Universe. In the context of galaxy formation, the CMB played a significant role in the understanding of the formation of the first structures in the Universe. Secondly, the observed stellar matter was not enough to explain the rotation curve detected in different galaxies. The discovery of Vera Rubin (1974) was decisive in establishing the concept of an unseen mass called dark matter.

Thus, the modern cosmology models evolved to then arise the Lambda Cold Dark Matter model ($\Lambda$CDM). This model is a cosmological framework that describes the structure, composition, and evolution of the Universe. It combines two fundamental components: lambda ($\Lambda$), which represents dark energy, and a cold dark matter. This model has successfully explained many observations such as the large-scale structure of galaxies and clusters, but it also offers predictions for other aspects of galaxy formation and evolution. In 1978 White and Ress suggested that dark matter halos are formed by hierarchical grouping,

whereas the luminous content of galaxies arises from the cooling of infalling gas in said halos. This model encloses the modern ideas of galaxy formation. In the 1980s and 1990s, the CDM was further developed and then studied with analytical models, N-body models, and semi-analytic approaches.

## 1.2 Galaxies in the context of ΛCDM

Galaxies are not isolated objects, but are part of a larger cosmic framework and form and evolve over large scales of time. The most important principle in cosmology is that the Universe is *homogeneous* and *isotropic*. Its geometric properties are defined by its curvature, and the scale factor $a(t)$, which changes with time. In the ΛCDM model, ∼70% of energy is dark energy due to lambda (Λ), ∼26% is cold dark matter, and ∼4% is conformed by baryonic matter (Hinshaw et al., 2013; Aghanim et al., 2020).

In the context of the ΛCDM model, galaxies are assembled in a hierarchical way, where smaller and lower mass objects collapse, interact, and suffer mergers over their history, forming more massive haloes, which can be represented as merger trees (White and Frenk, 1991; Kauffmann, White, and Guiderdoni, 1993; Springel et al., 2005). Eventually, they form the large-scale structures that we observe today, distributed along the cosmic web, a web-like pattern forming vast cosmic structures such as filaments, clusters, and superclusters. These structures arise due to the gravitational attraction of matter (both dark and baryonic) and are characterized by the initial conditions set during the early Universe. In this early Universe, the density perturbations, which were caused by quantum fluctuations during inflation, grew nonlinearly, and led to the formation of virialized dark matter halos. As a result, the densest regions of the Universe became increasingly dense, eventually reaching a point where they start to collapse and became gravitationally bound halos.

Virialization is the process by which a gravitationally bound structure such as a halo of dark matter or a cluster of galaxies becomes stable. This process results in the internal kinetic energy of the halo being -1/2 times the gravitational potential energy. This virialization process is a necessary condition for the formation of a stable structure. When halos are formed, they create the gravitational potential wells in which baryonic matter falls. Initially, the gas collapses under the influence of gravity by loosing energy through radiative processes. The angular momentum of the collapsing gas causes it to flatten into a disk-like structure (Mo, Mao, and White, 1998), that will eventually form a dense, rotationally supported galactic stellar disk. The disk can be formed when energy dissipation occurs at larger scales than the local Jeans length and angular momentum can be transferred outwards from inner parts. The formation of the first stars (Population III), made of primordial gas, is still being studied (Neeleman et al., 2020). On the other hand, the so called Population II can easily be born when the gas in the first galaxies is more metal-rich and therefore it can cool through different radiative processes. The metal enriched gas can then collapse and reach densities high enough to initiate nuclear fusion reactions. In this process the gas is highly unstable and can fragment into smaller clumps or cores creating a number of stars with a variety of masses. The number of stars at each mass range is defined by the so called Initial Mass Function which is still under study and may not be unique (Kroupa, 2001).

A high number of stars were formed in the Cosmic Noon, estimated between redshift ($z$) 3 and 1, corresponding to a lookback time of about 8 to 12 Gyr (Madau and Dickinson, 2014). This marked a crucial phase in the formation and assembly of galaxies, particularly massive galaxies. At these times, small, gas-rich galaxies interacted and merged to form larger and more massive galaxies. These mergers triggered vigorous star formation episodes, leading to the rapid growth of galaxies. However, massive galaxies would have begun to form much earlier than the Cosmic Noon according to recent results from the

James Webb Space Telescope (JWST), which show an unexpected abundance of relatively bright galaxies at $z > 10$ seen with this telescope (Atek et al., 2023; Harikane et al., 2023; Labbé et al., 2023).

Galaxies can display varied morphologies based on their structural and dynamical attributes. Following gas-rich mergers, as already mentioned, the gas settled into disk-like structures, causing galaxies to exhibit their distinct structured morphologies as a flattened disk. They can also form disks via gas accretion from filaments or gas cooling in the circumgalactic medium. They can also develop non-axysimmetrical structures such as spiral arms. In contrast, elliptical galaxies lack a disk structure and are upheld by velocity dispersion. Irregular galaxies, which lack a distinct elliptical or disc shape, are another type of galaxy. Within the lower mass range, there are Dwarf Spheroidal, which are abundant in our Universe. However, they emit less light and present more difficulties in terms of observation. All these different morhpologies provide a rich and varied Universe, where each type of galaxy tells about its own formation, environment and evolution processes.

The ΛCDM cosmological model has proven successful in predicting and explaining the structure and evolution of the Universe on a large scale. However, at scales smaller than ∼1 Mpc and masses smaller than $\sim 10^{11}\ M_{\odot}$ this theory has had difficulties in reproducing observations (Bullock and Boylan-Kolchin, 2017). For instance, the *missing satellites problem* arises when the theoretical models failed to reproduce the observed number of small satellite galaxies around larger host galaxies. In ΛCDM simulations of galaxy formation and evolution, large galaxies like the Milky Way are typically surrounded by numerous smaller satellite galaxies (Kauffmann, White, and Guiderdoni, 1993; Klypin et al., 1999b; Klypin et al., 2015). However, we observed a lower abundance of these objects. In posterior observations, there were many new dwarfs discovered which brought the number of satellites close to the predictions by theoretical models (Kim, Peter, and Hargis, 2018), solving this tension between observations and the ΛCDM model. There are also other solutions for this problem which propose the tuning of the baryonic components of the simulations, or use alternative dark matter models.

Another small-scale challenge of the ΛCDM cosmological model is the *Too-big-to-fail* (Boylan-Kolchin, Bullock, and Kaplinghat, 2011; Boylan-Kolchin, Bullock, and Kaplinghat, 2012; Garrison-Kimmel et al., 2014), where relatively massive sub-halos fail to form galaxies. It was suggested that this is probably due to the combination of stellar feedback, tidal or ram-pressure processes in groups and clusters where the gas is being stripped from satellite systems (Tomozeiu, Mayer, and Quinn, 2016; Ostriker et al., 2019). There are many other small-scale discrepancies, such as the orbit planes of the satellites (Pawlowski and Kroupa, 2013; Sawala et al., 2023), in which the distribution of the satellite orbits and positions seems to more be non-homogeneus in the observations compared to simulations. Even though there are still other unresolved small-scale discrepancies, the ΛCDM cosmological paradigm provides a theoretical frame in which we can develop numerical simulations to understand our observed Universe.

## 1.3 Numerical simulations as a tool to study disk galaxies

The complex behavior of galaxies has always been a key question in astronomy. Understanding and dynamics that have given shape to our Galaxy and its surroundings requires a comprehensive approach that extends beyond observational data. These observations of the current state of the Universe represents merely a single snapshot of its ongoing evolution. Thus, simulations provide a powerful tool to investigate complex systems, such as galaxies, galaxy clusters, or the large-scale structure of the Universe over cosmic timescales. These numerical tools are useful to build theoretical models in order to explain the present day observations, and serve as a complement where these observations might be limited due to the state of current technology,

The history of the initial N-body simulations in the field of galaxy formation and evolution can be traced back to Holmberg's early experiments with light bulbs in 1941, which used light detectors. Since the light flux diminishes with the square of the distance, this problem was analogous to gravity-based simulations. In the 1960s, astronomers first began to use computer simulations to model the evolution of galaxies. In 1960, P. O. Lindblad performed a two-dimensional numerical simulation of the galactic structure. In 1972 Toomre and Toomre studied bridges and tails fromed in galaxies in interaction in a set of models. Their disk consisted of several rings with 12 up to 36 particles. These numerical methods allowed for the direct integration of the equations of motion for a galactic system and could generate far more accurate representations of a galaxy's evolution than the analytical techniques of the previous decade. When Vera Rubin provided evidence for the existence of dark matter (1978), the simulations also started modeling this component.

The early simulations computed directly the interaction between each particle individually and reached a computational limit. Soon, new algorithms were developed, such as creating meshes for particles to efficiently compute forces. For example, in 1986, Barnes and Hut created the tree code, which efficiently calculated the gravitational interactions between numerous particles or bodies in a system. The algorithm constructs a hierarchical tree structure that represents the spatial distribution of particles. The simulation space is divided into smaller cells, and particles are grouped into nodes of the tree based on proximity. The gravitational forces are calculated using an algorithm that approximates distant particle groups as a single combined body, leading to a reduction in computational complexity from $O(N^2)$ to roughly $O(NlogN)$. This approach of hierarchy accelerated N-body simulations, rendering models of complex N-body systems like galaxies or star clusters with larger numbers of particles feasible.

With the development of computers and numerical techniques, the simulations could add more particles to their analysis which could generate far more realistic representations of a galaxy's evolution and allowed astronomers to investigate a wide range of phenomena such as stellar structures and spiral arms. In addition, astronomers began to incorporate additional physical processes such as star formation, gas dynamics, and radiation transport.

However, in order to include the collisional baryons in the simulation, it was essential to tackle the challenge of solving the hydrodynamical fluid equations. This task proved to be much more complex than dealing with the dynamics of dark matter alone. In addition, numerical simulations must take into account several additional physical factors, such as radiation fields, magnetic fields, and non-thermal particle components. In 1977 the Smoothed Particle Hydrodynamics (SPH) technique was implmented to simulate the behaviour of fluids, firstly in the context of star modelling (Lucy, 1977; Gingold and Monaghan, 1977) and then implemented in simulations of galactic evolution (e.g. Hernquist and Katz 1989). These techniques to simulate the gas component allowed us to understand processes such as gas accretion onto galaxies, interstellar medium, star formation, the feedback mechanisms from stellar activity, and the interplay between gravity and the fluid properties of the gas. It allowed for a more detailed and realistic representation of how gas interacts with other components of galaxies, such as stars and dark matter, and thus, a more comprehensive understanding of various astrophysical phenomena.

For a long time, one of the difficulties in computational galaxy formation were the simulation of star-forming, disk galaxies. Early works yielded galaxies with a dominant stellar spheroidal component and a less prominent disk (Navarro and White, 1994; Steinmetz and Navarro, 1999). The galactic systems are often modeled by a large number of individual particles, each of which has a position and velocity that is updated over time. However, if there are too few particles, the simulated galaxy will not be able to accurately represent the distribution of mass and angular momentum within the real galaxy, leading to a loss of angular momentum. This problem, called the *angular momentum catastrophe*, was due to an

artificial loss of angular momentum caused by poor resolution which derived in other numerical effects (Abadi et al., 2003; Okamoto et al., 2003), such as numerical viscosity. There were two main techniques that galactic simulations could use to mitigate this angular momentum loss. One approach was stricter conservation of angular momentum (Serna, Domínguez-Tenreiro, and Sáiz, 2003), which led to the first disks being found in cosmological simulations even at low numerical resolution. The other solution was to use high-resolution simulations which allowed for a larger number of particles, which helped to better resolve the distribution of mass and angular momentum within galaxies (Governato et al., 2004; Naab et al., 2007).

Other effective methods to avoid angular momentum loss were a more effective scheme for stellar feedback to counteract the excessive radiative losses of star-forming gas, and to expel material responsible for the formation of the dominant stellar bulge (low-angular momentum material, Brook et al. 2011; Brook et al. 2012). The efficient regulation of star formation driven by stellar feedback largely improved simulated disk galaxies. Along with the increase in resolution, the zoom-in method helped get more realistic disks (e.g. Klypin et al. 2001). This technique allows to increase the resolution in the regions of interest. within the simulation of a cosmological box. All these methods led to different types of simulations, represented in Fig 1.1, from large-scale simulations to zoom-in simulations to study specific galactic models.

In early simulations of interacting galaxies, satellites were simulated as rigid objects combined with dynamical friction formulae instead of a live object with numerous particles (Bosch et al., 1999). When an external galaxy enters the virial radius of the host, there is a loss of energy. However, in simulations with a rigid satellite, instead of internally losing this energy, there was a loss of energy in their orbit, which decayed too rapidly. This was solved by having a live satellite galaxy (Jiang and Binney, 2000; Fujii, Funato, and Makino, 2006). Furthermore, if the resolution was not high enough, sub-haloes were susceptible to early tidal disruption and loss of substructure, known as the *overmerging problem* (Klypin et al., 1999a; Diemand, Moore, and Stadel, 2004; Bosch et al., 2018).

All these developments have lead to a variety of simulation techniques which are performed for different purposes. One of the most notable simulations was the Millennium Simulation (Springel et al., 2005), which is a dark matter-only simulation of $2160^3$ particles to reproduce the large-scale structure properties of the Universe, up to 500 Mpc $h^{-1}$. Nowadays, simulations with more than several billion particles are performed with a variety of codes and algorithms, *e.g.* IllustrisTNG (Pillepich et al., 2019; Nelson et al., 2019), Horizon-AGN (Kaviraj et al., 2017), FIREbox (Feldmann et al., 2023), among many others.

## 1.4 N-body algorithms and hydrodynamics for simulations of galaxy evolution

The behavior of collisionless matter could be described by directly solving the equations of motion to calculate the positions and velocities of each particle. However, this is not feasible due to the high number of particles representing stars and dark matter. Thus, we resort to solving the phase space distribution with N-body methods, which optimize the calculations by hierarchically grouping particles with different techniques. The simplest algorithms for collisionless N-body methods consist of updating the position and velocities of $N$ particles by solving the gravitational acceleration/force of the ensemble of particles, representing the distribution of matter. These can be calculated for each particle individually, such as particle-particle (PP), or for grouping of particles such as Tree methods, the particle-mesh (PM), or Particle–Particle–Particle–Mesh ($P^3M$). For a more detailed explanation of all these methods, see Dolag et al. (2008).

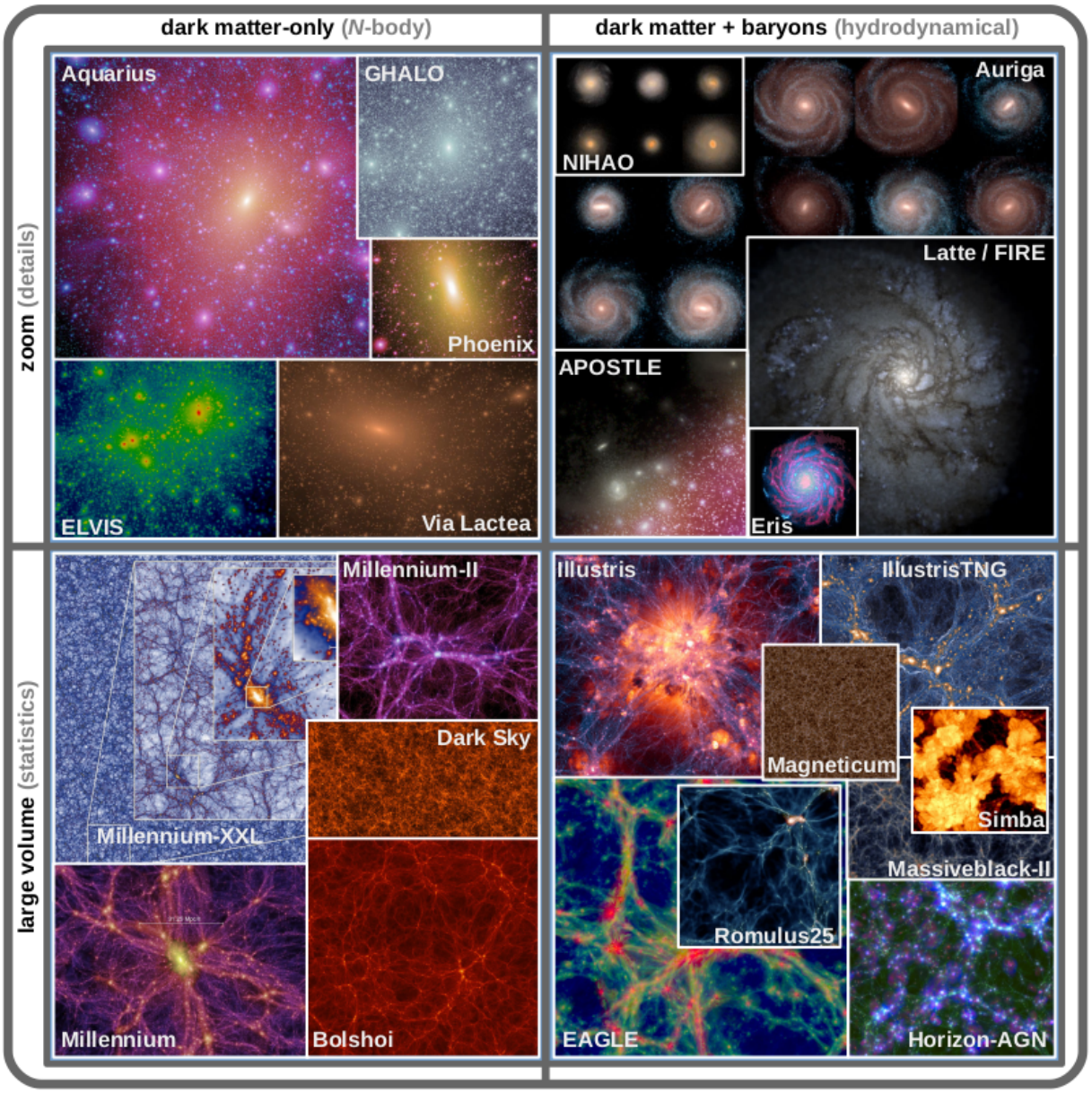


FIGURE 1.1: Different types of simulations, from large-scale structure to provide statistical samples of galaxies (bottom panels), to the zoom-in simulations to observe more details of certain gropus of galaxies (top panels). Simulations can be made with only dark matter with N-body algorithms (left panels) or they can include baryons, with a hidrodynamical component (right panels). From: (Vogelsberger et al., 2020).

Combining N-body methods with hydrodynamics, along with prescriptions for stellar formation and feedback, adds a new dimension to the study of the origin and evolution of galaxies. It allows us to study, among other things, but especially relevant for this thesis, the gas and stellar age distribution in different types of galaxies and the behavior of the properties of said gas in interacting galaxies. At galactic scales, it influences star formation and the physics and composition of the interstellar medium. There are several techniques for simulating gas in galactic simulations. In SPH, the gas is treated as particles using Lagrangian methods. Each gas particle represents a cloud with certain physical properties such as mass, density, temperature, and velocity. Its distribution is given by a smoothing kernel, which allows the interpolation of physical quantities between particles, allowing the calculation of gradients and integrals over the fluid.

In Adaptive Mesh Refinement (AMR, Berger and Oliger 1984) the space is divided into a three-dimensional mesh, which is further subdivided and reduced according to the desired level of resolution for the gas in each cell, where the densest regions can reach the maximum level of refinement. This dynamically refines the mesh in regions of complex structure or strong gradients, allowing detailed modeling of gas dynamics, shock fronts, and the formation of small-scale structures within galaxies. Due to this dynamic refinement of the mesh, the computational cost increases, which can limit the size and duration of simulations. In addition to this, treating gas as a cell complicates gas tracking since the AMR code updates the gas cells at each timestep, whereas SPH identifies each gas particle. However, the advantages of AMR are the high spatial resolution in the regions of interest and its large dynamic range.

Hydrodynamical methods have to be complemented by other galactic processes, in which the gas interacts with stars and vice-versa. These are the subgrid physics, in which gas cooling, stellar formation, and feedback take place. Nowadays, both N-body algorithms and hydrodynamics codes are often combined, and several major galaxy formation simulation codes are available to perform simulations with these algorithms. For instance, ART (Kravtsov, Klypin, and Khokhlov, 1997) and RAMSES (Teyssier, 2002) both use a multilevel particle-mesh algorithm for the collisionless part and AMR for the hydrodynamical one. Other codes such as GADGET-2 and ChaNGA use SPH. On the other hand, codes such as AREPO and GIZMO use moving-mesh (between SPH y AMR).

The physical processes involved in the formation and evolution of galaxies, in a cosmological context, include a wide range of spatial, energy, and temporal scales. This makes it impossible to include all of them in a single simulation, but some of these phenomena can be added manually. In the case of smaller scales than the minimum resolution, the subgrid (or sub-resolution) physical models play an important role. The subgrid physics models are models that are calibrated using higher resolution simulations, or observations, to reproduce the effects of the processes occurring at non-resolved resolutions on the simulated larger scales. In the case of the AMR codes, the stellar particles interact with the gas cell in terms of star formation and feedback. In the case of star formation, a stellar particle is created in a gas cell when certain density and temperature conditions are met, depending on the selected code or star formation recipe. In addition to this, there is an efficiency parameter that regulates star formation. Feedback recipes are used to model the effects of processes such as supernovae explosions, active galactic nuclei (AGN) activity, and stellar winds. These processes can have a significant impact on the evolution of a galaxy by regulating the formation of stars, the distribution of gas, and metallicity in both stellar and gaseous components.

The subgrid physics incorportate physical processes occurring at scales smaller than the cell size, and include radiative cooling, chemical enrichment, feedback mechanisms from stellar winds, radiation and active galactic nuclei (AGNs). Calibration of these models involved comparing the simulated galaxy properties with a broad range of observations, such as the galaxy luminosity function, gas content, galaxy clustering, and various scaling relations. Currently, there is no single consensus on the specific sub-grid

models and parameter choices to be used in simulations, and there is ongoing exploration and debate regarding the optimal choices. Different research groups and simulations employ a range of sub-grid prescriptions, depending on the goals of the simulation and the physical processes that are being studied, with the help of libraries such as Smith et al. (2017). In some cases, multiple feedback recipes may be combined to better capture the complex interplay between different physical processes.

## 1.5 Galactic disk's perturbations

Disk galaxies, like the Milky Way (MW), are relatively abundant in our Universe, being about 72% of the observed galaxies (Weinmann et al., 2006; Delgado-Serrano et al., 2010). Although in the Local Group, the more numerous are the dwarf galaxies, there are three prominent spiral galaxies: the MW, Andromeda, and M33. The stellar disk of this type of galaxies has complex dynamics due to the different structures of the galaxy and past interactions. Thus, studying the physics of these stars is of vital importance to understand the behavior of the galaxy and its environment. In this thesis, we focus on the dynamics of the stellar disk of this kind of galaxies.

Galaxies can undergo a variety of processes in their lifetime from diverse sources. As galaxies form and evolve, they are likely to interact with each other depending on their environment at that point in their evolution. For instance, a *major merger* takes place when a progenitor galaxy encounters another galaxy of comparable mass (around a ratio of mass of 1:4, Lotz et al. 2010) and they interact gravitionally. Mergers at this scale cause a deep change in the morphology of the galaxies involved and may result in the formation of entirely new shapes and structures (Toomre, 1977; Barnes and Hernquist, 1992; Athanassoula et al., 2016).

On the other hand, when a less massive satellite approaches the galactic disk (*minor merger*), it interacts with said disk at a more local scale. This interaction may disrupt the original orbits of the stars by displacing them when they are gravitationally pulled and pushed. Furthermore, not only does the direct gravitational interaction of the satellite affect the stellar disk. When a massive object enters the virial radius of a galaxy host, it generates density wakes through gravitational scattering of particles, which pull back on the satellite. This process is known as dynamical friction, resulting in the loss of both angular momentum and energy of the satellite (Binney and Tremaine, 2008). The density wakes produced in this process can also exert a torque on the stellar disk. In addition to this, a passing satellite can also bring new gas and alter star formation (Mihos and Hernquist, 1994; Teyssier, Chapon, and Bournaud, 2010; Ruiz-Lara et al., 2020).

Depending on the angular momentum vector and orbit associated with the external object's fall, satellites can reach the disk at different angles and velocities. The gravitational attraction from the host results in the strip of stars and/or gas from the satellite due to tidal effect when approaching the pericenter of the orbit. The liberated material populates both the leading and trailing tidal streams that follow the satellite's orbit. The satellite's progenitor may either continue to orbit the disk or reach a point in which it dissolves entirely (Oh, Lin, and Aarseth, 1995; Johnston, Hernquist, and Bolte, 1996).

Apart from other galaxies, also cold gas can fall into the virial radius along filaments and ultimately fall into the disk, bringing new gas into the system. The misaligned accretion of high angular momentum cold gas from the cosmic web or from a cooling hot gas halo (Jiang and Binney, 1999; Roškar et al., 2010) can be the source of perturbation of the galactic disk (Sellwood, 2010) and also result in the creation of new stars. Furthermore, it can serve as amplification mechanisms of the vertical perturbations of the disk when the gas falls along warps (Khachaturyants et al., 2022).

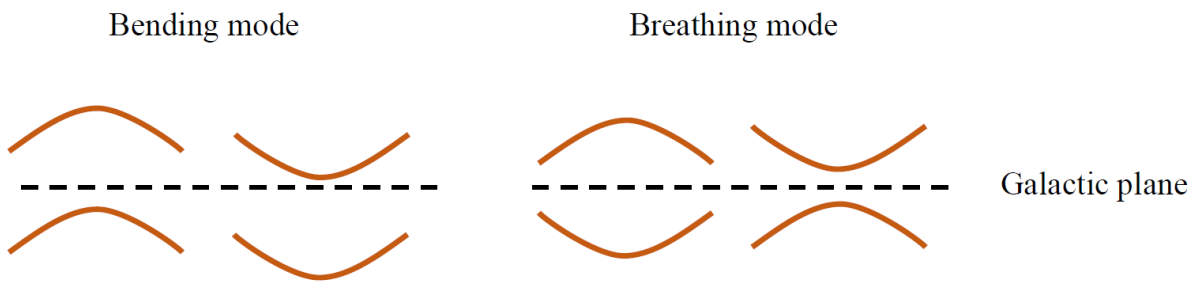


FIGURE 1.2: Bending and breathing modes of the stellar disk. The dotted black line represents the galactic plane, and the displacement of the stars with respect to this plane are represented by the solid orange line. The bending mode of the disk is a systematic deviation from the plane, whereas the breathing mode follows an expansion or contraction behavior.

However, sources outside the galaxy, like satellites or misaligned gas, are not the sole factors that can cause perturbations. Inner features of the galaxy can also be a source of instability to the stellar disk. Such features, like a central bar or the spiral arms can influence star formation, induce gas compression, resonances and radial migration (Binney and Tremaine, 2008; Athanassoula, 2013; Sellwood and Masters, 2022). In addition to this, the bar can become unstable and buckle vertically. In this process, the bar structure bends and tilts out of the plane of the galactic disk (Łokas, 2019). The buckling motion typically occurs perpendicular to the plane of rotation of the galaxy, which exerts a force on the stars of the galaxy (Khoperskov et al., 2019).

All these external and internal perturbations can induce non-equilibrium features in the structure of the stellar disk, and stellar velocities. In particular, for the vertical direction, these disturbances can be manifested as wave-like patterns in the vertical stellar density and vertical velocities (like in the case of the Solar Neighborhood, Widrow et al. 2012). For instance, external interactions with satellites may cause observable changes in the vertical distribution of stars in the galactic disk (Gómez et al., 2017). These vertical perturbations can be measured as bending and breathing waves according to the parity in density and vertical velocity as illustrated in Fig. 1.2.

One of the most prominent vertical deformations observed in late-type galaxies is the disk warp (Binney, 1992). The warp is a bending or twisting of the more external parts of the disk in the vertical direction, and it can be seen as a systematic deviation of the disk plane from a flat configuration, with a typical shape of an S (mode $m = 1$). A significant number of the observed disk galaxies exhibits this bending pattern (Reshetnikov and Combes, 1998; Ann and Park, 2006; Reshetnikov et al., 2016). The cause of the warp is still being studied in different simulated models of galactic disks. The studies of Voort et al. (2015), Gómez et al. (2017), and Semczuk et al. (2020) show different vertical patterns produced by close satellite encounters, distant flybys of massive companions, accretion of misaligned cold gas, and re-accretion of cold gas from the progenitors of gas-rich major mergers.

Over time, multiple minor interactions, typical in the ΛCDM paradigm, cause the stars' orbits to become dynamically hotter. This increases the stars' random movements, gradually heating the disk over time (Kazantzidis et al., 2009; D'Onghia et al., 2016), leading to flaring - an increase in the disk's scale height with greater distance from the Galactic center. The heated disk, with stars populating hotter orbits, becomes less responsive to perturbations.

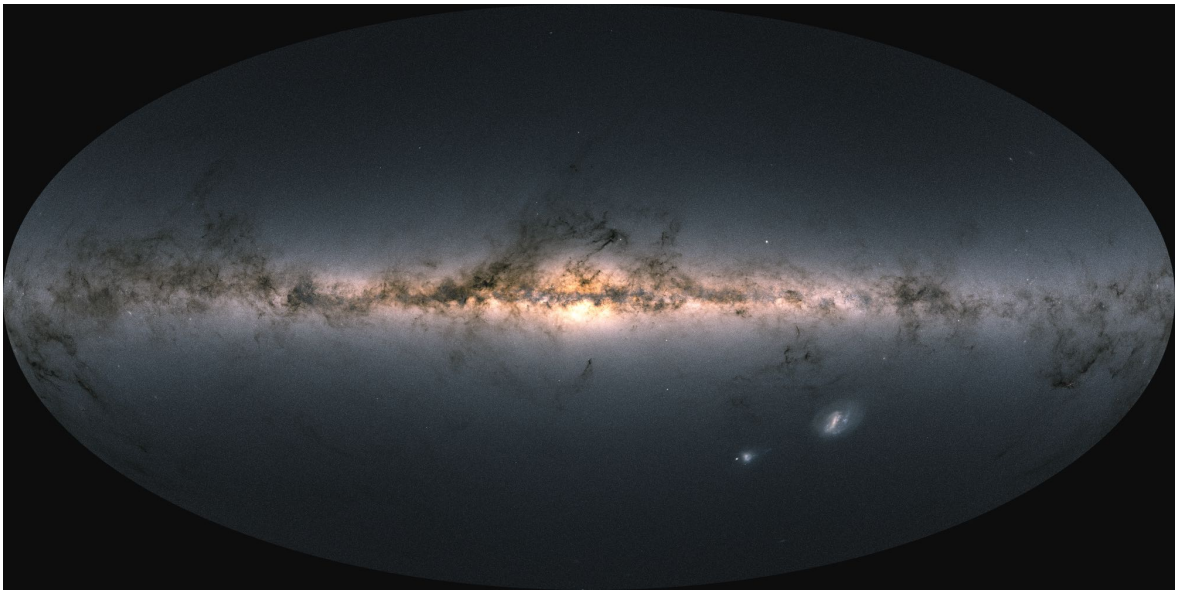

FIGURE 1.3: The Milky Way as seen by *Gaia*. From European Space Agency (ESA).

## 1.6 The Milky Way

The MW (Fig. 1.3) is of great interest to astronomers and scientists because it is our home Galaxy, and provides a unique laboratory for studying the formation and evolution of galaxies. One of the goals of modern galactic astrophysics is to determine which processes have given shape to the MW. By observing the stars, gas, dust, and other components of the MW, astronomers are able to gain insights into how galaxies form, how they evolve over time, and what processes govern the distribution of matter within them. Our Galaxy's disk is a rotating structure composed of stars, gas and dust, held together by gravity. It has different components that are well described in the review by Bland-Hawthorn and Gerhard (2016). The light-dominant component is its thin stellar disk but the existence of vertically thicker component (thick disk) has been established since Gilmore and Reid (1983). The thin and thick disks are chemically distinct (Bensby, Feltzing, and Oey, 2014; Hawkins et al., 2015; Masseron and Gilmore, 2015). The set of these structures is surrounded by a dark matter halo, also populated by globular clusters, and debris from galaxy satellites accretion (Searle and Zinn, 1978; Helmi, 2008; Helmi, 2020). The spiral arms extend outward from the galactic center, at which there is also a bar which can be seen as a peanut-shaped bulge (Blitz and Spergel, 1991; Nakada et al., 1991).

Our Galaxy is located in a relatively low-density region (the Local Group), and its total mass is estimated as $0.9 - 1.3 \times 10^{12}\ M_{\odot}$ (Kafle et al., 2012; Watkins et al., 2019). The MW has suffered interactions throughout its history. In the context of hierarchical growth in $\Lambda$CDM, the gravitational potential well attracts matter into the virial radius. For instance, one major merger occurred 10 Gyr ago, with the massive galaxy Gaia-Sausage-Enceladus and the MW progenitor (Belokurov et al., 2018; Helmi et al., 2018). This interaction produced a thick stellar disk and changed the stellar halo morphology and stellar populations (Gallart et al., 2019).

The most massive satellite galaxy currently orbiting the MW is be the Large Magellanic Cloud (LMC), which is believed to be gravitationally bound to the Small Magellanic Cloud (SMC). Their stellar mass is

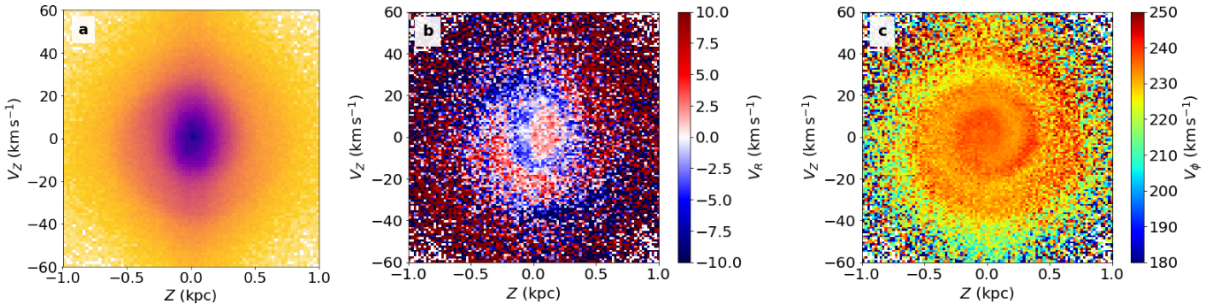


FIGURE 1.4: Local phase spiral of the Solar Neighbourhood as presented in Antoja et al., 2018 with data from *Gaia* DR2. The left panel shoes a 2D histogram of the local phase spiral, and central anf right panel shows this same phase spiral coloured by the cylindrical galactocentric velocities $V_R$ aand $V_\phi$, respectively.

estimated to be 1 $\times 10^9$ and 3.2 $\times 10^8$ $M_\odot$ respectively, and they are at a distance of 50 and 64 kpc from our Sun (Santos-Santos, Dominguez-Tenreiro, and Pawlowski, 2020).

Other dark and baryonic matter in the form of dwarf galaxies have also fallen into the halo of the MW. The Sagittarius Dwarf Galaxy's remnant was discovered in the direction of the Sagittarius constellation (Ibata, Gilmore, and Irwin, 1994). This satellite's core and debris have been widely studied by both observations and N-body simulations to constrain its kinematics and characteristics (Johnston, Spergel, and Hernquist, 1995; Ibata et al., 1996). Its first interaction with the MW is estimated to be between 8 and 6 Gyr ago (Law and Majewski, 2010) when the progenitor could have had an estimated mass between $10^{10}$ and $10^{11}$ $M_\odot$(Niederste-Ostholt et al., 2010). The recurrent interactions with the Sagittarius Dwarf Galaxy may also have induced episodes of stellar formation (Ruiz-Lara et al., 2020). After several orbits, the dSph Sagittarius galaxy is in the process of being disrupted by the gravitational tidal forces of the MW, and its stars and gas are being stripped away and incorporated into the MW's halo. Throughout its history, it has had several pericenters, perturbing the MW's disk (Purcell et al., 2011; Laporte et al., 2019). Its remnant is nowadays one of the closest neighbors of the MW with an estimated mass $10^8$ $M_\odot$.

## 1.7 The *Gaia* era and the Phase Spiral

In the last decade, several studies have shown that our Galaxy's disk is highly perturbed (e.g. Widrow et al., 2012; Williams et al., 2013). Recently, ESA's *Gaia* astrometric space mission has shown further evidence that the MW's disk is vertically disturbed. One discovery of *Gaia* DR2 (Gaia Collaboration et al., 2018a) was the spiral signal in the vertical phase space (Antoja et al., 2018). This spiral pattern appears in the vertical phase space distribution ($Z - V_Z$) of the stars in the Solar Neighbourhood. In Fig. 1.4 we can see the phase spiral presented in Antoja et al. 2018, which can also be seen when colored by the azimuthal velocity, $V_\phi$, and the radial velocity, $V_R$.

This spiral pattern seems to be a sign of an ongoing phase mixing process. This process occurs when a perturbation alters a system in which there are different motion frequencies. These differences in motion cause neighboring elements to evolve at different rates. Over time, there is a loss of coherence between the positions and velocities of the different elements, the phase-space distribution becomes increasingly striated and eventually the coarse grained distribution appears uniform. Stars, for instance, have complicated orbits defined by different frequencies, both inside the galactic plane (planar motion) and perpendicular to the galactic plane (vertical motion). It is the spread of vertical frequencies that generates this phase spiral.

In the studies of Antoja et al. (2018) and Binney and Schönrich (2018) they present a simplified model for the origin of the phase spiral of the Solar Neighbourhood after the passing of a satellite. If we consider the Galactic's vertical component of the gravitational potential which can be approximated by an anharmonic oscillator, we find that the orbits of the stars follow an ellipsoidal pattern in the phase plane $Z - V_Z$. However, the stars have different vertical frequencies, $\nu$. In a state of equilibrium, the local projection of $Z - V_Z$ appear smooth. However, when the galaxy suffers an interaction with a nearby object, the stars receive an energy kick in the vertical direction. The differences in vertical frequencies (which depend on the potential of the galaxy, the galactocentric radius and height over the galactic plane), result in a spiral shape in the vertical plane, which winds up over time. This spiral pattern can also be seen when colored by $V_\phi$, due to the dependence of the frequencies on the angular momentum, and also $V_R$, since the in-plane motions are also coupled with the vertical motions.

The estimation of the time of the perturbation has pointed to some of the previous passages of the Sagittarius Dwarf Galaxy, estimated to be between 200 and 1000 Myr ago (Law and Majewski, 2010; Purcell et al., 2011; Vasiliev and Belokurov, 2020). Further modeling has confirmed that the phase spiral can be a consequence of the galaxy tidal interaction with the dwarf (Binney and Schönrich, 2018; Laporte et al., 2019; Li and Shen, 2020; Bland-Hawthorn and Tepper-García, 2021; Hunt et al., 2021; Widmark et al., 2021; Gandhi et al., 2022). Nonetheless, other authors have presented alternative hypotheses in which the bar buckling (Khoperskov et al., 2019) or the halo substructure (Darling and Widrow, 2019) generate bending waves that can also result in phase spirals.

Since its discovery in 2018, the phase spiral phenomenon has been first studied with toy models and then with more complete N-body simulations. In the studies of Laporte et al., 2019 and Bland-Hawthorn and Tepper-García, 2021 they use these types of simulations and study the interaction of a MW-like disk and a perturber similar to Sagittarius, being the mass of the perturber $6 \times 10^{10}$ and $2 \times 10^{10}$ $M_\odot$, respectively. In the case of Bland-Hawthorn and Tepper-García, 2021 they analyze the vertical and planar coupled motions which results in the phase spiral weighted by $V_\phi$ and $V_R$.

However, the phenomenon of the phase spiral is still not well understood. The studies mentioned above consist of analytical models using the impulse approximation or isolated N-Body simulations considering a single perturber aimed at reproducing the formation of the phase spiral in simplified and controlled conditions. Although a single satellite galaxy could be the dominant cause of the phase spiral, it is not straightforward to infer how the addition of processes such as the gas effects or multiple perturbers and their derived collective effects (Weinberg, 1989) will influence the vertical perturbations.

## 1.8 Aims and scope of this thesis

The main goal of this thesis is to analyze the vertical deformations of galactic disks, with a special focus on the phase spiral phenomenon, and their relation to external perturbations. For this purpose, we have adopted two different approaches: A theoretical approach in which we use cosmological simulations for the study of a model of a disk galaxy similar to the MW, and the observational one with the analysis of the data from *Gaia* DR3.

For the theoretical study with simulations, we study the vertical behavior of the MW-sized model of the high resolution hydrodynamical + N-body zoom-in simulation GARROTXA (Roca-Fàbrega et al., 2016). We identify the signs of vertical perturbation of the disk of this specific model and its relation to external and internal influences. At the cost of having lower resolution and a larger analysis complexity than pure N-body galaxy models, we take one step further and gain realism by including most of the known

physical mechanisms that shape galaxies: gas, star formation, and multiple satellites perturbing the disc. In addition, we are able to study the full history of the galaxy, all in a self-consistent manner.

The study of the dynamics and phase spirals in cosmological simulations is a challenge due to its complexity and especially the resolution limits of these types of simulations. In addition, the lack of tuning of specific conditions makes it difficult to compare with the Milky Way. However, our model, which is described in Chapter 2, allows us to explore the disk and its phase space with enough resolution to detect and characterize the phase spirals, as well as have enough snapshots available to track the disk dynamics.

In the observational part of this thesis, we analyze the results from the *Gaia* DR3 to further explore the phase spiral seen in our Galaxy, by observing the differences when exploring in different azimuths and radius. We also infer the impact time of the perturbator.

There are challenging questions that we aim to answer in this thesis.

- **Can we use cosmological simulations for the study of disk dynamics?** Only recently we have the computational power to study a galaxy as a whole. In this thesis, we discuss the advantages of using this kind of simulation to study the vertical perturbations of the disk, along with insights into the difficulties and complexity they present. In recent years N-body simulations have been used to study different aspects of disk dynamics, including the phase spiral. However, in this thesis, we explore this phenomenon with a cosmological simulation that incorporates gas and all the cosmological context, which, as we will see, is vital to understand the complex vertical behavior of a disk.
- **Are phase spirals common phenomena along the history of galactic disks?** The only real galaxy in which the phase spiral has been observed is our own MW, and only in the regions of the solar Neighbourhood. It is not clear whether this phenomenon can be common and present in other spiral galaxies. However, the study with simulations can help us understand if this is the case.
- **To what extent can other mechanisms, apart from the direct tidal interactions with satellites, affect the vertical behavior of a galactic disk? Which one is the dominant cause of perturbations?** In this thesis, we aim to establish the relationship between the vertical disturbances seen in the simulated galactic disk and multiple perturbations, considering the effects of the halo, satellites, and gas in a more holistic manner. Disentangling the different effects of perturbation and their causes is a challenging task.
- **How does the MW's phase spiral look with *Gaia* DR3?** With this new data release, we gain more information on stars in a more extended region of the MW. This allows us to study the phase space in further regions away from the Solar Neighborhood, and thus have more range in which to infer the time of the phase mixing.

This thesis is structured as follows:

In Chapter 2 we describe in detail all the characteristics of the simulation used for this thesis, from its ancient merger history to the present stellar disk shape. We identify the different density structures of the stellar disk, along with the satellite galaxies orbiting the main system of this model. We also describe the Fourier techniques to analyze the behavior of the different components of the simulation that we have used throughout this thesis.

In Chapter 3, we find and characterize the phase spiral along galactic azimuth, radius and time in the last 6 Gyr of evolution of the galactic system. We find the regions and ages in which the phase spiral is more intense. We also explore their relation to possible external causes.

In Chapter 4, we further analyze the model to detect bending waves and their relation to external and internal phenomena. We perform an exhaustive study of the satellites orbiting the disk of the model and measure the impact of the different components of the model (satellites, dark matter, and gas) onto the stellar disk and study their relation to each other.

In Chapter 5 we analyze the observational data of phase spiral with the *Gaia* DR3. We present the local phase spiral and its variations along azimuth and radius ($L_Z$). We also calculate the impact time for different models of potential for the MW.

In Chapter 6 we conclude with a summary of the results, present our conclusions, and thoroughly answer and discuss the questions presented above. We also reflect on methodology, give our final conclusions and open the door to future prospects of research based on our results.

The results of this thesis provide insight into the complexities of galactic dynamics, while also offering potential avenues for further study of the vertical behaviour of the stars in galactic disks.

CHAPTER 2

# The GARROTXA simulation and methods

## 2.1 General properties

The GARROTXA simulation (GAlaxy high Resolution Runs in a cOsmological conTeXt using ART), presented in 2016 (Roca-Fàbrega et al., 2016), is a set of Eulerian hydrodynamics + N-body simulations obtained using the ART numerical code (Kravtsov, Klypin, and Khokhlov, 1997; Kravtsov, 2003). The simulations in this work were performed in the context of ΛCDM cosmology in agreement with the current concordant cosmological model, with the parameters of $\Omega_0 = 0.3$, $\Omega_\Lambda = 0.7$, $\Omega_b = 0.045$, and $h = 0.7$ (Dunkley et al., 2009). The ART code employs an adaptative mesh refinement technique to selectively increse resolution around regions with a high dark and/or baryonic density. In the GARROTXA suite, the authors used the so called zoom-in technique to allow the refinement (high resolution) only in a region of interest, for instance, where a MW-sized dark matter halo at $z = 0$ resides. First, a low resolution dark matter only simulation is run down to $z = 0$, and then, all dark matter particles belonging to $3R_{vir}$ around the halo of interest are selected and traced back to the initial redshift ($z = 100$ in GARROTXA). A flag is added to all these particles,and then, baryons are added and the simulation is re-run now including all baryonic physics and allowing refinement only in the regions where the flagged dark matter particles reside. The initial low-resolution simulation had $128^3$ particles in a 20 Mpc $h^{-1}$ box, initially covered by a mesh of $128^3$ cells (zeroth level cells). Then, each model was re-simulated from z$\sim$ 1.5 with a smaller value for the minimum mass of the particles i.e., an increased mass resolution in the galactic disk. This was done with the main goal of having enough mass resolution to study the stellar dynamics within the galactic disk. In this thesis, we have used model G.323 (Roca-Fàbrega et al., 2016, see also table 1 and 2), which is a variant of the original set of high-resolution models. It is important to note that this model has significant properties different from the MW (for a further comparison see Roca-Fàbrega et al., 2016), and despite their differences, this model allows us to study the variety of phenomena observed in different disk galaxies. In Fig.2.1 we show the distribution in the cosmological box of the three ingredients of the simulation: Stellar particles (top panels), dark matter particles (central panels) and gas (bottom panels).

The models include gas cooling/heating obtained from tabulated values got by running the CLOUDY radiative transfer code (Ferland et al., 1998) with different metallicities, redshift and the UV-background (Haardt and Madau, 1996). They also include a recipe for a deterministic star formation that needs only three free parameters: the efficiency of star formation, calibrated to supress the overcooling in the star forming regions, the density and the temperature thresholds for star formation. Finally, the stellar feedback (i.e. SNe) is implemented as described in Colín et al. (2010). The energy from SNe and stellar winds is deposited as thermal energy in nearby gas cells by liberating energy from both supernovae and stellar

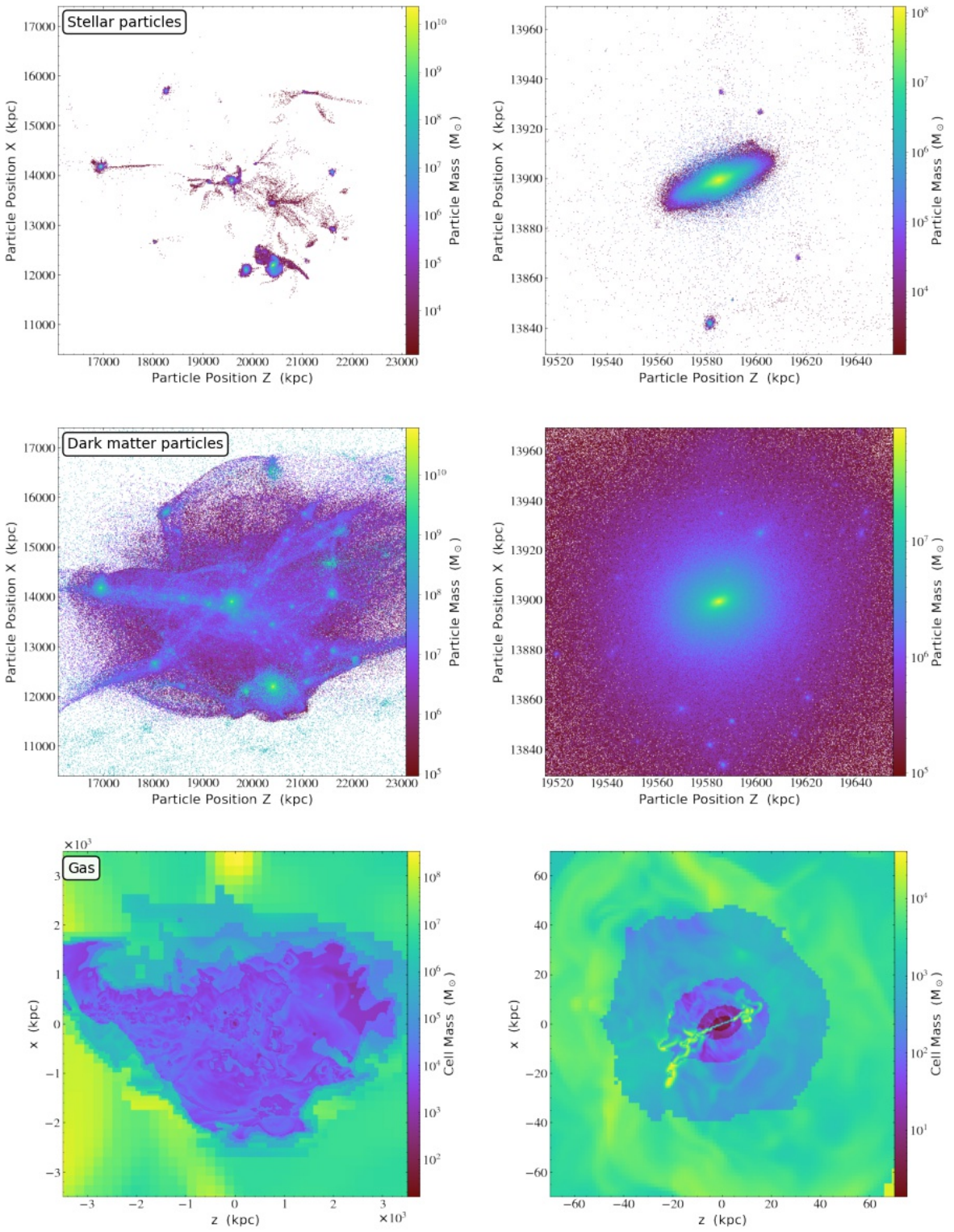


FIGURE 2.1: GARROTXA's MW model G.323 components in the cosmological box (left) and the MW model (right). From top to bottom, stellar particles, dark matter particles and gas cells colored by their respective mass.

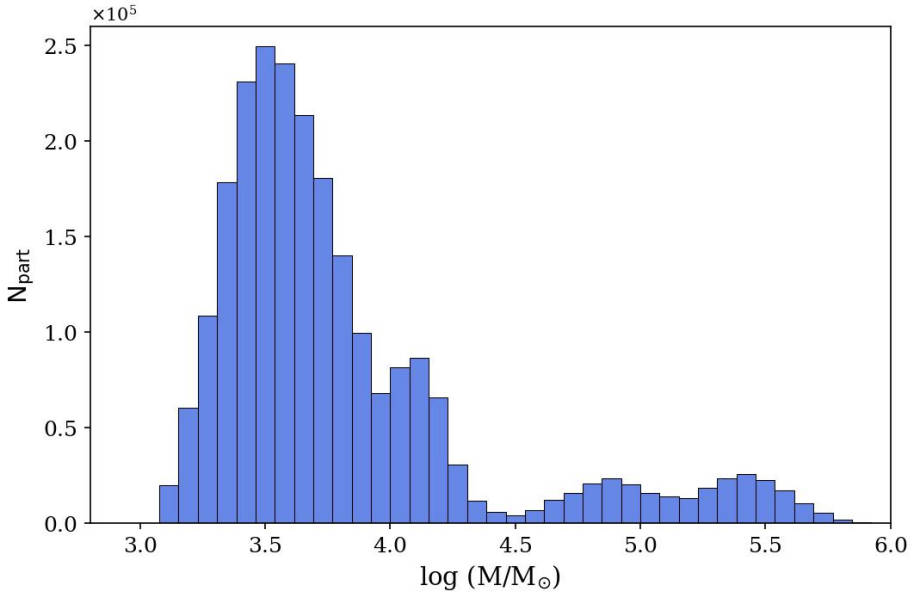


FIGURE 2.2: Mass distribution of the stellar particles inside the $R_{vir}$ at $z = 0$ for model G.323.

winds. This, combined with the star formation recipe, mitigates overcooling and prevents large-scale gas-to-star conversion. Other included phenomena are advection of metals, and UV heating from cosmological background radiation. This simulation does not include Active Galactic Nuclei (AGN) feedback.

From 6.3 Gyr in lookback time until the present we have 190 snapshots available, with a mean time span of 40 Myr between them. This allows us to undertake an exhaustive temporal evolution study of the disk's kinematics and density structures.

The stellar particles have different masses, depending on the conditions in which they are created. Their mass is primarily determined by the properties of the cell gas in which it is created. In Fig. 2.2 we show a histogram of the stellar mass distribution of the stellar particles inside the virial radius. In this model, the mass of stellar particles ranges between $10^3$ and $10^6$, where the 76% of them are less massive than $10^4$ $M_\odot$. Thus, each stellar particle represents an entire stellar population.

## 2.2 Centering and alignment

The first steps of the analysis are loading and reading each snapshot, which were performed with *yt* package (Turk et al., 2011): A Python-based open-source toolkit, which was built for analyzing and visualizing volumetric astrophysical simulation data, including cosmological simulations. It supports various simulation formats, including those from major simulation codes such as ENZO, GADGET, RAMSES.

The simulated galaxy, situated in the cosmological box, is not oriented in any privileged position nor direction. Thus, to establish our reference system, we need to center and align it. To center the galaxy, we calculate its center of mass by iteratively computing it within several shrinking spheres similar to Power et al. (2003). This process identifies the densest region within a dark matter halo which may also be populated by subhaloes. The virial mass, $M_{vir}$, is the total mass within a sphere of radius $R_{vir}$ that encompasses an overdensity of $\Delta(z)$, as defined in Bryan and Norman (1998, BN98 hereafter), where the spherical collapse model is applied to calculate the virial overdensity as a function of redshift. To compare

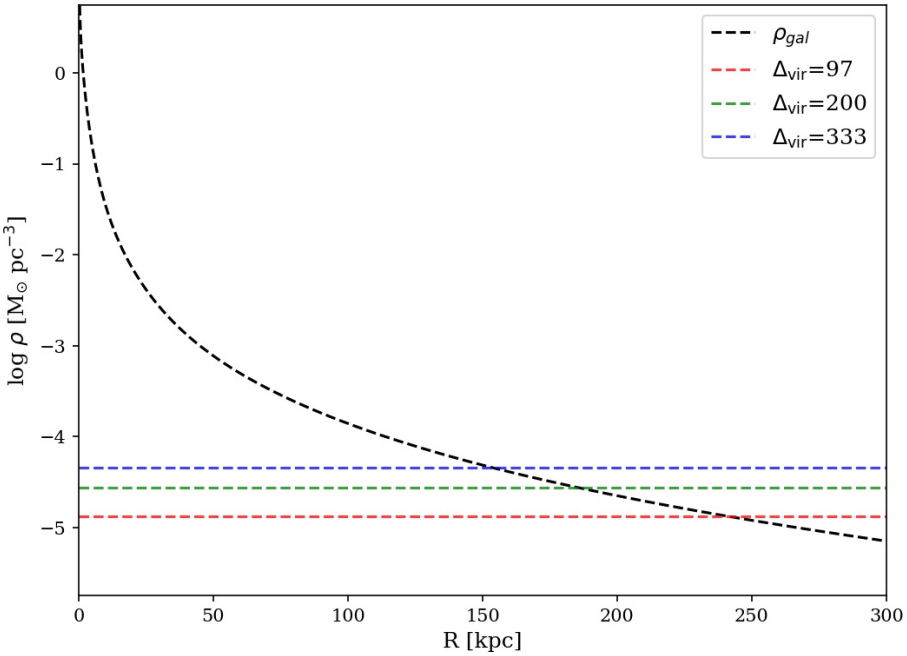


FIGURE 2.3: Density profile of the simulated galaxy at redshift $z = 0$. Horizontal lines represent each of the virial overdensities $\Delta_{vir} \times \rho_{crit}$, for $\Delta_{vir} = 97$ (red line),$\Delta_{vir} = 200$ (green line), and $\Delta_{vir}$ as in BN98 (blue line).

the different overdensity values ($\Delta_{\rm v}$), in Fig. 2.3 we show the density profile ($\rho_{gal}$, dotted black line) at $z = 0$ and $\Delta_{\rm v}\rho_{\rm crit}(z = 0)$ for the values $\Delta_{\rm v} = 97$ (dotted red line), $\Delta_{\rm v} = 200$ (dotted green line), and $\Delta_{\rm v}$ as in BN98 (dotted blue line). We generally take the BN98 definition for virial overdensity ($\Delta_{\rm v}(z)$), and we refer it to as $R_{\rm v}$ hereafter. At $z \sim 0$, the virial radius obtained is 154 kpc. The total mass in the enclosed space in this radius is $M_{\rm v}$ of $6.5 \times 10^{11}$ M$_\odot$.

In order to study the disk's dynamical properties, we choose cylindrical galactocentric coordinates. Calculating the angular momentum of a simulated galaxy is not a trivial task; one has to make a choice about which particles to include, among others. This becomes even less trivial when different density structures and age populations are present or when the galaxy is (highly) perturbed. The way the galaxy's inclination is 'corrected' will heavily influence the calculation of quantities such as $V_R$, $V_Z$, etc, and in turn, impact the distribution of stars in phase space. Indeed, variations in the determination of the galactic plane can lead to small inaccuracies in the measurements of dynamical properties (Beane et al., 2019).

After the centering, we locate the disk plane by calculating the average angular momentum of stars inside a radius 20% of $R_{\rm vir}$, and we then apply a change of basis to align this with the $Z$ axis. This places most of the galactic disk in a plane oriented with $Z = 0$, as a first approximation to our definition of the galactic plane. The X-axis is the projection of the original X-axis from the cosmological box onto the galactic plane whose normal vector is $L$. To further align the disk we apply a second alignment with the same algorithm. In the two next chapters, we apply two different second alignments. We take all stellar particles born after z$\sim$ 1.5 inside a fixed cylindrical region with $|Z| < 3$ and $R < 15$ kpc for Chapter 3 and $R < 7$ kpc for Chapter 4 and apply the same algorithm for change of basis. This difference allows for different regions to be better aligned with $Z = 0$, since different particles are being selected for the calculation of the average angular momentum. For instance, regions from 10 to 15 kpc will be more

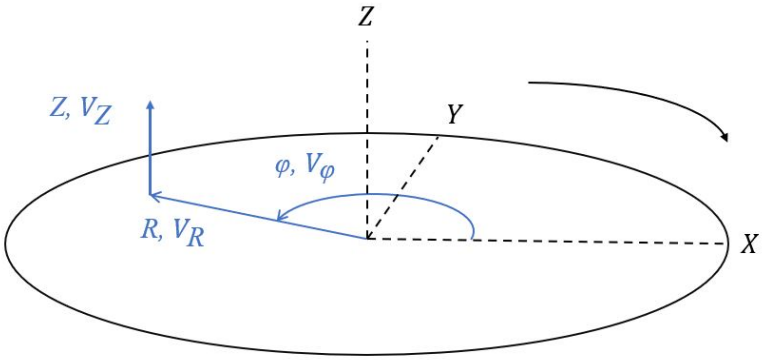


FIGURE 2.4: Reference system after centering and alignment of the galaxy. We use galactocentric cylindrical coordinates $(R, \phi, Z)$, and the system rotates in the clockwise direction.

aligned in the first scenario, whereas in the second case, only the inner region is being considered and will be aligned with the $Z = 0$ plane (we explain this process in detail in Appendix A). This alignment process, being done in two steps, is not affected by the older structures (see below), since the second step is done by taking into account only the stars born after redshift 1.5 ('young disk'). This method allows us to use galactocentric cylindrical coordinates $(R, \phi, Z)$, where $\phi$ and $V_\phi$ are negative in the direction of rotation. The direction of $\phi = 0$ is aligned with the positive direction of the $X$ vector, as in Fig. 2.4.

## 2.3 Properties of the MW-sized model

### 2.3.1 Ancient merger history

The ancient assembly history of this galactic model is essential to understand the different structures of the system. At z$\sim$ 0, the dark matter has a central triaxial substructure and old stars follow the same distribution, supported by velocity dispersion. At higher radii ($R > 10$ kpc), the halo has a more spheroidal shape. This inner triaxial structure is the product of a major merger that the galaxy suffers at z$\sim$ 3 (11.6 Gyr in lookback time). This merger destroys the stellar structures of the progenitors and generates a proto-elliptic galaxy of low mass. Over time, accreted gas forms a disk (seen as an old, thick disk at z$\sim$ 0). The galaxy grows from other mergers and the halo developes a spheroidal shape. The last major merger that the galaxy suffers occurs at z$\sim$ 1.5 ($\sim$1:10 merger at 9.55 Gyr of lookback time). After this point, the mass resolution in the simulation is increased, providing stellar particles of less mass, which allows to resolve the thinner stellar disk that grows in radius over time.

In table 2.1 we summarize the characteristics of this model at redshift $z = 0$ and compare it to the Milky Way. Our galaxy model is in the lower range of the viral mass estimated for the Milky Way, which has an estimated virial radius between $R_{\rm vir} \sim 200$ kpc and $M_{\rm vir} \sim 1.5 \times 10^{12}\ M_\odot$ (Dehnen, McLaughlin, and Sachania, 2006; McMillan, 2011; Gibbons, Belokurov, and Evans, 2014). The model is similar in terms of total stellar mass. However, from this stellar mass, the disk in the GARROTXA model ($2.6 \times 10^{10}$) is less massive than the Milky Way. The remaining mass ($3.3 \times 10^{10}\ M_\odot$) is in the old, velocity dispersion supported component.

TABLE 2.1: Main characteristics of the MW-sized model G.323 of GARROTXA simulation at z= 0 in comparison to the MW. From left to right, $R_{200}$ (on the left, calculated with our density profile analysis, on the right as calculated by Rockstar halo finder (Behroozi, Wechsler, and Wu, 2012)), virial radius, virial mass, the total stellar particles mass, the mass of the disk, the typical mass of the disk particles, and the number of disk particles. The estimations for the MWare from Dehnen, McLaughlin, and Sachania (2006), McMillan (2011), Gibbons, Belokurov, and Evans (2014), and Licquia and Newman (2015)

| | $R_{200}$ [kpc] | $R_{vir}$ [kpc] | $M_{\rm vir}$ [$M_\odot$] | $M_*$ [$M_\odot$] | $M_{\rm disk}$ [$M_\odot$] | $M_{\rm part,disk}$ | $N_{\rm part,*}$ |
|---|---|---|---|---|---|---|---|
| G.323 | 185 \| 216 | 154 | $6.5\times10^{11}$ | $6.05\times10^{10}$ | $2.6\times10^{10}$ | $10^3-10^4$ | $2\times10^6$ |
| MW | | 214-258 | 0.9-1.3 $\times10^{12}$ | $6.08\times10^{10}$ | $5.17\times10^{10}$ | | |

### 2.3.2 Stellar structures

We separate the different stellar structures in the galactic system based on the stellar particle's age and kinematics, in particular, their orbit with respect to the galactic plane. First, by analysing the age distribution we find that the particles belonging, geometrically, to the thin disk are the youngest ones. These stars were born after this last merger (1:10, 9.5 Gyr in lookback time) and populated the thin disk region. Thus, we define the stellar particles of the disk as the ones that were born after this last merger. In practice, we take a time of 9.05 Gyr (i.e. 500 Myr after the merger). It is important to note that we take this limit as a reference, and not as a definite division between "old" and "young" disk.

The stars older than this age belong to the inner halo/ellipsoid (ellipsoid hereafter), or to what we considere the thick/old disk. The ellipsoid structure is dispersion supported whereas the old disk is rotationally supported (although its particles have dynamically hotter orbits than the younger disk particles). Thus, we can distinguish the older disk from the ellipsoid by $\cos(\alpha)$ which is $L_Z/|L_{\rm tot}|$. Perfectly cold and circular orbits would have $\cos(\alpha)=1$ and $L_Z/|L_{\rm tot}|=1$. Thus, we set an additional kinematic condition to separate between the old disk and the ellipsoid, where the particles belonging to the old disk fulfill $\cos(\alpha)>0.7$. In Fig. 2.5 we show the different stellar structures of the model at the present time ($z=0$), where the left panels are the young disk, the central panels are the old disk and the right panels are the ellipsoid. We show their edge-on and face-on projections (top and central rows, respectively) and the face-on view colored by age (bottom panels). At this time, N = 1.53 $\times10^6$ stellar particles belong to the young disk, conforming a mass of $8.5\times10^9\ M_\odot$. The range of particle masses of this young disk varies typically from $10^3$ to $10^4\ M_\odot$. The old disk has a mass of $1.6\times10^{10}\ M_\odot$. Even though the particles of the ellipsoid are less numerous, they are the most massive ones, totaling 3.45 $\times10^{10}\ M_\odot$ inside 30 kpc of radius.

To better illustrate the dynamic distinctions between these groups, we present in Figure 2.6 a histogram of $L_Z/L_{\rm circ}$. We can see that the particles belonging to the disk tend to have their $L_Z/L_{\rm circ}$ distributed around 0.89, conforming to a completely rotationally supported disk. This implies that they are following relatively colder orbits. The old disk follows a similar pattern to the young disk, although its peak is 0.83, indicating that its particles are dynamically hotter. The particles of the ellipsoid are distributed more extensively around zero, since this structure is supported by velocity dispersion.

In this thesis, we analyse the kinematics of the dynamically cold disk, so, for further analysis, we select only select stellar particles with $|Z|<2.5$ kpc and $R<25$ kpc. In Fig. 2.7 we show the disk components colored by $Z$ and all velocity components in a cylindrical reference frame ($V_R$, $V_\phi$). The first feature we notice is that this disk shows several density structures. For instance, in the inner galactic regions (<5 kpc), there is an oval structure that contains stellar particles of the same age as the disk. The semi-major axis

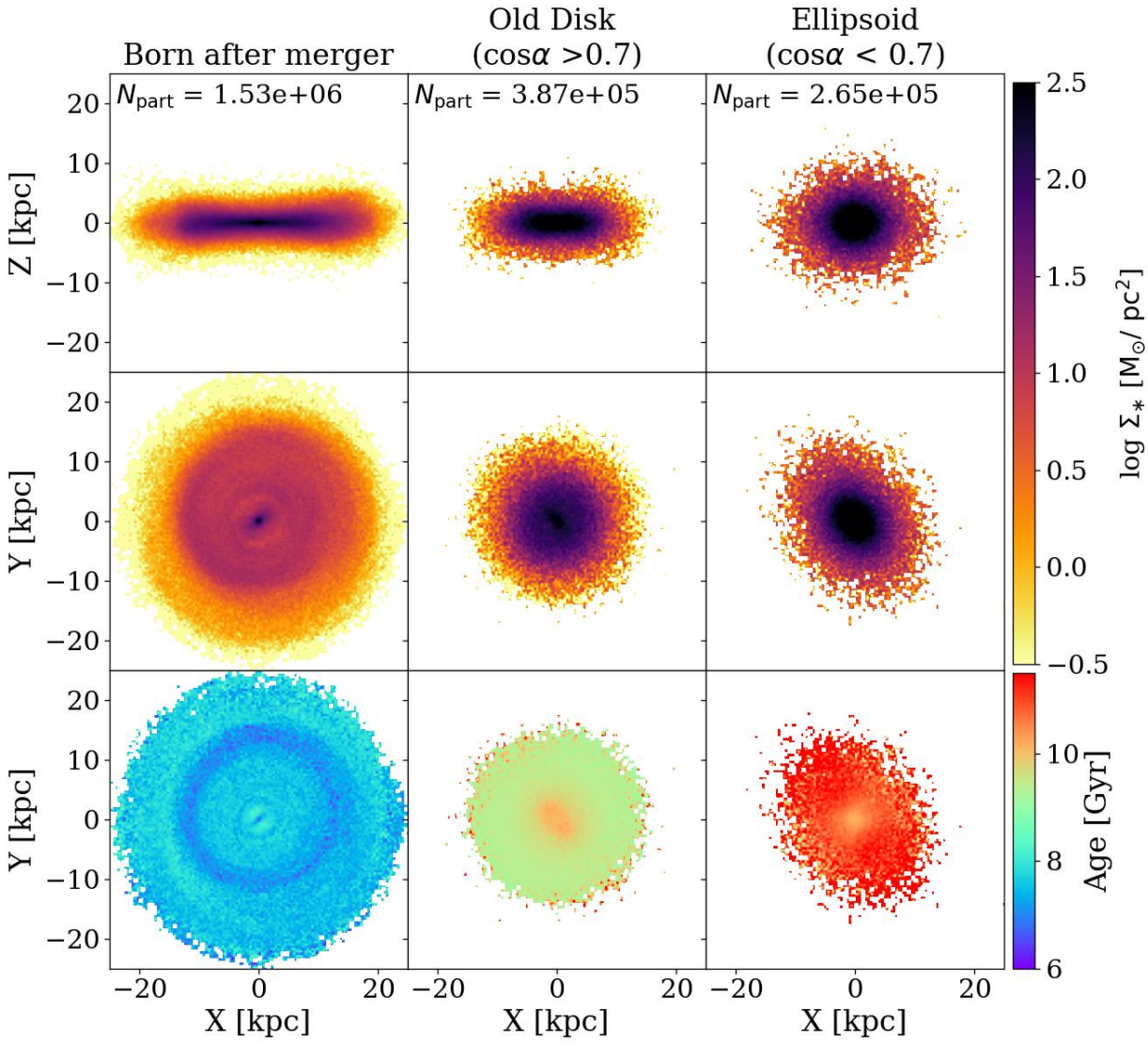


FIGURE 2.5: Different stellar structures at present times $z = 0$. The left panel shows stars born 500 Myr after the last major merger (at 9.55 Gyr in lookback time). The panels in the central column show the older, hot disk. Lastly, in the right column, we show the old stellar ellipsoid. The top two rows show the surface density of the stellar particles in the X-Z and X-Y projections, respectively. The last row shows the face-on projection colored by age.

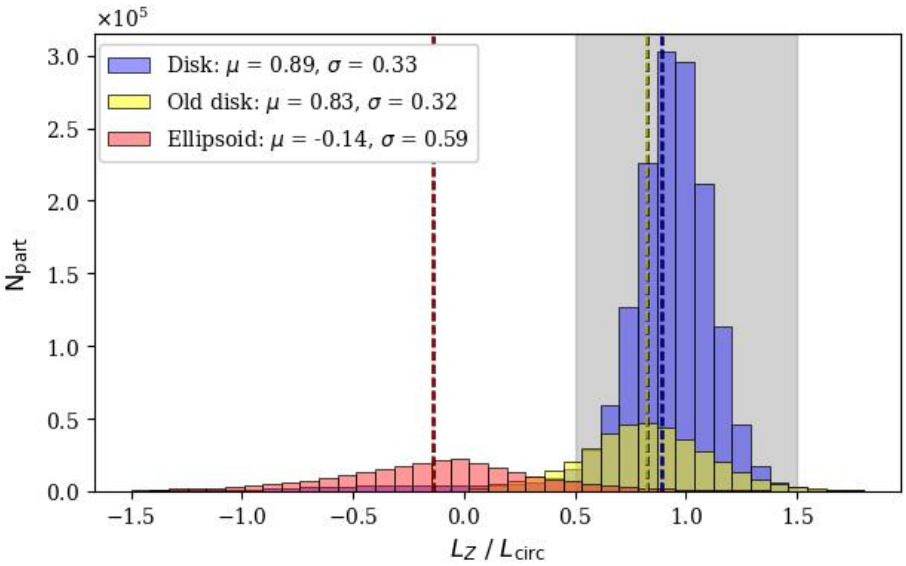


FIGURE 2.6: Histogram of the $L_Z/L_{\rm circ}$ of the different stellar structures described in Fig.2.5: disk, with particles younger than 9.05 Gyr (blue), and particles older than 9.05 Gyr with $\cos\alpha > 0.7$ old disk (yellow), and $\cos\alpha < 0.7$ that conforms the ellipsoid (red). The grey zone indicates the ranges in which the stellar structure is rotationally supported, defined by $0.5 < L_Z/L_{\rm circ} < 1.5$.

of this young elongated structure is oriented as the old-stellar and dark matter ellipsoid's minor axis. It extends to approximately 4-5 kpc of radius. This 4-5 kpc is also the limit for the kinematic $V_R$ quadrupole that we show in the bottom right panel. We observe that this is present along all timespan studied at a fixed angle in the X-Y plane. Since we do not detect a pattern speed, we do not consider it to be a bar and we refer to it as "oval" to avoid confusion. As seen from the overdensity plot with a Gaussian filter (left-most panel) we can see a one-armed spiral that has a retrograde motion in relation to the rotation of the disk. This density structure has its corresponding signatures in velocity space, leaving an armed structure when coloured by $V_\phi$ and $V_R$. We also can observe an inner quadrupole signal in the velocity $V_R$, which is provoked by the central oval.

### 2.3.3 Rotation curve

We calculate the circular velocity curve of the galaxy in two different ways. The circular velocity of stars in a galaxy can be estimated from the total mass enclosed in a spherical region of radius $R$. This is known as the spherical approximation, which simplifies the calculation of the circular velocity by treating the mass distribution as if it were spherically distributed throughout the galaxy.

$$V_{\rm circ}(r) = \sqrt{\frac{G \cdot M(r)}{r}} \tag{2.1}$$

However, in reality, dark matter halos are not perfectly homogeneous and spherically symmetric. In addition, the disk is an axisymmetrical distribution of mass, and therefore, produce significant deviations from the idealized spherical symmetry assumed. Another way to calculate $V_{\rm circ}$ is to calculate the radial

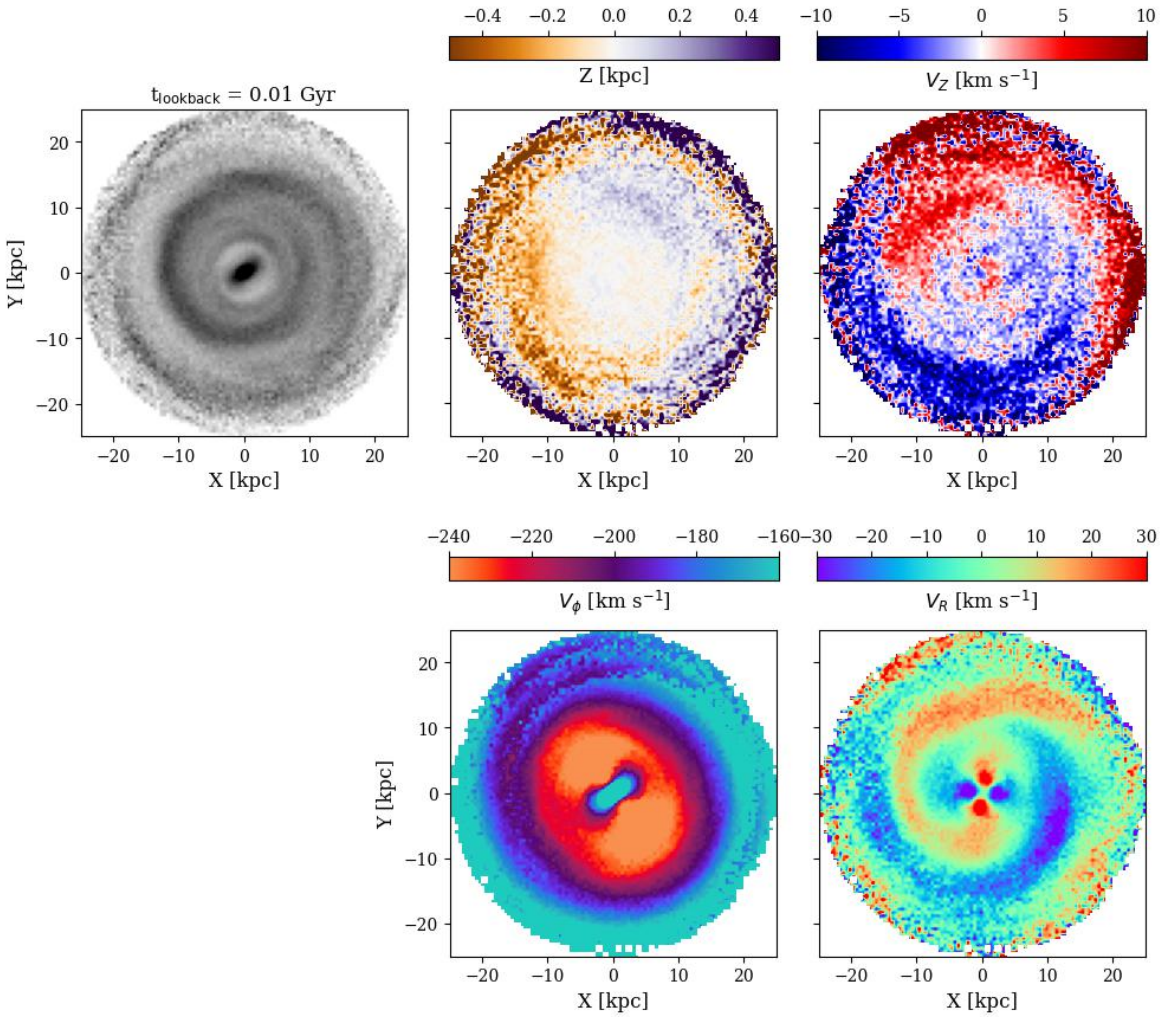


FIGURE 2.7: Face-on projection of the stellar disk at $\sim 0$ Gyr. The top left panel shows an overdensity plot with a Gaussian filter of $\sigma = 6$. The next panels show 2D histograms weighted by $Z$, $V_Z$, $V_\phi$ and $V_R$, respectively.

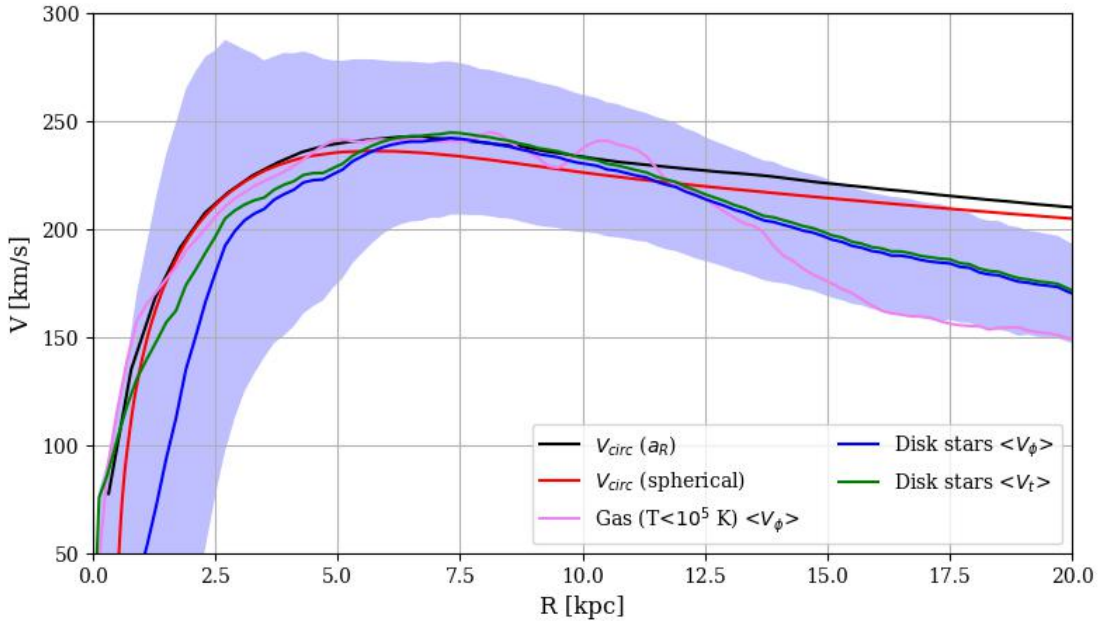


FIGURE 2.8: Rotation curve of GARROTXA's MW model. The red curve is the spherical approximation and the black one is derived from radial accelerations. We also show the azimuthal velocity of cold gas (pink line), and disk stars and their dispersion (blue line, and blue shade) as well as the spherical tangential velocity (green line) which is defined as $V_t = \sqrt{V_\phi^2 + V_Z^2}$.

acceleration that the different components apply to a mesh situated in $Z = 0$, which corresponds to the disk plane.

$$V_{\rm circ}(r) = \sqrt{a_r \cdot r} \tag{2.2}$$

This velocity represents the necessary azimuthal velocity to maintain a circular orbit when there is a centripetal acceleration $a_R$ at radius $R$. Contrary to the previous method, this is a more accurate calculation of $V_{\rm circ}$, since it takes into account all the forces influencing the plane $Z = 0$. In Fig.2.8 we show the rotation curves of both methods described above, where the red curve is the spherical approximation, and the black one is the one derived from radial accelerations. We also show the azimuthal velocity of cold gas (pink line), and disk stars and their dispersion (blue line, and blue shade) as well as the tangential velocity (green line).

Despite the aforementioned deviations between the spherical approximation and the radial acceleration, both are very similar in this case. We also show the azimuthal velocity of stars, $V_\phi$, which do not necessarily coincide with $V_{circ}$ due to different perturbations in this model. The gas generally follows the circular velocity since it is dinamically cold. At outer radii, it deviates from this curve due to the perturbations of this model.

We can see that, even though the total mass of the galaxy model is in the lower range of the mass predicted for the MW (Table 2.1), they have similar rotation curves (Roca-Fàbrega et al., 2016, see Fig. 4 and Table 1). This may indicate that the dark matter density distribution of the GARROTXA model is slightly different than the one estimated for the MW at external radii ($\sim$ 100 kpc).

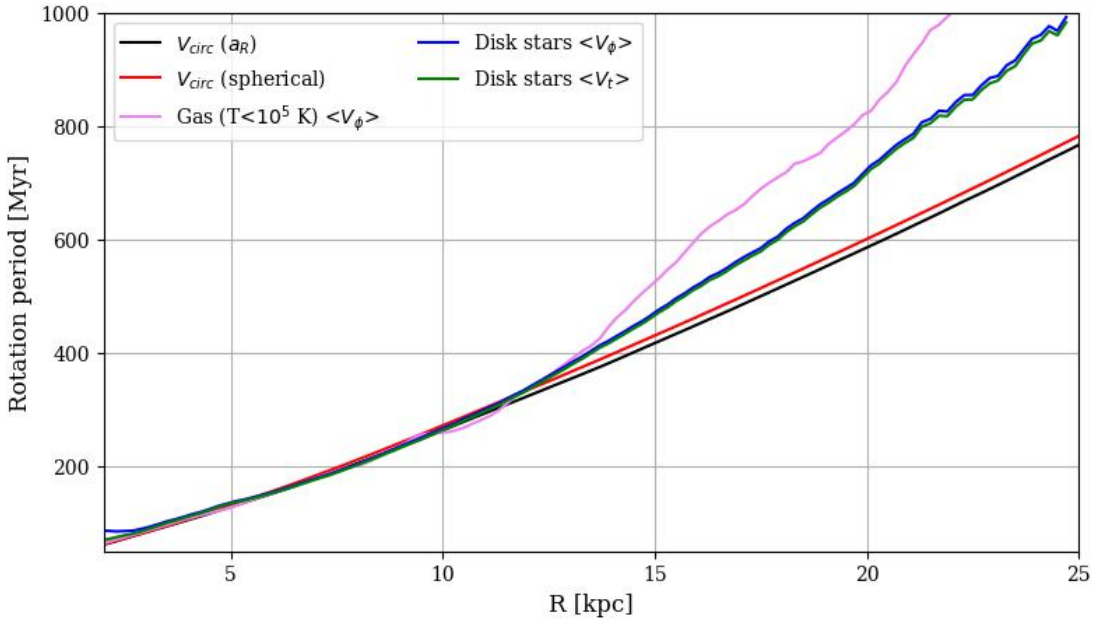


FIGURE 2.9: Rotation periods of GARROTXA's MW model calculated from the $V_{\rm circ}$ with Eq. 2.3. The color code is the same as in Fig. 2.8.

The rotation curve helps us to understand the period of rotation at the different radii, which can be calculated as the time it takes to a complete revolution:

$$T_{\rm rot}(r) = \frac{2\pi r}{V_{\rm circ}(r)} \tag{2.3}$$

In Fig. 2.9 we show the rotation periods at different galactocentric radii. At intermediate radius of 10 kpc the rotation period is approximately 260 Myr. At external radii, from 15 to 20 kpc, the rotation period is approximately 500 to 700 Myr.

At the moment of the realization of this thesis, this is a model that allows us to analyze a galaxy similar to the MW (spiral shape, similar rotation curve...), albeit in the (lower) limit of mass for MW analogues (Geha et al., 2017). Even though it is not exactly a MW, it is an excellent laboratory to study different phenomena observed in disk galaxies.

### 2.3.4 Satellites

At $z = 0$ the GARROTXA galactic system hosts many satellite galaxies and stellar streams that formed after $\sim 1.5$. However, obtaining the mass of satellites is not trivial in simulations, nor in observations. The outer parts of a satellite entering the densest regions of the dark matter halo of the host galaxy become disrupted quickly. Furthermore, inside the tidal radius of the satellite, there is a mixture of the dark matter particles that are bound to the host with the ones that are to the satellite. Therefore, the dynamical mass does not reflect the total mass enclosed within a sphere centered on the satellite's center of mass at each time, and it is not fully correct to fit a NFW density profile either.

TABLE 2.2: Properties of the largest satellite galaxies in the simulation. From left to the right: total mass at first infall, denoted as $M_{inf}$ (we give two different values corresponding to the mass inside the virial radius and the one from abundance matching at $z \sim 2$, respectively); tidal radius ($R_t$), total mass inside the tidal radius ($M_t$). The next columns are computed with Rockstar halo finder, $R_{200}$, $M_{bound}$, and stellar mass. Values separated by "-" are values measured at the start and the end of the time studied (6.3 Gyr and 0 Gyr respectively). The last column is the orbit inclination with respect to the galactic plane with the two values being at 6 and 0 Gyr lookback time. Satellites indicated by "DM" are dark matter subhaloes in which we have not found stellar particles. The missing values of the first three columns indicate that the data were not calculated and the satellites were only computed with Rockstar halo finder.

| Satellite | $M_{\rm inf}$ [$10^{10}$ $M_\odot$] | $R_{\rm t}$ [kpc] | $M_{\rm t}$ [$10^8$ $M_\odot$] | $R_{200}$ [kpc] | $M_{bound}$ [$10^8$ $M_\odot$] | $M_*$ [$10^8$ $M_\odot$] | $i$ [deg] |
|---|---|---|---|---|---|---|---|
| Arania | 1.3 \| 6.6 | 3.0-2.0 | 5.4-2.5 | 24-18.4 | 34-5.5 | 2.30-1.50 | 103-120 |
| Escarabajo | | | | 26-21 | 16-9.8 | 0.06 | 150 |
| Grillo | 0.1 \| 0.9 | 1.4-1.0 | 1.8-1.1 | 12.5-6.9 | 3.16-1.6 | 0.15-0.07 | 34-23 |
| Mosquito | 0.2 \| 2.5 | 1.0-1.0 | 0.7-0.6 | 10.9-10.7 | 2.3-0.77 | 0.04-0.03 | 75-97 |
| DM1119 | | | | 20.3 | 11 | 0 | 87 |
| DM479 | | | | 19.8 | 7.2 | 0 | 133 |
| DM2113 | | | | 18.06 | 4.9 | 0 | 139 |
| DM2512 | | | | 12.4 | 4.5 | 0 | 76 |
| DM2595 | | | | 11.4 | 2 | 0 | 96 |
| DM1747 | | | | 11.43 | 1.8 | 0 | 91 |

In this thesis, we have applied different methods to detect and measure the mass of the numerous satellites in this model. Firstly, we identified visually several luminous satellites in the system. For these satellites, we decided to obtain their mass at $z \sim$2, when satellites are still outside $R_{\rm vir}$ of the host galaxy, using two independent techniques: computing the total mass enclosed in its own $R_{\rm vir}$, and via a method related to abundance matching (Rodríguez-Puebla et al., 2017; Behroozi, Conroy, and Wechsler, 2010). We use the abundance matching relations as a statistical approach of inferring the $M_{vir}$ of the halo depending on its stellar mass, which we infer by summing the mass of the stellar particles inside the tidal radius. In our case, we have used eq. 66 and the parameters on table 6 of Rodríguez-Puebla et al. 2017. In Table 2.2 we show both results in the column labeled as $M_{inf}$. Results from the virial approximation (first value) are systematically lower than the ones from abundance matching (second). This result is not surprising as dwarf satellites may suffer tidally induced star formation and dark matter stripping well before entering the host's virial radius (Guo et al., 2020; Jackson et al., 2021), both acting against the theoretical $M_*/M_{\rm vir}$ relation used in the abundance matching approach.

To quantify their mass over time from 6.3 to 0 Gyr in lookback time, we defined their radii as their tidal radius at apocenter (where there is less contamination from dark matter particles from the main halo) and computed the mass within. This radius is updated at each apocenter (see Fig. 2.10) to account for the mass loss at the pericenters. These values are shown in the second column of the table ($R_t$).

A visual inspection, however, is not efficient to track all the satellites present in the simulation since dark matter subhalos are numerous. Thus, we applied the Rockstar halo finder (Behroozi, Wechsler, and Wu, 2012) to identify all subhalos that may impact the disk's kinematics.

Rockstar halo finder uses the 6D phase space, and therefore the particles that belong to a subhalo are better isolated from the particles belonging to the host once the subhalo has entered the virial radius of the host galaxy. This makes the calculation of the mass more reliable. The data of $M_{bound}$ of the satellites, as

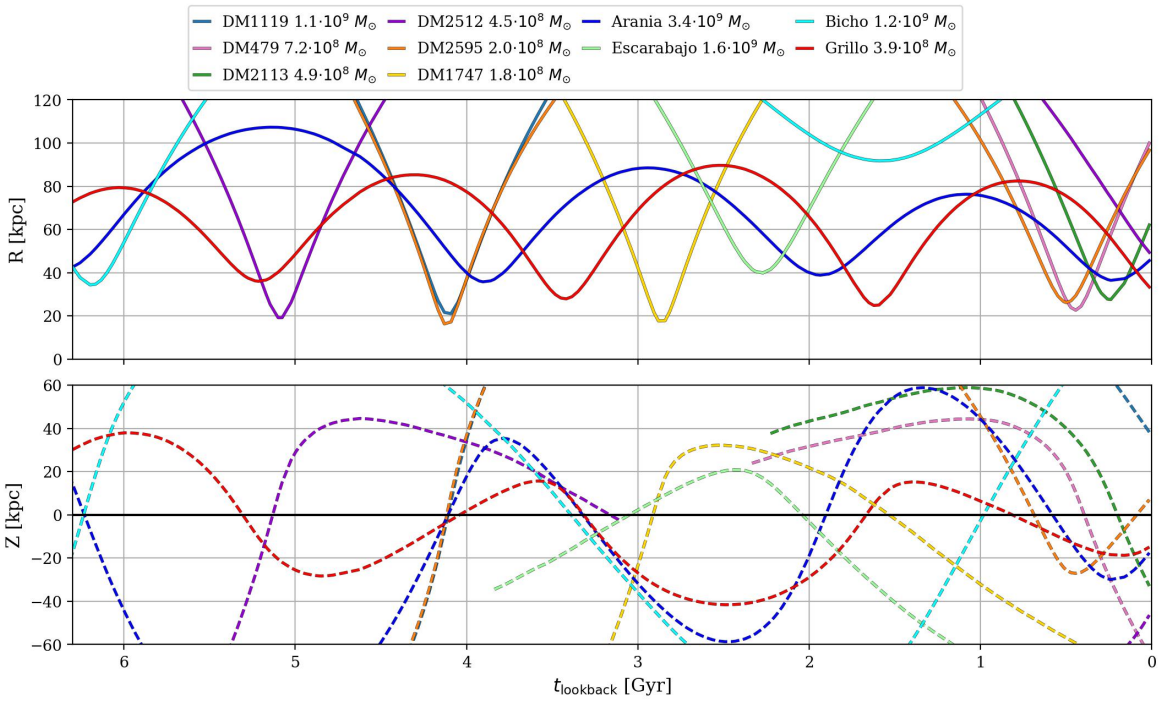


FIGURE 2.10: Orbits of the main satellites in GARROTXA MW-sized model. **Top panel**: galactocentric distance to the main galactic system. **Bottom panel**: vertical distance $Z$ from the plane $Z = 0$.

given by Rockstar, is calculated at several instances of the simulation. Throughout this thesis, we will use the data from Rockstar halo finder to track the characteristics of the satellites found in this simulation.

In Table. 2.2 we summarize the main characteristics of the most important satellites (more massive and reaching close proximity to the galaxy at some points) orbiting the main system over the last 6 Gyr of the evolution of the model. In the fifth column we show the mass at the moment they enter the host's virial radius, which is equivalent to $M_{200}$ . We use this quantity as a reference of the size and mass of the satellite at the moment of infall. However, once the satellite has fallen into the virial radius of the main system, the mass given by Rockstar is equivalent to the bound mass of each satellite. This quantity is used when we give masses before an interaction (after the satellite has entered the virial radius of the host), or calculate individual accelerations by each satellite. The complete data of subhalos (including both dark and luminous satellites) found by Rockstar can be found in Appendix B.

With this halo finder, we identify all dark matter structures with $M_{200} > 10^6\ M_\odot$ (to avoid poorly resolved subhalos and contamination by field halo dark matter particles), and, using the dark matter particle IDs we also find all gravitationally bound particles. If they have stellar mass inside of 20% of the $R_{200}$ (as calculated by Rockstar) we identify them as luminous.

In the total timespan analyzed, we found nearly independent 500 subhalos (luminous or dark). As expected from the ΛCDM Universe, we find a large number of dark satellites, i.e. subhalos with no stellar particles. For instance, at redshift $z = 0$, we find 139 subhalos without any stellar particle inside the virial radius of the studied galaxy, compared to 10 dwarf galaxies. These dark satellites, despite being generally less massive than dwarf galaxies, can interact with the disk as luminous satellites would.

In Fig. 2.10 we show the galactocentric distance (top panel) of the most massive satellites in the model as a function of time. The minima of these curves are the pericentric passages of each satellite. We also show their vertical distance $Z$ as a function of time, thus identifying the moment they cross the $Z = 0$ plane.

We bring attention to the most massive satellites found in the timespan studied. Firstly, "Arania" (blue lines) enters the host halo at $\sim 9$ Gyr (with an estimated $M_{inf}$ of $\sim 10^{10}\ M_{\odot}$) and has its first pericenter at 6.3 Gyr, with a bound mass of $3.4 \times 10^9\ M_{\odot}$. Throughout the timespan studied it loses mass at each pericenter. The dark satellite "DM1119" has $1.9 \times 10^9\ M_{\odot}$ and crosses the disk at approximately 4.1 Gyr in an almost polar orbit. Finally, satellite "Escarabajo" enters the galaxy with a more planar orbit, and with a mass of $1.6 \times 10^9\ M_{\odot}$, although its pericenter, at 2.2 Gyr, is more distant.

#### Gas in satellites

In this section, we analyze the gas which the satellites bring when they enter the halo and interact with the galaxy. Throughout the evolution of the galaxy, different satellites undergo different processes in which they lose their gas, which in turn interacts with the halo and at times, enters the galaxy.

In Fig. 2.11 we can see three different instances of the gas in the satellite Arania, which is the most massive one in our model. We can see that, with each pericenter, it loses its gas and the gas that remains in the satellite is hotter at later times.

The satellite Escarabajo brings cold gas when it enters the virial radios at >3 Gyr in lookback time. This gas is slowly ram-pressure stripped when approaching the galaxy due to the hot gas corona that envelopes the intermediate parts of the halo. In Fig.2.12 we can see the inner parts of the satellite dominated by cold gas, and the hot gas shock in the direction of the orbit.

In Fig. 2.13 we can see that the gas in DM1119 is generally hotter and less dense. This kind of gas is not capable of forming stars, and thus DM1119 appears as a dark subhalo. However, due to its content of baryons we do not consider this object to be a purely dark matter subhalo. After its interaction with the disk, it still conserves most of its gas.

## 2.4 Star formation

Throughout the evolution of the simulation, gas cells are constantly cooling, condensing, and forming new stellar particles. The conditions for a cell to create stellar particles are: $n_H > 1\ cm^{-3}$ and $T < 9 \times 10^4$ K, with a deterministic star formation efficiency of $\varepsilon_{SF} = 0.65$ (Roca-Fàbrega et al., 2016). This means that, when a cell fulfills the condition for density and temperature, a fraction of 0.65 of the gas mass will be transformed into stellar particles, which with this resolution and star formation conditions is an appropiate value to avoid overcooling (Colín et al., 2010).

The star formation history can also be an indicator of past interactions (Mihos and Hernquist, 1994; Teyssier, Chapon, and Bournaud, 2010; Ruiz-Lara et al., 2020). A gravitational impulse by an external perturbation can trigger an episode of star formation. Thus, to reach a more complete understanding of the processes that the galaxy suffers over time, we need to take into account the star-forming history. Firstly, we calculate the total mass created in stars in the disk region in relation to the previous snapshot. We select particles inside a cylindrical region of $|Z| < 2.5$ kpc $R < 25$ kpc to avoid stellar formation from satellites. We also calculate the total mass of gas which fulfills the conditions above in the region of the disk. This is the gas available for star formation.

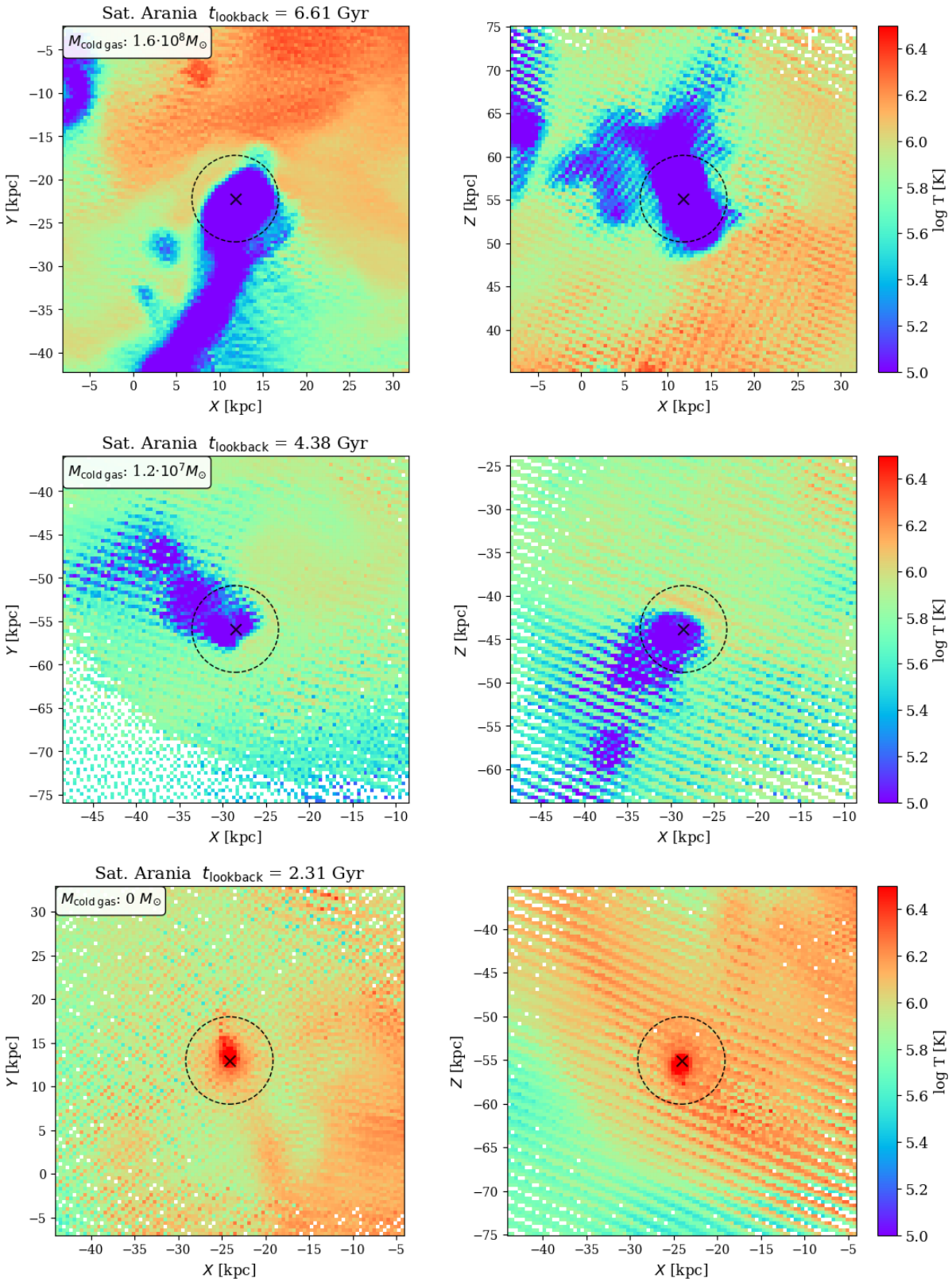


FIGURE 2.11: Gas in Arania satellite at three different times before pericenters, at galactocentric distances of 60, 76 and 78 kpc respectively. The position of the satellite is marked as an "x" and the dotted line marks a circle of 5 kpc of radius in which we compute the mass of the gas with $T < 10^5 K$.

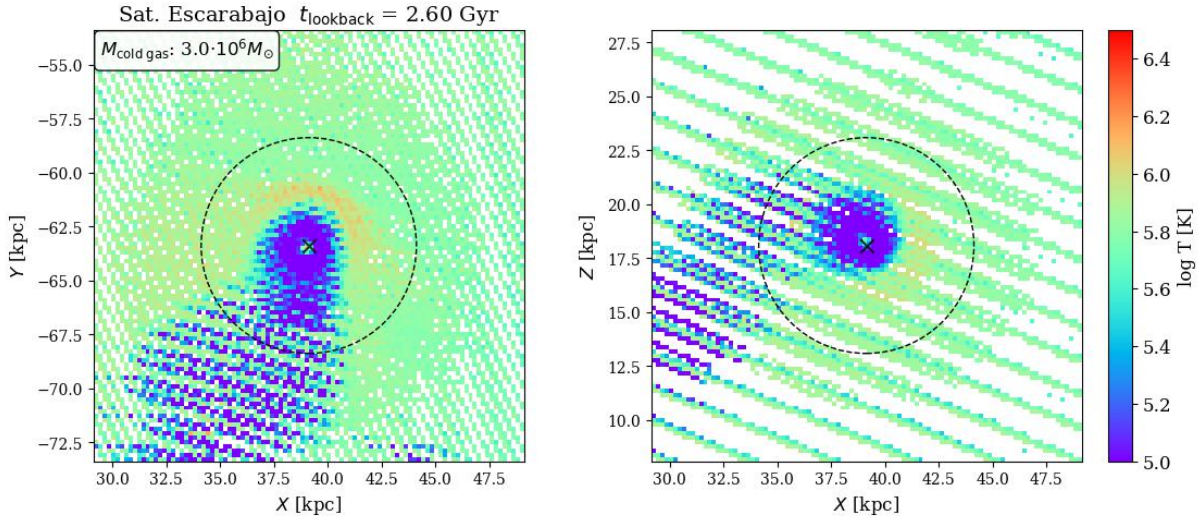


FIGURE 2.12: Same as in Fig. 2.11 but with Escarabajo satellite, when it has entered the virial radius of the galaxy (at a galactocentric distance of 76 kpc), and before its first pericenter.

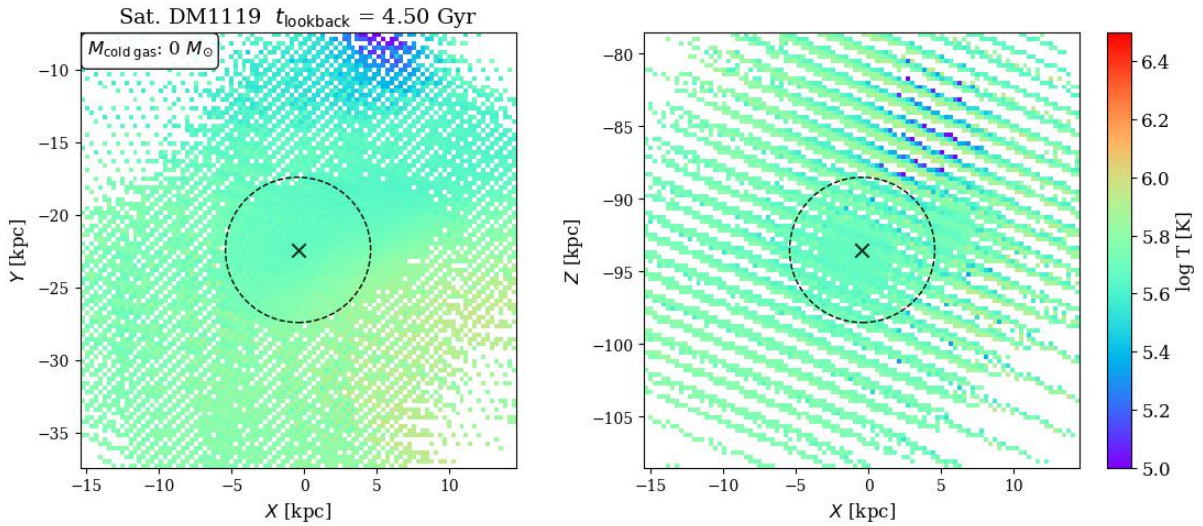


FIGURE 2.13: Same as in Fig. 2.11 but with gas in the DM1119 satellite before its first pericenter at a galactocentric distance of 96 kpc.

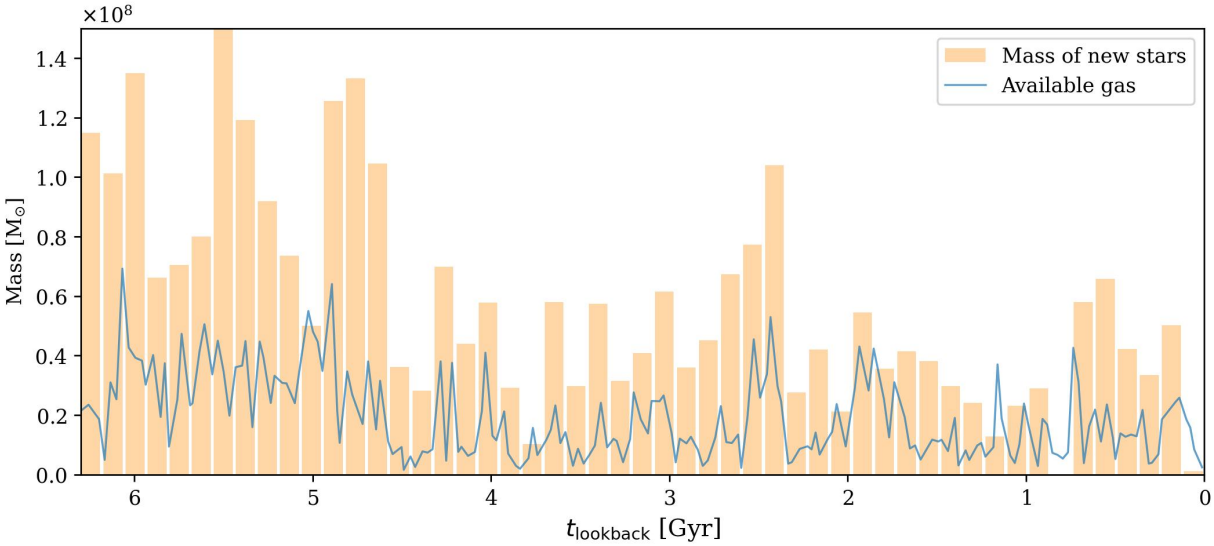


FIGURE 2.14: Newly formed star mass (yellow histogram) and available gas (blue line) along the last 6 Gyr of evolution.

In Fig. 2.14 we show the newly formed stellar particles of the last 6 Gyr of the evolution of the galactic model inside the region of the disk as a histogram weighted by mass, and the available gas for each snapshot is the blue line.

## 2.5 Fourier decomposition of stellar structures

Fourier decomposition is a powerful mathematical technique that breaks down complex periodic functions into a combination of simpler sinusoidal functions. When studying disk galaxies, this technique is applied to quantify different characteristics of the disk, such as density structures like bisymmetric arms or bars. In this thesis, this technique is applied for different goals, mainly the characterization of the phase spiral (Chapter 3) and the quantification of vertical deformations (Chapter 4).

We divide the two-dimensional space of the system into concentric rings originating from a central point. Then, we calculate the Fourier modes and amplitudes that contribute to an overall pattern.

$$\begin{aligned} a_m &= 2\sum_i^N W_i \cos\left(m\phi_i\right) \\ b_m &= 2\sum_i^N W_i \sin\left(m\phi_i\right) \\ A_m &= \sqrt{a_m^2 + b_m^2}/N \\ \phi_m &= \arctan(b_m/a_m) \end{aligned} \tag{2.4}$$

Each mode ($m$) represents a specific number of oscillations within the radial ring, while the corresponding amplitude ($A_m$) determines the strength of that particular wave component. As a result, the

combination of different modes, their respective amplitudes, and the phase of maximum amplitude ($\phi_m$) within each ring creates a unique and intricate wave-like pattern within the two-dimensional space. The Fourier decomposition can be weighted by any property ($W_i$).

We show an example of the Fourier decomposition technique in Fig. 2.15, for the face-on projection of the disk colored by $V_Z$ at 1 Gyr of lookback time. In this case, we are taking into account modes from 0 to 4. We observe that the original characteristics of the $V_Z$ patterns are well reconstructed. To see which modes are more relevant in this characterization, we show in Fig. 2.16 each mode separately. We can observe that the stronger mode is mode $m = 1$ (second panel). This is because, in this example, we have a clear spiral pattern with an arm of positive $V_Z$ and another of negative $V_Z$.

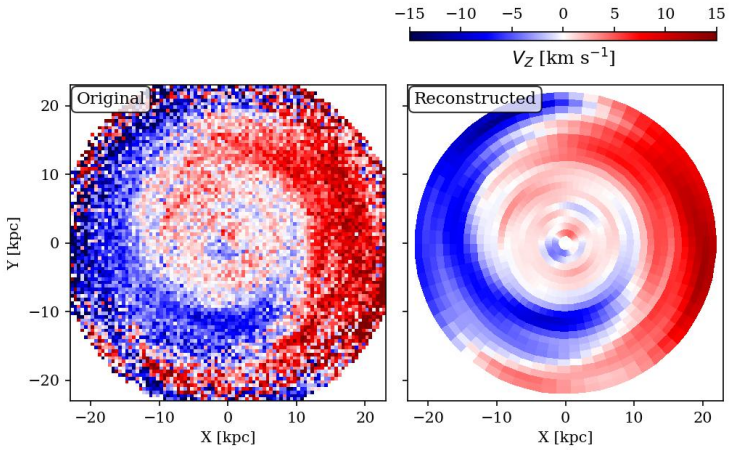


FIGURE 2.15: Comparison between the disk colored by $V_Z$ and reconstructed via Fourier decomposition from modes 0 to 4.

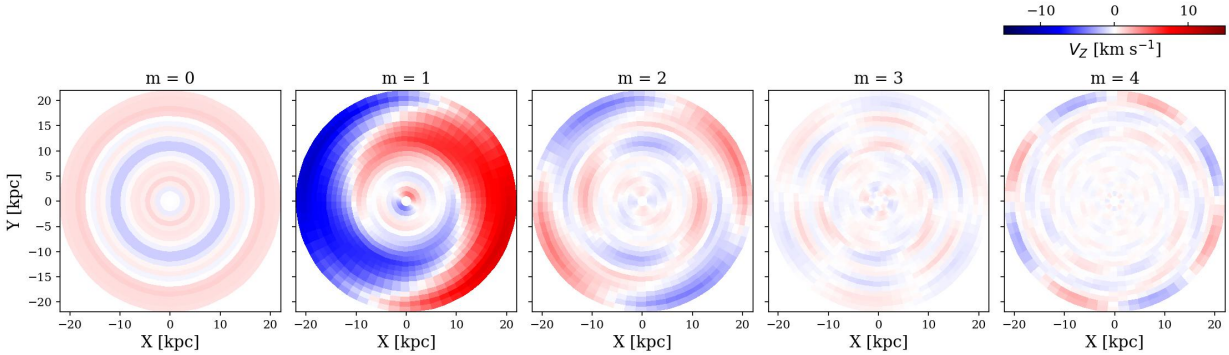


FIGURE 2.16: Fourier decomposition of $V_Z$ from modes 0 to 4. The sum of these modes leads to the reconstructed disk $V_Z$ shown in the right panel of Fig. 2.15.

We also take a look at the position of the maximum amplitude. In Fig. 2.17, we show the angles at which the maximum of amplitude is found for the two first Fourier modes. This maximum amplitude is positioned in the positive arm of the decomposition.

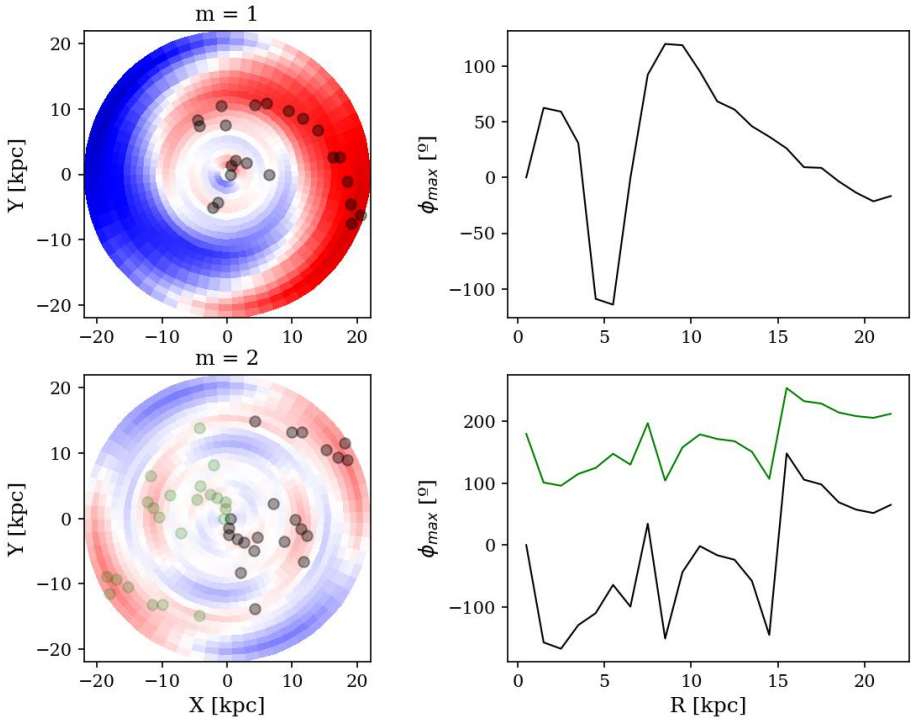


FIGURE 2.17: Results of the phase of the maximum amplitude of the Fourier decomposition. The left panels show the decomposition for Fourier modes $m = 1$ and $m = 2$ (top and bottm panels respectively), with the same color scale as Fig. 2.15. The dots show the positions of the maximum amplitude for each ring. For mode $m = 2$, due to the duplicity of the signal, we show both maximums (black and green dots). The right panels show this angle as a function of galacticentric radius.

CHAPTER 3

# Phase spirals in cosmological simulations

This chapter is mainly based on the article *Phase spirals in cosmological simulations of Milky Way sized galaxies*, by García-Conde, B., Roca-Fàbrega, S., Antoja, T., Ramos, P., Valenzuela, O., published in 2022 in *Monthly Notices of the Royal Astronomical Society*, of which I am first author. Thus, figures and text have been taken literally from said work.

## 3.1 Introduction

Several studies have shown that our Galaxy's disk is highly perturbed (e.g. Widrow et al., 2012; Williams et al., 2013; Antoja et al., 2018; Ramos, Antoja, and Figueras, 2018), which has become especially evident with *Gaia* DR2. The emergence of the phase spiral phenomenon (Antoja et al., 2018) has been attributed to the effects of perturbations resulting from interactions with the Sagittarius dwarf galaxy since its discovery. Research efforts with various modeling techniques have confirmed that the phase spiral can indeed be attributed to the tidal interaction between our Galaxy and the Sagittarius dwarf galaxy (Binney and Schönrich, 2018; Laporte et al., 2019; Li and Shen, 2020; Bland-Hawthorn and Tepper-García, 2021; Hunt et al., 2021; Gandhi et al., 2022; Widmark et al., 2021), with the estimated timing of the perturbation aligning with previous pericenter passages of Sagittarius, estimated to be between 200 and 1000 Myr ago (Law and Majewski, 2010; Purcell et al., 2011; Vasiliev and Belokurov, 2020). However, alternative hypotheses have also been proposed, suggesting that phenomena such as bar buckling (Khoperskov et al., 2019) or halo substructure (Darling and Widrow, 2019) could generate bending waves leading to the formation of phase spirals.

The studies mentioned above have primarily relied on analytical models using the impulse approximation or isolated N-Body simulations focusing on a single perturber. These approaches aimed to replicate the formation of the phase spiral under simplified and controlled conditions. However, understanding how additional factors like gas effects or the presence of multiple perturbers and their collective influence (Weinberg, 1989; Trelles et al., 2022) impact the vertical perturbations has remained a complex challenge.

To address this gap, our work takes a significant step by investigating the phase spiral phenomenon using a high-resolution cosmological simulation that combines N-Body and hydrodynamics methods. In this Chapter we detect the phase spiral phenomenon in the disk of the MW-sized model of the GARROTXA simulation (described in Chapter 2). This approach marks the first instance of studying the phase spiral within a cosmological simulation, which incorporates realistic physical mechanisms known to shape galaxies, such as gas dynamics, star formation, and the influence of multiple satellite perturbers on the disk.

The detection of disk phase spirals in cosmological simulations was a challenge due to its complexity, lack of tuning of specific conditions (such as satellites of a specific mass), and especially the resolution limits of these types of simulations, which may lead to a blurring of the phase space structures due to numerical diffusion (Sellwood, 2012; Colombi, 2021). However, our model allows us to explore the disk phase space at a resolution of ∼109 pc. Here we report the detection of resolved phase spirals in a cosmological simulation for the first time (Sect 3.2). We study its correlation with the pericenter passages of the main satellites of the system, as well as with the star formation history (Sect. 3.3). We conclude in Sect. 3.4 by discussing the possible origin of the phase spiral and describing the new avenues opened by analyzing the kinematics of galaxies in a fully cosmological context.

## 3.2 Phase spirals through space and time

In this section, we analyze the vertical projection of the phase space of the disk in GARROTXA at different times, different volumes, and for different populations.

Initially, we focus our analysis on stellar particles with ages between 0 and 5 Gyr (but see below an exploration with age). We first take stellar particles with galactocentric radii from 10 to 12 kpc, and a vertical position of $|Z| < 2.5$ kpc. This ring is then divided into twelve adjacent sectors spanning 30 deg in $\phi$, and we follow their temporal evolution from lookback time of 6 to 0 Gyr.

A first example of the phase-space spirals ($Z - V_Z$) can be seen in Fig. 3.1. In this figure, we show a single volume for a snapshot that is at 1.1 Gyr after the pericenter of the most massive satellite Arania. We show the vertical projection of phase space in the range of [-2.5, 2.5] kpc in the vertical position axis and [-80,80] km/s in the velocity axis with a 35 x 35 binning, in density (first column), weighted by the velocity $V_\phi$ (second column), and by $V_R$ (third column). Like in most of the previous studies using N-Body simulations, we also note that the agreement with the phase spiral in *Gaia* is only qualitative since we have much larger volumes and a much smaller number of particles. We see that the phase spirals are clearer when colored by velocities, especially $V_\phi$, as in observations (Antoja et al., 2018). However, we do not see as many wraps of winded phase spirals as in the *Gaia* data. Of course, this can be due in part to the numerical diffusion. We want to emphasize, though, that our objective is not to reproduce the *Gaia* phase spiral in its details, which is a really challenging task in a cosmological simulation, but to detect qualitatively similar phase spirals originating in a more complex model than the ones seen so far.

In Figs. 3.2 and 3.3 we show the vertical phase space density in each of these 12 regions defined above but for all snapshots, between 6 and 0 Gyr, in density (first column), weighted by the velocity $V_\phi$ (second column), and by $V_R$ (third column). Typically, in each region, we find about 5000 to 19000 stellar particles. In all panels, we see a non-uniform distribution, with most of them having a spiral shape.In fact, for the first snapshots that we study, there is already a certain degree of spirality. We note that there are previous passages of the satellites before 5.5 Gyr in lookback time. The formation of the stellar thin disk in our model is enhanced by the last merger at ∼9.5 Gyr, and, once formed, it remains almost permanently disturbed by the many following interactions with the satellites. However, we can see that the phase spiral becomes more perceptible around the 4 Gyr. At later times, the vertical phase space contains also thin short phase spirals, separated from the main distribution. Some of them seem to be formed by particles of similar ages, and therefore they could be phase-mixing structures from particular star-forming groups.

If we analyze the panels as a whole we observe retrograde diagonal patterns that go from top-right to bottom-left, especially in the density and weighted by $V_\phi$. There are also bands in Fig. 12 of Bland-Hawthorn and Tepper-García (2021), who presented a similar figure, but they have different slope and

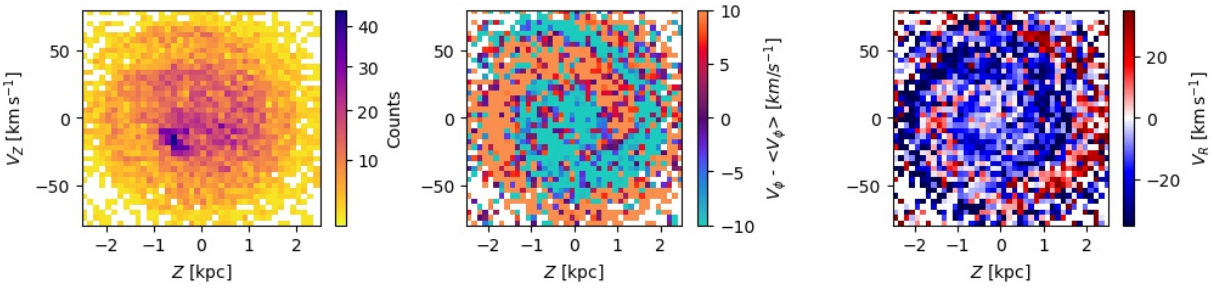


FIGURE 3.1: Phase space spirals ($Z - V_Z$) observed in the 0-5 Gyr stellar particles' age population of the GARROTXA simulation at 2.74 Gyr in lookback time, that is 1.1 Gyr after the pericenter of the most massive satellite (Arania). From left to right: a two-dimensional histogram with no weighting, $V_\phi$ weighted and $V_R$ weighted.

a clear $m = 2$ mode consistent with their bending wave model (the $Z$-$V_Z$ distribution repeats twice azimuthally) instead of an $m = 1$ like in our case. These patterns indicate that the perturbation has an angular dependence, and it moves through the disk. These bands are better observed in Fig. 3.6 and we come back to this later on.

In Fig. 3.4 we explore the vertical phase space structures as a function of radius for a single azimuth. We show the phase space density (top), $V_\phi$-weighted (middle), and $V_R$-weighted (bottom). We see that the global distribution changes from elongated in the velocity axis at small radii to elongated in $Z$ in the outer disk. This has been detected in the *Gaia* data (Laporte et al., 2019) and is a consequence of the smaller restoring vertical force in the outer parts of the disk. The phase spiral becomes visible at radii larger than 6 kpc and is present up to very large radius, showing that they are not exclusive of the range of 10-12 kpc chosen before. The short vertical extent of the distribution at inner radii, combined with the limitations in resolution, may be preventing our ability from seeing clear structure there.

In Fig. 3.5 we show seven stellar populations with increasing age, starting with the cold gas ($< 8000$ $K$) and newborn stellar particles. We observe that the global phase spiral is more pronounced in stellar particles with ages of about $1 - 5$ Gyr, which is compatible with the age analysis in Tian et al. (2018) and Bland-Hawthorn et al. (2019). Although there are some hints of structure in the older groups, it definitively fades out for particles older than 5 Gyr. This is due to younger stars being dynamically colder, thus reflecting more prominently the effects of perturbing phenomena. Also, as described in Li and Shen (2020), groups of older stars whose orbits are kinematically hot have a larger range of vertical frequencies, which may blur the phase spiral. We note here that the spiral pattern observed in the $V_\phi$-weighted maps (central row) differs from one age population to another (e.g. the $2 - 3$ Gyr group vs. the $3 - 4$ Gyr one). This result suggests that different stellar populations may have been perturbed and/or phase-mixed differently. Finally, we see that the very young stellar particles (less than 1 Gyr) are found in groups that do not fully cover the phase space but present some sort of spirality. In fact, we see in the first column that the cold gas appears to be distributed in non-isotropic phase space patterns and the newborn stellar particles (black dots) are not born close to $Z \sim 0$ and $V_Z \sim 0$. This will lead to subsequent phase mixing of the young populations which could create the thin spirals in the vertical phase space projection.

Above we show qualitatively that we detect phase spirals at multiple times and locations, but it is not trivial to distinguish the moment of their appearance. Here we present a method to quantitatively discern the emergence and development of said phase spirals. We do a Fourier analysis of the vertical phase space of the same disk regions and young and intermediate age population ($0 - 5$ Gyr) as in Figs. 3.2 and 3.3. We

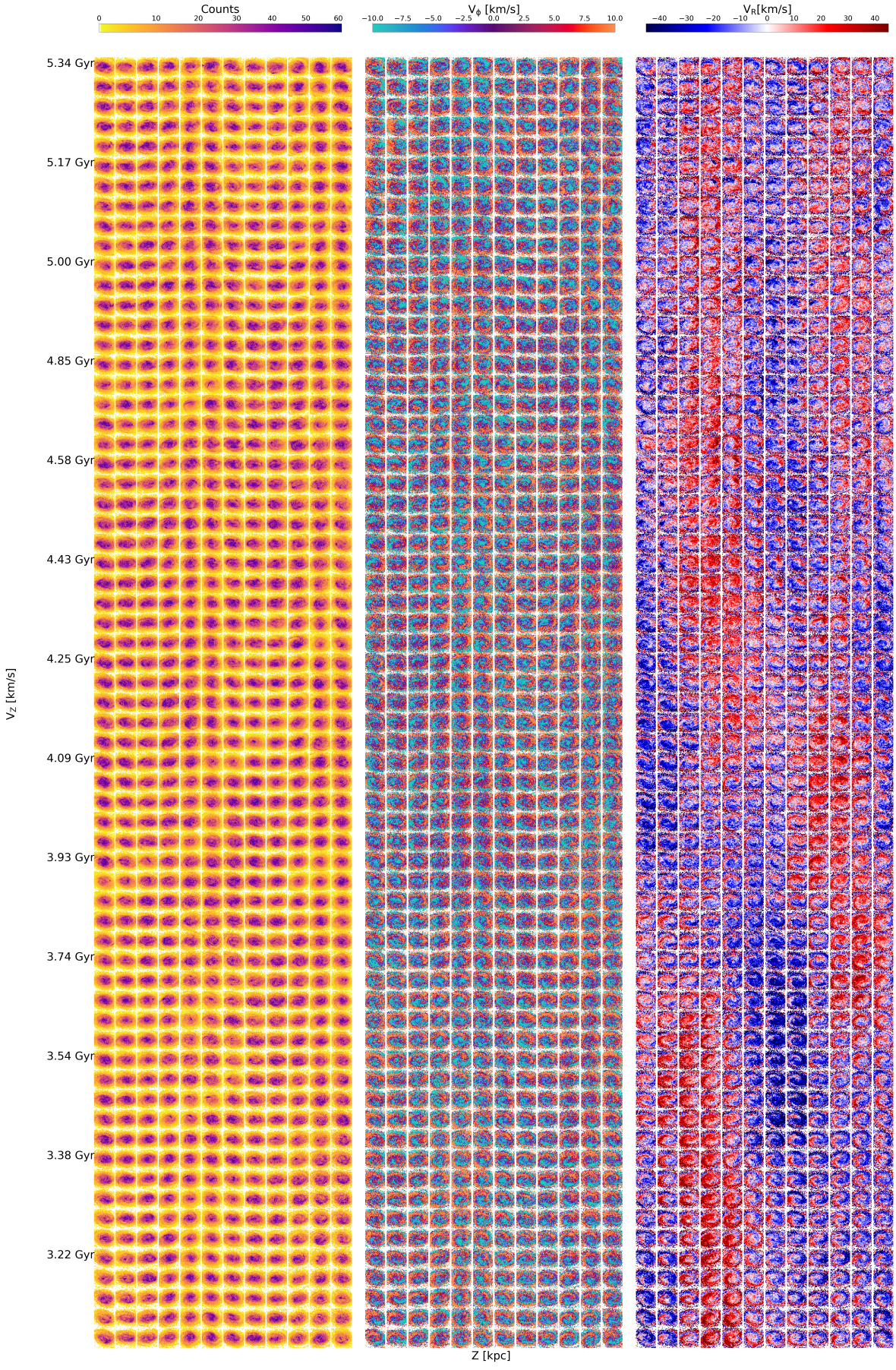


FIGURE 3.2: Phase spirals in the vertical phase space as scatter, (left columns), $V_\phi$ weighted (central panels) and $V_R$ weighted (right panels) at different azimuths and times between 5.3 - 3 Gyr in lookback time.

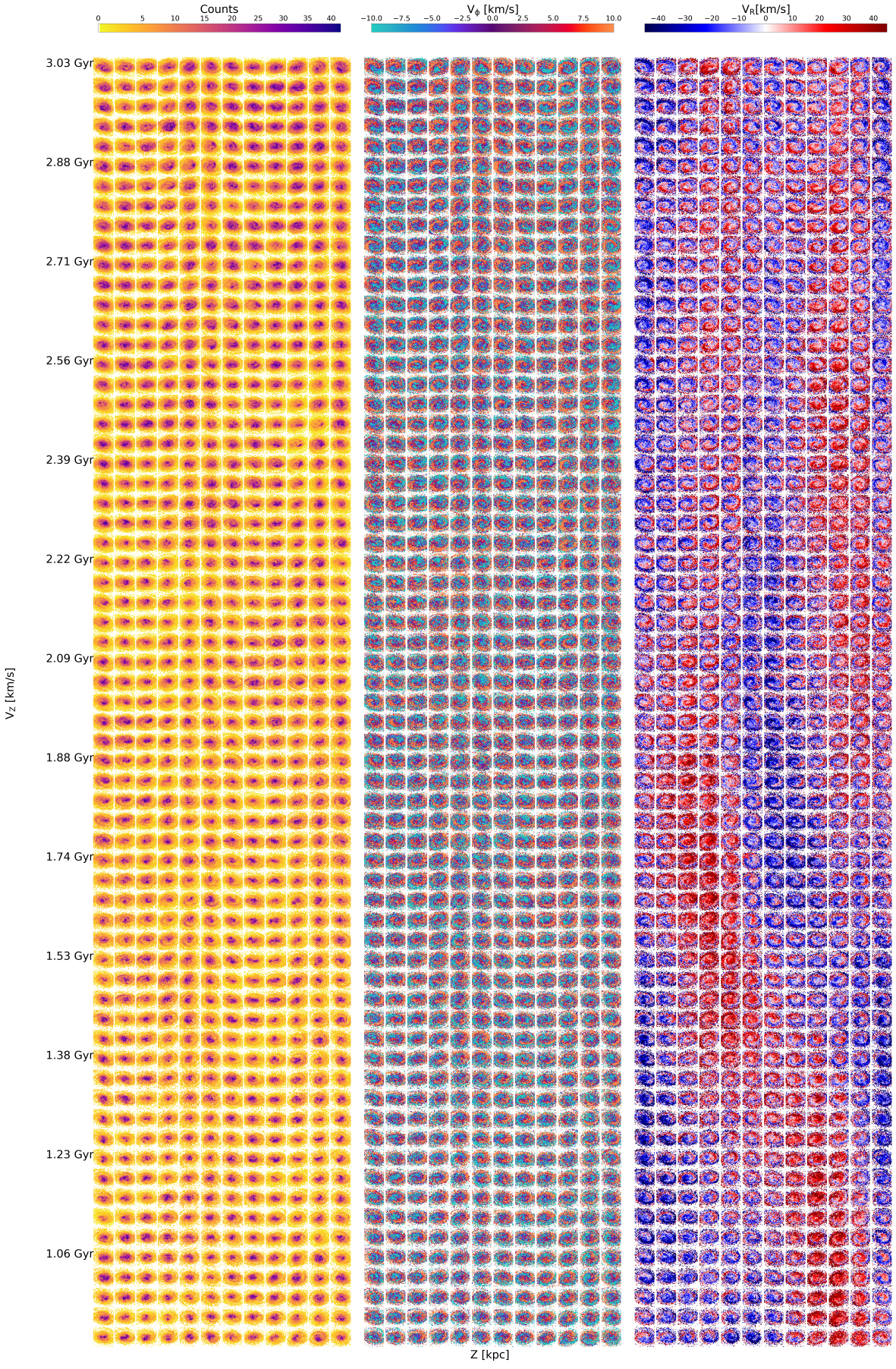


FIGURE 3.3: Phase spirals in the vertical phase space as scatter, (left columns), $V_\phi$ weighted (central panels) and $V_R$ weighted (right panels) at different azimuths and times between 3 - 1 Gyr in lookback time.

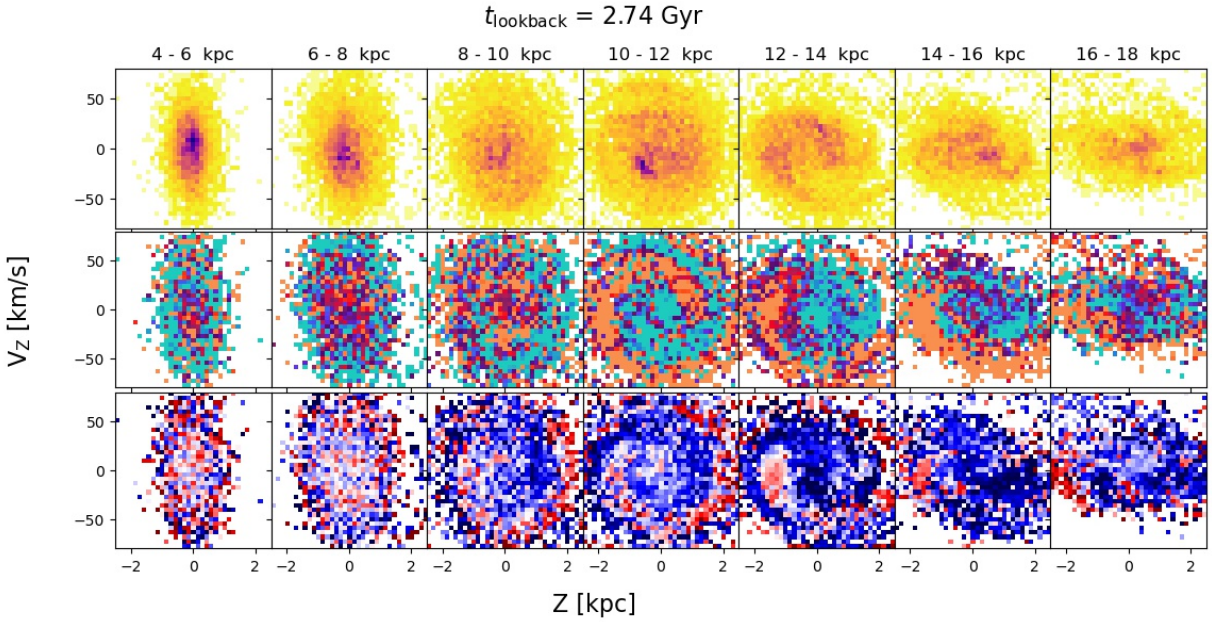


FIGURE 3.4: Vertical phase space distributions of stellar particles with age of $0-5$ Gyr at seven different radial bins (see top labels) and at a fixed azimuthal direction of 330° inside the disk, from the snapshot at 2.74 Gyr of lookback time. We show the phase space density (top), $V_\phi - < V_\phi >$ weighted (middle), and $V_R$ weighted (bottom). $< V_\phi >$ is the mean azimuthal velocity at each region.

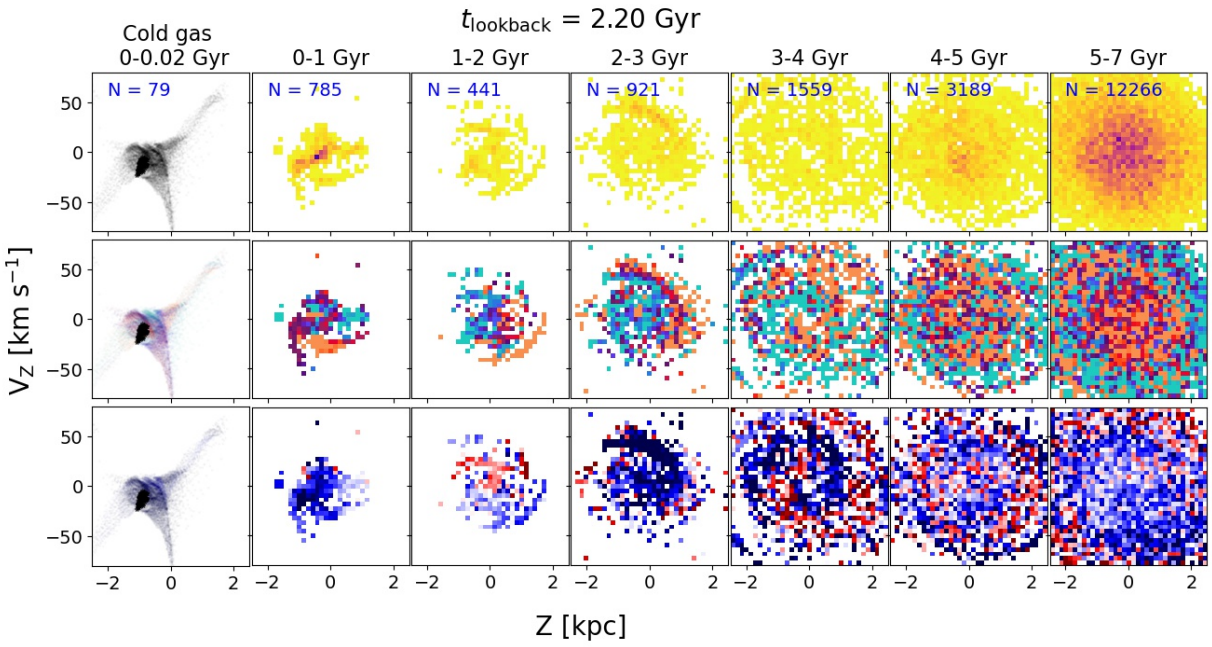


FIGURE 3.5: Vertical phase space of seven age populations within a region with fixed azimuth (150°) and distance to the galactic center (10-12 kpc), at lookback time of 2.2 Gyr. From top to bottom we show: density of stars; $V_\phi - < V_\phi >$ weighted; $V_R$ weighted. Additionally, the first column shows the cold gas and the newborn stellar particles as black dots.

normalize $V_Z$ with the dispersion of $Z$ so that both axis have the same scale. In this way, the distribution of the phase space have a circular shape, which can be divided in annular bins to proceed with the Fourier modes calculation at each one. A phase spiral will present a high amplitude of the m=1 mode in the $Z$-$V_Z$ space (or $m = 2$ mode if two-armed) and will have a phase of maximum amplitude ($\phi_{\max}$) varying with distance to the $(Z,V_Z) = (0,0)$ point. We require that the $m = 1$ amplitude relative to $m = 0$ is 1.1 times larger than for higher modes (from m=3 to m=6), and that $\phi_{\max}$ has a standard deviation of more than 30 deg across the annular bins. If these conditions are not fulfilled, we set the amplitude to 0, which will reduce the number of false positives due to noise or to the presence of a bi-modal distribution without angular dependence. We exclude the two first and last bins, since those are the ones which often are more prone to generate noise.

The result of this analysis is the map of the temporal and spatial evolution of the strength of the phase spiral in density and also $V_\phi$ and $V_R$-weighted (top three panels of Fig. 3.6). In these panels we see how spirals appear and propagate in time (right to left) and azimuth (bottom to top), following diagonal patterns consistent to the ones seen in the extended version of Figs. 3.2 and 3.3. We estimate that the azimuth propagation of phase spirals with high Fourier amplitude has a period of about 300 Myr, which is compatible with the rotation period at the range of 10-12 kpc in radius (250-320 Myr).

These bands are of unknown origin but we remark that they are not equivalent to the bands seen in Fig. 12 of Bland-Hawthorn and Tepper-García (2021) where these bands correspond to volumes that are re-aligned with the impact site of the perturber at outer radius. Our bands have a higher frequency than the re-encounters with impact sites. In fact, in our model most of the pericentres occur outside the disk region and even if we consider those points, we get re-encounter times of about 400 Myr or larger. We note that the differences between our bands and those of Bland-Hawthorn and Tepper-García (2021) are not surprising since the models that we are comparing here are significantly different (our satellites impact points are outside of the disk in most of the cases, the interactions are not as impulsive as in their model, and we may have collective effects due to the presence of many satellites at once, with pericenters at very similar times, as discussed in Sect. 3.4). Nonetheless, the period of these bands must be related to the physics of such phenomena and will be further discussed in the next chapters of this thesis.

Globally, the phase spirals are significantly more intense at certain times, which was already noticed in Figs. 3.2 and 3.3, but is now quantified using our Fourier technique. The top three panels of Fig. 3.6 present interesting differences. For example, the amplitudes of the $V_\phi$ weighted and $V_R$ weighted spirals (second and third rows, respectively) are higher around 4 Gyr while the ones for the density (first row) are higher around 2 Gyr. Moreover, the duration of high intensity phases is different, with the $V_R$-weighted coefficients decaying faster than for $V_\phi$. However, at recent times ($< 2$ Gyr), there are progressively less particles and the distribution is more compact in the $Z$-$V_Z$ space, which may have some effect on our strength estimator applied to different quantities (density or velocity-weighted).

## 3.3 Satellites and Star Formation

In this section we analyse the relation of the phase spiral with the main satellites in our model. We first characterized their properties and orbits in Chapter 2. We then computed the mean acceleration onto the disk applied by each satellite as a function of time (fourth panel of Fig. 3.6).

The satellites present different levels of impulsiveness. They also have different orbital inclinations, with Arania or DM1119 having almost polar orbits and Grillo or Escarabajo, a more planar one. Some other pericenters occur while the influence of previous ones must still be ongoing (e.g. Grillo's pericenters

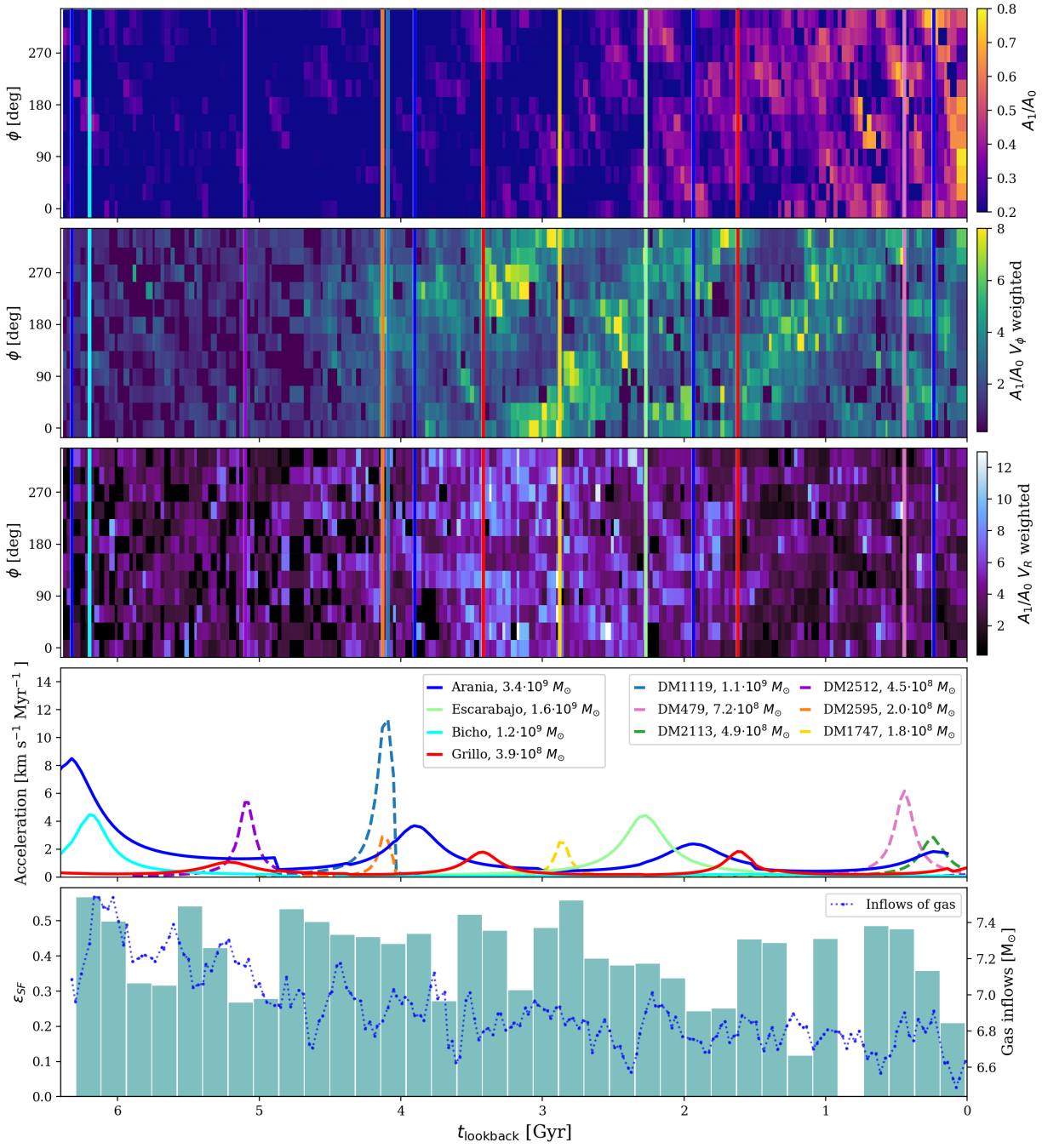


FIGURE 3.6: Amplitude of the phase spiral with time and relation with satellite orbits and star formation. **First three panels:** m=1 Fourier amplitude in the Z-$V_Z$ space, for the same regions and ages as in Fig. 3.2 and 3.3, computed for the density, $V_\phi$-weighted, and $V_R$-weighted, respectively. **Fourth panel:** acceleration onto the disk by the main satellites with darker colours indicating a lower vertical distance above/below the disk plane. Here the small discontinuities are artificially caused by our re-calculation of the virial radius. **Bottom panel:** star formation efficiency (histogram) and gas inflow histories (blue dots and line). Coloured vertical lines indicate the times of pericentres.

at 3.5 Gyr happens after the recent pericenters at 4.1 Gyr of DM1119 and 3.9 Gyr of Arania). Interestingly, we also see that, although the main satellites have different infall times, some satellite's pericenters tend to synchronize, occurring almost simultaneously by $z = 0$.

Comparing the fourth panel with the results from the Fourier analysis (three top panels) we see low amplitudes of the phase spiral at initial times but a clear coincidence between the presence of well defined phase spirals (warmer colors) and the pericenters (coloured vertical lines), for example after lookback times of 4 and 2 Gyr. It is difficult to establish a direct causality between the pericenters of specific satellites and the appearance of the phase spirals. For instance, the most important acceleration kick is at 4.1 Gyr with the crossing of the satellite DM1119, which has $10^9\ M_\odot$ at the moment of the pericenter and crosses at a galactocentric radius of 20 kpc approximately. Although the phase spiral in $V_\phi$ (second panel) starts to appear at around this time, it is not after 700 Myr that reaches a maximum in amplitude, also after satellites Arania and Grillo have reached pericenters of their respective orbits. This timespan of 700 Myr corresponds to two disk rotation periods at the galactic radius of the observed phase spiral (between 10 and 12 kpc). The phase spiral signal is present over the next gigayear. At later times, from 2 Gyr on, it appears stronger in density (top panel), and less intense in both $V_\phi$ and $V_R$.

All the complexity in the history of external perturbations described above might be the cause of the differences among the first three panels of Fig. 3.6. Although as mentioned previously, some differences might be caused by the estimator used, some others, might be telling us about aspects of the perturber's orbits beyond merely pericentre times and masses, a characteristic that would be worth exploring further.

Many different satellites with their many pericenters appear naturally in our simulation. This, combined with the fact that in our model dynamically cold stars are being formed all along the evolution of the galaxy, results in different stellar populations responding differently to the new perturbations (see Appendix F for more discussion), which is something not captured by isolated models without star formation and gas. Moreover, the maximum strength of the gravitational pull of our satellites remains rather constant with time, in contrast with an interaction with a Sagittarius-like system, where every new pericentre induces a larger kick in velocity than the previous one, making it easier to "overwrite" the existing phase-space substructure. In any case, although we see a decrease of the signal after the 4 Gyr rise and a small increase/stabilization at about the time of the next pericenter, we can not confirm if the "reset" proposed by Laporte et al. (2019) and Bland-Hawthorn and Tepper-García (2021) occurs in our model after each pericenter.

For the sake of completeness, we also analyzed the evolution of the gas and star formation in the disk. In the last panel of Fig. 3.6 we show the cold gas inflow rate (blue curve) defined as the amount of gas that penetrates a thin shell of 0.5 kpc at a radius of $0.15R_v$with a significant negative radial velocity ($< -50$ km/s). We also show the star formation efficiency ($\varepsilon_{SF}$, blue histogram) computed as the fraction of stellar mass formed since the previous snapshot to the mass of gas available in the disk, calculated from the data shown in Fig. 2.14 of Chapter 2. This gas meets the star-forming criteria of temperature ($T < 8000$ K) and density ($n_H > 1$ cm$^{-3}$) just as in Roca-Fàbrega et al. (2016). With this panel, we confirm that satellite pericenters not only perturb the disk's dynamics but also boost its star formation efficiency, with some coinciding with an increase in the cold gas inflow as well (e.g. at 2 Gyr).

## 3.4 Discussion and conclusions

In this work we have detected, for the first time, the phase spirals in a realistic zoom-in cosmological model of a Milky Way-like system. These spirals are present throughout the last several Gyr of the evolution,

suggesting that this phenomenon might be common in the life of certain galaxies. The spirals are more notable for younger to intermediate-age stars and are especially prominent near pericenter passages of the three main galaxy satellites. These passages coincide with the time when we observe star formation enhancements, an effect that has already been directly related to accretion events (see Ruiz-Lara et al., 2020, for a discussion on the particular case of the Milky Way).

Most of the recent studies that modelled the phase spiral considered Sagittarius as the main culprit and used a heavy Sagittarius dwarf galaxy ($\gtrsim 10^{10}$ M$_\odot$ at the time of impact). For example, in Binney and Schönrich (2018) only a massive perturber was able to generate prominent phase spiral signals. Similarly, the masses considered in Laporte et al. (2019) and Bland-Hawthorn and Tepper-García (2021) are $6 \times 10^{10}$ and $2 \times 10^{10}$ M$_\odot$, respectively. Even more, although their work is based on a simplified one-dimensional model, Bennett and Bovy (2021) recently claimed that even a heavy Sagittarius would not be able to generate the phase spirals seen in Gaia DR2, invoking the need for a combination of other effects. By contrast, our heaviest satellite (Arania), which has a mass at first infall of $\sim 10^{10} M_\odot$, ends up with $\sim 10^8$ $M_\odot$ after several pericenters. These values are in approximate agreement with the initial mass of Sagittarius (e.g. $\sim 10^{10}$ M$_\odot$ in Niederste-Ostholt et al. 2010) and with some recent empirical derivations of the total Sagittarius mass at current times (e.g. $\sim 4 \times 10^8$ M$_\odot$ in Vasiliev and Belokurov 2020). However, the pericenter distance of our heaviest satellite is larger than the ones of recent Sagittarius pericenters, and thus the effects of our perturbers should be far less strong. In conclusion, our satellites seem to belong to the low mass regime, yet we do observe phase spirals and a correlation between pericenters and the strength of the phase spirals.

This can be attributed to the many extra characteristics that our model has with respect to previous models (e.g., the evolution in a cosmological context, hydrodynamical processes, disk secular evolution) that can play a combined role in shaping the phase space. For example, we note that in our model pericenters get synchronized over time and that there is a combined mass of up to $\sim 10^9$ $M_\odot$ by the time they start affecting the disk. Collective effects such as the wake induced in the halo by infalling satellites have been shown recently to be of large importance (Weinberg, 1998; Conroy et al., 2021; Grand et al., 2023) and in particular, coeval infalls can lead to the generation of a collective effect with strong impact on the disk kinematics (Trelles et al., 2022). There are also other possible mechanisms that could be expected to produce perturbations, such as a highly anisotropic distribution of dark matter left over from the satellites, multiple dark subhalos, misalignment between disk and halo, resonances, and the presence of non-axisymmetric structures in the disk. In particular, the role of the internal structures such as the central oval and spiral arms needs to be evaluated in detail since these phenomena can trigger vertical perturbations as suggested in Khoperskov et al. (2019). Nonetheless, in our model we do not see signatures of a process similar to the bar buckling of the central oval in the studied interval of time.

Another important aspect that no other model of the phase spiral included before is the gas. The in-falling cold gas and the newborn stars can keep the disk kinematically cold and thus more unstable to internal and external perturbations. Additionally, as is the case of our model, the gas might be vertically perturbed and the young stellar particles could inherit its dynamical properties. We have observed the appearance of thin segments of phase spirals which seem to be connected to phase mixing of star formation complexes born from this perturbed gas. At this stage, however, it is not clear how these thin spirals are related to the global phase spirals. Interestingly, star forming regions organized in certain vertical patterns (Alves et al., 2020) and global vertical disturbances in the gas (Lallement et al., 2019) have been observed in the MW.

We can still not claim a perfect match between the phase spirals observed in the Gaia data and the ones found in our model. Nevertheless, using simulations like the one analyzed here allows us to study the

dynamical processes that give rise to the phase space spiral (or any other phase space structure, for that matter) in a much more realistic scenario for a MW-sized galaxy. Moreover, the possibility of connecting local dynamical phenomena with global perturbations from satellites, gas behavior and star formation processes in the same model in the context of a cosmological simulation is definitively a promising future avenue of work that we open in this thesis.

CHAPTER 4

# Vertical perturbations by dark matter, satellite galaxies and gas

This chapter is mainly based on the article *Galactoseismology in cosmological simulations: Vertical perturbations by dark matter, satellite galaxies and gas* by García-Conde, B., Antoja, T., Roca-Fàbrega, S., Gómez, F., Ramos, P., Garavito-Camargo, N., and Gómez-Flechoso, M. A., accepted for publication Astronomy & Astrophysics, of which I am first author. Thus, figures and text have been taken literally from said work.

## 4.1 Introduction

As discussed in Chapter 1, the stars of the MW's disk seem to be vertically disturbed. These disruptions can be measured as features in the stellar density distribution such as the warp, corrugations, and north-south asymmetries (Widrow et al., 2012; Williams et al., 2013; Schönrich and Dehnen, 2018), and more recently, the phase spiral (Antoja et al., 2018). All these can be seen as deformations in both the velocities and positions with respect to the galactic plane, and thus, they can also be detected as bending waves. This bending behavior has also been detected in other galaxies (Gómez et al., 2021; Nandakumar, Narayan, and Dutta, 2022; Urrejola-Mora et al., 2022). Several theoretical studies using N-body and analytical models have attributed vertical perturbations to interactions with satellites, (e.g. Gómez et al., 2013; Debattista, 2014; Vega et al., 2015; D'Onghia et al., 2016; Laporte et al., 2018; Semczuk et al., 2020; Bennett and Bovy, 2021), the dark matter wake as a consequence of the interaction between the halo and an external perturber (Weinberg, 1998; Gómez et al., 2016a; Laporte et al., 2018; Grand et al., 2023), and the interaction with dark matter subhalos (Feldmann and Spolyar, 2015; Chequers, Widrow, and Darling, 2018; Tremaine, Frankel, and Bovy, 2023). Other mechanisms that amplify the vertical perturbations of the disk include gas infall along warps (Khachaturyants et al., 2022) and misalignment of the plane of stars at different radii (Sellwood and Debattista, 2022). Thus, vertically disturbed stars can have a diverse range of origins and a perturbed disk may be a common state throughout galactic disks.

In the work of Grion Filho et al., 2021, they used a purely gravitational N-body simulation to calculate the accelerations produced by the disk, the Sagittarius-like dwarf galaxy, and the dark matter halo, with the aim to discern the dominant cause of perturbations in the different parts of the disk and at different times of evolution. They found that in their model there are moments when the dark matter halo's response to the passing of the satellite amplifies its effect. However, one should include the hydrodynamical component to have a complete picture of the dynamical mechanisms taking place in a galactic disk. Cosmological

hydrodynamical simulations include gas, and thus, they take into account realistic satellite accretion into the host galaxy. Furthermore, in these kind of models, multiple satellites can perturb the disk, whereas isolated N-body models usually only account for one perturbing satellite interacting with the disk. However, multiple satellites can lead to different effects when in interaction with the disk and with each other (Rocha, Peter, and Bullock, 2012; Widrow et al., 2014; D'Onghia et al., 2016; Trelles et al., 2022). In Gómez et al. (2017) they used cosmological simulations to study vertical patterns in galactic disks. They have observed that roughly 70% of the simulated galaxies exhibit evident vertical disruption, with different causes, from near encounters with satellites, distant flybys involving massive companions, the accretion of misaligned cold gas, and the subsequent re-accretion of cold gas derived from the progenitors of gas-rich major mergers. Nevertheless, the spatial resolution within the simulation constraints the study of scales equivalent to the Solar Neighborhood. The study of Voort et al. (2015) also used a cosmological model to follow the evolution of highly misaligned gas, where the inner parts of the galaxy re-align with it faster, resulting in a warp at later times of evolution of the simulation. In the work of Semczuk et al. (2020), they used galactic disks from the IllustrisTNG cosmological simulation to study tidally induced warps, and found that both satellite interaction and gas accretion may induce warps.

In Chapter 3, we found phase spirals in a Milky Way-like disk for the first time in the cosmological simulation GARROTXA (Roca-Fàbrega et al., 2016) model. However, its exact origin was not clear, since the satellites in this model are less massive ($\sim 10^9$ $M_\odot$ at the moment of the pericenter) than the minimum mass expected to excite phase spirals, at least in the context of the Sagittarius dwarf galaxy and the Milky Way. For example, the models by Laporte et al. (2019) and Bland-Hawthorn and Tepper-García (2021) used a mass of $6 \times 10^{10}$ and $2 \times 10^{10}$ $M_\odot$ respectively. We suggested that other effects such as the interaction of the collective effects of several satellites, or the misalignment of the angular momentum of the different components of the simulation, especially the stellar disk and dark matter halo, or the combination of some of them can generate strong perturbations in the disk. In subsequent work, Grand et al., 2023 utilized a high-resolution simulation featuring a galaxy akin to the Milky Way, drawn from the Auriga suite of cosmological simulations. In their study, they successfully identified and characterized phase spirals within the galactic disk. The primary driver behind the formation of these phase spirals in their simulation was attributed to the reaction of the dark matter halo following the passage of a satellite galaxy. It is worth noting that their investigation differs from our own, since they have a dominant source of perturbation, so they can identify the main cause of the triggering of the phase spiral.

Here, we further analyze the vertical behavior of the disk of the GARROTXA model. In this Chapter, we identify bending modes (as defined in Widrow et al. 2014) and we study their behavior using Fourier decomposition. We calculate the vertical acceleration of the dark matter particles onto the disk and its relation with the passing satellites and the inner structure of the halo itself. We also analyze the vertical gravitational acceleration applied by the gas to understand the relationship between its misalignment with respect to the disk. Thus, we present a more realistic picture of the satellites, halos, gas, and disk interactions.

In Sec. 4.2 we describe the behavior of the disk and quantify its disturbances, focusing on the vertical component. In Sec. 4.3 we calculate the vertical accelerations ($a_Z$) applied by dark matter and gas onto the disk and identify all satellites in the system. In Sec. 4.4 we link the measured bending modes and disk tilting to the different typology of interactions occurring in our model, characterized in the previous sections, and we find many intertwined agents involved in the bending of the disk. In the last section, we discuss the results and we present our conclusions.

## 4.2 Vertical bending modes of the disk

In this section, we direct our attention to the analysis of the $Z$ and $V_Z$ distributions within the disk, with an approach akin to that of Widrow et al. (2014), as a means to quantify the vertical deformations experienced by the disk. These deformations, expressed through bending modes, have been associated with the emergence of phase spirals (Bland-Hawthorn and Tepper-García, 2021; Darling and Widrow, 2019). Consequently, our additional objective is to provide insights into the phase spirals observed in the previous chapter. Through the precise identification of both the timing and spatial origins of these perturbations, we aim to establish a meaningful connection with the underlying processes, whether of internal or external origin, responsible for causing this deformation.

To calculate the vertical modes, we divide the X-Y plane into 70 bins from -25 to 25 kpc in both coordinates X and Y (bin size of $\approx 0.7$ kpc), and in $|Z| < 2.5$ kpc. This binning allows us to have enough stellar particles (an average of 350 particles per bin) to perform the following calculations. In each bin, we calculate the linear regression of $V_Z$ as a function of $Z$. The slope and the intercept correspond to the amplitudes of the breathing (A) and bending (B) amplitude respectively:

$$V_Z(x,y;z) = A(x,y)z + B(x,y) \tag{4.1}$$

An example of this method can be seen in Fig. 4.1, where we show the face-on projection of the galactic disk at two different lookback times of evolution corresponding to 2.33 Gyr (left columns) and 0.99 Gyr (right columns). We show an overdensity plot of the disk particles with a Gaussian filter (top panels), the bending (middle panels) and breathing (bottom panels) amplitudes of the young disk computed with Eq. 4.1. In the top panels, we can see a one-armed density structure, which is leading and retrograde (as seen in Chapter 2). In the central panels, we show how strong bending waves appear at specific times while they can be weaker in others (right vs left panels). In the breathing modes (bottom panels), we see a prominent mode $m = 2$, which follows the oval structure at the inner parts of the stellar disk, and it is present all through the recent galaxy evolution. This is consistent with previous studies, where this breathing behavior is linked to the bar or other non-axisymmetric internal structures (Widrow et al., 2014; Faure, Siebert, and Famaey, 2014; Monari, Famaey, and Siebert, 2015).

In this Chapter we mostly focus on the bending modes. In Appendix D we briefly study the breathing modes and their relation to the density patterns (i.e. the central oval structure and the retrograde one-armed pattern).

To visualize the evolution of the bending parameters over time, we take the values of $B$ in the $X$-$Y$ grid and apply a Fourier analysis that we evaluate in a polar grid, dividing the disk into radial sections with 1 kpc of width. For each ring, we have $N$ bins from the initial $X$-$Y$ grid, each of which is located in an azimuthal position $\phi_i$, and has a bending amplitude (weight in the Fourier decomposition) of $W_i = B_i$. Then, we perform a Fourier decomposition following the expression 2.4 described in Chapter 2. [1].

We estimated the amplitudes for each mode, $A_m$, at each radius and time. We focus on the results for $m = 1$ and $m = 2$ in the rest of the analysis. We also analyzed higher modes, but, even though at some times they are comparable with the amplitudes of modes $m = 1$ and $m = 2$, they are never dominant. We also study the phase at which the maximum amplitude for each mode is located at each radius, following the last expression in Eq.2.4.

[1] Similarly, we can analyze the breathing modes by doing $W_i = A_i$ and the density modes by using $W_i = M_i$. That is indeed what we do in Appendix D)

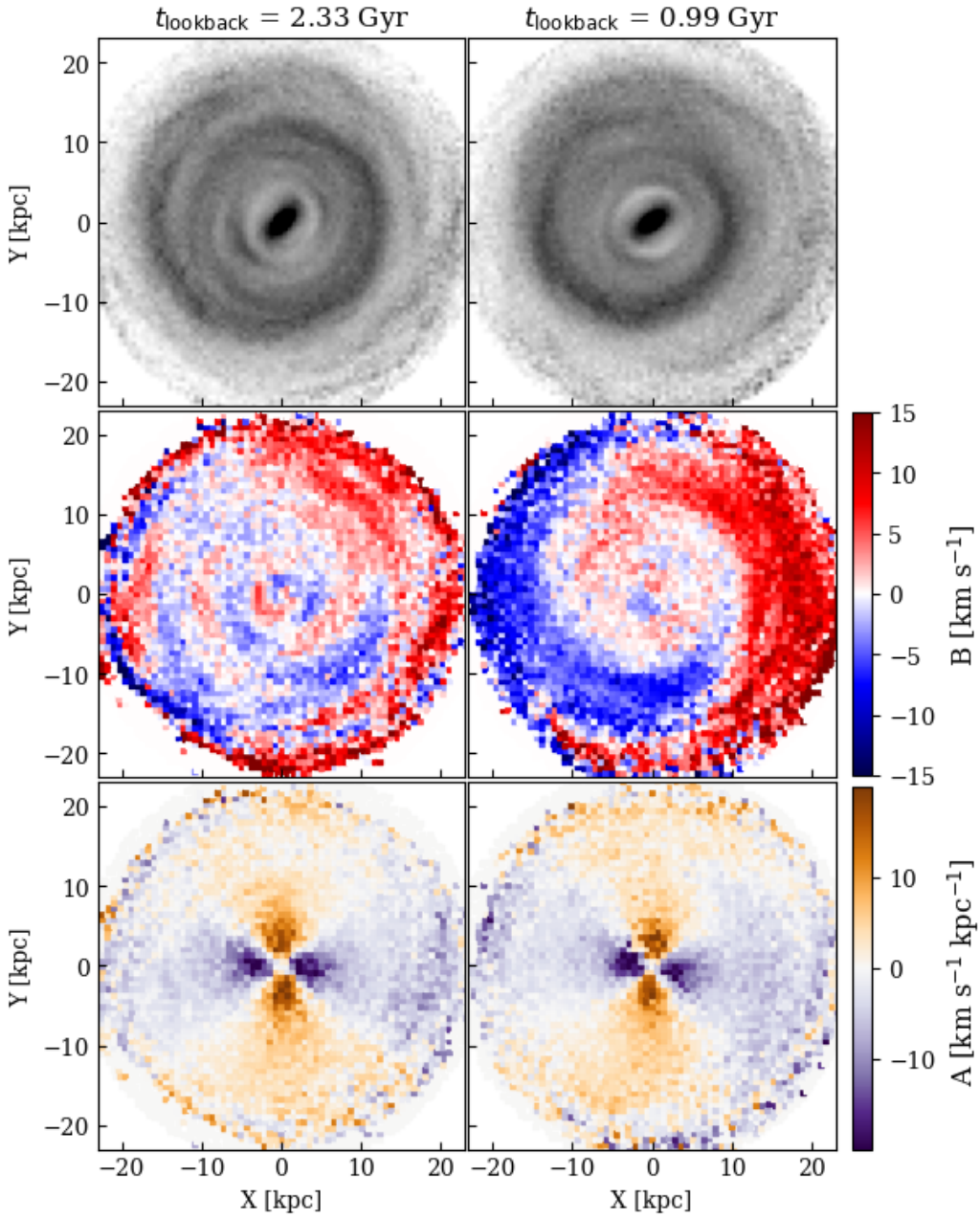


FIGURE 4.1: Overdensity plot of the disk particles with a Gaussian filter with $\sigma = 6$ (top panel), bending (middle), and breathing (bottom) maps at two different snapshots of the model of GARROTXA simulation in each column, 2.33 Gyr and 0.99 Gyr in lookback time. A strong bending mode can be seen at 0.99 Gyr (middle right panel).

In Fig. 4.2 we show the amplitude and phases of the bending modes $m = 1$ (left panels) and $m = 2$ (right panels) as a function of radius and time. The bending pattern seems to be very complex. Over the timespan studied, at $R > 7$, there is an overall dominance of red-black colors (corresponding to a phase of 0-100°), indicating that the bending is prone to be excited at this angle. At the beginning of the evolution (between 6.3 and 5 Gyr), there is a highly perturbed disk, as indicated by the higher amplitudes of the bending modes (top row of panels), which can be up to 20 km s$^{-1}$ at external radii. At these times, the phase of this bending mode $m = 1$ (bottom left panel) at radii $R > 7$ shows a slow retrograde pattern ($\dot{\phi} > 0$ in our reference system). From 2 Gyr to the present, we see that the amplitude of the bending mode $m = 1$ increases, with the phase oriented as in previous times, reaching its maximum at approximately 1.1 Gyr, with a value of 7.5 km s$^{-1}$ between 10 and 15 kpc, and 8.5 km s$^{-1}$ between 15 and 20 kpc with a leading shape.

At inner radii ($< 7$ kpc), we generally see a fast retrograde pattern ($\dot{\phi} > 0$, in the bottom left panel) that is excited at certain times (top left panel). We observe that its amplitude is maximum at 3.5 Gyr (with 3.5 km s$^{-1}$ of amplitude).

The $m = 2$ mode of the bending shows high amplitudes at earlier times (top left panel), and generally at higher radii, has prograde motion ($\dot{\phi} < 0$). From 2.5 Gyr to 1.8 Gyr we see an increase at intermediate regions of the disk, although the bending mode $m = 1$ generally dominates at these times and radii (we further discuss the behavior of the bending modes amplitudes in Sec. 4.5).

## 4.3 Perturbation agents: Dark matter, satellite galaxies and gas

To quantify the impact that the dark matter and gas have on the disk's vertical direction, we have calculated the vertical gravitational accelerations $a_Z$ they produce on the galactic disk which is on the $Z = 0$ plane at every snapshot. This is computationally faster than calculating accelerations on all disk particles. This mesh has 100 x 100 bins in the $X$ and $Y$ directions and extends to $R = 40$ kpc. We have used the following expression:

$$a_{z,bin} = \sum_{i}^{N_{part}} \frac{-Gm_i}{r_{i,bin}^2} \frac{r_{z;i,bin}}{r_{i,bin}}, \tag{4.2}$$

where $a_{z,\mathrm{bin}}$, the vertical acceleration at each bin, is the sum of all individual vertical accelerations from all the mass elements $N_{\mathrm{part}}$ (dark matter particles or gas cell) of each component (dark matter and gas). $m_i$ is the mass of each mass element, and $r_{i,\mathrm{bin}}$ is the total distance between the bin and the mass element. The relation $r_{z;i,\mathrm{bin}}/r_{i,\mathrm{bin}}$ takes the vertical component of the acceleration.

Certain mass elements, such as gas cells or dark matter particles, may be located very close to the $Z = 0$ plane, resulting in significant accelerations that contribute to increased noise in the Fourier analysis. To address this issue, we introduce a constraint on the maximum allowable acceleration within a bin. This limit corresponds to the maximum acceleration a mass element can exert when situated at a vertical distance of $\pm 54$ pc from the plane, equivalent to half of the gas cell's minimum size (which aligns with the spatial resolution of the simulation, measuring 109 pc). In cases where the acceleration within a bin surpasses this predefined threshold, it is subsequently set to this maximum value.

In Fig. 4.3, we present the variations in $a_Z$ in the $Z = 0$ plane during two distinct time intervals (three leftmost panels vs. the three rightmost), corresponding to specific instances when one or more satellites

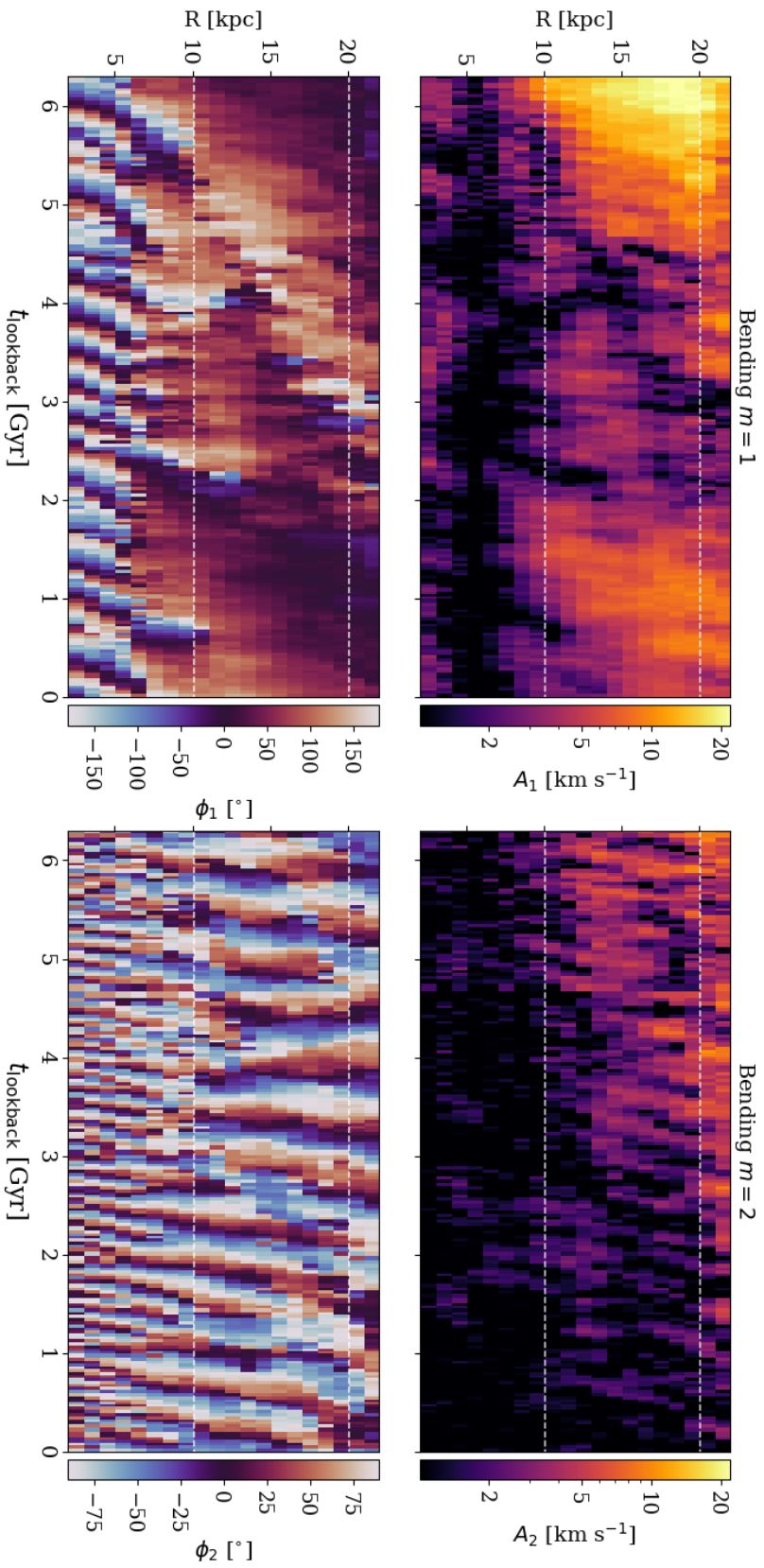


FIGURE 4.2: Temporal evolution of the Fourier amplitude $A_m$ (top panels) and phase $\phi_m$ (bottom panels) of the $m = 1$ (left panels) and $m = 2$ (right panels) modes. The phase of mode $m = 2$ ranges between $-90°$ and $90°$ due to the duplicity of the structures. The white horizontal grey-dashed lines mark the division of the disk at a radius of 10 and 20 kpc. The bending $m = 1$ dominates over $m = 2$ and shows higher amplitudes at outer radii (R$>$ 7 kpc) excited mainly at the beginning of the timespan studied and at later times from 2 Gyr on. The inner parts show faster retrograde bending waves with the highest amplitude happening around 4 Gyr of lookback time.

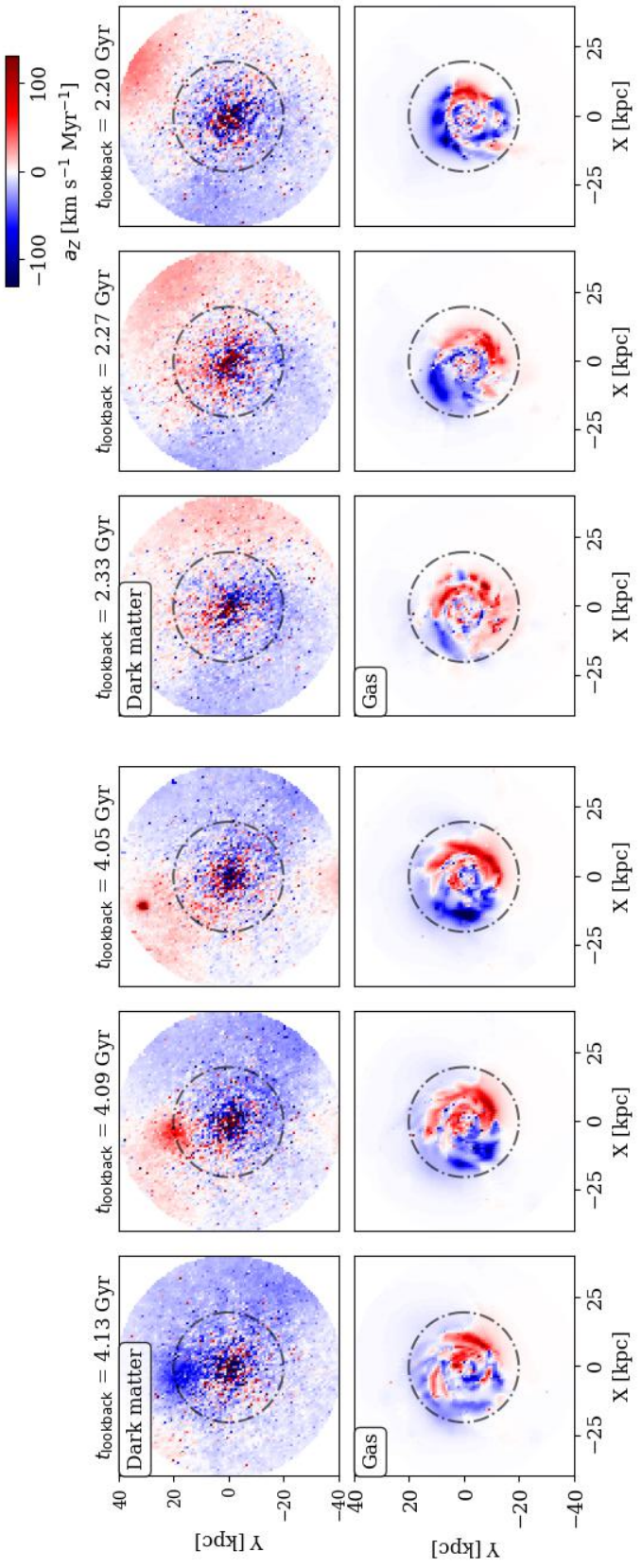


FIGURE 4.3: Vertical acceleration of dark matter (top panels) and gas (bottom panels). Black dot-dashed circles are situated at 20 kpc, illustrating the size of the stellar disk of the galaxy. The dark matter acceleration at the top three leftmost panels is dominated by the crossing of dark matter subhalos DM1119 and DM2595. The effect of gas at these times (bottom panels) is bimodal. The dark matter's $a_Z$ of the right block of panels is dominated by the satellite galaxy "Escarabajo", which applies positive $a_Z$ in the positive x - positive y region of the mesh.

approach their pericenters. The top row illustrates the acceleration by the dark matter particles. Notably, the effects of the satellite's crossing the plane between the first panel (at 4.13 Gyr with negative $Z$, negative vertical accelerations) and the next one (at 4.09 Gyr with positive $Z$, positive vertical accelerations). The three panels on the right side of the figure capture another interaction, wherein the satellite does not intersect the plane precisely at its closest approach. Nonetheless, we can discern the resulting vertical accelerations it induces in the outer regions of the grid, primarily highlighted in the upper right areas marked in red. It is important to note that these effects occur outside the confines of the galactic disk.

In the bottom row of Fig. 4.3, we illustrate the acceleration exerted by the gas component. Notably, this acceleration exhibits greater intensity within the disk region, where gas concentration is more pronounced. At specific instances (e.g., at 4.09 Gyr), the acceleration map exhibits a division, with one half of the gaseous component generating positive acceleration and the other half exhibiting a negative one. This observation raises the possibility of a gaseous disk that may be tilted or warped. This will be further analyzed in Sec. 4.3.3.

Once the calculation of $a_Z$ is made, we apply the same Fourier decomposition as in previous sections. This allows us to better visualize the evolution of the vertical accelerations with time, understand the effects that these have on the disk dynamics, and compare them with the results from the previous sections. In the next subsections, we present the accelerations from the different components.

### 4.3.1 Accelerations by dark matter

Here we first take the approach of considering the impact of the dark matter as a whole, without excluding any particles belonging to satellites. This will include the effects of the global structure of the halo, its satellites, and associated unbound material, and the possible wakes excited by these satellites. The results are shown in Fig. 4.4, where we display the amplitude of the $m = 1$ and $m = 2$ modes and their respective phases of maximum amplitude, $\phi_m$. At inner radii ($< 10$ kpc, and mostly in the $m = 1$ mode), the particles that are likely to dominate the acceleration are the ones from the gravity of the inner structure of the dark matter halo by proximity, over the particles situated at higher radius, like the ones from the satellites. Indeed, in Sec. 4.4 we show that the inner dark matter structure is triaxial and slightly tilted in relation to that of the disk, most of the time, producing a constant acceleration. This tilt is especially relevant at certain moments, such as 1.5 Gyr approximately, which coincides with the moments of higher accelerations at these radii.

In the outer parts of the disk, the acceleration produced by the dark matter component ($> 20$ kpc) comes mainly from the dark matter of satellites orbiting the system, especially when they cross the galactic plane. In the following Sect. 4.3.2 we study in detail the isolated effects of the satellites.

### 4.3.2 Accelerations by satellite dwarf galaxies and dark subhalos

As presented in Chapter 2, we employed the Rockstar halo finder (Behroozi, Wechsler, and Wu, 2012) to systematically detect all subhalos capable of exerting an influence on the kinematics of the galactic disk. With this halo finder, we identify all dark matter structures with $M_{200} > 10^6\ M_\odot$ (to avoid poorly resolved subhalos and contamination by field halo dark matter particles), and, using the dark matter particle IDs we also find all gravitationally bound particles. If the subhalos have stellar mass within 20% of the $R_{200}$ of the satellite (as calculated by Rockstar) we identify them as luminous. We use the value of $M_{200}$ right before the infall into the $R_{Vir}$ of the host galaxy as a reference of the size and mass of the subhalo. Once the satellites have entered the virial radius of the host, it is highly difficult to determine their mass. In these cases, we use or indicate the bound mass given by Rockstar.

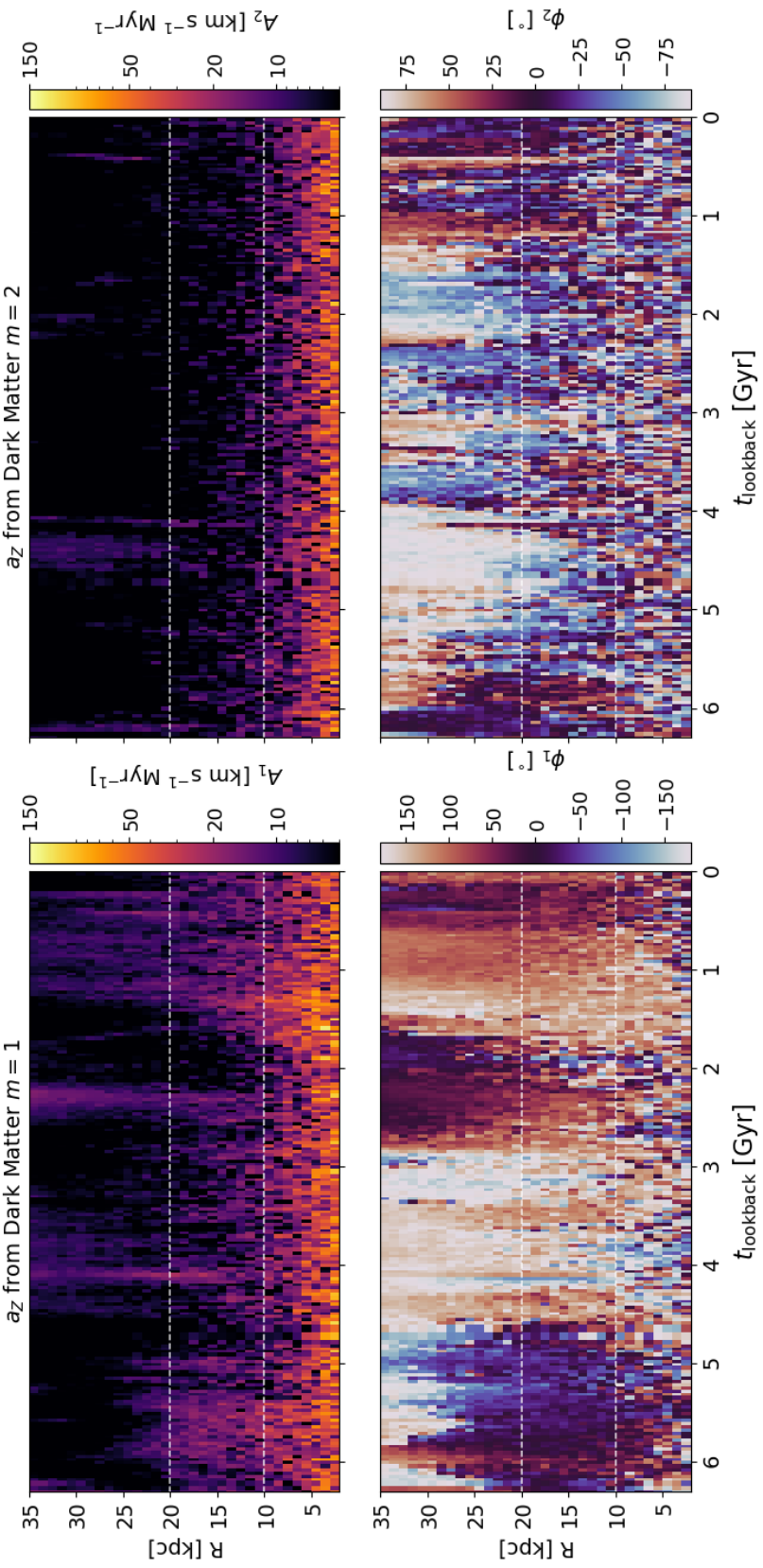


FIGURE 4.4: Fourier decomposition of the vertical acceleration by dark matter particles onto the $Z = 0$ plane. We show $m = 1$ (left panels) and $m = 2$, from which we have the amplitude of the mode (top panels) and the phase where the maximum amplitude is located (bottom panels). These are similar to 4.2, but extended to 40 kpc of radius. The inner acceleration is dominated by the inner dark matter structure.

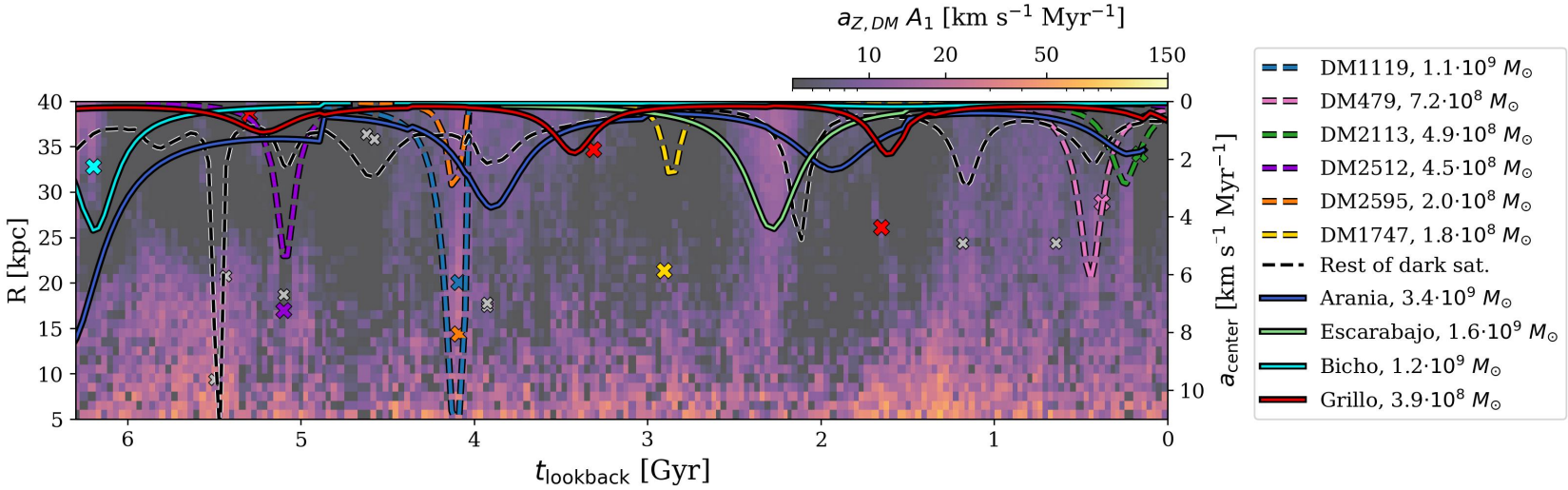


FIGURE 4.5: Total gravitational acceleration magnitude produced by each individual subhalo on the center of the galactic system (colored lines, right y-axis) and the sum of acceleration by the rest of (less massive) subhalos (black dashed line, right y-axis). Subhalos containing stellar particles are indicated as solid lines, and those with pure dark matter are shown as dashed lines. We also marked the moments and positions (cylindrical radius, left axis) when the satellites ("x") cross the galactic plane. The grey "x" symbols correspond to the crossings of less massive satellites. Background color and left axis are equivalent to the top-left panel in Fig. 4.4. Notice that, while the background color shows the vertical acceleration by all dark matter on the galactic plane $Z = 0$, lines show the total acceleration produced by subhalos at the galactic center, not at the $Z = 0$ plane. The latter gives proportionally lower values of acceleration due to the difference of the distance between the satellite and the closest point of the plane vs to the center of the galaxy. For the lines, we also use the data of $M_{\text{bound}}$ for each satellite, re-evaluated at each apocenter. The masses indicated on the label are the first mass registered for each satellite, which corresponds to $M_{200}$. In this figure, we see that the vertical acceleration from the dark matter halo between 25-40 kpc is correlated with the pericentric passages of several satellites, dark or luminous. The ones exerting more vertical acceleration are DM1119 and Escarabajo, as well as DM479 and DM2113 at later times.

The complete data of the subhalos (including both dark and luminous satellites) found by Rockstar can be found in Fig. B.1, in the Appendix B. In the timespan studied, we found nearly 500 independent subhalos (luminous or dark) that enter the galaxy. As expected from the ΛCDM Universe, we find a large number of dark satellites, i.e. subhalos with no stellar particles. For instance, inside the virial radius of the studied galaxy at redshift $z = 0$, we find 139 of the aforementioned subhalos (those of lower mass get destroyed over time) without any stellar particle, compared to 10 dwarf galaxies. These dark satellites, although they are generally less massive than dwarf galaxies, can interact with the disk as luminous satellites would.

In Fig. 4.5 we show again the top left panel of Fig. 4.4, i.e., the amplitude of $m = 1$ mode of the dark matter vertical acceleration, but now showing also the total, not just vertical, acceleration from each subhalo on the center of the galactic disk. The total acceleration by the most important dark satellites is shown with dashed lines, whereas the ones containing stellar particles are shown with solid lines. The radius and time at which each satellite crosses the plane are marked by a cross of the same color. We observe that the increase in the vertical acceleration in the regions from 25 to 40 kpc (background colors) is consistent with the close encounter with subhalos both dark and luminous (lines and crosses). The constant disk crossing of the many dark and luminous satellites is permanently perturbing the disk. However, only those of higher mass, and those that get closer to the galactic plane show significant $a_Z$ (see background colors vs. lines). For instance, at 5.1 Gyr or 2.9 Gyr the dark satellites DM2512 and DM1747 (violet and yellow lines) cross the disk but we do not observe a strong increase in $a_Z$ (background colors).

In contrast, the strongest interactions that we observe are the following. First, a strong interaction occurs at 4.1 Gyr, and it is due to a dark satellite (DM1119, blue dashed curve) containing a mass of $1.1 \times 10^9\ M_\odot$. This interaction is fast, and the pericentre occurs when the object is crossing the plane, at 20 kpc. This satellite is accompanied by another dark satellite, DM2595, with a mass of $10^8\ M_\odot$ (orange), and the dwarf galaxy Arania's second pericenter, whose mass at this moment is of $1.3 \times 10^9\ M_\odot$ (blue line with stars).

Secondly, another noticeable moment is the interaction occurring at 2.2 Gyr with a dwarf galaxy which we will refer to as "Escarabajo" (light green). This satellite starts its interaction with $1.6 \times 10^9\ M_\odot$, being a slower interaction than the previous example at 4.1 Gyr. In this case, the pericenter does not occur near the galactic plane yet we see a band of strong accelerations in the background colors. The black dashed line is the sum of the accelerations of those satellites whose mass does not exceed $10^8\ M_\odot$ or maximum acceleration does not exceed 2 km s$^{-1}$ Myr s$^{-1}$. This shows the accelerations of different dark matter subhaloes that, even though they are less massive, may have a relation to some of the increases seen in the $a_Z$ applied by the dark matter particles. However, the increase in acceleration by dark matter is not always related to passing satellites. We find that at 1.1 Gyr, the increase is not entirely explained by the passing of minor satellites, as in the case of Fig. 4.3. By examining the acceleration by dark matter in the X-Y projection, we find that this is related to the overall dark matter distribution. As will be discussed in Sec. 4.4.2, at these times there are instabilities of the galaxy that reflect as a net acceleration onto the plane. Finally, from around 1 Gyr until the present we observe several subhalos, which overall increase the accelerations in the intermediate and outer regions, like the pink and light green ones with pericenters occurring at 0.4 and 0.26 Gyr respectively.

### 4.3.3 Acceleration by gas

We apply the same method as in Sec. 4.3.1 to the gas cells of the simulation. The results are shown in Fig. 4.6. In the bottom left panel, which shows the phase of the mode $m = 1$, we see a sharp transition between the outer parts and the inner parts of the disk. This transition is located between 5 and 10 kpc

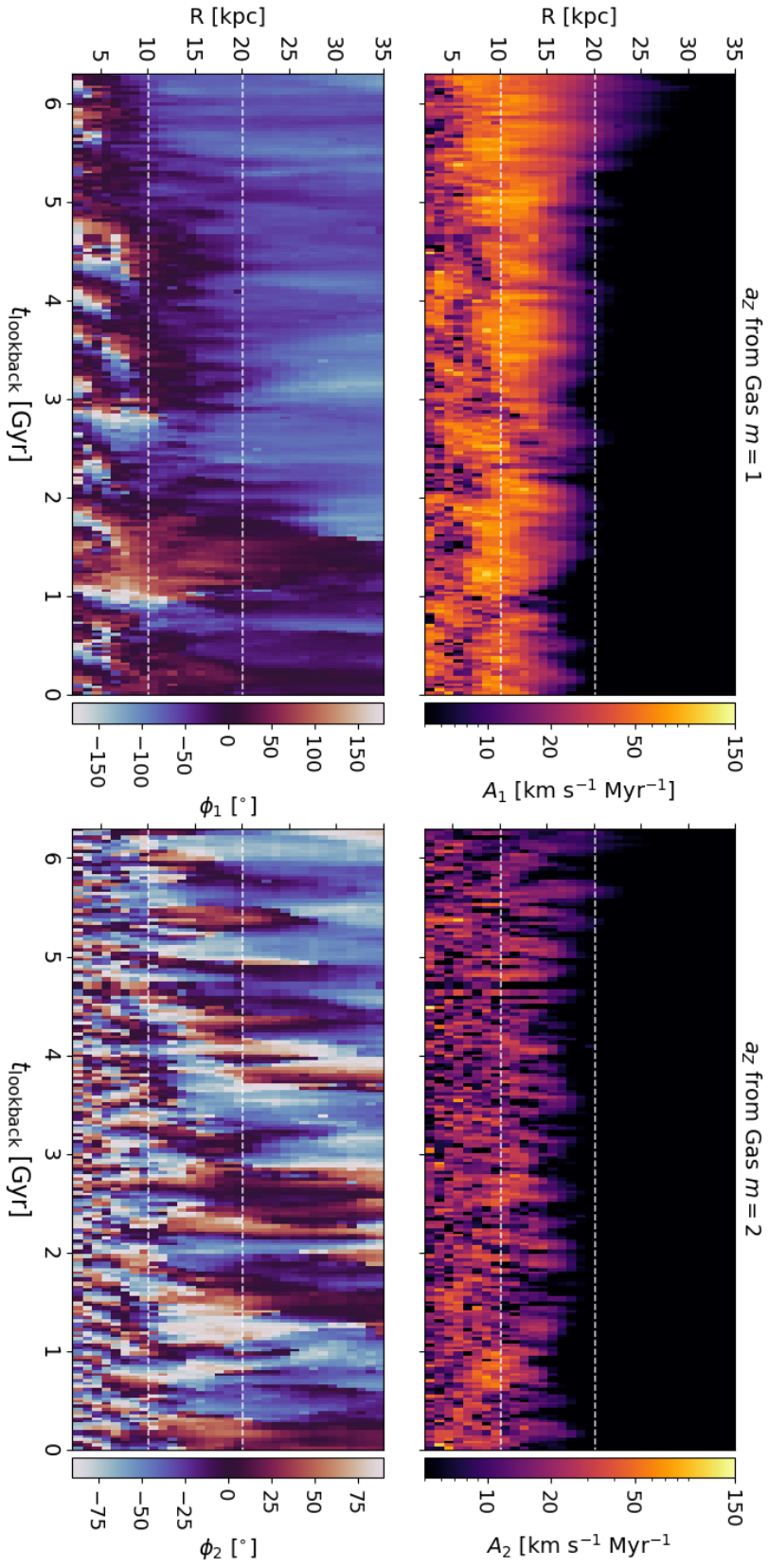


FIGURE 4.6: Fourier decomposition of the acceleration of the gas cells (similar to Fig. 4.4) onto the $Z = 0$ plane (galactic plane). We show $m = 1$ (left panels) and $m = 2$, from which we have the amplitude of the mode (top panels) and their corresponding phase of the maximum amplitude (bottom panels).

during the first snapshots and between 10 to 15 kpc from 5 Gyr on. This transition can also be seen as a sort of break in the amplitude.

At the inner regions, between 4.5 and 3.5 Gyr, we observe a retrograde rotating mode $m = 1$ that extends to 10 kpc approximately. This pattern has a period between 300 and 500 Myr and is similar to the one of the inner bending wave seen in the left panels of Fig. 4.2. Indeed, we see that at these times and radius, the gaseous disk can be misaligned with the stars by about 4 degrees (top panel of Fig. A.3), thus causing this specific mode $m = 1$ in acceleration.

At the outer parts (at radius of $R > 15$ kpc), we observe low amplitudes of the acceleration's mode $m = 1$ (top left panel). At these radii, there is a rather constant phase (bottom left panel), which corresponds to an approximate angle of -90° (blue colors). In this same panel, from 2 Gyr on, this phase changes to red/black (corresponding to angles between 50° and 100°), propagating towards the outer radius. This is accompanied by a higher amplitude (top left panel). From 1 to 0 Gyr the amplitude of $m = 1$ decreases, and the phase shows similar angles to previous instances. To study this in more detail we examined the gas distribution and its temperature in our model.

In Fig. 4.7 we show the gas in a zoom-out, face-on, projection (left column), a zoom-out, edge-on projection (central column), and a zoom-in, edge-on projection of the gaseous disk (right column) colored by temperature. In the first row (5.61 Gyr) we see a highly clumpy distribution of cold (blue) gas, stripped from Arania at its first encounter (at >6 Gyr). The right panel of this row (zoom-in) shows a deformed gaseous disk, highly tilted from the galactic plane.

Over time, as seen in the next zoom-out face-on panels rows, the gas falls into the galaxy preferably through a cold (blue) gas filament in the negative $Y$ and positive $X$ direction of -50° approximately at radii of $> 50$ kpc, and -90° approximately at smaller radii throughout almost all snapshots studied. This is especially well seen at the panels of 2.88, 2.56 and 1.88 Gyr (first column of the third, fourth and fifth row respectively, where the gas fall from the left parts of the plane, dominated by blue colors. Indeed, the latter direction of -90° is compatible with the observed phase of the acceleration in the Fourier mode $m = 1$. This gas is a mixture of the one that has been stripped from satellites (Arania's at early times, mostly tidally in its first pericenter, and ram-pressure stripped from Escarabajo at later times) and the one that outflowed from the disk at an early time through supernovae winds and initially kept in the circumgalactic medium. This metal-rich gas has shorter cooling times and thus falls into the galaxy (Dekel and Birnboim, 2006).

In particular, at 2.88 Gyr Escarabajo is already inside the virial radius and, as mentioned above, has suffered ram-pressure stripping due to the presence of a warm-hot gas corona around the galaxy. Gas stripped from Escarabajo mixes with the pre-existing inflowing gas (as seen at 2.88 Gyr and 2.56 Gyr in the third and fourth rows, respectively), cools down and, over the next half gigayear, enters the disk and increases the star formation (see Fig.2.14 in Chapter 2). Following this star formation event, from 2 Gyr on, we observe a change in the phase of the $m = 1$ mode (in Fig. 4.6), along with a higher amplitude of $m = 1$ in $a_Z$ which propagates from the inner parts towards the outer radii.At these times, the gaseous disk is tilted with respect to the stellar disk due to the recent interaction with the satellite Escarabajo. After examining the snapshots, we observe that there is also an anisotropic ejection of gas from the supernovae winds following the aforementioned star formation event in this direction which might be further perturbing the disk. As a consequence of these different phenomena, at 1.88 Gyr (right panel of 5th row in Fig. 4.7) the gaseous disk is tilted by about 4° to 8° (as seen in Appendix A, and in Sec. 4.4). Along the last gigayear of evolution, star formation is regulated by the galactic fountain leading to new supernovae events (although with weaker mass ejection than in the former case).

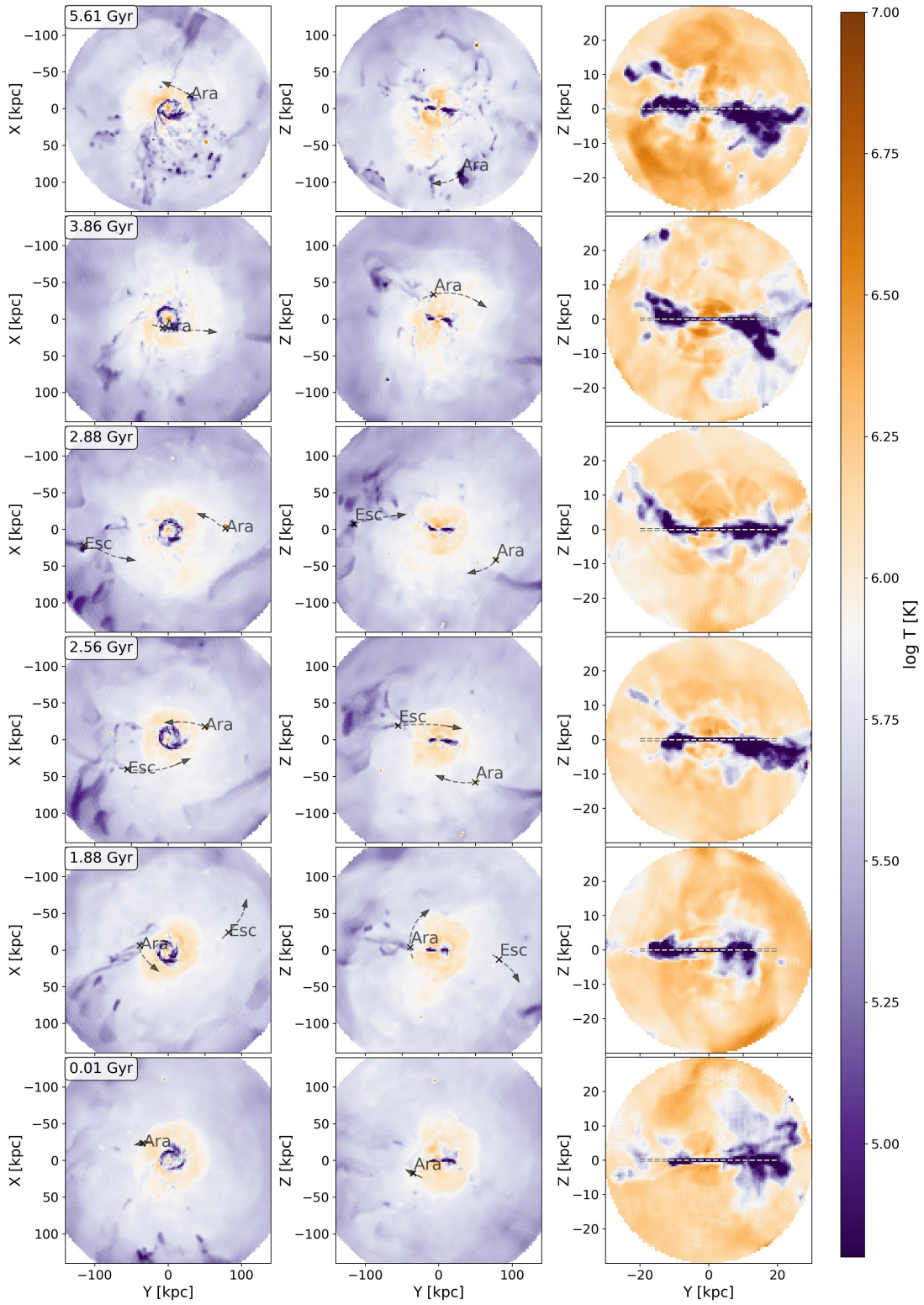


FIGURE 4.7: Distribution and temperature of the gas in GARROTXA. Left and central columns: Zoom-out face-on ($Y$-$X$ plane) and edge-on ($Y$-$Z$ plane) projection of the gas temperature at six different instances of the simulation colored by temperature. The crosses and dashed lines indicate the position and direction of the satellites Arania and Escarabajo. Right column: Edge-on projection of the gaseous disk, colored by temperature. The dotted horizontal line represents the plane of the stellar disk. The main inflow is reaching the galaxy from the negative Y direction.

## 4.4 Triggering agents of bending deformation

In this section, we make a connection between the times of higher vertical acceleration (from both dark matter and gas) and the behavior of the disk in terms of bending modes calculated in previous sections. In Fig. 4.8 we take the data from Figs. 4.2, 4.4, and 4.6, and get the mean amplitude of the Fourier modes within a radial bin (see top labels) to compare between them at specific radial regions. In panel A we show the mean amplitude of the $m = 1$ Fourier mode of the vertical acceleration produced by dark matter, between 20 and 40 kpc. In this region, the effects of satellites and dark matter subhalos are dominating, as seen in Sec. 4.3.1, and we see clear peaks at their moments of maximum approach. Panels B and F show the mode $m = 1$ of the acceleration by gas (orange line) and dark matter (blue line) at radii from 10 to 20 kpc and 0 to 10 kpc, respectively. We observe that the amplitude of the $m = 1$ mode of $a_Z$ applied by the gas is as significant as the one by the dark matter and even more dominant in the region from 10 to 20 kpc, due to its strong misalignment with the disk. At radii from 0 to 10 kpc, the $m = 1$ acceleration by the gas is comparable to that exerted by the dark matter halo. However, in terms of total vertical acceleration, the inner dark matter triaxial structure dominates due to the contribution of higher modes (Fig. 4.4).

In addition to this, we calculate the angle between the angular momentum vector of the stellar disk and that of the gas measured in spherical shells with radii between 10 to 20 kpc and between 0 and 10 kpc (dashed orange line in panels C and G, respectively). We observe that there is a correlation between the acceleration applied by gas and its angular misalignment with the disk. As mentioned in Sec. 4.3.1, here we also obtained the tilt of the central dark triaxial structure with respect to the stellar disk by calculating its maximum height and correspondent radius, with the former being the Fourier amplitude of the vertical distribution of dark matter particles in a cylinder with $|Z| < 10$ kpc. Although this tilt is only of 0.5-1.25° at times (blue lines in panels C and G), given the total mass of the triaxial inner dark matter structure this is enough to create large accelerations like the ones observed in Fig. 4.4. We also measure the changes in the angular momentum direction of the stellar disk in relation to the previous snapshot taking the cosmological box as a reference (panels D and H). Panels E and I show the mean amplitudes of the bending modes $m = 1$ (green lines) and $m = 2$ (purple lines), for regions between 10 and 20 kpc and between 0 and 10 kpc, respectively.

The perturbed initial state of the galaxy, in addtition to the subsequent series of interactions with satellites, complicates the identification of a specific moment in which the galaxy is at equilibrium along its history. However, in Section 4.3, we have described the key moments where interactions with satellites and dark matter subhalos occur. Based on these key events, we divide our analysis into two intervals. The first is defined by the interaction with the dark satellites (at 4.1 Gyr), and the other is that of the dwarf satellite galaxy Escarabajo (at 2.2 Gyr).We study both interactions in more detail and their possible consequences on the disk. In Appendix E we briefly study how these variables correlate to each other more quantitatively. In the next sections we show a more descriptive explanation based on Fig. 4.8 and the correlations between the variables.

### 4.4.1 Multiple dark and luminous satellites and bending waves

At 4.1 Gyr, in Fig. 4.2,we can see that a relatively higher amplitude of bending mode $m = 1$ is excited in the inner ($< 5$ kpc) parts of the disk. In the external parts ($> 10$ kpc) the increase starts later (from 3.9 Gyr on approximately). Both increases are in relation to previous instances where the amplitude is lower. In the case of outer radii, we observe a very slow bending mode $m = 1$ and prograde bending mode $m = 2$, which coincide with the pericenters of two of the dark satellites (DM1119 and DM2595) at 4.1 Gyr. These have, respectively, virial masses $M_{200}$ of $10^9$ and $10^8$ $M_\odot$, plane-crossing positions at

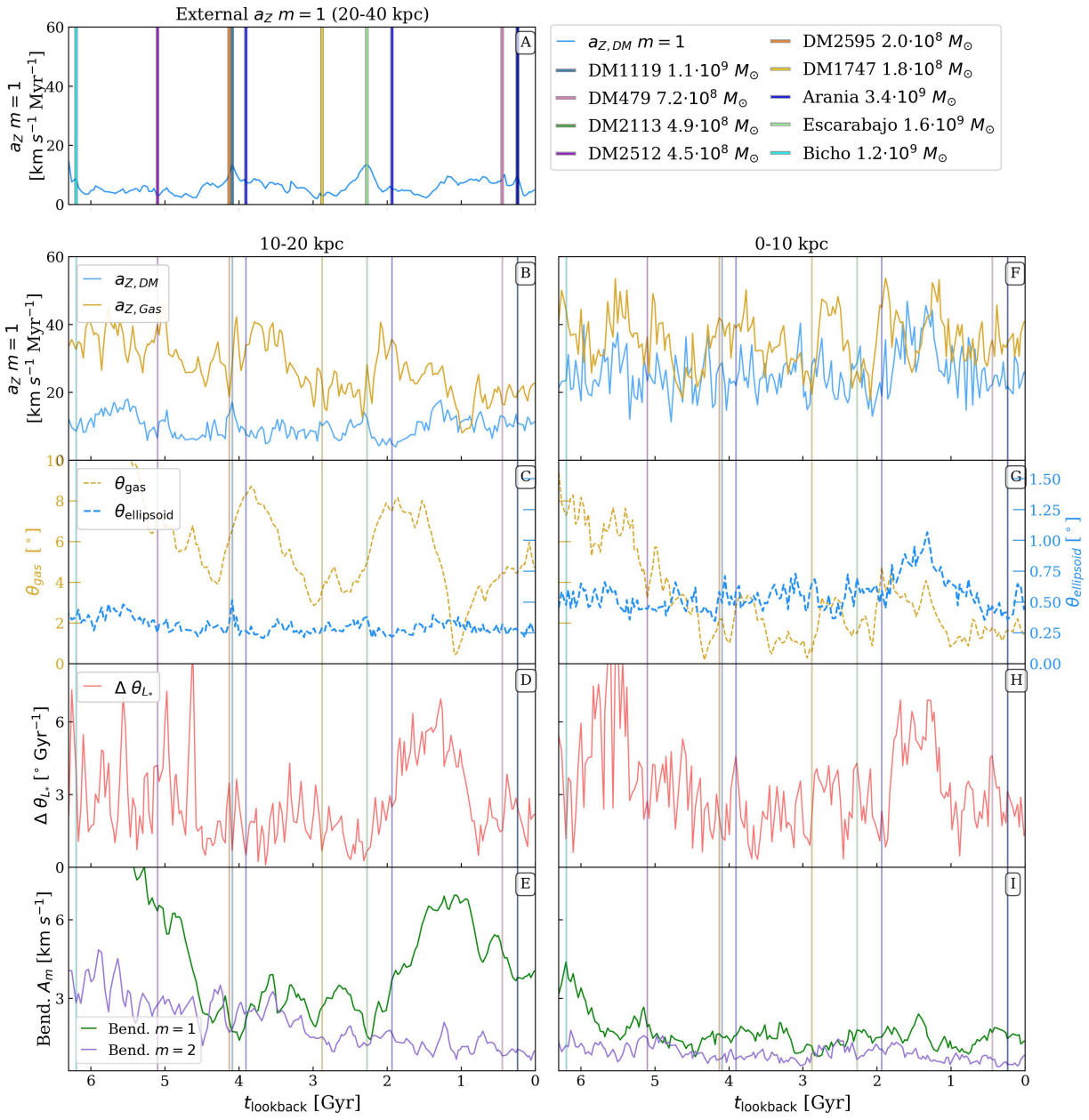


FIGURE 4.8: Top left panel (**A**) mean value of the amplitude of Fourier mode $m = 1$ of $a_Z$ by the dark matter (blue lines) at external radii (20-40 kpc). The vertical lines show the moments of maximum approach to the disk by those satellites of higher mass, and the labels indicate their $M_{200}$ at infall. The left panels show the calculated properties at radii from 10 to 20 kpc, whereas the right panels show between 0 to 10 kpc. Panels **B** and **F** show the mean value of the amplitude of mode $m = 1$ of the vertical acceleration of dark matter (blue lines) and gas (orange lines). Panels **C** and **G** show the angle difference between the angular momentum of stars and the angular momentum of gas (dotted orange lines, leftmost axis) and the tilt of the central dark matter triaxial structure with respect to the disk (dotted blue lines rightmost axis), denoted by $\theta_{gas}$ and $\theta_{ellipsoid}$, respectively. Panels **D** and **H** show the angular momentum vector variation in relation to the previous snapshot divided by the timespan. Panels **E** and **I** show the mean amplitude of Fourier amplitudes for bending modes $m = 1$ (green lines) and $m = 2$ (purple lines).

cylindrical galactocentric radii of 20 kpc and 15 kpc, and velocities $V_Z$ of 364 km s$^{-1}$ and 386 km s$^{-1}$, respectively. Their gravitational acceleration can be seen in the first three top panels in Fig. 4.3, and in Fig. 4.5. The pericenters of these satellites are compatible with the increase in bending modes at outer radii. During this time, the second pericentric passage of the satellite Arania also takes place at 3.9 Gyr (blue line in Fig. 4.5), which at the time of this interaction has a bound mass $M_{\rm bound}$ of $1.1 \times 10^9$ $M_\odot$, as calculated by Rockstar ($5 \times 10^8$ $M_\odot$ as calculated by measuring the tidal radius at apocenters of the orbit), which may also reinforce the bending patterns.

The inner retrograde bending pattern does not have a clear origin. It seems to be present throughout all the timespan studied. The oscillation of the inner bending mode (panel I of Fig.4.8) could be related to the inner density structures of the disk (see Appendix D). But, specifically from 4 Gyr, it has a higher amplitude with a maximum at 3.5 Gyr (top left panel of Fig. 4.2) and a more clear phase (bottom left panel of Fig. 4.2). In Sec. 4.3.3 we found that the accelerations from the gas show a wave-like pattern with similar behavior in rotation and periodicity. Its amplitude (panel F) increases approximately 400 Myr before the interaction with the dark satellites DM1119 and DM2595 (blue and orange line respectively, at 4.1 Gyr), and other less massive subhalos near the disk at that moment. Thus, it is unlikely that these subhalos are the cause of the increase in inner bending. At these times, we also see a slight misalignment in the gas (panel G). Our hypothesis is that gas is being accreted and destabilizing both the stellar and gaseous disk, inducing these specific bending waves, or at least enhancing the already existing one.

### 4.4.2 Distant interaction triggering bending modes via disk misalignment

The dwarf satellite Escarabajo has a total mass of $M_{200}$ of $1.6 \times 10^9$ M$_\odot$, and a stellar mass of $6 \times 10^6$ M$_\odot$ at its first infall, before its closest approach (2.2 Gyr). This interaction is slower ($V_Z = -50$ km s$^{-1}$ at the moment of the pericenter) than the ones mentioned in the previous subsection (see Sec. 4.4.1). Escarabajo's pericentric passage occurs at $R = 40$ kpc and at 16 kpc above the plane, thus far from it. We saw in Fig. 4.5 that the vertical acceleration by this satellite is mostly at the outer disk and barely reaches the inner parts. Even though the amplitude of the bending mode $m = 1$ (panel E of Fig. 4.8) reaches its maximum a Gyr later, its increase starts approximately 300 Myr after the pericenter of Escarabajo, which is half of the rotation period at these outer parts (600 Myr at 20 kpc). Furthermore, we need to take into account that, this being a slower interaction, the acceleration is not only applied at the moment of the pericenter but also several Myr before and after its maximum approach. Thus, this initial increase is compatible with the passing of Escarabajo.

The angular momentum of the stars also starts to change at 300 Myr after Escarabajo's passing (as seen in panels D and H). This indicates that Escarabajo's passage pulls and tilts the disk, especially at outer radii, where self-gravity is smaller. It also slightly shifts from its alignment with the central triaxial structure of the dark matter halo, which also generates accelerations that prevail longer in time. This creates a misalignment between the disk and the central dark matter and old stars (panel G) triaxial structure, which also exerts an acceleration into this disk. This is reflected in the amplitude of mode $m = 1$ of the acceleration by dark matter (panels B and F, blue lines), which reaches its maximum at approximately 1.2 Gyr.

Furthermore, in Sec. 4.3.3, we have seen how Escarabajo loses its gas and this mixes with previous existing inflows. We measure the cold gas inside Escarabajo's virial radius before its maximum approach and we find that this satellite contributes to $10^7$ $M_\odot$ of cold gas ($T < 10^4$ $K$). At these times, the misalignment of the gas disk in relation to the plane is 8 degrees (panel C of Fig. 4.8) and has an associated increase in the vertical acceleration by the gas at radii of 10-20 kpc (panel B). This is a period of destabilization of

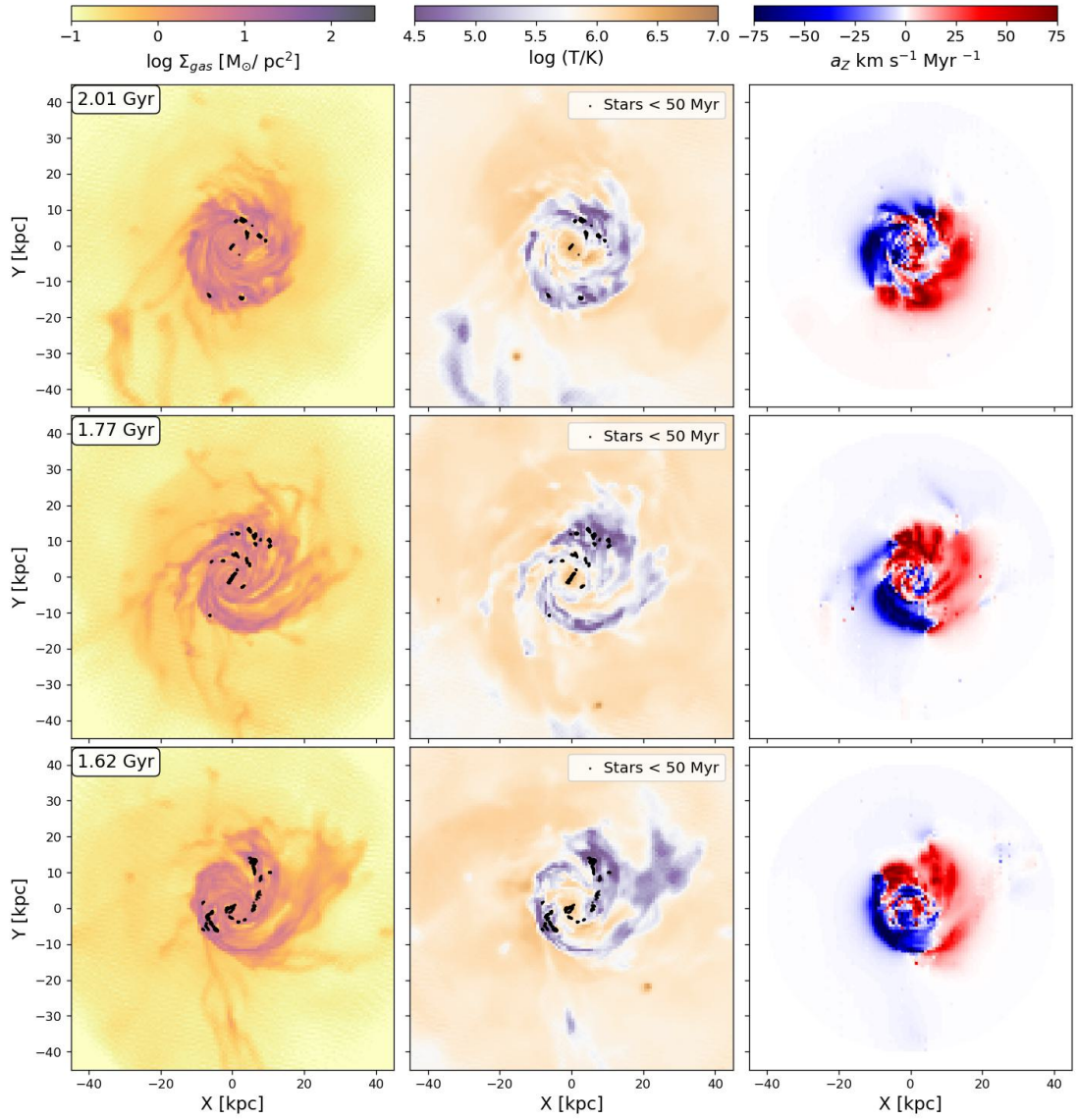


FIGURE 4.9: Column density (left panels), temperature (central panels), and $a_Z$ by the gas at three different snapshots after the interaction with Escarabajo. The black dots represent newly formed stellar particles with ages smaller than 50 Myr. Apart from the initial misalignment of the gaseous disk in relation to the stellar disk, the star formation and subsequent SNe further displaces and perturbs the disk in this direction.

both the gaseous and stellar disk as a consequence of the direct interaction with Escarabajo. Even though the infalling gas may not induce large perturbations by itself due to its mass, this new gas is settling in a different angle in respect to the disk. This new gas forms stars and the subsequent SNe bubbles may further perturb the disk, as seen in Fig. 4.9.

The bending mode $m = 1$ finally reaches its maximum at approximately 1.1 Gyr. This perturbation is present across stellar populations as a whole, but we find that it is stronger in stellar particles from 4 to 6 Gyr of age, approximately. The phase of this bending mode (bottom left panel of Fig. 4.2) indicates that it is aligned with the major axis of the central triaxial dark matter structure, which at this moment is tilted in the opposite direction. Thus, the central triaxial structure of dark matter halo appears to be crucial to the behavior of the bending pattern once it has been triggered. In Sect. 4.5, we also discuss briefly the possible effects of the disk itself on the shape of the bending wave.

Being such a complex system implies the existence of interactions that are amplified (or dampened) by the different components and structures. Thus, the gas and especially the central triaxial dark matter structure seem to contribute to a general destabilization between different parts of the disk, leading to the amplification and prolongation in time of the bending mode. It is expected to have a delay in the large-scale effects caused by the "tug" of satellites if they induce other imbalances. In addition to this, there are also all the new passages of other, less massive, but non-negligible, satellites from 1 Gyr on (see Fig. 4.5).

## 4.5 Discussion and conclusions

### 4.5.1 Summary

The existence of vertical waves and vertical phase mixing in the MW and in other galaxies has motivated our exploration of the bending modes in the stellar disk of the GARROTXA cosmological simulation. Using Fourier decomposition, we analyzed these modes and the vertical gravitational accelerations produced by the dark matter halo, gas, and satellite galaxies. Our main findings on the study of the bending of the stellar disk are:

1. The bending behavior of the stellar disk is much more complex than previously seen in N-Body simulations with different regimes at different radii and times. Throughout the simulation, we find different $m = 1$ modes coexisting but being excited at different times: One is slower and extends from $\sim$7 kpc to 20 kpc. This external mode is generally aligned with the major axis of the inner structure of old stars and dark matter. We also find an inner, with much lower amplitude, retrograde mode with high frequency dominating at $<$5 kpc.
2. The amplitudes of the bending mode are high in the early stages of the thin disk formation (20 km $s^{-1}$) and they can be up to 8.5 km $s^{-1}$ in the late disk evolution.
3. The slow pericentric passage of a satellite galaxy of mass $M_{200}$ of $1.6 \times 10^9$ $M_\odot$ triggers a disk tilting. When the stellar disk is tilted, it becomes misaligned with the inner dark matter triaxial structure (formed in an ancient major merger) which is less responsive to these perturbations as it is more massive. The effect on the disk bending is magnified by this new misalignment with the dark matter inner structure, leading to the highest vertical deformation in the last several Gyrs of evolution.
4. When the satellite enters the virial radius of the host, the gas of the satellite is also stripped by ram-pressure and it slowly cools down and falls into the disk along with pre-existing inflows. This cold gas enters the stellar disk non-isotropically, settles in a slightly tilted new gaseous disk, and,

lately, induces new star formation events and the creation of supernovae bubbles. Even though these processes may have a weaker impact on the disk, they are compatible with the accelerations seen exerted by the gaseous disk. Thus, all these processes might magnify the initial bend.

5. After one of the several interactions with dark subhalos, the inner $m = 1$ retrograde bending mode increases its amplitude and shows a phase pattern that correlates with the one of the gas vertical acceleration. Although this amplitude is relatively lower than the external bending discussed above, this may suggest that the gas-stellar disk misalignment plays an important role in the observed inner disk bending.

### 4.5.2 Discussion

We thus identified the following agents that trigger the bending of the stellar disk:

1. *Dark subhalos*: Dark satellites with masses $\sim 10^9\ M_\odot$ interact with the stellar disk on many occasions coinciding with a higher amplitude of the bending mode $m = 1$. The presence of such dark subhalos is expected in the ΛCDM galaxy formation theories and their interaction with the disk has been mostly studied as a source of disk heating (see e.g. Benson et al. 2004; D'Onghia et al. 2016). Here we highlight the role of such structures as triggers of bending perturbations of the disk.
2. *Satellite galaxies*: Satellite galaxies in the GARROTXA simulation at z$>$ 2 have at most $M_{200} \sim 10^{10}$ $M_\odot$ before their first infall, and most of them do not reach inner regions of the galaxy. However, although their direct tidal influence in the inner stellar disk is not large, they lead to a cascade of events that trigger some perturbations as discussed below.
3. *Inner density profile:* The inner tri-axial structure of the dark matter is an imprint of its ancient accretion history. At certain times, the largest vertical gravitational acceleration comes from a misalignment between the stellar disk and this dark matter ellipsoid. The misalignment is triggered by the tilting of the stellar disk, and the resulting bending can last for more than 1 Gyr. Similar phenomena have also been observed in Sellwood and Debattista (2022), where slow bending waves arise from misalignment between the inner and outer regions of the disk. We cannot discard an intrinsic coupling mode between the disk and halo contributing to this deformation. Furthermore, it is possible that the overall inner density profile of the disk also exerts a torque after the initial disk tilting, resulting in the leading shape of the warp (Shen and Sellwood, 2006; Gómez et al., 2016a), which is worth exploring in future analysis.
4. *Gas accretion and misaligned gaseous structures:* The vertical accelerations from the gaseous structures, often misaligned with the stellar disk, are comparable to those from satellites and dark matter. The origin of this misalignment is the inhomogeneity of the cold flows, the slightly different angular momentum of the incoming gas with respect to the actual stellar disk, and the expansion of supernovae bubbles. We speculate that all these phenomena may have a further impact on the bending behavior of the stellar disk, although we cannot measure in which exact proportion. The effect of extra-planar non-homogeneous distributed gas has also been detected as a source of vertical patterns and disk tilting in other models (e.g. Gómez et al., 2017; Khachaturyants et al., 2022).

Below we discuss other perturbation mechanisms that we have not looked into in detail but may need special consideration:

5. *Wake:* We have not found a dominant global asymmetry like the one expected when a strong wake is present in the Fourier analysis of the GARROTXA model. This could be because there is only one satellite galaxy with comparable mass to the Sagittarius Dwarf Galaxy, and its pericenter occurs at

large radii from the main host's center. This satellite has a mass above $10^{10}\ M_{\odot}$ before entering the virial radius of the host for the first time, and it loses mass down to $4.7\times10^{9}\ M_{\odot}$ at the moment of the first pericenter. Since the orbit of the satellite is mostly polar and slightly retrograde, we expect most of the torques to be in the vertical direction. However, in our case, both the collective and transient response to the wake would be weaker than expected for a Sagittarius-like satellite. Even if we have not quantified the exact torque applied by the wake, its effects are already captured by our calculation of accelerations by all dark matter particles. Furthermore, due to the dipolar nature of the halo's response, the wake effects are accounted for in our Fourier analysis.

6. *Streams:* We also have studied the tidal streams from Arania after its first pericenter (both stellar and dark matter debris) and we have found that the maximum vertical acceleration applied by this material is negligible in comparison with the progenitor and the rest of the dark matter halo. However, in the case of more massive satellites, their debris could be significant enough to affect the general structure of the dark matter halo (Garavito-Camargo et al., 2021).

7. *Density structures of the disk:* Other structures present in the GARROTXA model are a central stellar oval and a one-armed retrograde density pattern (see Appendix D). We have found some weak correlations between these stellar disk's non-axisymmetric structures and the breathing mode. Thus, we suspect that the physics of the vertical behavior in our model is also related to the density structure of the disc. However, we will study how these self-gravitating structures can perturb the disk in the future (see e.g. Grion Filho et al. 2021 for an analysis in a pure N-Body simulation).

In Chapter 3 we detected an increase in the amplitude of the phase spirals in intermediate-age stars coinciding with the most important satellites' percienters. We observe that the periodicity of the thick bands present in Fig. 3.6 of Chapter 3 is of approximately 1.2 Gyr, which is roughly coincident with the period of the one-armed density mode (Appendix D). This suggests that the phase spiral may propagate as this density mode in our model. The observed phase spirals are related to the phase mixing of the bending modes of the disc studied here, even if these appear to be not very large compared to other models (amplitudes of 8.5 km $s^{-1}$ in this model compared to amplitudes up to 30 km $s^{-1}$ in Gómez et al. 2017). In (Tremaine, Frankel, and Bovy, 2023) they propose a mixed scenario with several large-scale perturbations and numerous small-scale perturbations. This is qualitatively compatible with our model in the sense of having multiple dark-(and not dark) satellites affecting the disk. However, due to the resolution limitations, and the several interactions occurring simultaneously, we could not accurately track the spiral pattern or measure the winding of the phase spiral and, except for some temporal coincidences, we cannot attribute them to a specific event. The conclusions of this work point also to a mix of many processes (not present in the model of Tremaine, Frankel, and Bovy 2023) such as the structure of dark matter halo, accretion history, gas content, etc.

We conclude that although further study is needed, the phase spirals we observed can be a consequence of the many perturbations that the stellar disk suffers directly or indirectly related to the satellite galaxies' infall but also gas accelerations and inner dark matter structure.

CHAPTER 5

# The phase spiral in *Gaia* DR3

This chapter is mainly based on the article *The phase spiral in Gaia DR3*, by Antoja, T., Ramos, P., García-Conde, B., Bernet, M., Laporte, C.F.P., and Katz, D., published in 2023 in the journal Astronomy & Astrophysics, of which I am third author. Thus, figures and text have been taken literally from said work.

## 5.1 Introduction

As discussed in Chapter 1, the spiral pattern that appeared in the vertical projection of the phase space (Antoja et al., 2018) in the *Gaia* DR2 data (Gaia Collaboration et al., 2016; Gaia Collaboration et al., 2018b) showed a process of phase mixing after a certain perturbation from which the MW is still recovering. This provided further information about the vertical asymmetries discovered by Widrow et al. (2012) and Williams et al. (2013).

We learned that, when moving from the outer to the inner parts of the Galaxy, the phase spiral shrinks in the $Z$ direction (Laporte et al., 2019; Wang, Athanassoula, and Mao, 2020), that it is more prominent for cold orbits (Bland-Hawthorn et al., 2019; Li and Shen, 2020), that it shows mild changes with azimuth (e.g. slightly different density of stars along the phase spiral, Bland-Hawthorn et al. 2019), and that it is present in different age ranges (Tian et al., 2018; Laporte et al., 2019; Bland-Hawthorn et al., 2019), even in samples younger than 0.5 Gyr. The fanning of the phase spiral when coloured by the azimuthal velocity can be explained by the different vertical frequencies at different angular momentum (A18).

Regarding the origins of the phase spiral phenomenon, most studies suggests that it is primarily influenced by the encounters with the Sagittarius dwarf galaxy ((A18, Binney and Schönrich 2018; Laporte et al. 2018; Bland-Hawthorn and Tepper-García 2021; Banik, Weinberg, and van den Bosch 2022)). However, the causes involved are complex and involve various intricate aspects, such as the impact of self-gravity, which has been explored in the work of Darling and Widrow (2019), or the mass of the Sagittarius dwarf galaxy required to trigger the phase spirals (García-Conde et al., 2022; Bennett, Bovy, and Hunt, 2022).

Other explanations suggests that the phase spiral might have been initiated by bending waves resulting from the buckling of the galactic bar (Khoperskov et al., 2019), or the presence of multiple (dark) sub-halos has been proposed as a potential contributor to the phenomenon (Chequers, Widrow, and Darling, 2018; Tremaine, Frankel, and Bovy, 2023). Furthermore, the wake generated by satellite passages through the halo could also have played an important role in the emergence of the phase spiral (Grand et al., 2023).

Analysing the shape of the phase spiral is a way to constrain both the perturber and the potential of the Galaxy through the vertical orbital frequencies of the stars. In A18 it was assumed a set of frequencies of the MW and derived a perturbation time of 300-900 Myr. Ideally, both the potential and the perturbation times can be fitted at the same time as in Widmark et al. (2021), although these two quantities appear degenerated in the fit.

The presence of the phase spiral has also raised questions about the assumption of a Galaxy in equilibrium, potentially introducing biases in determinations such as the estimation of dark matter quantities using the Jeans equations (Haines et al., 2019; Chrobáková et al., 2020). In addition, the vertical perturbations that led to the phase spiral might have other important consequences for the Galaxy. It might have come accompanied by perturbations in the other phase space components and changes in the morphology of the MW, like spiral arms (Laporte et al., 2018; Bland-Hawthorn and Tepper-García, 2021; Antoja et al., 2022), as previously proposed by Younger et al. (2008) and Purcell et al. (2011). The event might also be related to different episodes of strong star formation in the disk discovered with *Gaia* data as well (Mor et al., 2019; Ruiz-Lara et al., 2020).

The Gaia Data Realease 3 (Gaia Collaboration et al., 2022c) offers now a new opportunity to explore the phase spiral across the disk and its stellar composition by applying a better selection of populations. For example, Gaia Collaboration et al. (2022a) showed that the phase spiral also appears when painted by metallicity due to the correlation between metallicity and angular momentum. Recently, Hunt et al. (2022) discovered double spirals in the inner parts of the Galaxy and they demonstrated that they could be due to breathing modes excited by internal structures such as the bar (but not necessarily a buckling bar) and also by an external perturber, similar to the double spirals from their simulations (Hunt et al., 2021).

In this Chapter, we explore the phase spiral with *Gaia* DR3 data and try to do a new determination of the perturbation time. In Sec. 5.2 we describe the data selection and corrections. In Sec. 5.3.1 we explore the local phase spiral now with many more stars and better resolution; we describe our method to detect the phase spiral and obtain its exact position in the $Z$-$V_Z$ plane 5.3.2; and we further explore its spatial variations as a function of radius and angular momentum (Sec. 5.3.3 and Sec. 5.3.4) as well as azimuth (Sec. 5.3.5). In Sec. 5.4 we provide a fit to the time of perturbation similar to A18 but now considering the phase spiral at different angular momenta, which show interesting inconsistencies. In Sec. we discuss our findings and conclude.

## 5.2 Data

We used data from *Gaia* DR3 (Gaia Collaboration et al., 2022c). We selected stars with available radial velocity and applied the following quality selections:

1. astrometric quality selection:
$$\texttt{RUWE} < 1.4, \tag{5.1}$$
2. selection in parallax quality:
$$\texttt{parallax_over_error} > 5, \tag{5.2}$$
3. selection of non-spurious solutions (Rybizki et al., 2022):
$$\texttt{fidelity_v2} > 0.5. \tag{5.3}$$

We used by default distances from StarHorse (hereafter SH, Anders et al., 2022). We also used the photogeometric distances from Bailer-Jones et al. (2021, BJ hereafter) for comparison. In addition, we applied the following correction to the line-of-sight velocity for stars with `grvs_mag` $\geq 11$ and `rv_template_teff` $< 8500$ (Katz et al., 2022):

$$\begin{aligned} \texttt{radial_velocity} = \texttt{radial_velocity} \\ -0.02755 * \texttt{grvs_mag}^2 \\ +0.55863 * \texttt{grvs_mag} - 2.81129 \end{aligned} \tag{5.4}$$

As discussed in Blomme et al. (2022), a correction is also necessary for the stars with $8500 \leq$ `rv_template_teff` $\leq 14\,500$ K & $6 \leq$ `grvs_mag` $\leq 12$ but after the correction there is still a residual bias of a few km s$^{-1}$. Since these stars are not very numerous, in our samples we keep only stars with `rv_template_teff` $< 8500$ K.

After all the above selections, the final sample with SH distances has 25 397 569 stars, while the one with distances contains 26 407 121 stars. More detials of the queries and discussion of selection bias can be found in Appendices A, B, C and D of (hereafter A23, Antoja et al., 2023).

We transform the *Gaia* observables into usual cylindrical phase space coordinates. For this we use $R_0 = 8.277$ kpc (Gravity Collaboration et al., 2022), $Z_\odot = 0.0208$ kpc (Bennett and Bovy, 2019), and $U_\odot = 9.3$, $V_\odot + V_c(R_0) = 251.5$ and $W_\odot = 8.59$ km s$^{-1}$, from the combination of the proper motion of SagA* from Reid and Brunthaler (2020) and its radial velocity from Gravity Collaboration et al. (2022), where $U,V,W$ are the usual heliocentric Cartesian velocities and $v_c(R_0)$ as the circular velocity curve at the Sun's position. Our reference system is a right-handed one with $\phi < 0$ in the sense of rotation, and thus also $V_\phi < 0$ for most of the stars. We set the origin at the Sun's azimuth ($\phi_\odot = 0$).

## 5.3 The phase spiral in DR3

### 5.3.1 The local phase spiral

In Fig. 5.1 we show the local phase spiral in the $Z$-$V_Z$ plane of the Solar Neighbourhood. We select stars with $R_0 - 0.1$ kpc $< R < R_0 + 0.1$ kpc and $-20 < \phi < 20$ deg. This large range in $\phi$ is justified by the phase spiral not changing much with $\phi$ compared to $R$, as seen in the next sections. In A18 with DR2 data, only the radial cut was performed, making a sample of 935 590 stars. Now we have a local sample with 2 328 004 stars. We note that we have increased the range in $Z$ and $V_Z$ of the panels in Fig. 5.1 compared to (hereafter A18, Antoja et al., 2018). We used bins with size $\Delta Z = 0.02$ kpc and $\Delta V_Z = 1$ km s$^{-1}$. The three panels of Fig. 5.1 (counts and coloured by median $V_R$ and by median $V_\phi$, respectively) show now a sharper signal. For instance, the middle panel presents defined spiral segments of different $V_R$, including two blue segments in the upper left part. In the right panel the phase spiral has a secondary branch at 50 km s$^{-1}$. This could be partially observed in DR2 (A18, Laporte et al. 2019), but now it emerges clearly separately from the other (main) spiral. This branching reaches now $Z = -1.2$ kpc, thus about 3 to 5 scale heights of the thin disk (taken to be 220–450 pc, Bland-Hawthorn and Gerhard, 2016, and references therein).

### 5.3.2 Detection of the phase spiral

In this section, we describe the method that we used to detect and study the shape of the spiral. It is based on an edge-detector algorithm applied to the counts in the $Z$-$V_Z$ space. We used the implementation in

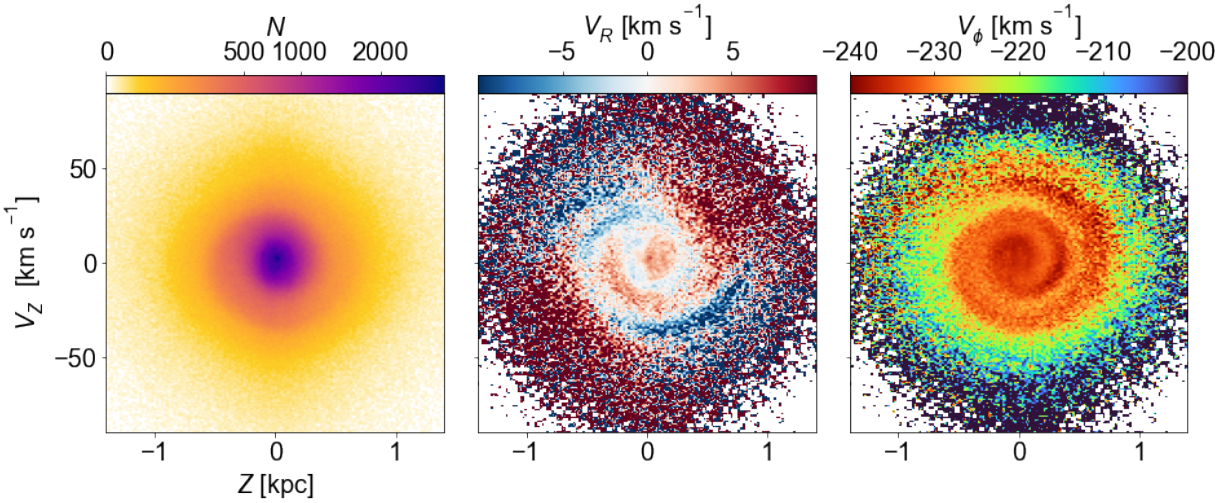


FIGURE 5.1: Phase spiral in the solar neighbourhood with *Gaia* DR3 data. **Left**: Two-dimensional histogram of the vertical projection of phase space ($Z$–$V_Z$) from the sample of stars with Galactocentric radii of $R_\odot \pm 0.1$ kpc and $\phi = 0 \pm 20$ deg. We used bins of $\Delta Z = 0.02$ kpc and $\Delta V_Z = 1\,\mathrm{km\,s^{-1}}$. **Middle**: Same projection but colour-coded by median radial velocity $V_R$. **Right**: Same projection but color-coded by median azimuthal velocity $V_\phi$, adjusting the colour bar limits so as to maximize the appearance of the spiral.

*python* feature.canny (Canny, 1986) from skimage (van der Walt et al., 2014). We start by calculating the 2D histogram. In most cases starting with a histogram on the logarithm of the number counts worked better (this is our standard option unless stated otherwise). Next, the method reduces the noise using a Gaussian filter kernel with a certain $\sigma$ (in pixel units). We used a $\sigma$ found empirically to provide good detections. For instance, for the solar neighborhood and binning defined in the previous section we used $\sigma = 3$. For volumes at smaller angular momentum $|L_Z|$ explored in later sections, a larger $\sigma$ worked better. In particular, we used $\sigma$=4.5 for $|L_Z| < 1600\,\mathrm{km\,s^{-1}kpc}$ and $\sigma$=3.5 for $|L_Z| \geq 1600\,\mathrm{km\,s^{-1}kpc}$. The differences when using different $\sigma$ are very small for most of the cases, and, by construction, they will be within the error bars of the detections. Next, the algorithm of the edge detector calculates the gradients for each pixel (bin) through the horizontal and vertical Sobel operators, takes the pixels with the maximum gradients, which are always perpendicular to the edges and further selects the edge bins by hysteresis thresholding. This consists of taking all pixels with gradients above the high threshold (set to 20%) and also, recursively, all the pixels above the low threshold (set to 10%) that are connected to an already taken pixel. All the pixels with gradients below the low threshold are discarded. In practice, the algorithm returns a numerical matrix with 1's at the detected edges and 0 otherwise. We note that this detector sometimes has problems in detecting the inner parts of the spiral. However, this is counterbalanced by the simplicity and speed of the algorithm and the good overall detection.

In Fig. 5.2 we show the performance of the edge detector for the local phase spiral. In the top left panel, we superpose the detected edge to the vertical phase space density. The edge detector accurately traces the main spiral and also finds signs of the upper branch in the local phase spiral. There is also a residual detection of an edge at $V_Z \sim -70\,\mathrm{km\,s^{-1}}$ but with not so clear counterpart in the $V_\phi$-coloured projection. We note that the edge detector obtained from the counts' projection approximately follows the spiral in the projection colored by $V_\phi$ (bottom left panel).

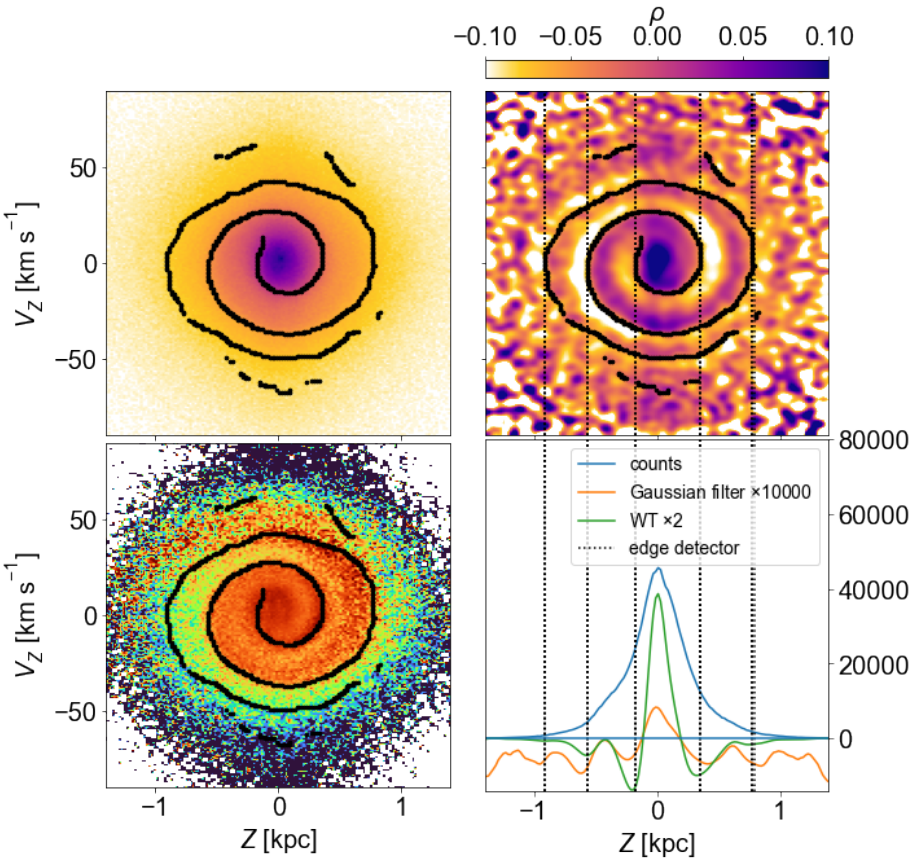


FIGURE 5.2: Phase spiral detected by the edge detection. **Top left**: Output of the algorithm applied to the same selection of stars as in Fig. 5.1, superposed to the counts from which it has been computed. We used $\sigma = 3$. **Bottom left**: Same but superposed to the projection coloured by $V_\phi$. **Top right**: Comparison with the Gaussian filter (colour, see text). **Bottom right**: Comparison with the Gaussian filter and the WT, with the respective values scaled to fit in the same plot, as indicated in the legend, in a one-dimensional case (see text).

We have compared the results from the edge detector with previously used methods, namely the Gaussian filter and the Wavelet Transform (WT) (Antoja et al., 2015, and references therein). The former is similar to Laporte et al. (2019) but here we do $\rho = H_2/H_4 - 1$, where $H_2$ and $H_4$ are the original histogram of counts smoothed by a Gaussian filter (implementation `gaussian_filter` from `scipy`, Virtanen et al. 2020) with a $\sigma_G = 2$ and $\sigma_G = 4$ (in units of the pixel size, $\Delta Z$ and $\Delta V_Z$), respectively. For the WT we use the implementation `signal.cwt` from `scipy` with a width of the mother wavelet (Mexican hat) of 3 pixels. The top right panel compares the edge detector with the usual Gaussian filter while the bottom right panel compares the three methods for a one-dimensional projection with stars of $|V_Z| < 3\,\mathrm{km\,s^{-1}}$. The determinations from the three methods are very similar but the edge detector, by construction, manages better to detect the caustic edge that we are after.

### 5.3.3 The phase spiral with radius and angular momentum

In this section, we explore the spatial evolution of the phase spiral. In Fig. 5.3, we show the phase spiral colored by median $V_\phi$ for different, from inner (left) to outer (right) Galactocentric radii, taking only stars with $|\phi| < 20\,\mathrm{deg}$. The phase spiral becomes flatter with radius as previously noticed before (e.g. Laporte et al., 2019; Bland-Hawthorn et al., 2019). In DR3, the phase spiral becomes observable within a range of 6 to 11 kpc, surpassing the previous radial boundaries. Additionally, there are indications of asymmetries extending to 5 and 13 kpc, potentially limited by selection effects in those regions.

In comparison to DR2, we see a clear additional branching at $V_Z \sim 50\,\mathrm{km\,s^{-1}}$ in the volume at $R = 8\,\mathrm{kpc}$, which was already seen in Fig. 5.1. This branch seems to extend slightly towards negative $V_Z$ as well. From the animations [1], which employ a more continuous sweeping in $R$, we observe that this arch/branch shifts to lower $V_Z$ with $R$ and becomes mixed with the upper part of the main phase spiral and turns to a pronounced red ($V_\phi$ lower than the local median) We also find what seems to be another turn of the phase spiral or faint arch at $V_Z \sim -50\,\mathrm{km\,s^{-1}}$ at the region of 7 kpc. Interestingly, we also see a pattern with a "hole" close to the $(Z, V_Z) = (0,0)$ at 10 kpc (already noticed in *Gaia* DR2, e.g. Laporte et al. 2019).

Stars that currently reside within the Solar Neighborhood did not always travel together within the same enclosed volume. Separating by $L_Z$ instead of radius enhances the spiral signal by grouping stars with similar vertical frequencies, i.e., similar histories. This approach has been effectively demonstrated in studies by Li (2021), Gandhi et al. (2022) and Hunt et al. (2021). However, separating by angular momentum introduces biases, including the dominance of eccentric orbits at extreme angular momentum (Hunt et al., 2022).

In the top row of Fig. 5.4 we show the phase spiral in counts for different bins of angular momentum, where we only take stars with $|\phi| < 20\,\mathrm{deg}$. In these panels an approximate measure of the guiding radius is given by simply doing $R_g = L_Z/V_c(R_0)$, assuming a flat circular velocity curve. The black lines show the results of the edge detector. For the last three panels (large angular momentum $L_Z$) we applied the algorithm to the histogram of the counts (instead of the logarithm of the counts as in the other). This detects a better-defined spiral for these cases but tends to detect a spiral biased toward inner parts. Thus we only use it for this figure but not when a quantitative comparison between panels needs to be done. In colors we plot the Gaussian filter as in the top right panel of Fig. 5.2. These panels show well-defined phase spirals from $R_g \sim$6 to 11 kpc, and some hints of them beyond these radii. In the left panels, we see a vertical band empty of stars that is explained by the lack of stars at low $|Z|$ towards the inner Galaxy due to extinction. The flattening of the spiral and their lower number of turns as one moves towards large $|L_Z|$ is evident. We note that the double spiral at small angular momentum discovered by Hunt et al. (2022)

[1] The animations are available at `https://zenodo.org/record/7970710`

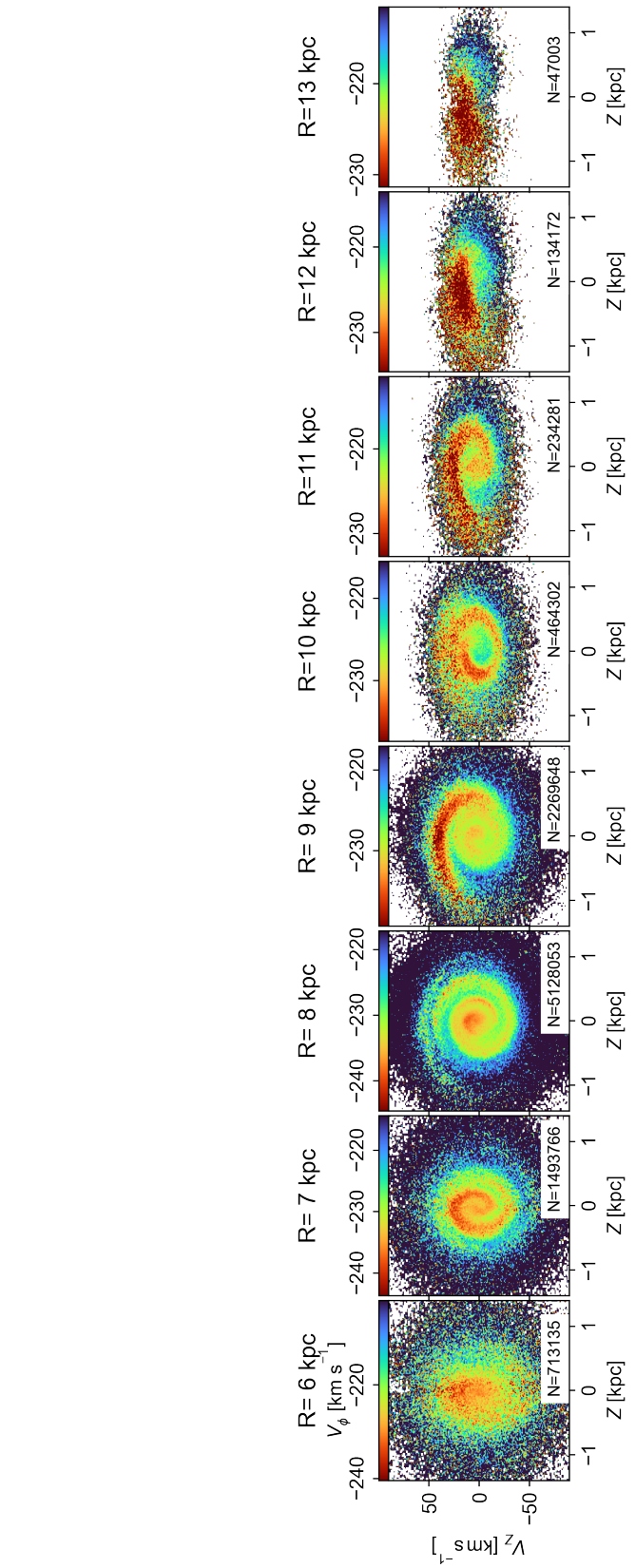


FIGURE 5.3: Phase spiral at different Galactocentric radii with *Gaia* DR3 data. The panels show the vertical projection of phase space ($Z$–$V_Z$) colored by median $V_\phi$. We only use stars with $|\phi| < 20$ deg. Each region has a total radial width of 1 kpc and their centers are separated by the same amount. We used bins of $\Delta Z = 0.02$ kpc and $\Delta V_Z = 1\,\mathrm{km\,s^{-1}}$. The color-map ranges correspond to the percentiles 30 and 70 of the distribution of $V_\phi$ in each volume to maximize the appearance of the spiral. In the bottom part of the panels we indicate the number of stars.

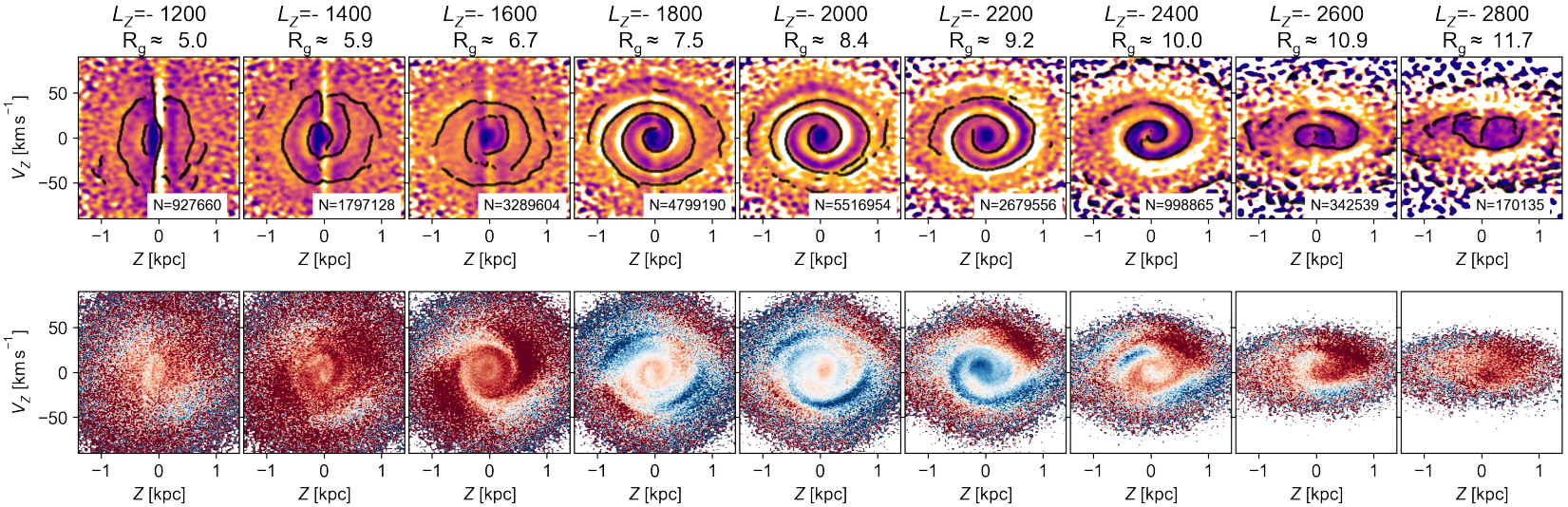


FIGURE 5.4: Phase spiral for different angular momentum with *Gaia* DR3 data. We only use stars with $|\phi| < 20$deg. The selections have a total angular momentum width of 200 km s$^{-1}$kpc and their centres are separated by the same amount. We used bins of $\Delta Z = 0.02$ kpc and $\Delta V_Z = 1$km s$^{-1}$. **Top:** Counts projection after Gaussian masking (see text for details). The color bar is the same as in the top left panel of Fig. 5.2. We superpose our detected phase spiral via the edge detector method where we used $\sigma$=4.5 for $|L_Z| < 1600$km s$^{-1}$kpc and $\sigma$=3.5 for $|L_Z| \geq 1600$km s$^{-1}$kpc. We indicate the number of stars in the bottom part of the panels. **Bottom**: Projection colored by $V_R$ with the same color scale as in the central panel of Fig. 5.1.

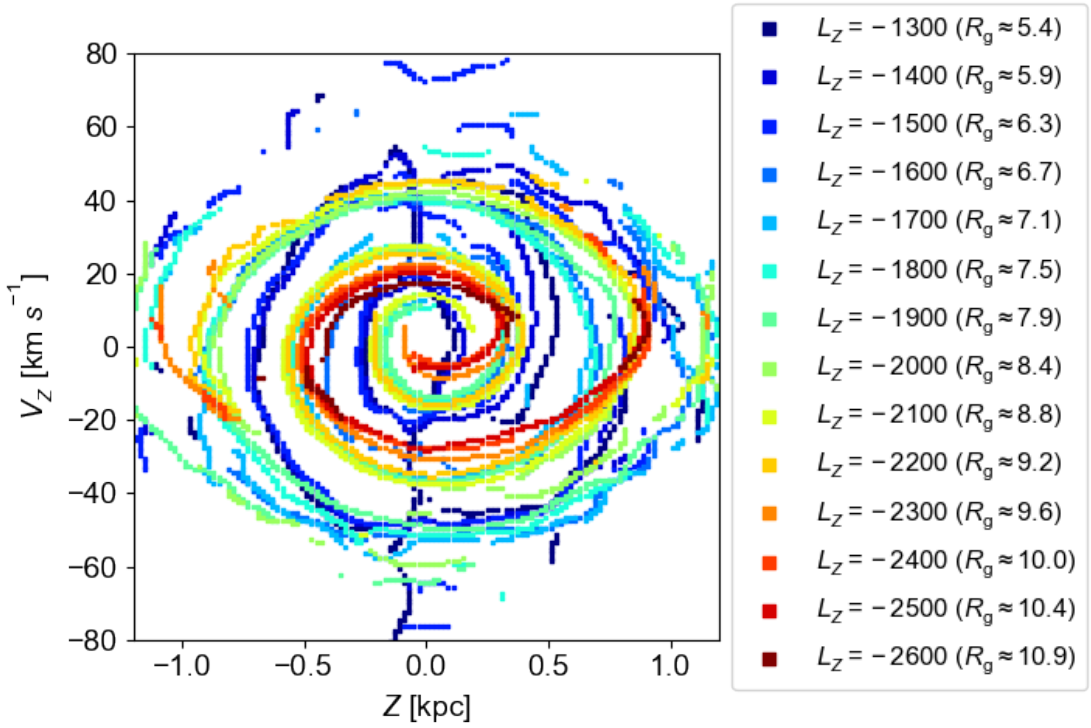


FIGURE 5.5: Superposed phase spiral for different angular momentum with *Gaia* DR3 data. We select only stars with $\phi \in [-20, 20]$ deg. We use bins of $\Delta L_Z = 200\,\mathrm{km\,s^{-1}kpc}$ and centres of bins separated by $100\,\mathrm{km\,s^{-1}kpc}$, from $L_Z = 1300\,\mathrm{km\,s^{-1}kpc}$ (bluer lines) to $L_Z = 2500\,\mathrm{km\,s^{-1}kpc}$ (redder lines) as indicted in the legend. In parenthesis, we give an indicative measure of guiding radius assuming a flat circular velocity curve.

is not seen here. This could be due to a main phase spiral dominating and masking the double branches here. Alternatively, it could be that, since Hunt et al. (2022) shows the phase spirals for a selection of nearby stars (1 kpc) split by angular momentum, the double spiral is only present for local stars with a small $|L_Z|$, that is when they are observed towards their epicenters. The upper separated branching seen at $R \sim 8\,\mathrm{kpc}$ can be seen in the Gaussian filter from $R_g \sim 7.5$ to 10 kpc ($|L_Z|$ from 1800 to 2400 $\mathrm{km\,s^{-1}kpc}$). In some cases, for example at $|L_Z| = 2200\,\mathrm{km\,s^{-1}kpc}$, further turns at larger $|Z|$ and $|V_Z|$ can be seen in the background colours.

In the bottom row of Fig. 5.4 we colour-coded the vertical phase space by median $V_R$. A trend of the global $V_R$ with $L_Z$ is noticeable with redder colours (positive $V_R$) for small $|L_Z|$, bluer (negative $V_R$) for intermediate $|L_Z|$, and again redder for large $|L_Z|$. This is related to the $V_R$-$L_Z$ waved detected in Friske and Schönrich (2019) (see also Antoja et al. 2022, and the middle panel of the fourth row of fig D.1 in Appendix D of A23). We also see a quadrupole at the outer parts of these diagrams that are explained by the tilt of the velocity ellipsoid (Bland-Hawthorn et al., 2019). Aside from these, the phase spiral segments appear clear and sharp. We notice that the correspondence between the density phase spiral and colored by $V_R$ is not univocal. For example, the blue $V_R$ branch of the phase spiral at $L_Z = -2200\,\mathrm{km\,s^{-1}kpc}$ extends to $Z = 1.4\,\mathrm{kpc}$ while the spiral segment in density continues to curl upwards. In some cases, we see that $V_R$ changes sign along the spiral segments ($L_Z = -2000\,\mathrm{km\,s^{-1}kpc}$).

In Fig. 5.5 we superpose all the phase spirals detected by the edge detector (Sect. 5.3.2) for different

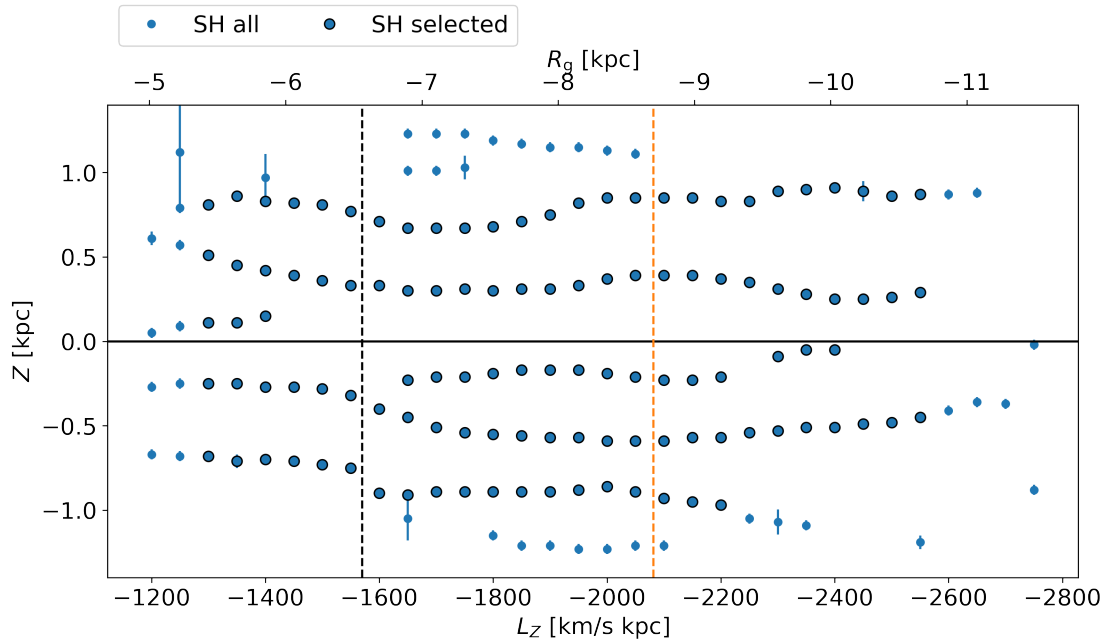


FIGURE 5.6: Crossing positions of the phase spiral ($Z_c$). The blue circles and error bars mark the $Z$ coordinate for $V_Z = 0$ of the phase spiral determined from the edge detector for the SH sample. We mark the positions used for inferring the impact time with empty black circles. The dashed orange vertical line marks the angular momentum of the Sun.

$L_Z$ values (with the corresponding guiding radii $R_g$ by assuming a flat circular velocity curve), selecting only stars at the azimuth of the Sun with $|\phi| < 20\,\mathrm{deg}$. We observe an approximately continuous evolution of the phase spiral with angular momentum. The pitch angle increases with higher $L_Z$, as expected. The dark blue curves show some vertical lines related to the selection effects explained above. We note that for the same incremental value in $L_Z$, we do not see the same amount of morphological change, that is for some angular momentum the phase spiral changes more abruptly than for others (from dark to light blue, for instance).

### 5.3.4 Crossing points of the phase spirals with $L_Z$

In this section, we calculate the crossing points ($Z_c$) of the phase spiral with the $V_Z = 0$ line for the analysis of the impact time. These crossings were calculated using our edge detection algorithm applied to the $Z$-$V_Z$ counts for different selections of angular momentum. The samples are centered every 50 $\mathrm{km\,s^{-1}kpc}$ (thus, with more continuity) with a total width of $\Delta L_Z = 100\,\mathrm{km\,s^{-1}kpc}$ (thus, with some overlap and smaller than before to minimize variations of $L_Z$ within a bin). We select stars with $|\phi| < 20\,\mathrm{deg}$. Figure 5.6 shows the crossing points as a function of $L_Z$. The blue points represent all the $Z_c$ from the edge detector, which shows many continuous sequences corresponding to crossings that are well detected across several $L_Z$ but also noisy/spurious detections at the extreme $L_Z$, where data is less numerous and distance errors are larger.

Formally, the corresponding error would be of the order of the bin size of the histogram in the $Z$ coordinate, which is 0.02 kpc, to each $Z_c$ to which the edge detector is applied. However, we observe that when using a slightly different $\sigma$ in the edge detector (ranging from 2 to 5), differences of approximately 0.03 kpc may arise in some instances. As a result, we consider this as our reference error. We also repeated

the measurement of the $Z_c$ with the BJ distances, computed the difference $\delta Z = |Z_{c(SH)} - Z_{c(BJ)}|$ between the crossings from SH and BJ (considering the closest points) and to each $Z_c$ from SH we arbitrarily assign an error of MAX$(0.03\,\mathrm{kpc}, \delta Z)$. Also, for the final analysis, we only considered $Z_c$ with errors smaller than 0.1 kpc (i.e. not considering points in SH that differ from BJ more than 0.1 kpc). More details about the comparison between detections with SH and BJ can be found in the Appendix B of A23. As anticipated, the differences are typically small, consistent with the narrow variations in distances within the probed ranges. Our selection process involved exclusively points with $|Z| < 1$kpc, given that detections beyond this height exhibit noise. Furthermore, there are instances where we are not certain whether they genuinely correspond to a phase spiral crossing or to an edge of the overall distribution. Our criteria also considers only points with $L_Z \in [-2600, -1300], \mathrm{km\,s^{-1}kpc}$, since the phase spiral is not clear beyond these limits.

In Fig. 5.6 the points that we consider valid after all the filters from above are circled in black. At angular momentum where there are more stars (mostly left to the Sun's one marked with a vertical dashed orange line), more turns are detected (3 for $Z < 0$ compared to 2 at larger and smaller angular momentum), which is likely a combination of the selection effects and true differences in the phase spiral (smaller pitch angle for larger $|L_Z|$). We also see some abrupt jumps such as at $L_Z \sim -1600\,\mathrm{km\,s^{-1}kpc}$ in the lowest turn ($Z_c \approx -0.8\,\mathrm{kpc}$). The influence of the selection function on the determinations of $Z_c$ is analyzed in Appendix D of A23.Besides these jumps, the sequences of $Z_c$ show undulations. Such features are inconsistent with a straightforward interpretation of the phase spiral, where we would expect a smooth rise in $|Z_c|$ as we move towards the outer regions of the Galaxy (higher $|L_Z|$ values). This deviation occurs because typical models of the Galactic potential indicate a smaller gradient of vertical frequencies with vertical amplitude in the outer Galactic regions (as shown in Extended Data Figure 4 of A18). Consequently, this leads to a less tightly wound phase spiral. The will carry significant implications for the phase mixing inferred times in Section 5.4.

### 5.3.5 The phase spiral with azimuth

We present the azimuthal variations of the phase spiral at fixed angular momentum in Fig. 5.7. We select $L_Z \in [-2100, -1800]\,\mathrm{km\,s^{-1}kpc}$ since this is the range around the value of $L_Z$ with the peak of density in our sample. We observe less variations with $\phi$ in comparison to those in $L_Z$, but there is a clear gradual change. In some sections of the phase spiral, there is a higher variation with azimuth (turn at $Z \sim 0.4$ for instance) than in other turns (at $-0.5\,\mathrm{kpc}$, for instance). For the crossings $Z_c$ at $V_Z = 0$ we have a slope with $\phi$ of -0.006, -0.004 and 0.002 kpc/deg for the crossings at 0.8, 0.3, and -0.6, respectively. The turns at $Z \sim -0.2$ and $Z \sim -0.9$ remain nearly constant with azimuth. A simple phase difference with $\phi$ would produce the same level of fanning for each turn. Therefore, our observations require having different level of winding-up at different azimuths (different phase spiral pitch angle) and/or having strong population differences with positive/negative $Z$. Finally, we observe that the lowest turn of the spiral at $V_Z \sim -50\,\mathrm{km\,s^{-1}}$ is only seen in the azimuths close to the Sun likely attributed to a larger star population within these spatial regions.

## 5.4 Inferring the impact time

### 5.4.1 Method

When a phase mixing process occurs, the phase spiral winds up over time. We can link the time of the perturbation which originated it by 're-winding' the spiral to calculate the onset time of the phase mixing process. In A18 they used the consecutive turning points of the local phase spiral to infer the impact time

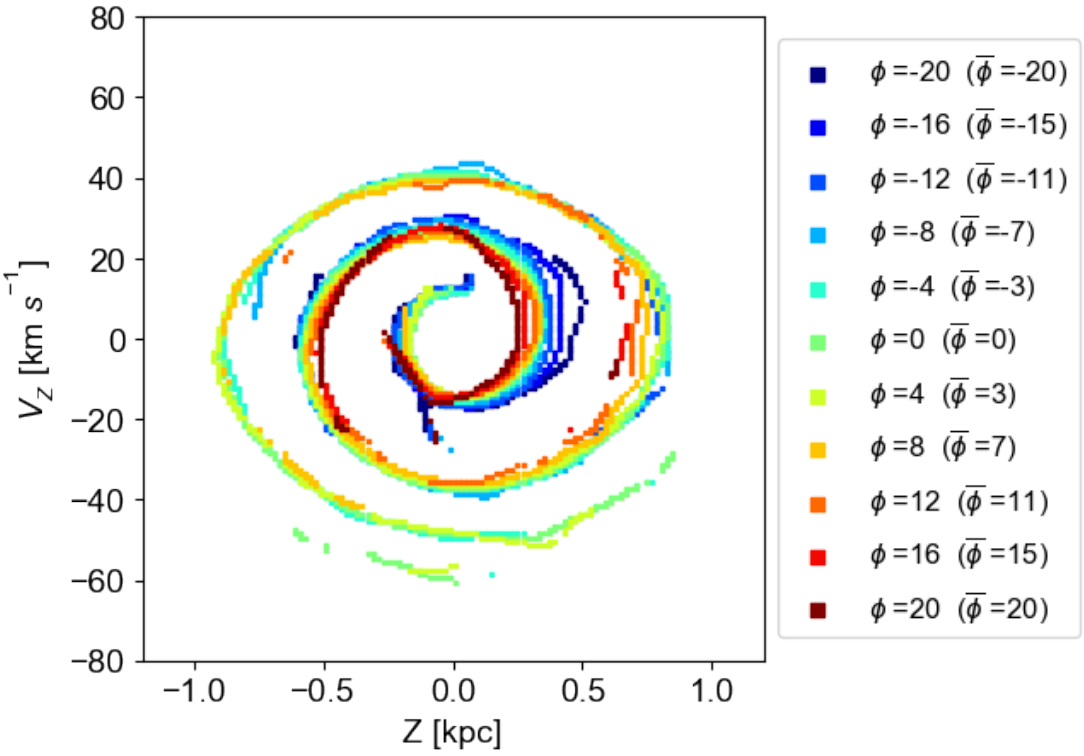


FIGURE 5.7: Superposed phase spiral for different azimuths with *Gaia* DR3 data. We select only stars with $L_Z \in [-2100, -1800]$. We use bins of $\Delta\phi = 4$ deg and centers of bins separated by the same amount, from $\phi = -20$ deg (bluer lines) to $\phi = 20$ deg (redder lines) as indicated in the legend. In parenthesis, we give the average azimuth of the selection, which can differ by 1 deg compared to the center of the selection in some cases. For the edge detector, we used $\sigma = 3.5$.

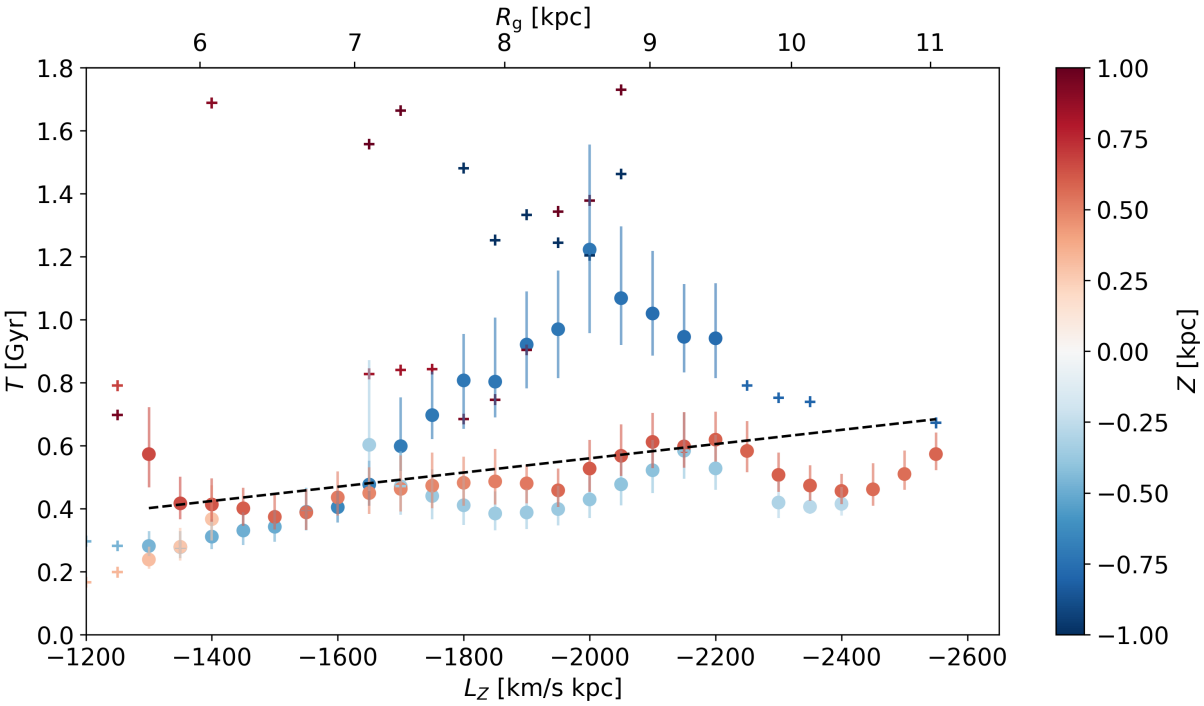


FIGURE 5.8: Start time of the phase mixing as a function of angular momentum. The symbols indicate the time inferred from Eq. 5.5 for the different consecutive crossing points of the phase spiral and are coloured by height above the plane. The circles with error bars are the points that we consider valid while crosses are the rest of cases. An indicative guiding radius corresponding to the circular velocity curve of the McM17 potential is given in the upper horizontal axis. The dashed line marks a linear fit to the data points.

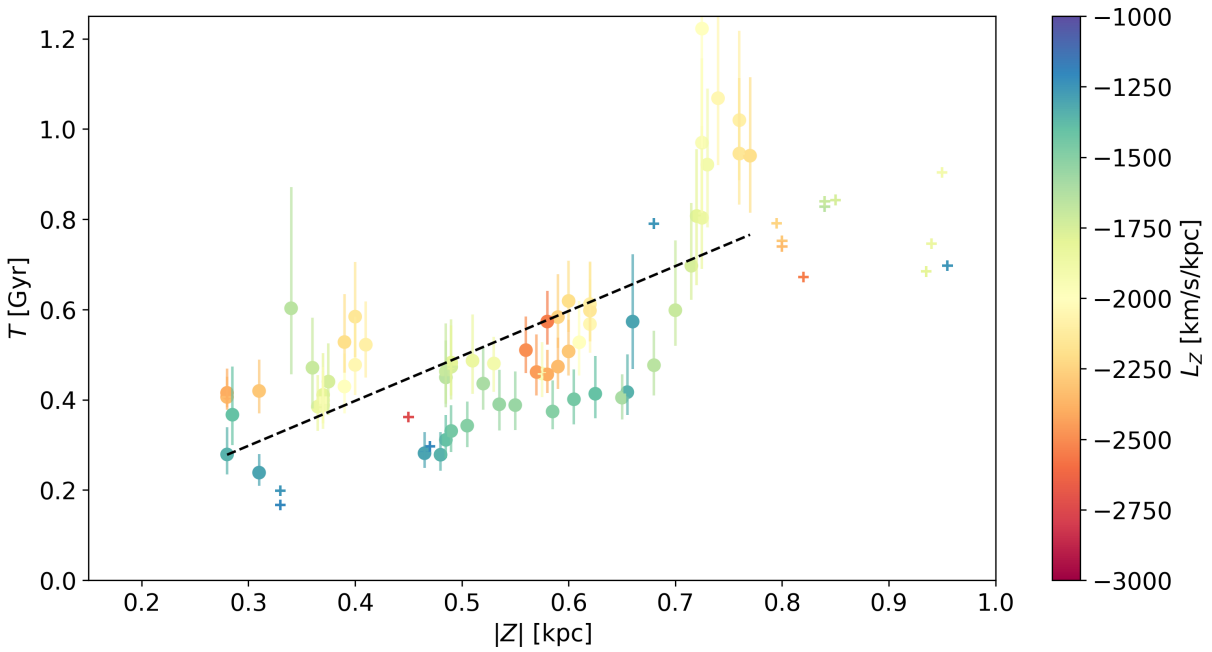


FIGURE 5.9: Time of start of phase mixing as a function of height above the plane. The symbols give the time inferred from Eq. 5.5 for the different consecutive crossing points of the phase spiral and are coloured by angular momentum. The circles with error bars are the points that we consider valid while crosses are the rest of cases. The dashed line marks a linear fit to the data points.

by assuming a MW potential model from which the vertical frequencies were derived empirically. Here we repeat this process, but using data of the phase spiral at different angular momenta, helped by the increase of data at different positions across the Galaxy with the new *Gaia* DR3. Ideally, one could fit simultaneously the potential and time of the perturbation in the line of Widmark, Laporte, and de Salas (2021). This is, however, a degenerated problem and is not so straightforward after the findings of this work. Therefore, it will be a subject of a future study.

For this analysis we use the crossings $Z_c$ of the phase spiral at $V_Z = 0$ from the previous section (Fig. 5.6). Stars that are in the crossing points, which have $V_Z = 0$, are currently in their maximum vertical height (above or below the plane): $Z = Z_{max}$. Thus, we can estimate the vertical frequencies of said points by interpolating into a grid of frequencies computed as a function of $L_Z$ (or $R_g$) and $Z_{max}$. Then each pair of consecutive crossings[2] $(Z_{c_1}, Z_{c_2})$ are separated by a phase $2\pi$ and, thus, we can infer the impact time by their difference of vertical frequencies:

$$T = \frac{2\pi}{\nu(L_Z, Z_{c_1}) - \nu(L_Z, Z_{c_2})}. \tag{5.5}$$

If we assume that a single perturbation caused the phase spiral across the disc, this simple analysis should result in the same perturbation time at all $L_Z$ and for each pair of crossings. We note that with DR3 we are able to use more pairs of crossings (two in the $Z < 0$ part of the spiral and one in the $Z > 0$

[2]Here we refer to consecutive crossings for pairs of $Z_c$ that have both positive or negative $Z$. However, we note that one could also use pairs of $Z_c$ with different signs and change $2\pi$ for $\pi$ in Eq. 5.5. This is examined in Appendix E of A23

part) at angular momentum closer to the Sun's one, while in A18 they could only use two pairs in total. Furthermore, in A18 they used the crossings detected in the vertical phase space coloured by $V_\phi$ and here we use the crossings from the edge detector on the counts.

To build the grid of frequencies we used `AGAMA` (Vasiliev, 2019) and simulated more than 8,000 orbits at $Z \geq 0$ and use the vertical symmetry of the potential for the $Z < 0$ part. We use the McMillan (2017) potential (McM2017) as our fiducial potential model. The orbits were integrated for about 50 revolutions. They all started with null $V_Z$, i.e., at the top of their vertical oscillation. The other components of the initial conditions were set as follow: $\phi = 0°$, $V_R = 0\,\mathrm{km\,s^{-1}}$ (equivalently radial action $J_R = 0$, but see below for orbits with non-null radial action). Then we run through $Z$ (from -4 kpc to 4 kpc every 50 pc) and $L_z$ (from $500\,\mathrm{km\,s^{-1}}$kpc to $3000\,\mathrm{km\,s^{-1}}$kpc every $25\,\mathrm{km\,s^{-1}}$kpc), solving numerically the implicit equation

$$L_z - \sqrt{-\frac{\partial\Phi(R,Z)}{\partial R}R^3} = 0. \tag{5.6}$$

to obtain the $R$, and thus $V_\phi = L_Z/R$, of the corresponding circular orbit. Subsequently, we sample each orbit with 20,000 points and measure the vertical frequency with a Fast Fourier Transformation (Cooley and Tukey, 1965) of the signal in $Z$ as a function of time by taking the frequency of the dominant peak (multiple peaks can appear for very eccentric orbits with large vertical amplitude oscillations). We have tested the sensitivity of the measured frequency to both the number of samples used and the number of revolutions, finding a negligible dependence on the former (as long as there are more than a few hundred points) and an asymptotic behaviour as a function of the latter. For 50 revolutions, the error on the measured frequency tends to be of the order of less than 1%. Below we explore other potential models and frequencies for different kinetic temperatures.

### 5.4.2 Time results

We have interpolated in the above mentioned grid of frequencies and used Eq. 5.5. Thus, we infer the time of start of the phase obtained from each pair of crossings $Z_c$. In Fig. 5.8, and show the results as a function of $L_Z$ (horizontal axis) and $Z$ (colour scale), where for the plot, we used the average $(Z_{c_1} + Z_{c_2})/2$ of the points of the pair. We have marked the time determinations from the $Z_c$ that we do not consider valid with small + signs (see text in Sect. 5.3.3, small blue circles in Fig. 5.6). These appear randomly scattered around the plot (many of these points are outside the vertical range). Instead, circles with error bars are the ones from the valid $Z_c$ after the considerations of Sect. 5.3.3. The error bars are not symmetric because of the dependency of the frequencies with $Z$. To compute the upper (lower) limit in each derived time we used the limits of the errors of $Z_c$ that minimize (maximize) the frequency difference. That is, for pairs of crossings with $Z > 0$, we considered the lower limit of the smaller $Z_c$ and the upper limit of the larger $Z_c$to obtain the lower limit of the time (maximum vertical frequency difference). Conversely, the upper limit of time is obtained by combining the upper limit of the smaller $Z_c$ and the lower limit of the larger $Z_c$.

The valid times in Fig. 5.8 (error bars) show different coherent sequences. The sequences from small $|Z_c|$ (both positive and negative, lighter colours) are distributed around 0.5 Gyr and in many cases are consistent within the errors at a fixed $L_Z$. However, these points show increasing estimated times with $|L_Z|$. In addition, the darker blue points corresponding to the second crossing at $Z < 0$ are at significantly larger times and show also a tendency to increase with angular momentum. Indeed, a linear fit with $L_Z$ to all the valid times (dashed line in Fig. 5.8) illustrates this global trend.

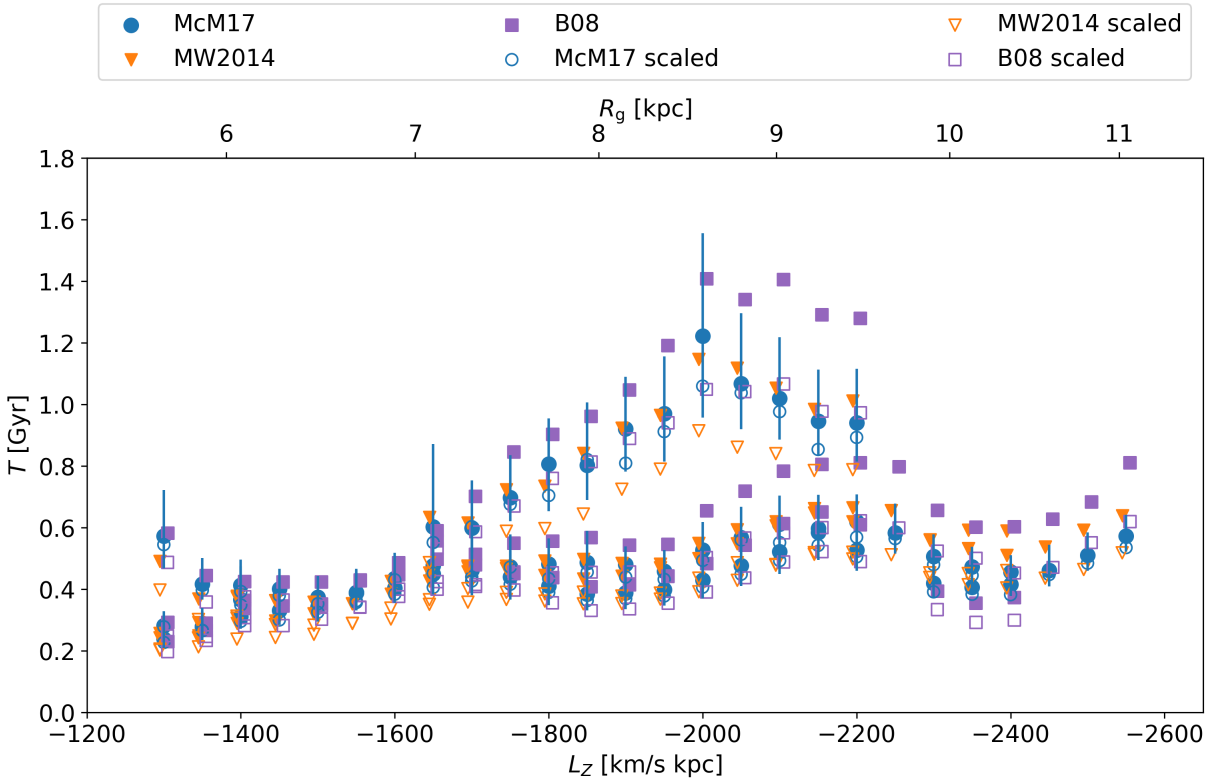


FIGURE 5.10: Time of start of phase mixing for different potentials. The figure is similar to Fig. 5.8 but we use frequencies of different potential models of the MW, as indicated in the legend.

However, we see several oscillations in the different sequences, some of them corresponding to the oscillations in the $Z_c$ (Fig. 5.6) already mentioned. This is examined further in Appendix D of A23, where it is concluded that while some oscillations could be related to changes in the dominating populations, the global trends with $L_Z$ and $Z$ might require a different explanation that we discuss in Sect. 5.5.

We note that there is certain ambiguity in linking the different $Z_c$ into coherent sequences in Fig. 5.6. For example, it is not clear whether the sequence at $Z \approx -0.25$ kpc starting at $L_Z = -1200\,\mathrm{km\,s^{-1}\,kpc^{-1}}$ continues towards higher or lower $Z$ when reaching $L_Z = -1600\,\mathrm{km\,s^{-1}\,kpc^{-1}}$. However, the time determinations do not depend on this link to neighbouring points since they are done independently at each $L_Z$ from consecutive crossings in $Z$. There might be a problem if some crossings are missing but it is unlikely that we have missing crossings in between detected ones: the undetected crossings would be likely located at lower |Z| (the phase spiral is highly undetermined in the central parts of the $Z$-$V_Z$ diagram) and/or at higher |Z| (due to fewer counts). These missing crossings would not bias the estimated times from the intermediate crossings (i.e. would not change from the ones appearing in Fig. 5.8).

Fig. 5.9 is equivalent to Fig. 5.8 but as a function of $|Z|$ (horizontal axis) and $L_Z$ (colour scale). A general trend of time increasing with $|Z|$ is observed. The linear fit gives $T = (1.0 \pm 0.1\mathrm{Gyr(kpc)^{-1}})|Z| - 0.0005 \pm 0.0800\,\mathrm{Gyr}$ (dashed line in Fig. 5.9), but this fit would depend on the angular momentum (colours in Fig. 5.9). Part of these time discrepancies for different $Z$ at fixed $L_Z$ could be explained by the fact that the vertical frequency is not perfectly defined for eccentric orbits that do large oscillations about the midplane. Since we estimate the frequency numerically and take the one of the dominant peak, we expect

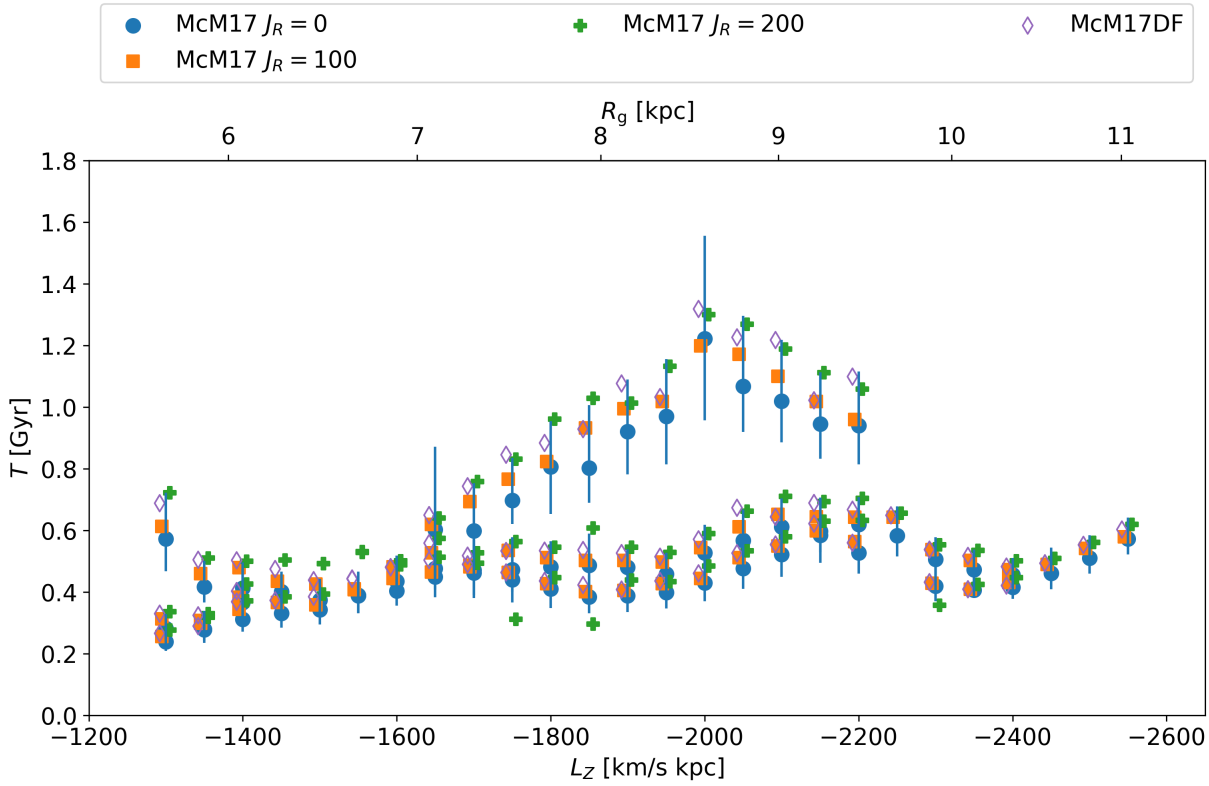


FIGURE 5.11: Time of start of phase mixing for different kinetic temperatures. The figure is similar to Fig. 5.8 but we use orbits with different radial actions and methods, as indicated in the legend.

that part of this problem is mitigated.

Ignoring for now the trend with $Z$ and $L_Z$ (which we discuss in Sect. 5.5), we obtain an average start of phase mixing time of 0.5 Gyr (0.4 Gyr for the error-weighted average, $w = 1/\sigma^2$). We find that 80% of the time determinations are within $[0.3, 0.9]$ Gyr. The variations with $L_Z$ and $Z$ are larger than the statistical error (error bars). In Table 5.1 (first row) we give also other statistics such as the minimum and maximum values.

### 5.4.3 Results for different models and data

We examined the dependency of the results on different potential models (Fig. 5.10), frequencies for different kinetic temperatures (Fig. 5.11), possible systematics in distance (Fig. 5.12), and taking the $V_Z$ crossings of the spiral with the $Z = 0$ axis (see text below, Fig. 5.13). In all these figures blue circles show our fiducial case presented above, which consist of using the McM17 potential (non-scaled), SH distances and $J_R = 0$. The time statistics are given in Table 5.1, where the last two columns indicate the differences between the times of these new cases and the times from the fiducial case ($T_0$). In most cases, the times are within the error bars of the fiducial case. We find the largest differences when we change the assumed potential model for the MW. In particular, we obtain systematically larger times for Model I (here B08) from Binney and Tremaine (2008) (on average 0.09 Gyr larger), and systematically smaller times for the MWpotential2014 (here MW2014) from Bovy (2015) when scaled to fit the values of $V_c$ and $R_0$ used in the

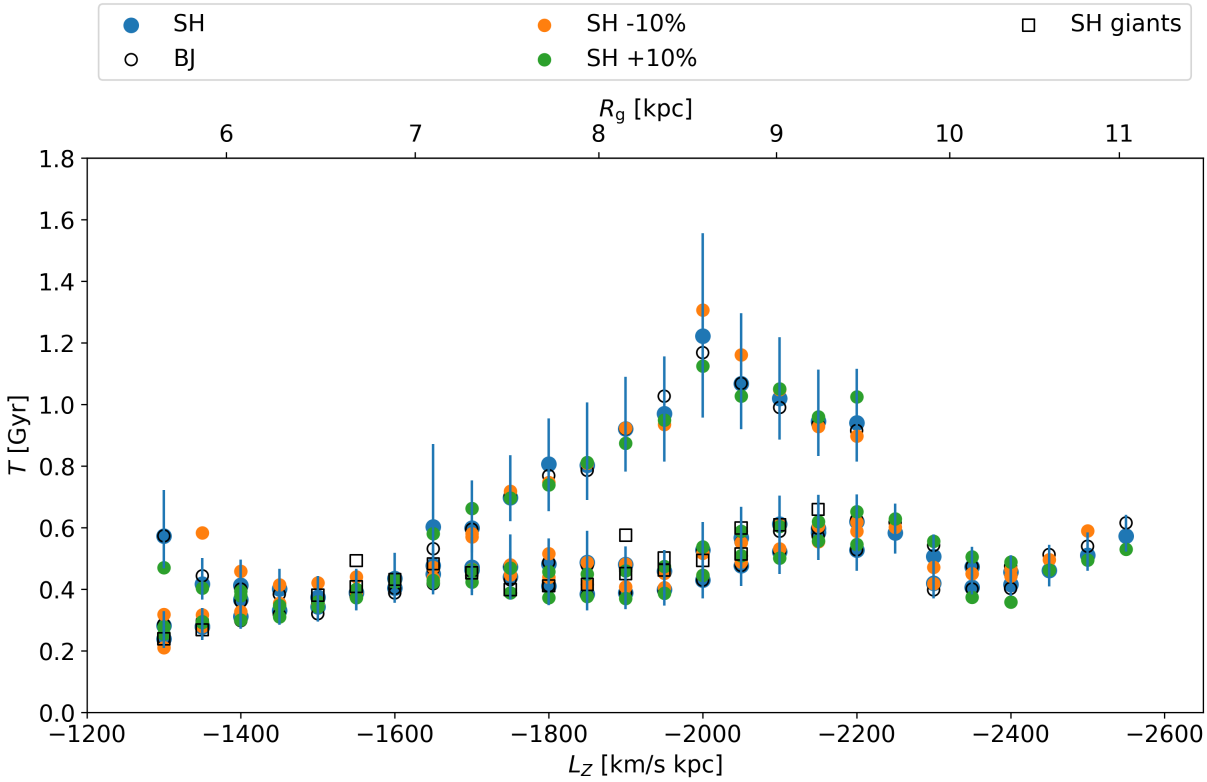


FIGURE 5.12: Time of start of phase mixing for different distances and data. The figure is similar to Fig. 5.8 but we use distances from BJ, from SH with distance biases of ±10% and for a selection of giant stars, as indicated in the legend.

TABLE 5.1: Phase mixing times from the phase spirals. We show weighted and unweighted average (columns 2 and 3) with their standard errors, minimum and maximum values (columns 4 and 5), and ranges enclosing 80% of times (column 6). The last two columns (7 and 8) compare the times with the fiducial case (first row), showing the average differences and the ranges of differences. The different rows are for different cases as explained in the text. For the times derived from the $V_{Zc}$ (last row) we do not compute the differences with the fiducial case since there is not a point by point correspondence.

| Model | mean($T$) | weighted mean($T$) | min($T$) | max $T$ | [P10, P90]$_T$ | mean($T - T_0$) | [P10, P90]$_{T-T_0}$ |
|---|---|---|---|---|---|---|---|
| McM17 $J_R = 0$ | $0.5 \pm 0.03$ | $0.4 \pm 0.01$ | 0.2 | 1.2 | [0.3, 0.9] | - | - |
| MW2014 | $0.6 \pm 0.03$ | $0.4 \pm 0.01$ | 0.2 | 1.1 | [0.3, 0.9] | 0.02 | [-0.04, 0.08] |
| B08 | $0.6 \pm 0.04$ | $0.5 \pm 0.01$ | 0.2 | 1.4 | [0.4, 1.0] | 0.09 | [-0.00, 0.21] |
| McM17 scaled | $0.5 \pm 0.02$ | $0.4 \pm 0.01$ | 0.2 | 1.1 | [0.3, 0.8] | -0.03 | [-0.05, -0.01] |
| MW2014 scaled | $0.4 \pm 0.02$ | $0.3 \pm 0.01$ | 0.2 | 0.9 | [0.3, 0.7] | -0.09 | [-0.17, -0.03] |
| B08 scaled | $0.5 \pm 0.03$ | $0.4 \pm 0.01$ | 0.2 | 1.1 | [0.3, 0.9] | -0.03 | [-0.06, 0.02] |
| McM17 $J_R = 100$ | $0.6 \pm 0.03$ | $0.5 \pm 0.01$ | 0.3 | 1.2 | [0.4, 1.0] | 0.03 | [0.01, 0.07] |
| McM17 $J_R = 200$ | $0.6 \pm 0.03$ | $0.5 \pm 0.01$ | 0.3 | 1.3 | [0.4, 1.0] | 0.08 | [0.04, 0.15] |
| McM17 DF | $0.6 \pm 0.03$ | $0.5 \pm 0.01$ | 0.3 | 1.3 | [0.4, 1.0] | 0.06 | [0.02, 0.12] |
| $d_{\mathrm{SH}-10\%}$ | $0.5 \pm 0.03$ | $0.4 \pm 0.01$ | 0.2 | 1.3 | [0.4, 0.9] | 0.02 | [-0.03, 0.05] |
| $d_{\mathrm{SH}+10\%}$ | $0.5 \pm 0.03$ | $0.4 \pm 0.01$ | 0.3 | 1.1 | [0.3, 0.9] | -0.01 | [-0.05, 0.03] |
| $d_{\mathrm{BJ}}$ | $0.5 \pm 0.03$ | $0.4 \pm 0.01$ | 0.2 | 1.2 | [0.3, 0.9] | -0.00 | [-0.03, 0.03] |
| SH giants | $0.5 \pm 0.02$ | $0.4 \pm 0.02$ | 0.2 | 0.7 | [0.4, 0.6] | 0.04 | [-0.02, 0.10] |
| SH $V_Z$ | $0.6 \pm 0.04$ | $0.4 \pm 0.01$ | 0.3 | 1.7 | [0.3, 0.9] | - | - |

data (on average 0.09 Gyr smaller). We also obtained systematically larger times when using not-circular orbits: for example 0.08 Gyr larger times for orbits with radial action $J_R = 200\,\mathrm{km\,s^{-1}kpc}$.

However, the main trends in the time determinations (in angular momentum and in height) remain the same in all cases. Our conclusions, thus, will be applicable to all the sets examined. Below we give details of this analysis but for a quick reading one could jump directly to the conclusions.

We first explored different potential models (Fig. 5.10 (whose circular velocity curves are compared in fig F.1 of A23 and the gradient of the vertical frequencies of these models in F.2). The gradients are slightly different as a function of radius and height but yield only small differences in the time determinations.

- Orange triangles in Fig. 5.10 use MW2014. This model returns slightly smaller times at smaller $|L_Z|$ and larger times at larger $|L_Z|$ but with null average differences when taking all individual time measurements. Purple squares are for B08. With this case we obtain the largest differences from all the variations explored in this section, systematically larger than our fiducial case and with several points at $2\sigma$. The average differences are of 0.09 Gyr and 80% of time measurements are within $[0.4, 1.]$ Gyr.
- While in the item above we use the original potential models from the respective articles, we also used them scaled to fit the values of $V_c$ and $R_0$ used in the data. To do this we use the built-in scaling mechanism of `AGAMA` by providing a mass scaling factor $(V_c(R_0)_{\mathrm{desired}}/V_c(R_0)_{\mathrm{default}})^2$ at the time of creating the gravitational potential, which results in the velocities and frequencies being scaled as the square root of said scaling factor. The results for the scaled potentials are the empty symbols in Fig. 5.10. It is now the MW2014 (scaled) model that gives maximum differences with the fiducial case, yielding smaller times ($[0.3, 0.7]$ Gyr).

Secondly, we examined different orbital conditions (Fig. 5.11), using frequencies for different kinetic temperatures. In our fiducial case we use orbits with $J_R = 0$, that is nearly circular orbits. Here we increase the eccentricity of the orbits in two different ways and use the corresponding new frequencies:

- Frequencies for orbits with larger radial actions ($J_R = 100$ & $J_R = 200\,\mathrm{km\,s^{-1}kpc}$, orange squares and green crosses in Fig. 5.11). These cases yield in general larger times since hotter orbits have smaller differences between frequencies at different heights. The average time, though, does not change much.
- Frequencies for the most populated part of the distribution function (DF, purple diamonds in Fig. 5.11). This is done by fixing $R$ and $Z$ and estimating the vertical frequency of the orbit with the highest probability in the DF at that location of space, that is at $Z_{\mathrm{max}}$ ($V_Z = 0$). With these different frequencies we obtain also larger times, similar to the $J_R = 200$ case.

Thirdly, we compare our results with the ones using another set of distances, possible distance biases and a selection of giant stars (Fig. 5.12, and discussed in Appendix C of A23).

- Using the BJ distances our results barely change (empty black circles in Fig. 5.12). This is not surprising given the agreement between both sets of distances for our selected samples.
- Distance bias. If we decrease/increase the distances by 10% (orange and green circles in fig B.2 of A23, mimicking a correction of overestimated/underestimated distances, there is an increase/decrease in the value of $|Z_{\mathrm{c}}|$ approximately by the same amount, except at the extreme $L_Z$ where selection effects might be playing a role. However, since Eq. 5.5 uses differential frequencies, we see that the times obtained do not change significantly (orange and green triangles in Fig. 5.12, consistent with the non-biased SH distances within the errors in most cases).

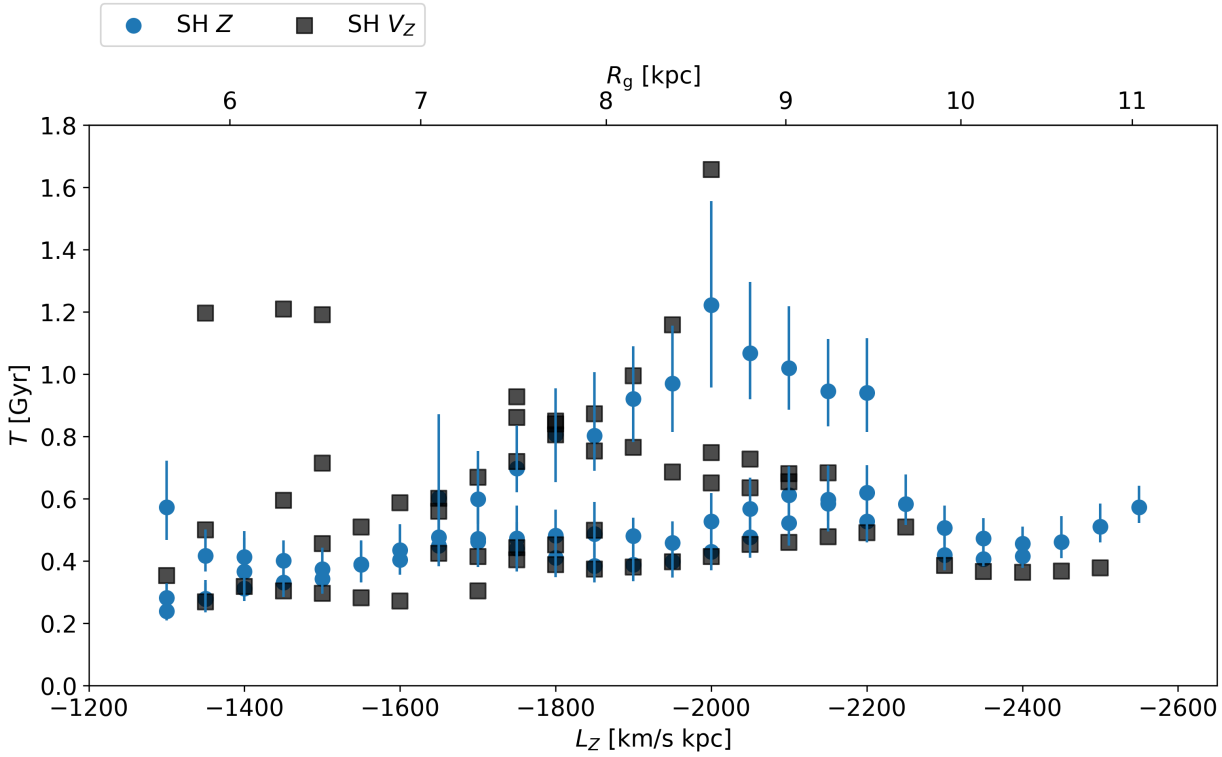


FIGURE 5.13: Time of start of phase mixing for different parts of the phase spiral. The figure is similar to Fig. 5.8 but we use the fiducial case (blue dots) computed from $Z_c$ but also from $V_{Zc}$ (grey squares) to derive the times, as indicated in the legend.

- Sample of giant stars. We also redid our analysis using the selection of giant stars from Gaia Collaboration et al. (2022b) obtained from the parameters of the *Gaia* `gspphot` pipeline with also the same quality filters as for our main sample. The new $Z_c$ and derived times are shown in fig B.2 of A23 and Fig. 5.12 (empty black squares in both figures), respectively. In almost all cases the new values fall within the error bars of the fiducial case and the trend in angular momentum remains the same. We cannot check whether the times also increase with $|Z|$ since only the inner parts of the spiral are detected due to the small number of stars in this selection (4 901 270).

Finally, we also derive the times from the $V_Z$ crossings of the phase spiral at $Z = 0$, which we name $V_{Zc}$, in addition to the $Z$ crossings at $V_Z = 0$ ($Z_c$), as in A18. The location of $V_{Zc}$ with respect to the $Z_c$ ones suggest, among others, that the assumed potential to infer the frequencies (and then the impact times) is not fully correct. We return to this point in our discussion (Sect. 5.5). As for the obtained times, the overall numbers do not change when considering these new crossings (Fig. 5.13).

## 5.5 Summary and conclusions

We have examined the phase spirals with the new data from *Gaia* DR3 and we find:

- A clear increase in the $Z$ and $V_Z$ ranges in which the phase spiral is detected. Surprisingly, we see phase spiral extending down to $-1.2$ kpc, thus well into the realm of the thick disk. This does not

necessarily mean that it is made of thick disk stars but could be made of thin disk stars that have been largely displaced.

- Phase spiral turns that extend in $V_Z$ beyond $\pm 50\,\mathrm{km\,s^{-1}}$, meaning that the perturbation produced a velocity kick at least of this amount and/or affected stars with these high vertical velocities.
- An increase in the range of detection of phase spiral in Galactic radius and azimuth. We see clear phase spirals between 6 and 11 kpc in radius and also evident asymmetry, probably indicative of a poorly resolved spiral, down to 5 kpc and up to 13 kpc (Fig. 5.3).
- Clearer phase spirals in counts and its colored versions in radial and azimuthal velocities.
- A secondary branch of the phase spiral at large positive $V_Z$ detected in the counts' projection and painted by $V_\phi$. This is observed in the local phase spiral (see also A18 and Laporte et al. 2019) but also between angular momentum 1800 and 2400 $\mathrm{km\,s^{-1}kpc}$. This branch seems to merge with the well-defined main phase spiral moving toward the outer Galaxy. A somehow similar branching is seen in the simulations by Hunt et al. (2021) (their figure 5). This secondary branch might be caused by the complexity of the phase mixing process (e.g. different groups of actions, stemming from non-uniform initial conditions, or with a strong dependence on the position of the disk) or different perturbations.
- Different morphology of the phase spiral when splitting by angular momentum, including the expected flattening with $Z$ at larger $|L_Z|$ (also seen in DR2, e.g. Laporte et al. 2019, Bland-Hawthorn et al. 2019) but also trends departing from this expected flattening in a usual MW gravitational potential. While part of these trends could be due to selection effects (Appendix D of A23), an easier explanation is our too-simplistic modeling of the phenomena involveds.
- Differences in the spiral in counts and colored by $V_R$ at certain angular momentum. As seen in the simulations in Bland-Hawthorn and Tepper-García (2021) for an impact with a galactic satellite, the vertical projection colored by $V_R$ could be showing the combination of: 1) the density wave induced after a perturbation (mostly a density two-armed spiral structure in the impulsive and distant impact conditions, Toomre and Toomre 1972; Struck, Dobbs, and Hwang 2011) that is linked to a $L_Z$-$V_R$ wave (Antoja et al., 2022), and 2) the vertical waves induced after the same perturbation. However, the exact way in which the planar and vertical disturbances are coupled is not yet well understood. Joining simple modeling of satellite perturbations such as the one in Gandhi et al. (2022) (vertical) and Antoja et al. (2022) (planar) could help in this. Exploring more complex models with enough resolution such as in Hunt et al. (2022) is also necessary.
- Mild changes of the phase spiral at different azimuths. These can be up to -0.006 kpc/deg but these changes are not uniform (i.e. depend on the turn of the phase spiral).

Finally, we have estimated the phase mixing times from the phase spiral variating in angular momentum and we find that:

- There is a large variation with the times derived from measurements of the phase spiral at different heights (different turns) and at different angular momentum: we see an increase of time with $|L_Z|$ and especially with $|Z|$. The time differences can be of 0.7 Gyr using a single phase spiral at the angular momentum close to the Sun's one but different turns of the phase spiral (i.e. different $Z$) and of 0.4 Gyr considering different angular momentum.
- The average time is of 0.5 Gyr. For 80% of our determinations, we find times in the range of 0.3-0.9 Gyr.

- We find slightly larger times when using the B08 model (0.4-1. Gyr), systematically larger times for hotter orbits (0.4-1. Gyr), and smaller times for a re-scaled version of MW2014 (0.3-0.7 Gyr).
- The values obtained are very similar to the ones given in A18 which were 0.3-0.9 Gyr and are consistent in their upper limits with the determinations from the frequency of the wave $L_Z$-$V_R$ from Antoja et al. (2022). As in our original work A18, these times are consistent with the previous pericentre passage of Sagittarius.
- The mentioned trends with angular momentum and height are robust to using frequencies for hotter orbits, different potential models, different distance determinations, and possible (small) distance biases.

We note that our modeling of the phase spiral can be over-simplistic. For example, we only consider the crossings of the phase spiral with the $Z = 0$ and $V_Z = 0$ axis but it would be better to use the continuity of the entire phase spiral. This is more in line with the work by Widmark, Laporte, and de Salas (2021). Recently, we found out that studies simultaneous to ours (Frankel et al., 2023; Darragh-Ford et al., 2023) used action-angle variables in an assumed potential to unwind the spiral into a "straight" line for the time fit. While our method does not use the full information of the phase spiral at the same time, it has the small advantage of not requiring to assume a potential until the final steps, making it easier to use in a combined fit of the phase mixing time and potential. In any case, these studies find also different time determinations at different angular momenta (between 0.2 and 0.6 Gyr in Frankel et al. 2023; 0.3 and 1 Gyr Darragh-Ford et al. 2023) or radius and azimuth (between 0.3 and 0.8 Gyr in Widmark, Laporte, and Monari, 2022), thus similar to our results.

These variations in the times are not expected for the simple interpretation of the phase spiral and a signal that comes from the same phase mixing process. Below we discuss different explanations.

It could be that we are seeing the differences in the time of response to the perturbation of different disk regions. However, for the case of the Sagittarius impact in Gandhi et al. (2022) they found differences in the onset of the perturbation effects at different radii of the order of 100 Myr, which is smaller than what we measure. Besides, they do not see a clear trend with a guiding radius. Widmark et al. (2022) tested their machinery of determining the potential from the phase spiral shape on the N-Body simulation from Hunt et al. (2021) and found time differences in small ranges of $R$ of the order of 100-200 Myr. In test particle simulations, Darragh-Ford et al. (2023) find slightly larger ($\approx$ 200 Myr) time variations with position (guiding center coordinates). In addition, the time differences with $Z$ at a fixed angular momentum would be hard to explain with this hypothesis alone, although as discussed before, our method could have some biases for large $Z$. The spatial and temporal propagation of different bending waves remains poorly studied and we plan to examine this with various models in the future.

Another explanation is that there is a mismatch between the vertical and radial dependence of the potential in the models (that we used to compute the vertical frequencies) and in the real MW. We also find possible evidence of this mismatch by considering and comparing the coordinates of the phase spiral when crossing the $Z = 0$ and the $V_Z$ axis (Appendix E of A23). One could actually infer the potential that could make these trends disappear. For example, the linear trend was seen with $L_Z$ (dashed line in Fig. 5.8) could be used to "correct" the potential (the gradient in frequencies) in order to obtain similar times. This is not trivial due to the degeneracy and the possible self-gravity effects.

Indeed, the time variations could also be evidence for self-gravity acting differently in different parts of the disk. Self-gravity tends to amplify the phase mixing times (Darling and Widrow, 2019) and in particular could be of less importance in the outer parts of the disk (e.g. Shen and Sellwood, 2006). This could mean that the times that we obtain in the outer parts, that is the larger times, are closer to the true

perturbation time. However, the radial behavior of different kinds of bending waves that originate from different perturbations might be different (e.g. bending waves associated with the bar or due to external torques from galactic satellites or even from a misaligned halo) and has not been deeply studied. Recently, Darragh-Ford et al. (2023) found large offsets between the interaction time and the recovered time in their N-Body simulation using their action-angle modeling, which they attribute to self-gravity or the effects of the associated halo wake.

Finally, our findings could be related to other aspects of the disk dynamics and how they interact with each other. By this we mean the effects of the bar, the spiral arms, the warp, and different bending and breathing modes, that could have acted or be acting in addition to the vertical perturbation causing the phase spiral. For instance, Widmark, Widrow, and Naik (2022) recently showed that some features of the vertical density and velocity seem related to the local spiral arm, while theoretical work has identified vertical velocity effects in spiral arm models (e.g. Faure, Siebert, and Famaey, 2014; Kumar et al., 2022). In addition, if the disk mid-plane oscillates due to one of these additional distinct phenomena, the $Z$-$V_Z$ centroid of the phase spiral would oscillate and affect the time determinations.

To conclude, we see now more complexity in the morphology of the vertical projection and unexpected trends, possibly indicating, different perturbations (perhaps from different agents or different times), as already pointed out by Hunt et al. (2022) -after the discovery of the double phase spirals- and/or complex phase mixing processes. The variations of our derived phase mixing times with vertical position and angular momentum likely indicate too poor modeling due to uncertainties in the potential model for the Galaxy, neglecting self-gravity, existence/interaction of multiple perturbations, or combinations of these. Although the new *Gaia* DR3 data definitively brings us a clearer picture of the MW phase spirals, there is still much to be understood and modeled.

CHAPTER 6

# Conclusions

## 6.1 Summary

This thesis is composed of three research papers that collectively explore the phenomenon of phase spirals and vertical perturbations in the galactic disk of the MW. The research is mainly based on the study of high-resolution hydrodynamical cosmological simulations named GARROTXA, as well as data from the Data Release 3 of the *Gaia* mission.

In Chapter 3, we analyzed the GARROTXA simulation and detected for the first time in cosmological simulations the phase spirals in the vertical projection $(Z - V_Z)$ of the disk's stellar particles across the disk and over certain times of evolution. The spirals were detected in younger groups of stellar particles and became visible from a radius of 6 kpc outwards, but are better seen in radius from 10 to 12 kpc. We employed Fourier decomposition to measure the intensity of the spiral and find a correlation with satellite pericenters. Since the satellites present in our model are less massive than the expected from N-body models to trigger the phase spirals, we concluded that there might be other mechanisms at play beyond single massive perturbers, such as gas accretion, collective effects of multiple perturbers, and the continuous renewal of a dynamically cold population through star formation.

In Chapter 4 we further analyzed the vertical behavior of this same model. We examined the relationship between vertical disturbances in the galactic disk and various perturbations, such as the effects of the halo, satellite galaxies, and gas infalls. Our analysis reveals complex bending patterns at different radii and times, characterized by retrograde modes and significant amplitudes during the stages of disk formation. Multiple agents, such as satellite galaxies, the inner dark matter profile, and misaligned gaseous structures, are identified as responsible for the perturbations leading to the bending of the stellar disk. Along with this, dark matter subhalos coincide temporally with bending waves, indicating their potential influence on the dynamic behavior of the disk.

In Chapter 5, we shift focus to observational data from Gaia DR3 and aim to use the phase spiral as a tool to infer the late-time evolution of the Milky Way. By employing an edge detection algorithm, we delineate the shape and extent of the phase spiral at different positions. Our analysis reveals that the spiral's is present at larger ranges in $Z$ and $V_Z$ and is detected down to significant heights below the galactic plane. The morphology of the phase spiral varies with angular momentum, showing the expected flattening with increasing $L_Z$ related to MW gravitational potential but also other complex deviations, with some of them possibly due to selection effects. Additionally, we detect signatures of vertical asymmetries beyond certain ranges and emphasize the need for refined models considering non-equilibrium dynamics, self-gravity, and the interaction between different mechanisms. The measurements of the phase spiral show significant

variations in the derived times when observed at different heights (different turns) and angular momentum values. On average, the derived time is approximately 0.5 Gyr. In 80% of the determinations, the time values fall within the range of 0.3 to 0.9 Gyr.

## 6.2 Discussion

**Can we use cosmological simulations for the study of disk dynamics?**

The kinematics of the stars in disk galaxies have been traditionally studied using non-cosmological simulations. Until recently, the requirements in computation time to obtain cosmological simulations with enough spatial and mass resolutions have been prohibitive. Also, as shown in this thesis, the analysis of so complex models, which include for example interactions with many perturbers and inflows of multiphase gas, has always been challenging. In the previous studies of Gómez et al. (2016b) and Gómez et al. (2017), they also use a cosmological simulation (Auriga) to study bending patterns in different disks. However, there is not an in-depth temporal tracking of each of the presented models. Both spatial resolution and temporal cadence of our model allow us to study the disk's behavior in timescales in which we can capture enough details of the evolution of the bending patterns and with enough spacial resolution to study the details in the thin disk. In this thesis, we have reached this balance for an in-depth study of the vertical distribution of the disk and *we have successfully used cosmological simulations for the study of disk dynamics*, which opens the door to future research on more detailed dynamics of galactic disks.

Furthermore, new cosmological simulations with high resolution and high cadence are recently available to do such an in depth study as in this thesis, which provides an invaluable tool to understand many processes not entirely captured by isolated models. Not all cosmological simulations are designed for the type of analysis carried out in this thesis. New state-of-the-art cosmological simualtions (such as TNG50, among others) are large volume simulations that do not resolve the thin disk scale's height. Other works, such as Grand et al. (2023) use a resolution enhancement technique on pre-existing simulation to increase their space and mass resolution which reduces computational costs. Other new promising zoom-in simulations with enough temporal and spatial resolution to study details of the disk are available, such as VINTERGATAN (Agertz et al., 2021). All these new progress in technology of the last years definitely constitute a promising avenue to the study of disks in very different cosmological contexts.

It is important to note that, due to the lack of tuning for specific conditions, it is still necessary to combine the knowledge of different types of simulations and techniques to better undestand the complex processes that a galactic disk undergoes throughout its lifetime. Cosmological simulations, despite having some limitations, have proven to be useful tools in comprehending the intricacies of disk dynamics that isolated models cannot fully capture.

**Are phase spirals common phenomena along the history of galactic disks?**

In the first chapter of this thesis, we asked if phase spirals were a common phenomenon in the history of a galaxy disk. We have observed these phase spirals in prolonged times of our cosmological simulated model (also seen in the RAMSES version of the GARROTXA simulation, see Appendix C), which leads us to conclude that this may be a quite common and persistent feature in the history of galaxies.

In addition, many different perturbations have been proved to trigger phase mixing resulting in phase spirals. For instance, previous studies with N-body models (e.g. Laporte et al., 2019; Bland-Hawthorn and Tepper-García, 2021; Hunt et al., 2021) have revealed that the phase spirals appear in direct tidal interactions with a perturber similar in size to the Sagittarius Dwarf Galaxy. Even though in our model

we cannot stablish a direct cause-effect relation with the multiple perturbers of the disk, the appearance of the phase spirals are coinciding with interactions with said perturbers, which are of lower mass than the estimated for the Sagittarius dSph.

Recently after our work of García-Conde et al., 2022, Grand et al., 2023 used a high-resolution simulation of a Milky Way-like galaxy from the Auriga suite of cosmological simulations and resolved phase spirals in the disk. The main formation mechanism of the phase spiral in that simulation was found to be the dark matter halo response to the passage of a satellite galaxy. In the case of the phase spirals present in GARROTXA, we have not found a dominant global asymmetry like the one expected when a strong wake is present.

Other proposed mechanisms are the bar buckling (Khoperskov et al., 2019), where the bar instabilities lead to vertical bending waves. In our work, we have found an oval structure producing a quarupole in the velocity $V_R$, but we do not detect buckling instabilities in the oval structure in the timespan studied. However, in Appendix D, we relate this structure with the breathing behaviour, and will be further studied in future work.

The recent work of Tremaine, Frankel, and Bovy (2023) proposed Gaussian noise from numerous small-scale encounters as mechanism for the phase spiral, instead of a single perturber exerting a larger kick. This might be compatible with our case, since we cannot associate the appearance of the phase spiral with a single event. However, our models are difficult to compare since they use a toy model with a single degree of freedom.

We have also studied other mechanisms that can contribute to a galactic disk's bending patterns. For instance, in Chapter 4 we discussed that the vertically disturbed stars can have a diverse range of origins and a perturbed disk may be a common state throughout galactic disks. *This suggests that the consequent phase mixing process from these perturbations that result in phase spirals may also be a common feature in disk galaxies that reside in a more dense environment, prone to interact with these types of galaxies and accrete gas*. This phenomenon is still under study and future research with more variety of disks and environments could give a definitive answer to this question.

**To what extent can other mechanisms, apart from the direct tidal interactions with satellites, affect the vertical behavior of a galactic disk? Are they the dominant cause of perturbation in the disk?**

In Chapter 4, we have discussed the bending behavior of the disk in our model with a more holistic approach, taking into account dark matter, satellites, and gas. We have traced the vertical perturbations source to a combination of the satellites applying a torque on the disk, and other contributors to the overall shape of the warp such as the accretion of gas and the inner shape of the dark matter halo. Throughout this thesis we found that, in our model, the inner dark matter structure also plays a role in determining the morphology of the different structures of a disk galaxy in the present. The interplay between the inner density profile and disk tilting (triggered by external sources) can alter the vertical behaviour of the disk. The shape of the inner dark matter profile is given by the ancient merger history of the galaxy, which can be very unique for each system. This allows us to conclude that not only the recent history of the interactions can determine the behavior of the disks, but the ancient mergers can also play a role in the shape of the deformations observed, triggered by recent interactions. Our findings also suggest that gas may have a further impact on the bending behavior of the stellar disk, although we have not been able to measure in which exact proportion.

Other works have studied other mechanisms of the vertical perturbations of the disk which are not strictly tied to the direct tidal interaction with satellites (although they can be related to their passing). This

mechanisms include gas infalls (Voort et al., 2015; Gómez et al., 2017; Semczuk et al., 2020; Khachaturyants et al., 2022), misalignment of the plane of stars at different radii (Sellwood and Debattista, 2022), the dark matter halo wake (Grion Filho et al., 2021; Grand et al., 2023), and bar buckling (Khoperskov et al., 2019). This thesis provides further proof that *throughout the life of a galaxy there are a variety of mechanisms which can influence the disk apart from the direct gravitational interaction with satellites*. Thus, we cannot consider satellites as point gravity sources that interact only with the stellar disk. Satellites contain dark matter, stars and gas, and each of these components interacts in a complex way not only with the main galaxy's stellar disk but also with its gas and its dark matter structure. All direct and indirect effects of the infall of a satellite galaxy need to be studied to understand the effect that an accretion event has on the central galaxy. These include accretion of gas, induced star formation and the following supernovae, variations on the structure and orientation of the host dark matter distribution, and the effect of the internal structure of the satellite that may play a role on the exchange of angular momentum with the main host.

We state that in our case, with a more realistic model with variety of perturbations, all processes are interacting and influencig each other, resulting in complex effects perturbing the disk. This may well be the case of the MW, since, as discussed in Chapter 5, the different shapes of the phase spiral when varying in $L_Z$ may hint at complex phase mixing rates of the phase spiral signal, which could be attributed to self-gravity or additional mechanisms acting appart from the original vertical kick. These different processes may difficult the determination of the origin of the phase spiral. Other recent studies also claim that the origin of the phase spiral as a result of a single impact is too simple to explain all the observations (Tremaine, Frankel, and Bovy, 2023; Frankel et al., 2023). In the recent work of Hunt et al. (2022) they also found double-armed phase spirals, whose nature can be related to a breathing mode. They conclude that there are signatures of different perturbations in the phase space of the explored regions by *Gaia* DR3. Thus, we state that *we cannot pinpoint the dominant cause of disk perturbation* in realistic models such as the one studied in this thesis or even in the case of the MW.

Answering the question of which is the role of the mechanisms other than the tidal interactions on shaping the vertical behavior of the disk, and if these are dominant has been challenging. The cosmological simulation studied here is highly perturbed since the beginning of the analysis, something expected also in real galaxies, which was attributed to an on-going process of disk formation, along with different satellite perturbing the still young disk. New data from James Webb Space Telescope has shown well-defined stellar disk at high redshift (Robertson et al., 2023), which could help find answers to how do external perturbers influence the evolution of these disks and how they can affect the present-day disk dynamics.

**How does the Milky Way's phase spiral look with Gaia DR3? What new information can we gain in relation to DR2?**

*Gaia* DR3 (Gaia Collaboration et al., 2022c) expands the sample of stars with 6D phase space data. There is an increase in definition compared to the view from Gaia DR2 to DR3, which yields a more clear phase spiral signal. The wider region coverage has allowed us to explore better the spiral pattern when moving in azimuth and radii (angular momentum), to estimate phase mixing times at different guiding radius, and with more crossing points than the previous data release. *This new data release has shown that the phase spiral morphology is more complex than previously expected*, with hints of multiple perturbations, as discussed in Chapter 5

Other works have also studied this spiral pattern with *Gaia* DR3, such as the work of Hunt et al. (2022), where they also discuss the possibility of multiple perturbations and the double-armed breathing

spirals. It also has open the door to new studies taking into account age and metallicity when combined with other surveys, as well as the fitting and parametrization of the phase spiral (Alinder, McMillan, and Bensby, 2023; Frankel et al., 2023). All these new studies show that the observations of this Data Release provide many features of the vertical phase space that still need to be researched in a theoretical frame. There are also exciting perspectives for *Gaia* DR4, expected by the end of 2025, such as the expansion of the regions in which we can study the phase space.

## 6.3 Caveats

**Limitations in resolution**

All simulations suffer of limitations due to the spatial, temporal, and mass resolutions. The level of detail we can study is thus limited by non-resolved physics. In the case of the GARROTXA cosmological simulation, it is important to acknowledge certain constraints when interpreting the results, particularly regarding the detection and characterization of phase spirals, which we have only been able to study at intermediate altitudes and vertical velocities but not the ones close to the thin disk plane as in the *Gaia* data. While our simulation possesses sufficient resolution to identify their presence, it is worth noting that our level of resolution is not on par with that of more detailed N-body models, which can provide a higher level of detail. Therefore, it is challenging to discern whether the difficulty in distinguishing the phase spirals arises from the limitations in resolution or from if they are intrinsically weak.

This is certainly an important limitation in all simulations which must be considered when studying processes which may not be well resolved. The resolution limitations have indeed presented a challenge when resolving the details of the phase spiral in Chapter 3. However, we do not encounter this difficulty in Chapter 4, where the resolution is enough to characterize the bending waves and to analyze the disk as a whole. Thus, while we must approach our conclusions with caution in relation to the more intricate details when we approach the thin disk scales, our simulation provides valuable insights into the nature of the bending patterns.

**Direct comparison with the Milky Way**

The MW, like all other galaxies, is the product of numerous physical processes that occurred since the beginning of star formation in its primordial halo, its surrounding environment, and many other coincidental developments. Additionally, it is important to note that observations have limitations, and most structural parameters of the MW are still not fully constrained. As a result, attempting to create an exact model of the Galaxy is unreasonable. However, it is possible to study global properties and their origin such as the formation of thin disks, non-axyssimetric structures and physical processes outside the state of equilibrium.

While the model in our simulation may have a comparable size to the MW, there are fundamental differences in their respective natures, as discussed in Chapter 2 (Table 2.1). We noted that the galaxy in this model lies at the lower end of the estimation for the MW's mass and size. Another notable distinction lies in the presence of a bar within the MW, characterized by an estimated pattern speed of $\sim$ 35-40 km $s^{-1}$ $kpc^{-1}$ (Portail et al., 2016; Pérez-Villegas, Wegg, and Gerhard, 2017; Clarke and Gerhard, 2022). In contrast, the inner structure of the disk in our model exhibits a distinct oval shape that remains stationary relative to our reference system, although it clearly shows the distinct quadrupole in $V_R$. Furthermore, in our case, the last major merger left a distinctive tri-axial dark matter structure in the inner parts of the galaxy, and it is not known if the MW could also have a similar structure.

Additionally, even if the number of satellites in this model is compatible with the predictions for the MW's mass (Bullock and Boylan-Kolchin, 2017), a lack of interaction with massive satellites ($M_*>10^{10}$ $M_\odot$) in this system that could be equivalent to the LMC and SMC makes it challenging to compare directly with the Milky Way at the present time. However, this exercise helps us to understand the evolution of disk galaxies in a global way, where past interactions can have a long-lasting impact on stellar disk morphology and kinematics.

Therefore, these disparities in the internal structures and recent merger history of the two systems complicate direct comparisons between our model and the MW. In particular, it is important to acknowledge that we cannot establish a direct comparison between the phase spirals and bending behaviour observed in our simulation and those observed in the MW, although it is not our main goal. Further research and more sophisticated models are necessary to bridge the gap between our simulation and the intricacies of the MW.

**Lack of statistics**

It is important to acknowledge that we have focused on examining the bending waves and phase spirals within the context of a single cosmological model in depth. While these phenomena have been explored in various N-body models, it is essential to extend our investigations to cosmological models as well. Each cosmological model is also very unique (like real galaxies), with different histories, satellites, and conditions that determine their dynamics. The nature of cosmological simulations, their computational expense, and the complexity of the phenomena being studied make it difficult to conduct a comprehensive analysis across multiple simulations. Furthermore, simulated models face other difficulties such as numerical effects, subgrid physics, or nature of dark matter. In addition, it is worth noting that adopting a more statistical approach by studying a broader range of cosmological simulations poses significant challenges, such as the lack of tuning, storage, or the time needed to fully understand all the characteristics and environment of such models.

However, techniques for cosmological simulations are rapidly improving over time, and are now much better than the GARROTXA simulation. For instance, nowadays a stochastic star formation is being preferred in the community, in contrast to the deterministic star formation, as is the case for the GARROTXA simulation. Stochastic star formation accounts for turbulence in a more realistic way and allows more inhomogeneity in star formation regions (Caplar and Tacchella, 2019; Wang et al., 2022). Furthermore, the inclusion of AGNs can also add more realism to the cosmological models and are currently being included in the new age of simulations of galaxy formation and evolution (Kaviraj et al., 2017). In general, the increasing computational capacity is leading to an improved resolution and storage capacity for snapshots with thinner timesteps. The sub-grid physics, with star formation and feedback recipes, are also being perfected thanks to new observational data and smaller scale simulations (Schaye et al., 2023).

In this thesis, we have developed software techniques that rapidly process the snapshots, centering, aligning, and analyzing their vertical behavior. Thus, this methodology serves as a foundation for further investigations and highlight the need for future studies to incorporate a more extensive and statistically significant analysis involving a diverse set of cosmological simulations. By repeating this anaylisis in other cosmological simulations, we can enhance our understanding of the general behavior and characteristics of bending waves and phase spirals across different cosmological scenarios, ultimately advancing our knowledge of galactic dynamics on a broader scale.

### Alignment

In this thesis, it is crucial to have a well-defined galactic plane, which is a challenging task in cosmological simulations with numerous perturbers. As a result, we have developed a new method to address this issue. However, as explained in Chapter 2 (see also Appendix A), the choice of alignment of the galaxy and the definition of a reference frame is a delicate and challenging task, and it is not trivial to define a midplane with such a complex vertical structure, with different bending at different radii or for different populations. Variations in the determination of the galactic plane can lead to inaccuracies in the measurements of dynamical properties (Beane et al., 2019). Unfortunately, there is no established process in the literature beyond the use of angular momentum. Different techniques for alignment have been adopted across different research groups. Throughout the thesis project, we have explored multiple ways of aligning the galaxy, and finally we have adopted a two-step alignment where we apply a change of basis, as described in Chapter 2.

This two step alignment allows to align the disk in the $Z = 0$ plane and avoids interference from possible external satellites. However, the complex nature of the different density structures, combined with a two-step change of basis, may introduce slight, non-accumulative rotations in the X-Y plane which may introduce small inaccuracies in the angular positions of the simulation particles.

### Fourier

The application of tools such as those used in this work is necessary to detect and analyze the variety of processes taking place in cosmological simulations. They are also necessary in order to automatically analyze a larger set of models, which is crucial for a more global understanding of disk dynamics in real galaxies. Throughout this work, we have heavily relied on Fourier $m = 1$ analysis to detect and analyze various characteristics in our cosmological simulations. We want to remark that another caveat in our methodology is that our Fourier analysis does not always provide conclusive evidence to establish true causality or to analyze structures in 2D. This likely comes from two aspects. Firstly, when numerous intricate processes are at play, some of which are intertwined, it is not straightforward to differentiate real agents of perturbation from mere coinciding effects. Additionally, it can be challenging to separate causes from their corresponding effects. Secondly, it is important to consider the inherent nature of Fourier analysis. Localized accelerations, such as those caused by subhalos and satellite galaxies, tend to undergo some level of smoothing through the sine/cosine decomposition, especially when we limit our analysis to the first-order ($m = 1$ and $m = 2$ modes). In the case of the internal non-axisymmetric dark matter structure, its overall acceleration is not entirely encapsulated by the $m = 1$ mode, since it is also dominant in higher modes. Finally, since there are different disk regimes with radial limits that change with time, our analysis can be biased by exploring the disk in rings of fixed radius that might not be the natural ones. Although we find this Fourier technique simple, useful and intuitive for comparison between the numerous different characteristics of the galaxy, it is worth considering other methodologies that do not heavily rely on region selections.

Some alternative methodologies that could be explored in the future could be Basis Function Expansions or Multichannel Singular Spectrum Analysis, which are more sophisticated tools to link the different agents and effects, which might improve our correlation analysis (Appendix E). These techniques are starting to be applied to disc dynamics in more controlled simulations (Weinberg and Petersen, 2021; Garavito-Camargo et al., 2021; Johnson et al., 2023) and this might establish the foundations for its application in more complex cases such as the model used here. These expansions might be also useful for a more global study of the dynamics, not centered exclusively on the vertical or planar dimensions.

## 6.4 Future work

**Propagation of phase spirals**

Due to the limited spatial resolution of our model we cannot conclude on the specific way in which the phase spiral seen in this model phase mixes and/or propagates. We observe that the propagation of the phase spiral (thick bands seen in the estimator of its strength in Chapter 3) seems compatible with the retrograde density mode $m = 1$ (Appendix D ). The similarity may be an indication that these two phenomena are related, with the retrograde spiral arm being a driver of propagation. In future work, we will focus on the retrograde spiral arm and its possible relation with breathing behavior and the propagation of the phase spiral.

**Very young phase spirals**

One of the most compelling questions about the phase spiral is how perturbed are the orbits of the newly formed stellar particles. In Chapter 3 we have seen that newly born stellar particles may appear very displaced from the galactic plane. This can be attributed to being born from highly perturbed gas. In future work we want to study how do the newly formed stars evolve in the vertical phase plane $Z$ - $V_Z$ when a recent perturbation has occured, since they are already born out of equilibrium. This analysis could be performed with this same model since we can identify recently born stars and track their evolution over time in the scales of position and velocity already seen in Chapter 3.

**Bending patterns across age populations**

Preliminary analyses, as outlined in Appendix F, have indicated that the bending pattern exhibits variations across different stellar populations. In future work, we want to study the mechanisms driving these differences and their connection to the presence and characteristics of phase spirals within these specific populations. By examining these populations separately, we gain realism to compare with real galaxies such as the MW. Since we have developed the necessary tools to study the vertical behavior of disk galaxies in the context of cosmological simulations, we open the door to further exploit the stellar formation and evolution features in other cosmological models.

**Satellite with hot gas**

In this simulation, we have found satellites that interact with the disk but do not have stellar particles. These are satellite galaxy-mass structures that contain hot gas. For instance, the DM1119 has diffuse, hot gas with no stellar particles. We find hints of this object influencing the disk dynamics at its pericenter, such as bending waves in the outer regions of the disk, or the appearance of phase spirals. This satellite is composed of a dark matter halo and diffuse gas that, due to its temperature and density, has not been able to form stellar particles. In a real case scenario, this satellite would have been difficult to observe and to estimate its mass, but can influence the disk nonetheless. The existence of these types of objects and their influence on the galactic disk can help us better understand the nature of dark matter. In future work, we want to better study this specific satellite and track its mass, size, gas content, etc, over time since its assembling to gain more insights on the processes preventing this satellite from forming stars and compare it with its luminous counterparts.

**Influence of satellite streams**

We find that the most massive satellite of the model, Arania, leaves a more significant mass of debris with each interaction with the main galaxy than the other satellites. This debris contributes in mass to the halo and may influence the stellar disk. Therefore, it is essential to conduct a detailed analysis of these stellar streams from both modeling and observational perspectives.In Appendix G we calculate the acceleration that the debris of the satellite Arania exerts onto the disk. Even though in this specific model this quantity is not as significant as that of the satellite itself, other models with more massive satellites may yield a stronger acceleration from streams that may be worth quantifying. In terms of observations, currently, only the brightest streams have been observed from the ground (Martínez-Delgado et al., 2023; Miró-Carretero et al., 2023). However, future space-based observation missions, such as ESA's ARRAKIHS, will provide an in-depth understanding of these structures, enabling us to analyze their role in the dynamic and morphological evolution of galaxies.

## 6.5 Final conclusions

The main conclusion we obtained from this work is that galaxies like the MW that have been traditionally considered to have a quiet recent merger history (with the last major merger occurring at $z \sim 1.5$ in the case of the MW) are in fact also highly dynamically perturbed. We have seen that the many processes related with satellites and gas accretion are continously influencing the disk. Such processes which all galaxies suffer in their lifetime can keep the galactic disk out of the equilibrium most of the time.

The theoretical part of this thesis emphasizes the importance of a *holistic* approach to disk dynamics. Our model is one of the few to consider additional factors in the context of vertical perturbations: the effects of the inner profiles of dark matter and old stars from previous major mergers, and the gas brought in by satellites and accreted through filaments. These factors are often overlooked by more simplistic models that therefore do not capture the full complexity of galactic systems. The phase spiral pattern of the simulated model is highly complex in terms of times of phase mixing and propagation. There are diverse factors that can determine its behaviour such as different perturbations. Even though in the simulated galactic model studied in this thesis the appearance of the phase spiral is coincident with the times of satellite passing, it is yet not clear the exact mechanism in which they develop. It is undoubtedly a huge effort to bring cosmological simulations into the picture of disk dynamics. Although detecting and understanding the complex interplay between all existing phenomena and the different dynamical regimes in the disk in cosmological simulations is challenging, the analysis of coexisting perturbative processes will lead to more realistic galactoseismology.

The observational part of this thesis shows that the morphology of the observed phase spiral of the neighboring regions of the Sun is highly complex. The variations of our derived phase mixing times point to uncertainties in the potential model of the MW or different perturbations coexisting in the phase space, challenging the notion of a single perturber being the culprit. This new *Gaia* DR3 has shown that there is still so much to be understood about the nature of our Galaxy.

The results of this thesis demonstrate that the complexity of realistic models is comparable to that of observations, but these models are necessary to obtain a more complete picture of a Universe where disk galaxies are frequently found in a state of constant interaction and lack equilibrium. The origin of these instabilities may not be unique and cannot be studied in isolation, but with a *holistic* perspective, taking into account the interplay between various factors such as satellite galaxies, dark matter structures, and gas dynamics.

APPENDIX A

# Alignment: Change of basis

The definition of a galactic plane in a cosmological simulation is not a trivial task. The cosmological box's cartesian coordinates are usually not coincident with the main axis of the simulated galactic disk. Thus, we need to set a strategy to find an appropiate coordinate system to be aligned with the galactic disk for analysis purposes. In this thesis we align the galaxy in two steps with the same algorithm, but taking $L$ for diferent subsets of particles for each step.

After the centering process, our algorithm calculates the angular momentum vector of all stellar particles of the galaxy inside the 20% of $R_{\rm vir}$ at each snapshot. This vector will define the Z-axis of the new reference system, as shown in Fig A.1. The algorithm then uses this vector and the point (0,0,0) to create a plane whose normal vector is $L$. We then take the point (1, 0, 0) in the original X axis and project it on this plane, which will define the X-axis in the new reference system (left panel of Fig A.1). The Y axis is defined as the cross-product of these two unitary vectors aligned with the X and Z axis. (right panel of Fig A.1). Thus the algorithm consists of these expressions, where $x'$, $y'$ and $z'$ are the new axis vectors:

$$\mathbf{z}' = \frac{\mathbf{L}}{\|\mathbf{L}\|}$$
$$\mathbf{x}' = \mathbf{x} - (\mathbf{x}\cdot\mathbf{z}')\mathbf{z}'$$
$$\mathbf{y}' = \mathbf{z}'\times\mathbf{x}'$$

To further adjust the reference system, we take a cilindrical region with $|Z| < 3$ and $R < 15$ kpc for Chapter 3 and $R < 7$ kpc for Chapter 4 of all stellar particles born after z$\sim$ 1.5. From these new selection of particles we recalculate $L$ and perform a new realigment, with the same ecuations as above. However, since we do not have a perfectly thin disk and usually have a vertically perturbed state, some stellar particles and gas remain misaligned with respect to the newly defined $Z = 0$ plane. In Fig. A.3 we show this misalignment, $\theta$, for annular regions of 5 kpc of width from inner radii (top panel) to outer radii (bottom panel). In this second reference system, the stellar particles at $R < 5$ kpc (top panel) are well aligned with the plane, with generally less than $1^\circ$ of misalignment. At the external radii, both stars and gas are less aligned with this plane, especially in the first gigayear of the period studied, due to the different perturbations discussed in the text.

In Fig. A.4 (alignment used in Chapter 3) we show this misalignment $\theta$ for stars and gas in the second reference system, which in this case uses $R < 15kpc$. for its second step. We see that the regions better

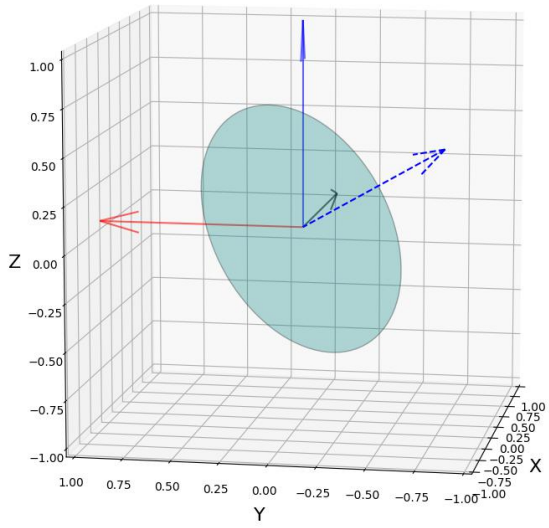


FIGURE A.1: 3D example of a tilted stellar disk (tilted blue circle) in the cosmological box. The solid arrows represent the cosmological box original axis. The dotted blue arrow represents $L$ of the disk, and the new axis $z'$ after the change of basis.

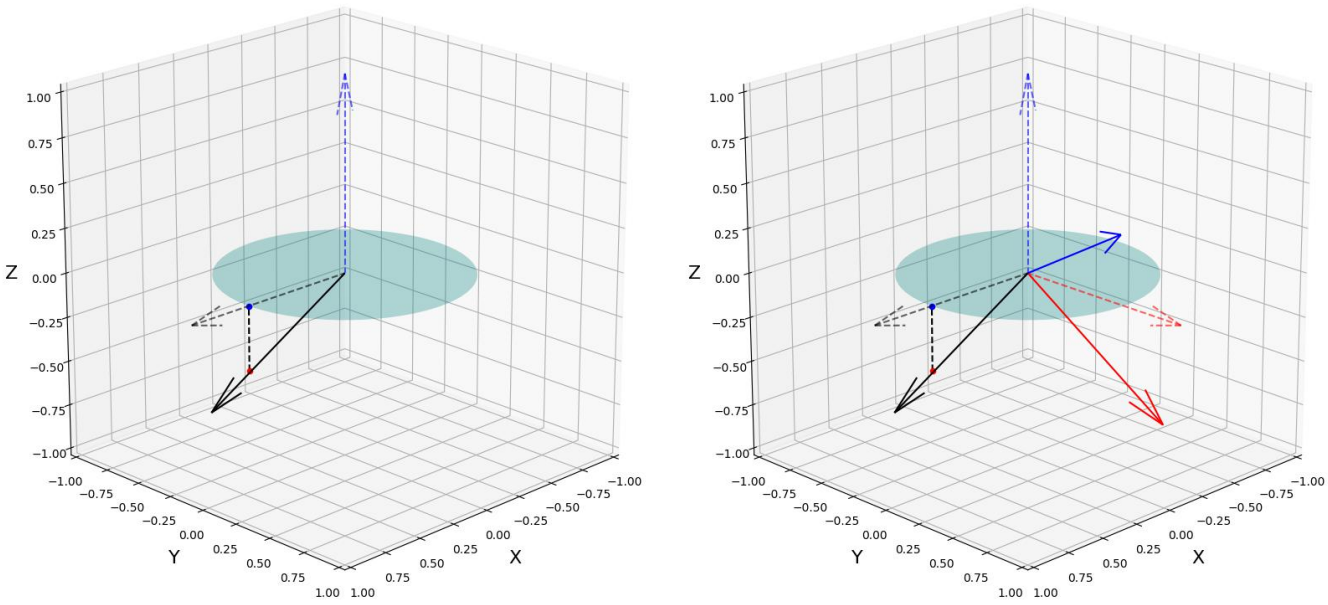


FIGURE A.2: **Left panel**: Definition of the $x'$ axis (dotted black arrow), which is a projection onto the galactic plane of the old $x$ axis (solid black arrow). **Right panel**: Definition of the $y'$ axis (dotted red arrow), defined as the cross product of $z'$ (dotted blue arrow) and $x'$ (dotted black arrow).

aligned are from 10 to 15 kpc, and the inner regions show a 1° of misalignment overall, due to galactic bend at some instances, since we are taking these intermediate parts as reference for alignment.

This two step alignment where we select a wide cylindrical region after a first broad alignment ensures that the disk is well placed in our reference system and that almost no stellar particles from satellite getting nearer than 20% $R_{vir}$ introduce variations in the angular momentum calculations (compared to taking a spherical region). However, we want to note that a single step process would help reduce the number of transformations, diminishing the possible artificial angular variations. Even though our aim was to desing an universal alignment process which would be applied to any type of model, we note the need of adaptation of the selection of particles and regions for each model.

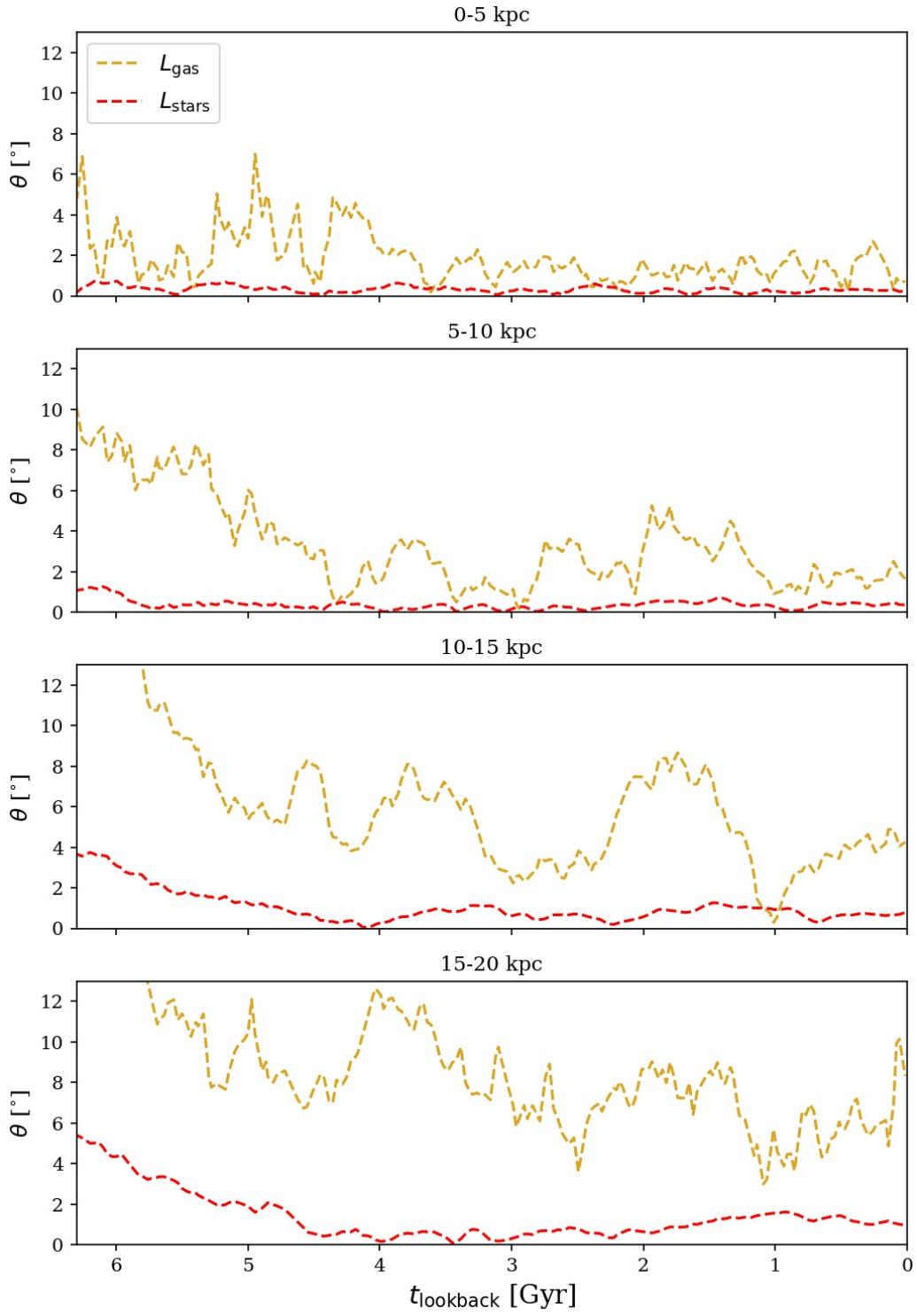


FIGURE A.3: $L_Z$ misalignment of stars and gas in respect to the established $Z = 0$ plane where the second alignment has been done using stellar particles in the radial region of $R < 7$ kpc as a function of time (recomputed at each snapshot). From top to bottom, regions from 0 to 5 kpc, 5 to 10 kpc, 10 to 15 kpc and 15 to 20 kpc.

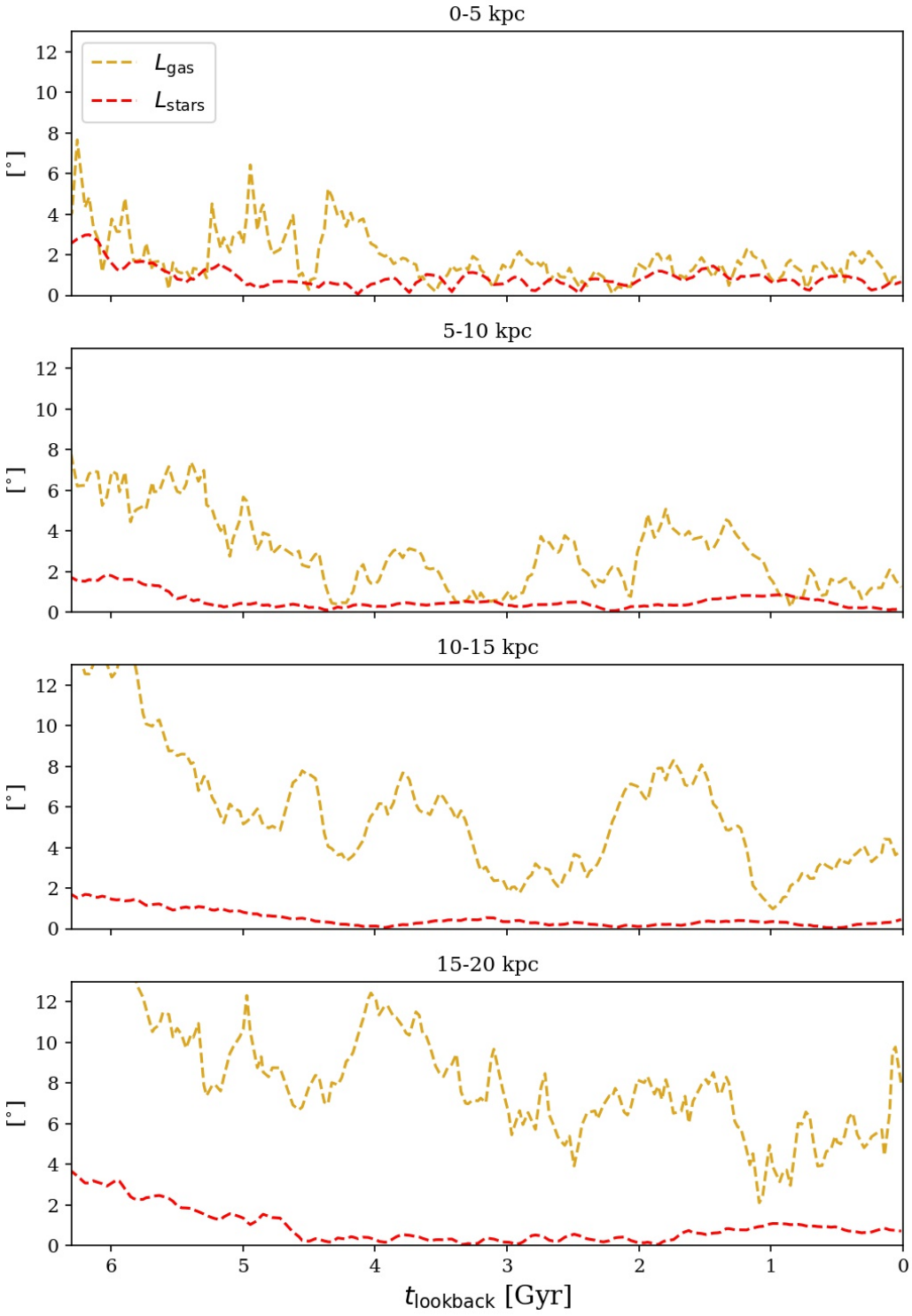


FIGURE A.4: $L_Z$ misalignment of stars and gas in respect to the established $Z = 0$ plane, similar to A.3 where the second alignment has been done using stellar particles in the radial region of $R < 15$ kpc as a function of time (recomputed at each snapshot). From top to bottom, regions from 0 to 5 kpc, 5 to 10 kpc, 10 to 15 kpc and 15 to 20 kpc.

APPENDIX B

# Rockstar: Sub-halos and dwarf galaxies as satellites

The Rockstar halo finder (Robust Overdensity Calculation using K-Space Topologically Adaptive Refinement) is a commonly used algorithm in astrophysics for identifying and characterizing dark matter sub-haloes within large-scale cosmological simulations (Behroozi, Wechsler, and Wu, 2012). It is designed to locate these substructures, which represent gravitationally bound regions of dark matter particles within a larger halo or cluster. The approach is based on adaptive hierarchical refinement of friends-of-friends groups in six phase-space dimensions and the time dimension. The method runs on the largest current simulations with high efficiency.

As an initial step, the algorithm utilizes an accelerated version of the 3D friends-of-friends (FOF) technique to identify dense regions. These regions are subsequently distributed across multiple processors for further analysis. Then, the algorithm constructs a hierarchy of FOF subgroups based on phase space, progressively and adaptively reducing the 6D linking length. The hierarchy of FOF groups is then transformed into a list of particle memberships for halos. Furthermore, the algorithm determines the relationships between host halos and subhalos by using information from the previous timestep if it is available. Rockstar dynamically adjusts the linking length in phase space during the hierarchy construction process. This adaptive approach allows for a more refined and precise identification of substructures within halos, leading to improved accuracy in halo characterization.

In this appendix, we show the complete information about the results from the Rockstar halo finder. In Fig. B.1 we show the distance to the center of the galaxy of all satellites with $> 10^6\ M_\odot$. The minimum of the curves are the moments of the pericentric passages of each satellite. The top three panels show satellites with no stellar mass, from $M < 10^7\ M_\odot$, $10^7 < M < 10^8\ M_\odot$, and $M > 10^8\ M_\odot$. The last panel shows satellites with stellar mass.

In Table B.1 we show some characteristics of the satellites with $M > 10^7\ M_\odot$. From left to right we show the ID of the halo assigned by Rockstar, $R_{200}$, $M_{200}$, the stellar mass ($M_*$) in the 20% of the $R_{200}$, minimum distance to the galaxy over its orbit, and the lookback time interval ($t_{init}$ - $t_{fin}$) in which we detect them.

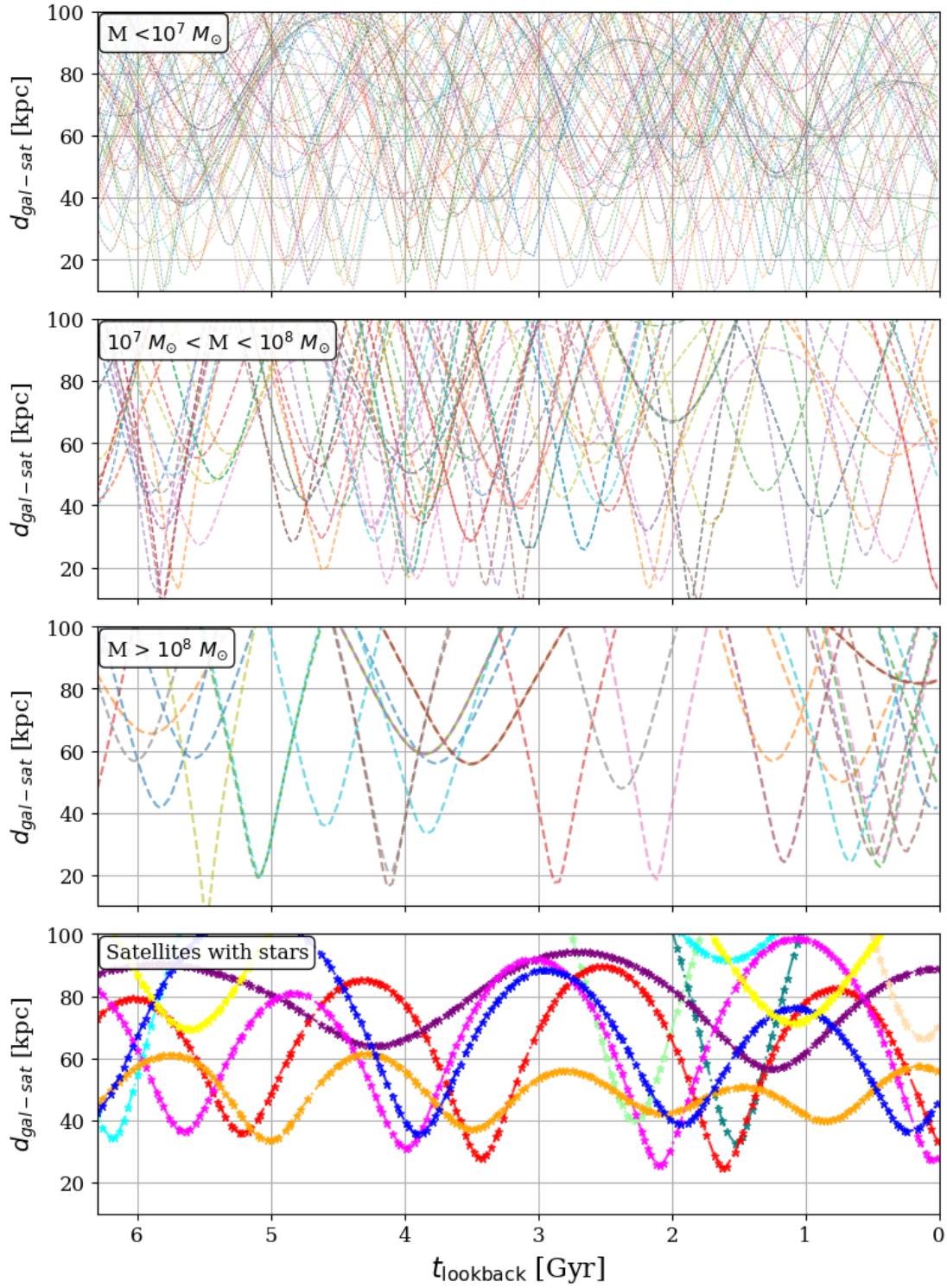


FIGURE B.1: Distance of satellites to the center of the galaxy. The top panel shows dark satellites of $10^6\ M_\odot$ < M <$10^7\ M_\odot$. The second panel are satellites $10^7\ M_\odot$ < M <$10^8\ M_\odot$. Third one M > $10^8\ M_\odot$. The bottom panel shows all subhalos containing stellar particles.

| **ID** | $R_{200}$ [kpc] | $M_{200}$ [$M_\odot$] | $M_*$ [$M_\odot$] | $d_{\min}$ [kpc] | $t_{\text{init}}$ [Gyr] | $t_{\text{fin}}$ [Gyr] |
|---|---|---|---|---|---|---|
| 27 | 26.24 | 1.61e+09 | 5.94e+06 | 39.9 | 3.84 | 0.01 |
| 57 | 14.57 | 2.34e+08 | 0.00e+00 | 139.55 | 4.09 | 0.01 |
| 58 | 13.56 | 1.69e+08 | 0.00e+00 | 189.22 | 2.61 | 0.01 |
| 62 | 12.31 | 1.28e+08 | 0.00e+00 | 58.99 | 7.64 | 0.01 |
| 63 | 12.86 | 1.68e+08 | 0.00e+00 | 56.74 | 2.65 | 0.01 |
| 90 | 9.21 | 9.15e+07 | 0.00e+00 | 31.86 | 6.66 | 0.01 |
| 182 | 5.87 | 1.51e+07 | 0.00e+00 | 180.98 | 0.85 | 0.01 |
| 187 | 5.15 | 1.31e+07 | 0.00e+00 | 166.24 | 3.58 | 0.01 |
| 479 | 19.86 | 7.21e+08 | 0.00e+00 | 22.67 | 2.33 | 0.01 |
| 480 | 7.63 | 4.95e+07 | 0.00e+00 | 75.38 | 6.1 | 0.01 |
| 489 | 2.43 | 1.73e+07 | 0.00e+00 | 7.23 | 2.56 | 1.23 |
| 494 | 2.6 | 2.08e+07 | 0.00e+00 | 150.8 | 5.63 | 4.28 |
| 498 | 8.93 | 5.61e+07 | 0.00e+00 | 75.93 | 7.57 | 0.01 |
| 502 | 7.73 | 2.75e+07 | 0.00e+00 | 118.9 | 1.25 | 0.01 |
| 527 | 6.23 | 1.55e+07 | 0.00e+00 | 74.78 | 1.4 | 0.01 |
| 1747 | 11.92 | 1.76e+08 | 0.00e+00 | 17.71 | 4.22 | 0.01 |
| 1749 | 9.72 | 8.01e+07 | 0.00e+00 | 44.81 | 2.88 | 0.01 |
| 1751 | 9.53 | 7.16e+07 | 0.00e+00 | 81.49 | 2.96 | 0.01 |
| 1799 | 7.54 | 3.88e+07 | 0.00e+00 | 60.05 | 3.97 | 0.01 |
| 2044 | 15.3 | 2.20e+08 | 0.00e+00 | 226.05 | 1.18 | 0.01 |
| 2051 | 11.91 | 1.05e+08 | 0.00e+00 | 232.06 | 1.09 | 0.01 |
| 2052 | 11.75 | 1.33e+08 | 0.00e+00 | 81.88 | 3.58 | 0.01 |
| 2091 | 6.08 | 1.66e+07 | 0.00e+00 | 98.48 | 2.18 | 0.01 |
| 2095 | 2.24 | 4.11e+07 | 0.00e+00 | 134.58 | 5.76 | 4.09 |
| 2100 | 12.81 | 1.88e+08 | 0.00e+00 | 44.79 | 2.06 | 0.01 |
| 2113 | 18.06 | 4.92e+08 | 0.00e+00 | 27.58 | 7.64 | 0.01 |
| 2116 | 6.48 | 4.52e+07 | 0.00e+00 | 55.23 | 6.26 | 0.01 |
| 2133 | 6.43 | 2.79e+07 | 0.00e+00 | 23.98 | 2.45 | 0.01 |
| 2134 | 13.67 | 2.20e+08 | 0.00e+00 | 25.67 | 7.48 | 0.01 |
| 2143 | 7.39 | 3.30e+07 | 0.00e+00 | 69.83 | 2.01 | 0.01 |
| 2144 | 9.88 | 8.73e+07 | 0.00e+00 | 110.52 | 6.9 | 0.01 |
| 2198 | 11.5 | 1.70e+08 | 0.00e+00 | 90.7 | 4.85 | 0.01 |
| 2200 | 11.63 | 1.35e+08 | 0.00e+00 | 98.49 | 6.61 | 0.01 |
| 2201 | 11.81 | 9.83e+07 | 0.00e+00 | 222.16 | 0.74 | 0.01 |
| 2212 | 8.25 | 6.26e+07 | 0.00e+00 | 157.69 | 2.65 | 0.01 |
| 2227 | 9.07 | 4.66e+07 | 0.00e+00 | 47.83 | 6.9 | 0.01 |
| 2238 | 7.14 | 3.83e+07 | 4.67e+03 | 32.69 | 7.57 | 0.01 |
| 2254 | 2.82 | 3.82e+08 | 0.00e+00 | 62.08 | 4.43 | 1.65 |
| 2280 | 7.33 | 7.35e+07 | 0.00e+00 | 36.35 | 6.49 | 0.01 |
| 2289 | 7.04 | 5.35e+07 | 0.00e+00 | 44.69 | 5.69 | 0.01 |
| 2369 | 4.94 | 1.85e+07 | 0.00e+00 | 73.37 | 5.89 | 0.01 |
| 2470 | 16.54 | 1.20e+09 | 2.19e+07 | 34.38 | 6.9 | 0.01 |
| 2524 | 12.18 | 1.92e+08 | 0.00e+00 | 82.62 | 6.61 | 0.01 |
| 2540 | 9.07 | 6.87e+07 | 0.00e+00 | 47.04 | 6.9 | 0.01 |

*Continue in the next page*

*Continuation of the previous page*

| **ID** | $R_{200}$ [kpc] | $M_{200}$ [$M_\odot$] | $M_*$ [$M_\odot$] | $d_{\min}$ [kpc] | $t_{\text{init}}$ [Gyr] | $t_{\text{fin}}$ [Gyr] |
|---|---|---|---|---|---|---|
| 2550 | 5.26 | 1.00e+07 | 0.00e+00 | 38.85 | 7.64 | 0.01 |
| 2552 | 5.66 | 1.13e+07 | 0.00e+00 | 35.99 | 7.64 | 0.01 |
| 2568 | 7.41 | 2.65e+07 | 0.00e+00 | 59.12 | 1.74 | 0.01 |
| 2585 | 23.71 | 1.42e+09 | 4.82e+06 | 69.6 | 6.66 | 0.01 |
| 2586 | 4.86 | 1.05e+07 | 0.00e+00 | 78.49 | 7.24 | 0.01 |
| 2587 | 7.67 | 3.44e+07 | 0.00e+00 | 56.71 | 7.39 | 0.01 |
| 2601 | 5.61 | 1.52e+07 | 0.00e+00 | 12.92 | 7.15 | 0.01 |
| 668 | 8.55 | 4.45e+07 | 0.00e+00 | 13.65 | 2.45 | 0.01 |
| 684 | 7.85 | 3.03e+07 | 0.00e+00 | 202.99 | 1.8 | 0.01 |
| 718 | 15.7 | 3.71e+08 | 0.00e+00 | 191.37 | 0.79 | 0.01 |
| 726 | 16.69 | 3.07e+08 | 0.00e+00 | 193.16 | 2.01 | 0.01 |
| 1119 | 21.89 | 1.14e+09 | 0.00e+00 | 21.08 | 5.02 | 0.01 |
| 1123 | 8.14 | 5.67e+07 | 0.00e+00 | 56.07 | 5.4 | 0.01 |
| 1125 | 13.91 | 1.41e+08 | 0.00e+00 | 34.45 | 7.64 | 0.01 |
| 1126 | 13.91 | 3.90e+08 | 1.50e+07 | 24.85 | 7.64 | 0.01 |
| 1134 | 11.47 | 1.52e+08 | 0.00e+00 | 19.73 | 5.89 | 0.01 |
| 1141 | 12.27 | 1.50e+08 | 0.00e+00 | 55.98 | 5.34 | 0.01 |
| 1143 | 9.68 | 6.28e+07 | 0.00e+00 | 91.5 | 1.88 | 0.01 |
| 1154 | 17.42 | 5.49e+08 | 2.29e+05 | 56.7 | 7.64 | 0.01 |
| 1156 | 11.34 | 1.77e+08 | 0.00e+00 | 24.19 | 2.01 | 0.16 |
| 1157 | 10.35 | 1.28e+08 | 0.00e+00 | 58.95 | 7.64 | 0.01 |
| 1175 | 35.6 | 3.42e+09 | 1.03e+07 | 66.48 | 1.88 | 0.01 |
| 1179 | 10.97 | 2.35e+08 | 4.34e+06 | 25.68 | 7.64 | 0.01 |
| 1181 | 12.35 | 1.41e+08 | 0.00e+00 | 34.44 | 7.64 | 0.01 |
| 1189 | 10.03 | 2.13e+08 | 4.25e+06 | 33.71 | 7.64 | 0.01 |
| 771 | 9.21 | 9.15e+07 | 0.00e+00 | 31.86 | 6.66 | 0.06 |
| 1138 | 4.64 | 2.13e+07 | 0.00e+00 | 47.9 | 7.45 | 0.82 |
| 1156 | 11.34 | 1.77e+08 | 0.00e+00 | 24.19 | 2.01 | 0.16 |
| 1171 | 8.55 | 1.25e+07 | 0.00e+00 | 81.92 | 4.62 | 2.81 |
| 1173 | 10.39 | 8.66e+07 | 0.00e+00 | 121.72 | 4.03 | 0.06 |
| 1543 | 6.28 | 4.06e+07 | 0.00e+00 | 34.0 | 7.33 | 0.79 |
| 1544 | 3.56 | 1.57e+07 | 0.00e+00 | 48.37 | 6.13 | 4.18 |
| 1577 | 7.41 | 2.94e+07 | 0.00e+00 | 83.18 | 1.88 | 0.06 |
| 1616 | 2.68 | 2.37e+07 | 0.00e+00 | 36.46 | 7.48 | 0.01 |
| 1634 | 24.71 | 3.42e+09 | 2.43e+08 | 35.79 | 7.37 | 0.01 |
| 2073 | 2.22 | 1.92e+07 | 0.00e+00 | 38.93 | 4.22 | 2.37 |
| 2564 | 6.28 | 1.92e+07 | 0.00e+00 | 13.31 | 7.64 | 0.01 |
| 2592 | 5.38 | 1.20e+07 | 0.00e+00 | 41.84 | 5.56 | 3.2 |
| 2595 | 11.39 | 1.96e+08 | 0.00e+00 | 16.32 | 5.02 | 0.01 |
| 2633 | 10.68 | 1.14e+08 | 0.00e+00 | 64.59 | 7.64 | 0.85 |
| 844 | 4.64 | 2.13e+07 | 0.00e+00 | 47.91 | 7.45 | 0.85 |
| 902 | 3.78 | 1.67e+07 | 0.00e+00 | 31.24 | 7.39 | 0.01 |
| 2441 | 5.63 | 4.40e+07 | 0.00e+00 | 40.58 | 7.39 | 0.01 |

*Continue in the next page*

*Continuation of the previous page*

| **ID** | $R_{200}$ [kpc] | $M_{200}$ [$M_\odot$] | $M_*$ [$M_\odot$] | $d_{\min}$ [kpc] | $t_{\text{init}}$ [Gyr] | $t_{\text{fin}}$ [Gyr] |
|---|---|---|---|---|---|---|
| 2479 | 2.37 | 1.04e+08 | 0.00e+00 | 86.67 | 5.08 | 3.1 |
| 2502 | 3.09 | 2.03e+07 | 0.00e+00 | 26.28 | 7.64 | 1.93 |
| 1052 | 17.37 | 5.39e+08 | 0.00e+00 | 69.51 | 3.51 | 1.38 |
| 1065 | 14.49 | 3.32e+08 | 0.00e+00 | 18.56 | 3.3 | 1.4 |
| 1403 | 8.36 | 5.41e+07 | 0.00e+00 | 56.2 | 3.45 | 1.23 |
| 440 | 7.44 | 3.66e+07 | 0.00e+00 | 103.06 | 3.38 | 1.49 |
| 447 | 7.43 | 3.88e+07 | 0.00e+00 | 40.59 | 7.64 | 1.53 |
| 489 | 2.43 | 1.73e+07 | 0.00e+00 | 7.23 | 2.56 | 1.23 |
| 1713 | 5.63 | 4.40e+07 | 0.00e+00 | 39.63 | 7.39 | 0.01 |
| 1715 | 8.01 | 4.55e+07 | 0.00e+00 | 73.82 | 3.54 | 1.47 |
| 1719 | 13.19 | 2.17e+08 | 0.00e+00 | 87.73 | 3.79 | 1.8 |
| 1727 | 15.1 | 3.48e+08 | 0.00e+00 | 47.82 | 3.61 | 1.53 |
| 1744 | 4.64 | 2.13e+07 | 0.00e+00 | 47.75 | 7.45 | 0.82 |
| 1766 | 5.42 | 2.15e+07 | 0.00e+00 | 38.08 | 3.61 | 1.59 |
| 1789 | 8.54 | 6.98e+07 | 0.00e+00 | 69.0 | 4.62 | 0.06 |
| 1795 | 10.9 | 1.68e+07 | 0.00e+00 | 6.49 | 6.39 | 5.0 |
| 2249 | 5.4 | 1.83e+07 | 0.00e+00 | 81.79 | 4.95 | 1.8 |
| 2254 | 2.82 | 3.82e+08 | 0.00e+00 | 62.08 | 4.43 | 1.65 |
| 2263 | 19.64 | 6.00e+08 | 0.00e+00 | 152.05 | 3.12 | 1.53 |
| 2502 | 3.09 | 2.03e+07 | 0.00e+00 | 26.28 | 7.64 | 1.93 |
| 2731 | 4.89 | 1.22e+07 | 0.00e+00 | 59.0 | 3.9 | 1.74 |
| 2734 | 8.13 | 5.86e+09 | 5.85e+06 | 190.16 | 4.45 | 3.54 |
| 2771 | 9.68 | 8.71e+07 | 0.00e+00 | 55.05 | 3.66 | 1.53 |
| 2782 | 4.74 | 1.08e+07 | 0.00e+00 | 53.58 | 3.79 | 1.68 |
| 2788 | 17.84 | 6.13e+08 | 0.00e+00 | 84.51 | 4.22 | 1.77 |
| 2796 | 7.66 | 4.25e+07 | 0.00e+00 | 25.61 | 3.93 | 1.65 |
| 2797 | 7.66 | 4.25e+07 | 0.00e+00 | 25.71 | 3.93 | 1.74 |
| 1793 | 5.25 | 3.14e+07 | 0.00e+00 | 13.55 | 7.57 | 0.01 |
| 2058 | 7.24 | 3.82e+07 | 0.00e+00 | 92.05 | 3.93 | 2.31 |
| 2066 | 6.09 | 2.67e+07 | 0.00e+00 | 55.24 | 4.62 | 2.45 |
| 2350 | 6.67 | 5.18e+07 | 0.00e+00 | 13.67 | 7.15 | 0.01 |
| 2375 | 11.34 | 1.28e+08 | 0.00e+00 | 58.95 | 7.64 | 0.01 |
| 2382 | 20.05 | 8.49e+08 | 0.00e+00 | 92.35 | 4.62 | 2.88 |
| 2393 | 4.74 | 1.78e+07 | 0.00e+00 | 14.33 | 4.28 | 2.6 |
| 2416 | 3.91 | 3.05e+07 | 0.00e+00 | 28.43 | 5.63 | 3.74 |
| 61 | 5.36 | 2.37e+07 | 0.00e+00 | 13.47 | 7.64 | 2.94 |
| 325 | 2.52 | 1.44e+08 | 0.00e+00 | 110.48 | 5.99 | 4.62 |
| 350 | 6.67 | 3.90e+07 | 0.00e+00 | 54.27 | 4.89 | 2.43 |
| 351 | 6.85 | 3.26e+07 | 0.00e+00 | 42.38 | 3.99 | 1.93 |
| 356 | 7.64 | 5.55e+07 | 0.00e+00 | 67.5 | 4.25 | 2.37 |
| 372 | 4.54 | 1.54e+07 | 0.00e+00 | 26.34 | 7.64 | 2.01 |
| 404 | 4.42 | 1.22e+07 | 0.00e+00 | 43.18 | 4.45 | 2.6 |
| 429 | 20.98 | 1.03e+09 | 0.00e+00 | 62.58 | 4.62 | 2.94 |

*Continue in the next page*

*Continuation of the previous page*

| **ID** | $R_{200}$ [kpc] | $M_{200}$ [$M_\odot$] | $M_*$ [$M_\odot$] | $d_{\min}$ [kpc] | $t_{\text{init}}$ [Gyr] | $t_{\text{fin}}$ [Gyr] |
|---|---|---|---|---|---|---|
| 699 | 9.67 | 1.13e+08 | 0.00e+00 | 130.58 | 5.76 | 3.84 |
| 750 | 5.83 | 3.85e+07 | 0.00e+00 | 172.24 | 4.18 | 3.1 |
| 753 | 6.2 | 4.27e+07 | 0.00e+00 | 159.46 | 5.34 | 3.74 |
| 912 | 4.05 | 1.02e+07 | 0.00e+00 | 81.64 | 4.28 | 2.16 |
| 978 | 9.96 | 1.10e+08 | 0.00e+00 | 157.91 | 4.25 | 3.1 |
| 1171 | 8.55 | 1.25e+07 | 0.00e+00 | 81.92 | 4.62 | 2.81 |
| 1192 | 10.52 | 1.30e+08 | 0.00e+00 | 106.96 | 4.5 | 3.1 |
| 1195 | 17.11 | 5.53e+08 | 0.00e+00 | 107.34 | 4.58 | 3.1 |
| 1197 | 5.55 | 1.95e+07 | 0.00e+00 | 42.39 | 4.72 | 3.1 |
| 1198 | 4.73 | 1.18e+07 | 0.00e+00 | 46.02 | 4.62 | 3.03 |
| 1223 | 11.22 | 1.55e+08 | 0.00e+00 | 118.35 | 4.86 | 3.1 |
| 1294 | 14.57 | 7.33e+07 | 0.00e+00 | 34.0 | 4.81 | 2.65 |
| 1510 | 4.6 | 1.84e+07 | 0.00e+00 | 88.59 | 6.39 | 3.84 |
| 1740 | 4.26 | 1.14e+07 | 0.00e+00 | 32.8 | 5.17 | 3.1 |
| 2070 | 5.79 | 2.08e+07 | 0.00e+00 | 7.25 | 7.64 | 2.31 |
| 2073 | 2.22 | 1.92e+07 | 0.00e+00 | 38.93 | 4.22 | 2.37 |
| 2189 | 4.84 | 1.29e+07 | 0.00e+00 | 77.27 | 5.08 | 2.6 |
| 2191 | 5.72 | 2.47e+07 | 0.00e+00 | 70.79 | 5.56 | 3.1 |
| 2259 | 16.24 | 5.95e+08 | 0.00e+00 | 130.62 | 5.15 | 3.45 |
| 2348 | 4.42 | 1.42e+07 | 0.00e+00 | 62.41 | 7.45 | 1.32 |
| 2357 | 4.11 | 1.05e+07 | 0.00e+00 | 199.45 | 4.25 | 3.35 |
| 2427 | 7.51 | 5.15e+07 | 0.00e+00 | 53.82 | 5.38 | 0.01 |
| 2479 | 2.37 | 1.04e+08 | 0.00e+00 | 86.67 | 5.08 | 3.1 |
| 423 | 6.3 | 2.81e+07 | 0.00e+00 | 137.84 | 4.25 | 2.56 |
| 2522 | 16.3 | 6.01e+08 | 0.00e+00 | 35.81 | 5.47 | 3.35 |
| 2592 | 5.38 | 1.20e+07 | 0.00e+00 | 41.84 | 5.56 | 3.2 |
| 2618 | 7.19 | 4.30e+07 | 0.00e+00 | 105.31 | 6.3 | 0.01 |
| 2830 | 7.22 | 5.28e+07 | 0.00e+00 | 28.13 | 5.17 | 3.1 |
| 2850 | 6.85 | 5.39e+07 | 0.00e+00 | 18.46 | 4.81 | 3.1 |
| 2851 | 8.36 | 7.33e+07 | 0.00e+00 | 33.96 | 4.81 | 3.1 |
| 2883 | 4.83 | 1.40e+07 | 0.00e+00 | 36.8 | 4.58 | 3.1 |
| 325 | 2.52 | 1.44e+08 | 0.00e+00 | 110.48 | 5.99 | 4.62 |
| 331 | 17.11 | 5.53e+08 | 0.00e+00 | 107.29 | 4.62 | 2.65 |
| 494 | 2.6 | 2.08e+07 | 0.00e+00 | 150.8 | 5.63 | 4.28 |
| 563 | 4.62 | 1.13e+07 | 0.00e+00 | 82.29 | 4.62 | 2.65 |
| 769 | 5.14 | 1.91e+07 | 0.00e+00 | 52.52 | 5.5 | 3.38 |
| 2095 | 2.24 | 4.11e+07 | 0.00e+00 | 134.58 | 5.76 | 4.09 |
| 2414 | 6.38 | 4.14e+07 | 0.00e+00 | 36.69 | 5.34 | 3.42 |
| 2416 | 3.91 | 3.05e+07 | 0.00e+00 | 28.43 | 5.63 | 3.74 |
| 2420 | 7.58 | 5.34e+07 | 0.00e+00 | 68.23 | 5.02 | 2.65 |
| 2447 | 7.13 | 4.82e+07 | 0.00e+00 | 14.69 | 5.02 | 2.65 |
| 2503 | 10.26 | 1.78e+08 | 0.00e+00 | 41.47 | 6.32 | 0.01 |
| 2682 | 6.58 | 3.52e+07 | 0.00e+00 | 17.47 | 4.86 | 2.65 |

*Continue in the next page*

*Continuation of the previous page*

| **ID** | $R_{200}$ [kpc] | $M_{200}$ [$M_\odot$] | $M_*$ [$M_\odot$] | $d_{\min}$ [kpc] | $t_{\text{init}}$ [Gyr] | $t_{\text{fin}}$ [Gyr] |
|---|---|---|---|---|---|---|
| 2683 | 5.03 | 1.54e+07 | 0.00e+00 | 16.63 | 4.85 | 2.65 |
| 2693 | 7.68 | 5.20e+07 | 0.00e+00 | 18.58 | 4.81 | 2.65 |
| 2737 | 25.61 | 2.36e+09 | 0.00e+00 | 164.16 | 5.4 | 4.33 |
| 2800 | 7.69 | 6.69e+07 | 0.00e+00 | 193.14 | 4.45 | 3.9 |
| 2805 | 4.84 | 1.50e+07 | 0.00e+00 | 77.21 | 5.08 | 2.6 |
| 2814 | 7.36 | 4.86e+07 | 0.00e+00 | 83.84 | 6.17 | 4.17 |
| 2820 | 6.62 | 3.59e+07 | 0.00e+00 | 175.06 | 4.38 | 2.65 |
| 2958 | 7.3 | 6.96e+07 | 0.00e+00 | 41.16 | 5.56 | 3.3 |
| 2963 | 4.35 | 1.03e+07 | 0.00e+00 | 21.28 | 7.64 | 0.01 |
| 2967 | 7.21 | 6.41e+07 | 0.00e+00 | 39.88 | 5.15 | 3.58 |
| 2985 | 5.67 | 3.85e+07 | 0.00e+00 | 29.0 | 5.53 | 2.65 |
| 1294 | 14.57 | 7.33e+07 | 0.00e+00 | 34.0 | 4.81 | 2.65 |
| 1369 | 5.81 | 2.31e+07 | 0.00e+00 | 14.03 | 4.38 | 2.65 |
| 1567 | 3.95 | 1.07e+07 | 0.00e+00 | 32.54 | 4.89 | 3.31 |
| 1609 | 4.59 | 1.41e+07 | 0.00e+00 | 65.75 | 5.89 | 0.01 |
| 1616 | 2.68 | 2.37e+07 | 0.00e+00 | 36.46 | 7.48 | 0.01 |
| 1624 | 4.58 | 1.50e+07 | 0.00e+00 | 66.07 | 5.43 | 3.1 |
| 319 | 11.5 | 1.70e+08 | 0.00e+00 | 90.52 | 4.86 | 1.96 |
| 325 | 2.52 | 1.44e+08 | 0.00e+00 | 110.48 | 5.99 | 4.62 |
| 598 | 9.36 | 1.15e+08 | 0.00e+00 | 93.19 | 5.69 | 3.64 |
| 18 | 12.98 | 2.09e+08 | 0.00e+00 | 49.98 | 6.9 | 0.01 |
| 20 | 12.18 | 1.92e+08 | 0.00e+00 | 82.67 | 6.61 | 4.28 |
| 242 | 23.71 | 1.14e+09 | 4.78e+06 | 69.49 | 6.66 | 0.01 |
| 2512 | 12.38 | 4.48e+08 | 0.00e+00 | 19.19 | 5.89 | 0.01 |
| 508 | 5.83 | 3.52e+07 | 0.00e+00 | 56.5 | 6.03 | 3.99 |
| 772 | 12.65 | 4.59e+08 | 0.00e+00 | 39.22 | 6.9 | 5.67 |
| 821 | 4.9 | 1.94e+07 | 0.00e+00 | 49.63 | 6.39 | 4.85 |
| 1080 | 6.07 | 6.16e+07 | 0.00e+00 | 40.55 | 6.82 | 5.67 |
| 1088 | 4.33 | 1.93e+07 | 0.00e+00 | 95.06 | 6.54 | 5.08 |
| 1106 | 12.26 | 4.19e+08 | 0.00e+00 | 42.85 | 7.2 | 5.81 |
| 1125 | 13.91 | 1.41e+08 | 0.00e+00 | 34.45 | 7.64 | 0.01 |
| 1436 | 6.11 | 3.90e+07 | 0.00e+00 | 12.97 | 6.3 | 4.89 |
| 62 | 12.31 | 1.28e+08 | 0.00e+00 | 58.99 | 7.64 | 0.01 |
| 338 | 7.44 | 8.63e+07 | 0.00e+00 | 72.83 | 6.9 | 5.47 |
| 346 | 9.41 | 1.70e+08 | 0.00e+00 | 56.72 | 6.66 | 5.1 |
| 1504 | 9.86 | 1.56e+08 | 0.00e+00 | 7.93 | 6.1 | 4.43 |
| 1506 | 5.9 | 3.57e+07 | 0.00e+00 | 112.34 | 6.03 | 4.62 |
| 1544 | 3.56 | 1.57e+07 | 0.00e+00 | 48.37 | 6.13 | 4.18 |
| 1593 | 5.44 | 2.71e+07 | 0.00e+00 | 123.39 | 6.03 | 4.81 |
| 1784 | 7.41 | 7.31e+07 | 0.00e+00 | 63.07 | 6.46 | 5.21 |
| 1795 | 10.9 | 1.68e+07 | 0.00e+00 | 6.49 | 6.39 | 5.0 |
| 1798 | 3.86 | 1.01e+07 | 0.00e+00 | 12.08 | 6.46 | 5.08 |
| 1811 | 5.76 | 3.43e+07 | 0.00e+00 | 8.09 | 6.54 | 0.01 |

*Continue in the next page*

*Continuation of the previous page*

| **ID** | $R_{200}$ [kpc] | $M_{200}$ [$M_\odot$] | $M_*$ [$M_\odot$] | $d_{\min}$ [kpc] | $t_{\text{init}}$ [Gyr] | $t_{\text{fin}}$ [Gyr] |
|---|---|---|---|---|---|---|
| 1819 | 5.02 | 2.55e+07 | 0.00e+00 | 15.77 | 7.64 | 0.01 |
| 1839 | 5.7 | 4.78e+07 | 0.00e+00 | 90.23 | 6.66 | 5.3 |
| 1847 | 11.25 | 2.11e+08 | 0.00e+00 | 23.1 | 7.53 | 0.01 |
| 2011 | 7.69 | 7.72e+07 | 0.00e+00 | 84.86 | 6.49 | 5.08 |
| 2014 | 18.98 | 1.16e+09 | 0.00e+00 | 76.46 | 6.42 | 5.02 |
| 2018 | 3.62 | 1.37e+07 | 0.00e+00 | 44.01 | 6.49 | 4.95 |
| 2019 | 8.27 | 1.21e+08 | 0.00e+00 | 41.83 | 6.54 | 4.86 |
| 2027 | 3.94 | 1.31e+07 | 0.00e+00 | 54.59 | 6.9 | 5.43 |
| 2031 | 7.66 | 2.93e+07 | 0.00e+00 | 83.97 | 6.49 | 4.95 |
| 2059 | 4.03 | 1.22e+07 | 0.00e+00 | 82.69 | 6.82 | 4.95 |
| 2504 | 7.47 | 6.81e+07 | 0.00e+00 | 64.58 | 6.03 | 4.72 |
| 2520 | 8.84 | 5.58e+07 | 0.00e+00 | 59.63 | 7.64 | 0.01 |
| 2939 | 3.9 | 1.31e+07 | 0.00e+00 | 43.77 | 6.57 | 4.95 |

TABLE B.1: Complete satellite characteristics. R200, M200, stellar mass, minimum distance reached, and moment where they enter virial radius.

APPENDIX C

# Phase spirals in other cosmological models

## C.1 Phase spirals in GARROTXA RAMSES

In this section, we make a first analysis of the phase space in the GARROTXA RAMSES model. This set of simulations uses the same initial conditions as the original run that used the ART code, but with the RAMSES code (Teyssier, 2002). In particular, we look at another Milky Way-sized galaxy using RAMSES code, with a $M_{200} \sim 0.8 \times 10^{12}\ M_{\odot}$. This model reaches $z \sim 0.3$, equivalent to a lookback time of 3 Gyr, with $10^8$ stellar particles (higher than the ART model studied) inside the $R_{vir} = 180$ kpc. We take this last snapshot to explore the phase space of stars younger than 2 Gyr of age ($3.8 \times 10^6$ particles).

In Figs. C.1 and C.2 we show the phase spiral present in GARROTXA RAMSES colored by $V_\phi$ and $V_R$ respectively. In general, we can see the spiral pattern along the different panels, across azimuths and radius. They are more notable when colored by $V_\phi$ than $V_R$, and the resolution allows to see more details of the spiral than in the ART version of the simulation. Although both versions start with the same initial conditions, there might be time discrepancies due to the different refinement criteria and tuning of baryonic physics. Thus, the phase spiral shown here might not be triggered in the exact same conditions or timing as in Chapter 3. We cannot pinpoint the origin of the phase spiral without a thourough exploration, which will be made in future work. From this preliminary analysis we highlight the presence of the phase spiral in this RAMSES model. This supports the discussion held in Chapter 6, where we regard the phase spiral as a common phenomena found in disk galaxies.

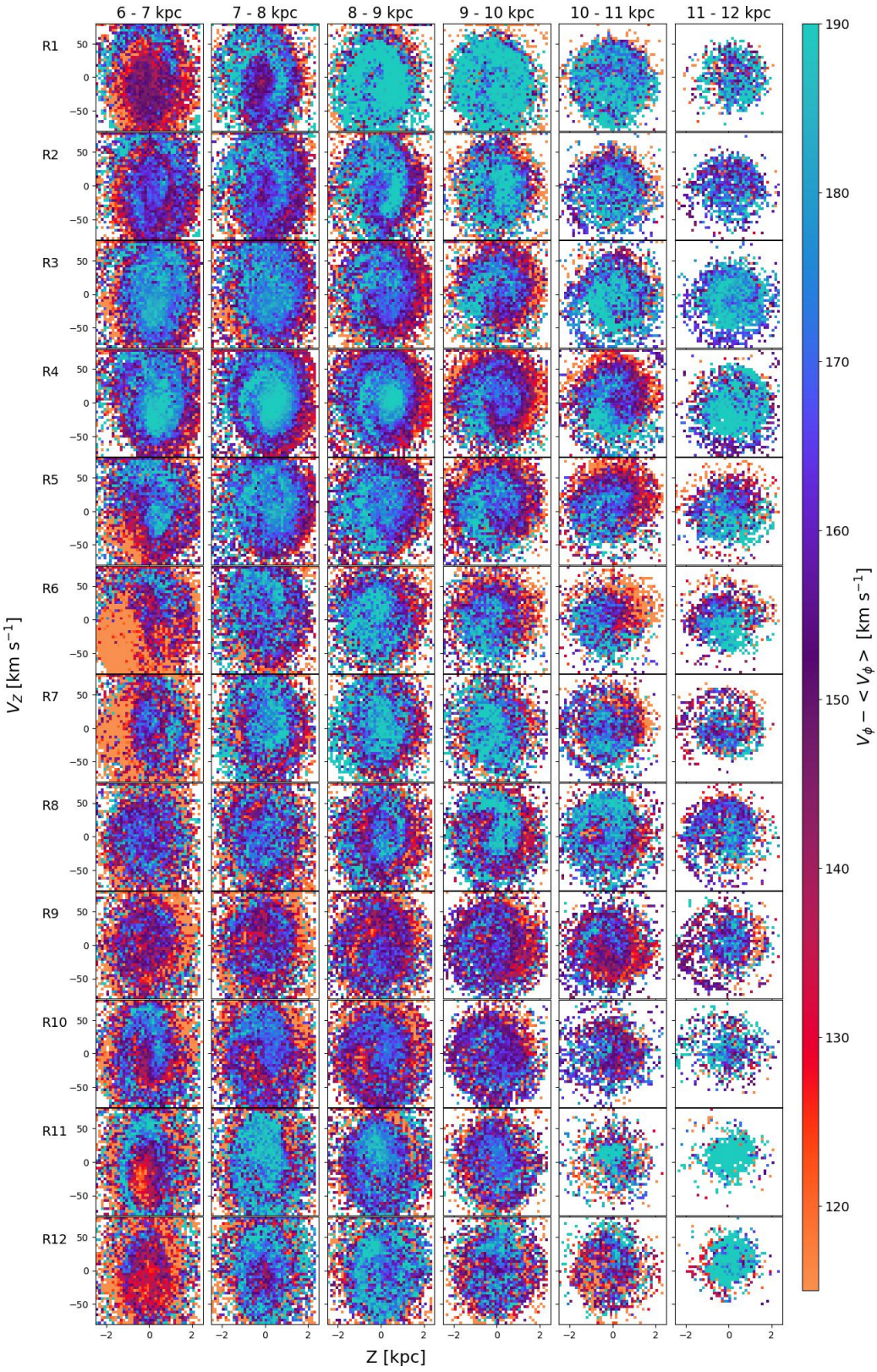


FIGURE C.1: Phase spirals colored by $V_\phi$ of the model GARROTXA RAMSES along radius (from 6 kpc on the left to 12 kpc on the right) and azimuths (from 0° on the top panels to 330° on the bottom panels).

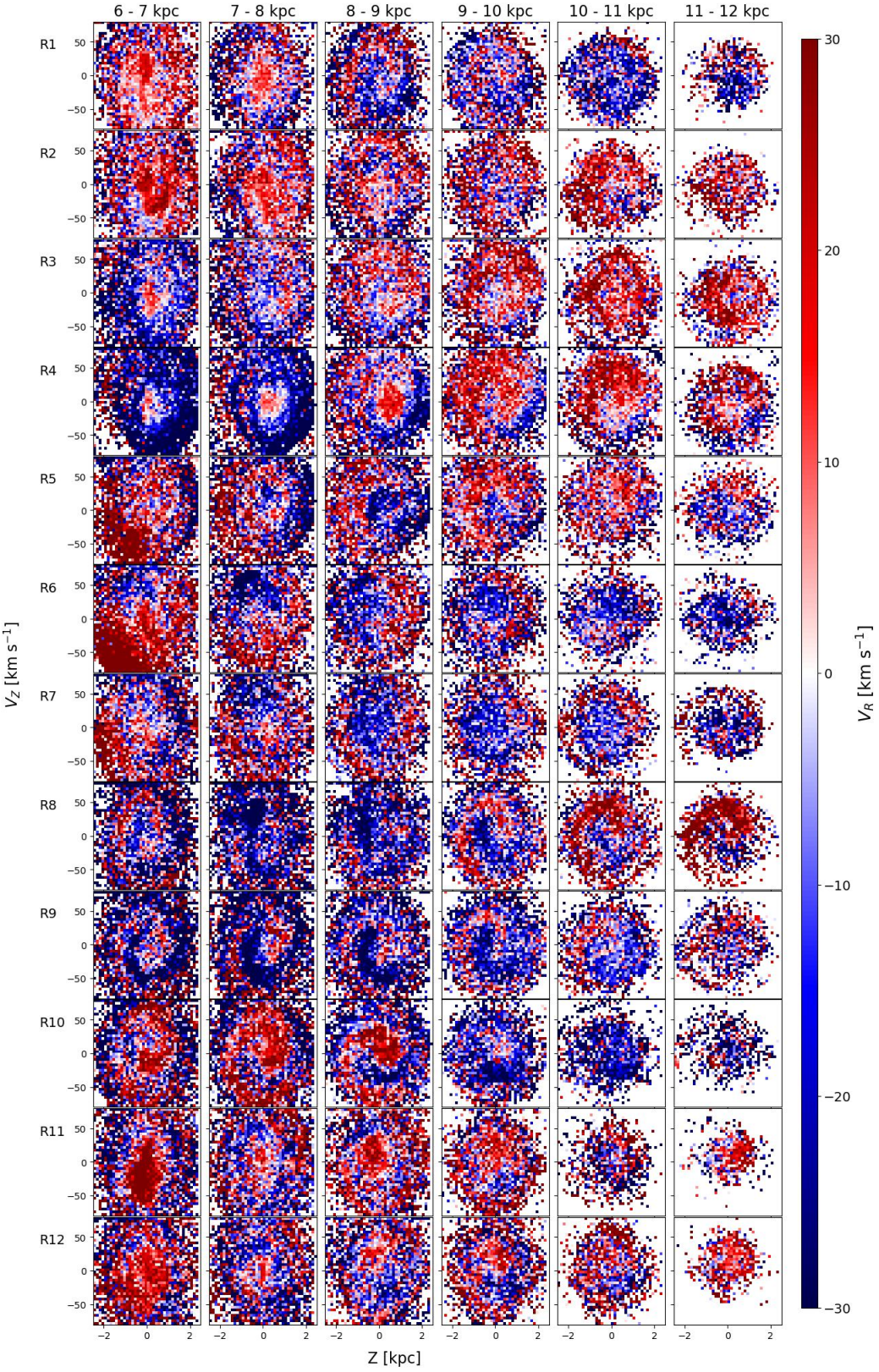


FIGURE C.2: Similar to Fig C.1 but colored by $V_R$

APPENDIX D

# Density and breathing

In this section, we apply the same Fourier-based algorithms described throughout this thesis to study the density structures of the disk. In this case, the weights in Eq. 2.4 are the mass of each stellar particle. In Fig. D.1 we show the Fourier decomposition. In this figure, in the $m = 1$ case, we observe a retrograde, one-armed spiral described in Chapter 2. The phase of $m = 1$ (bottom left panel) becomes more coherent from 4 Gyr on, and its amplitude (top left panel) appears to be higher at radii $> 7$ kpc.

This density mode has an unclear origin. At external radii, this mode seems to be present since the beginning of our study, although its amplitude seems to be higher at certain times. At radii where this amplitude is lower, the phase also becomes less defined and noisier. However, we do not see a clear link between this density mode and other phenomena such as the passing of satellites, since its amplitude's increases and decreases are not abrupt. We hypothesize that because this structure is so noticeable across all the timespan studied, it is probably not set off by a single interaction. It seems that the characteristics of the galactic system's density leads to the formation of this structure.

In regard to the second Fourier mode (right panels), we see a difference between the inner and outer parts. The amplitude of the inner parts ($<$4 kpc) is dominated by the central oval (also seen in Fig. 4.1 of Chapter 4), and from 4 to 7 kpc periodic bisymmetric arms dominate. The intermediate and outer parts have at times an increased amplitude of this second mode, which could be related to spiral arms. In general, this mode propagates in the direction and with the periodicity of the rotation.

In regards to the breathing modes in Fig. D.2, we observe that the amplitude is dominated by the Fourier mode $m = 2$, which stays approximately constant between 0 and 7 kpc of radius and grows at certain times in the intermediate and outer regions of the disk. Its phase shows a small oscillation over time, but overall this angle coincides with the position of the disk's central oval, described in Chapter. 2. Previous studies have also linked this breathing behaviour to the bar (Widrow et al., 2014; Faure, Siebert, and Famaey, 2014; Monari, Famaey, and Siebert, 2015; Carrillo et al., 2018) Although weaker and noisier, the breathing mode $m = 1$ becomes more noticeable (top left panel) and with a more clearly defined phase (bottom panel) in the period of 2 to 0 Gyr. In the studies of Widrow et al. (2014), Carrillo et al. (2018), and Hunt et al. (2021) and Kumar et al. (2022), they link the apparition of breathing modes in the disk with fast interaction with satellites. However, at these times, we do not have a fast (in terms of $V_Z$) crossing, but instead, the satellite Escarabajo has a slow interaction and reaches its pericentre at higher $Z$. Thus, the increase in breathing mode as a direct consequence of the interaction with Escarabajo is improbable.

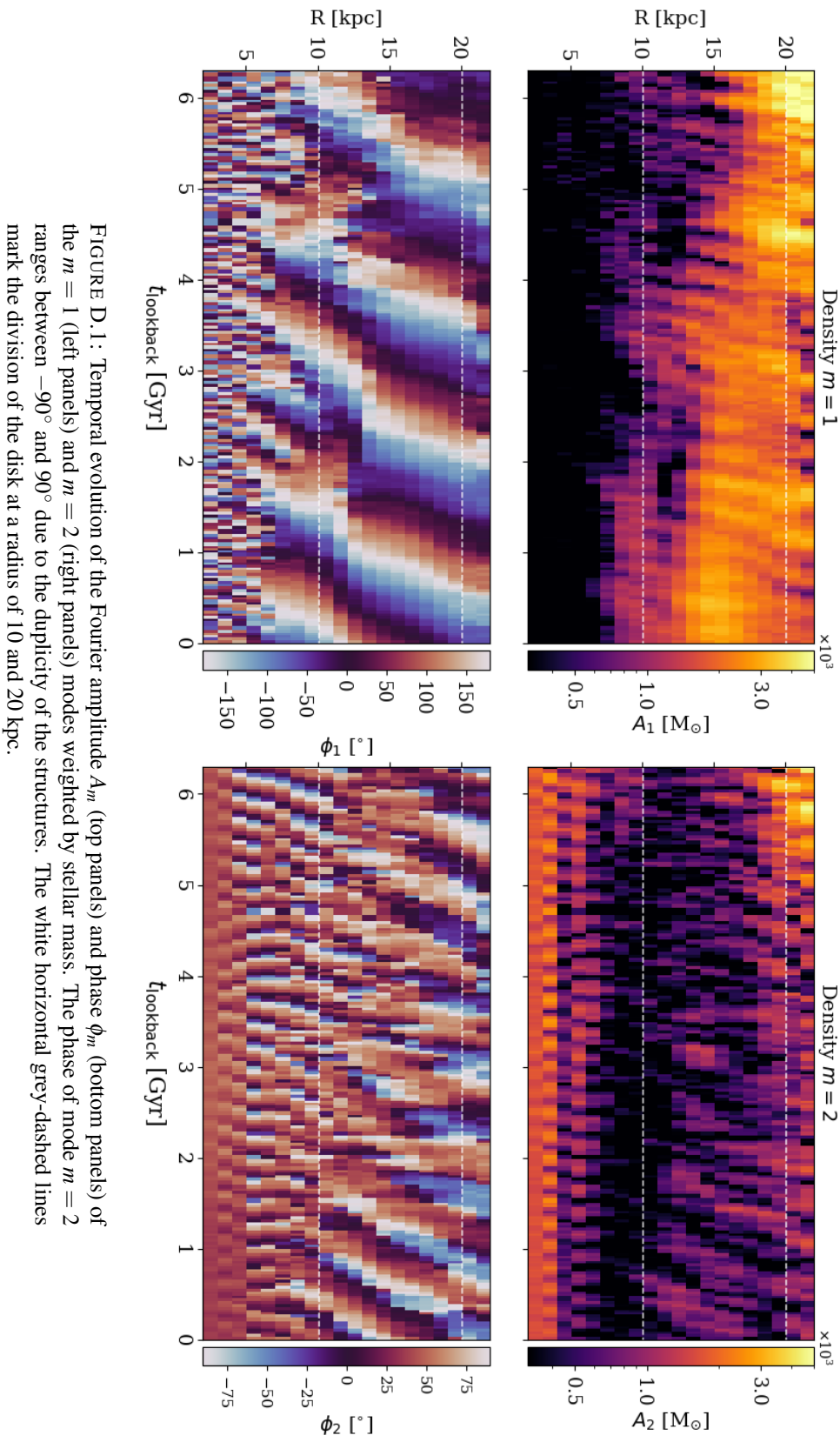


FIGURE D.1: Temporal evolution of the Fourier amplitude $A_m$ (top panels) and phase $\phi_m$ (bottom panels) of the $m = 1$ (left panels) and $m = 2$ (right panels) modes weighted by stellar mass. The phase of mode $m = 2$ ranges between $-90°$ and $90°$ due to the duplicity of the structures. The white horizontal grey-dashed lines mark the division of the disk at a radius of 10 and 20 kpc.

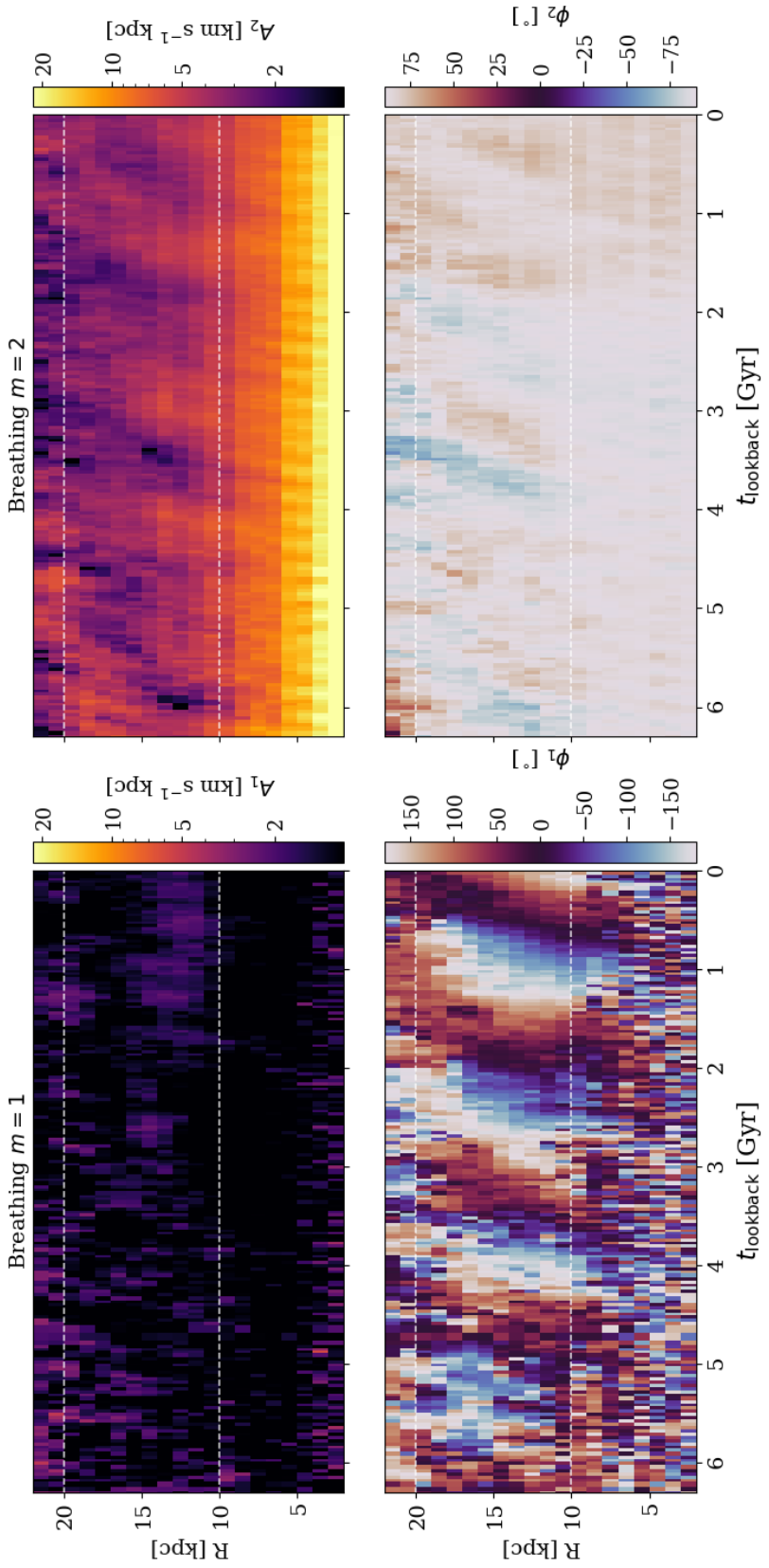


FIGURE D.2: Similar to Fig. 4.2 but for the breathing.

APPENDIX E

# Correlations

In this work, we have calculated the accelerations of the dark matter particles and gas, which we have characterized in different regions using the Fourier mode $m = 1$, which is dominant in both cases at most times. We have used the mean amplitude of said mode in regions from 0 to 10 kpc and 10 to 20 kpc. The same has been made with the variables tracing the vertical behavior of the disk, namely bending, breathing, and density modes. In this case, however, we also considered Fourier modes $m = 2$ for bending, breathing, and density.

To begin to understand the relationships between all these variables at all times we define a moving window of 800 Myr of width, moving along lookback time. At each snapshot, we define a window spanning from the previous 400 Myr to 400 Myr later. These windows have an average of 23 snapshots. We calculate the Pearson's correlation coefficient $r$ and its p-value at each window for different pairs of the variables. Since the pairs of variables are numerous, we present the results in three different figures. In Figs. E.1, E.2, and E.3 we present the correlation coefficient (lines), and the most notable correlations (where $|r| > 0.4$ and p-value $< 0.05$ circles).

We observe that the first gigayear of the studied period presents high correlations between all variables due to the highly perturbed state of the galaxy and the subsequent relaxation over the next gigayear. We have a special interest in the correlations with the bending $m = 1$ at external radius starting at 2 Gyr, since it is the higher bending mode we find over time and radius. In the bottom panel of Fig. E.1, we find a high correlation between this bending mode and the mode $m = 1$ of $a_Z$ applied by dark matter. We also find breathing modes being excited at these times, which also correlate with the acceleration by dark matter.

At more internal radii between 0 and 10 kpc (top panel of Fig. E.2, light blue and orange dots, respectively) from 2.2 Gyr until 1.6 Gyr the density mode $m = 1$ correlates with the acceleration by dark matter and gas. At this same radius, there is also a correlation between the density mode $m = 2$ and the breathing mode $m = 2$ (dark green dots) in the top panel of Fig. E.3.

At external radii (bottom panel of said figure) there is not a clear tendency. What we do observe is a correlation between the density mode $m = 2$ and the breathing mode $m = 2$ (dark green dots) in the top panel of Fig. E.3, as well as between the modes $m = 1$ of density and bending (light blue dots), which are also seen between 10 and 20 kpc. In this same figure, we observe a high correlation between the modes $m = 1$ of density and bending (light blue dots), seen in both of the regions shown.

These figures serve as a visual aid to identify in which moments different variables increase or decrease in relation to each other, and, combined with Fig. 4.8, can help to better understand the causes and effects at play at the different time intervals discussed in Sec. 4.4. We can extract general behaviours between

the variables. However, due to the small number of snapshots per window (average of 23 snapshots), we cannot extract a definite quantification of the correlations between the variables studied.

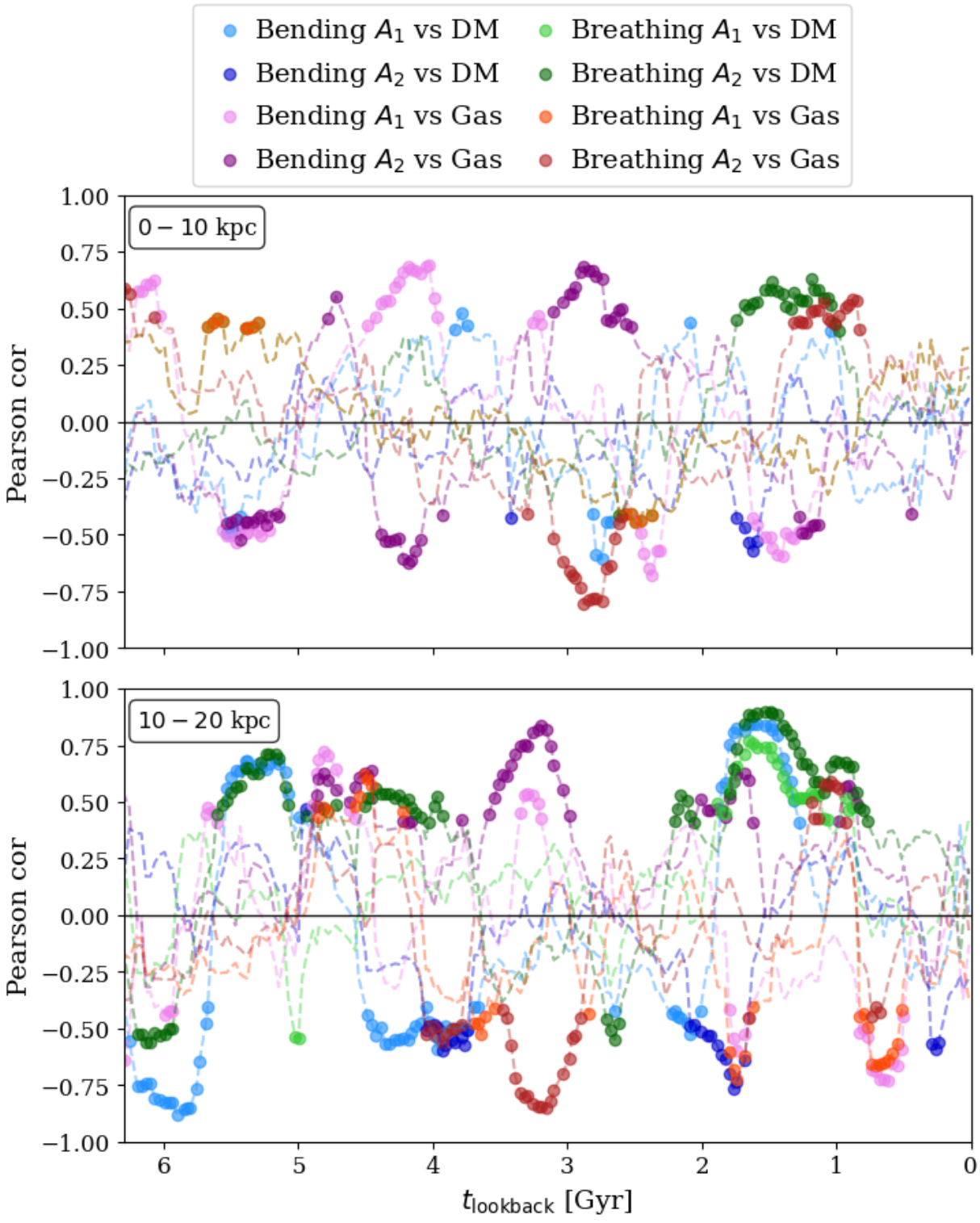


FIGURE E.1: Pearson's correlation coefficient in moving windows of 800 Myr of width for bending and breathing modes vs accelerations of gas and dark matter. We mark as circles the moments where Pearson's coefficient fulfils $|r| > 0.4$ and $p - value < 0.05$

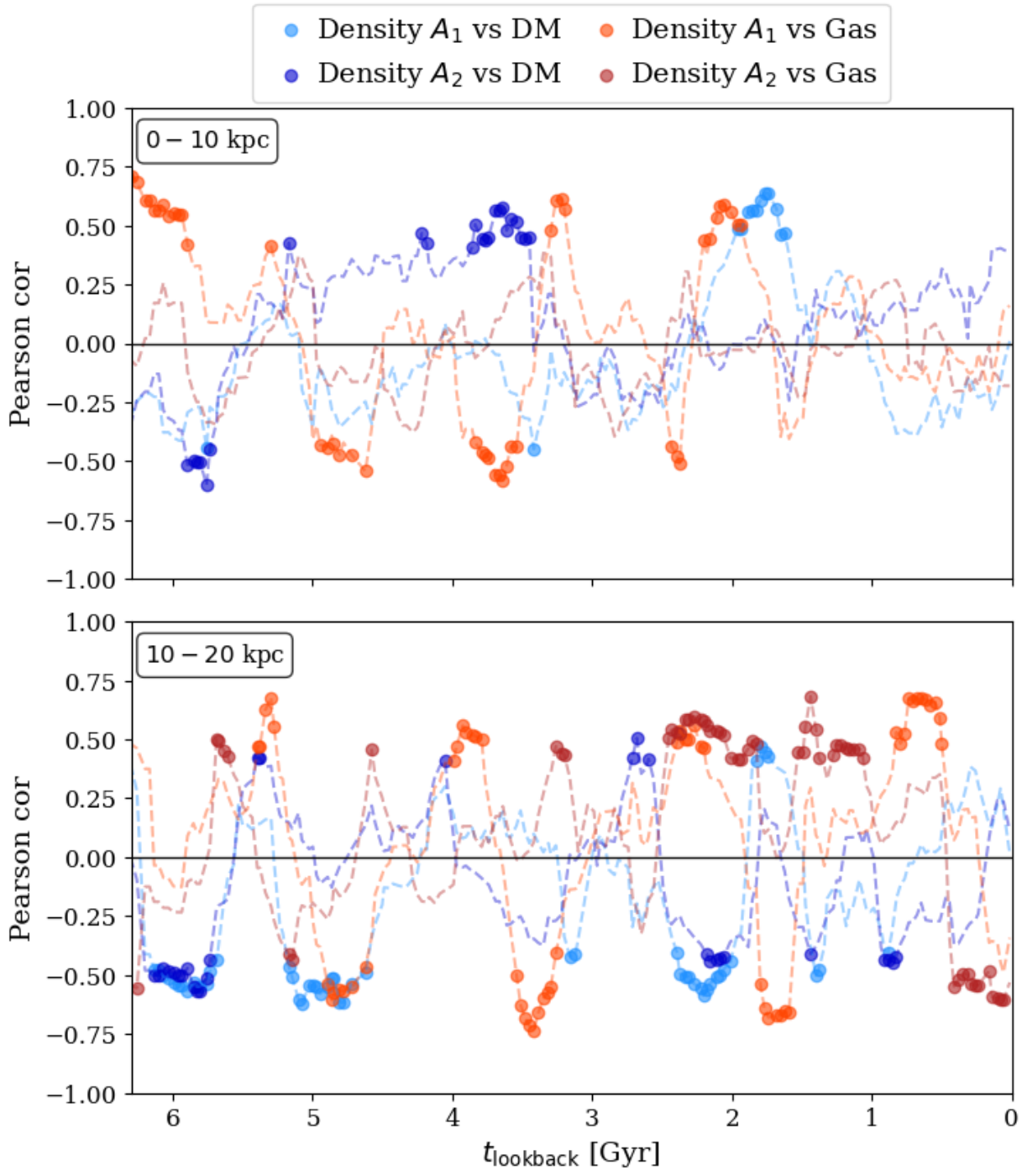


FIGURE E.2: Same as Fig E.1 but with variables of density vs gas and dark matter acceleration's $m = 1$.

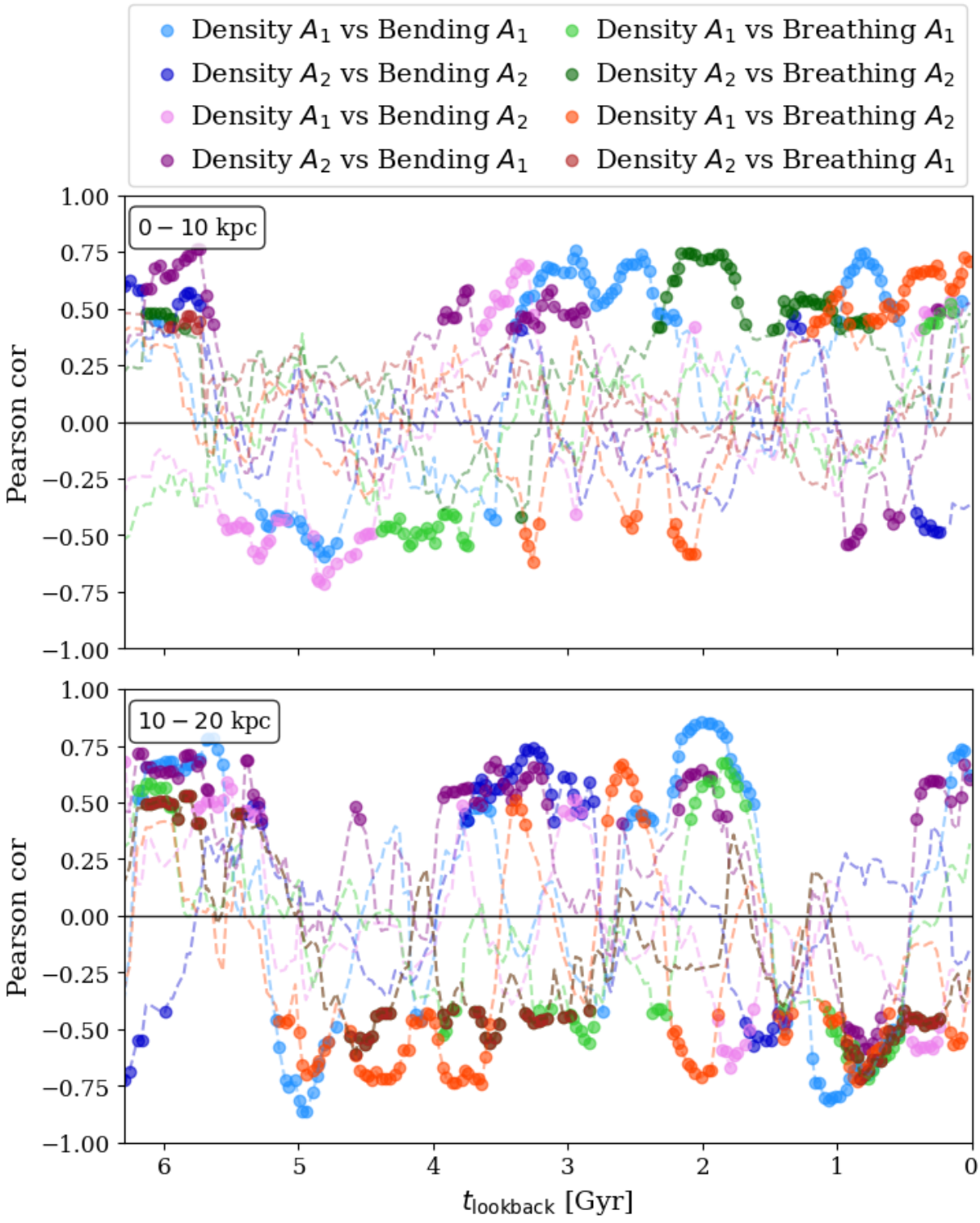


FIGURE E.3: Same as Fig E.1 but with variables of density vs bending and breathing modes.

APPENDIX F

# Bending populations

In this appendix, we show preliminary results from the study of bending modes across different age populations. In Fig. F.1 we show the vertical velocity $V_Z$ in four stellar populations from 0 to 8 Gyr in intervals of 2 Gyr, from left (younger) to right (older).

We observe that the bending maps show different patterns. From 4 Gyr to 8 Gyr, the bending pattern appears to be a well defined warp present at external radii, whose origin was discussed in Chapter 4. We observe that the younger particles show different bending modes. This shows that particles of different populations are being perturbed differently, even if they are perturbed by the same conditions.Younger stellar particles have different dynamical properties than the older counterparts. These particles colder orbits, with velocities closer to circular velocity and contained in the disk, are more prone to be perturbed from their orbits.

In Chapter 3, we showed how the phase spiral changed with different stellar particles of different ages. These differences, along with the study of the bending pattern of each stellar age group is worth exploring in future work.

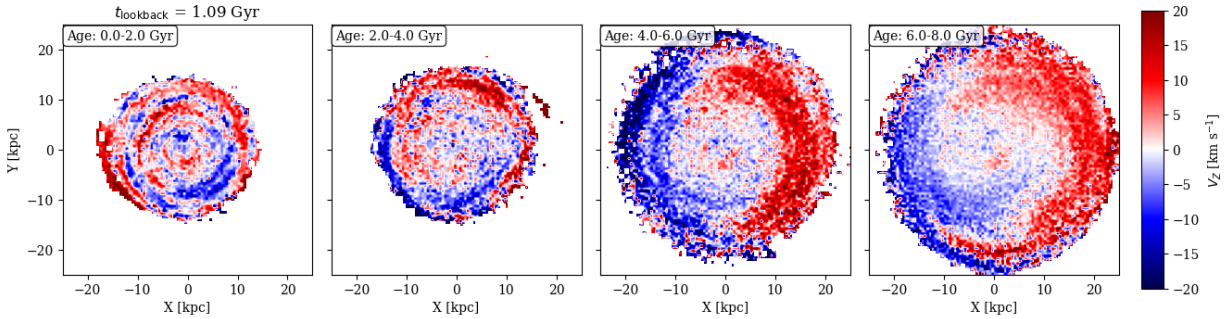


FIGURE F.1: Different age populations colored by $V_Z$ (bending modes), from younger particles (left) to older ones (right).

APPENDIX G

# Arania's streams

In this Appendix, we explore the force generated by the streams of Arania satellite. This satellite is the most massive one at the moment of entering the virial radius of the host (at $z \sim 1.5$), generating streams along its orbit.

To determine the particles which belong to the streams, we took the particles inside the tidal radius before its first interaction and track them over time. As explained in Chapter 2, we calculated the tidal radius for each apocenter for some of the satellites of the galaxy, including Arania. We consider particles inside $5 \times R_{tidal}$ to belong to the progenitor, and the rest of particles to belong to the stream. In Fig. G.1 we show the position of the streams (top panel) and the vertical acceleration applied onto the disk by the progenitor (bottom left panel) and the streams (bottom right panel).

In general, we observe that the streams do not apply a significant acceleration, which is of the order of $\sim 0.5$ km s$^{-1}$ Myr$^{-1}$ compared to $\sim 10$ km s$^{-1}$ Myr$^{-1}$ of some satellites at pericenter (Chapter 4). The acceleration of the stream can be comparable/larger to that of the progenitor only at apocenter but it is small nevertheless. For example, in Fig. G.1 we see comparable accelerations (left and right) but these do no correspond to pericenter but to 0.5 Gyr afterwards. However, we cannot discard that more massive satellites in other models leave enough debris to apply a significant force onto the disk and thus, this is worth exploring in other models with heavier interacting satellites and streams, as in the case of the LMC, whose debris' impact is explored in Garavito-Camargo et al. 2021.

The streams are common objects in galaxies which have had interactions. The accurate quantification of the mass of said streams may be significant to determine to what extent they are interacting gravitationally with a galactic disk. However, observationally, they would appear as diffuse, low luminosity objects in the sky. Space missions like ARRAKIHS will be able to observe and characterize the streams in distant galaxies.

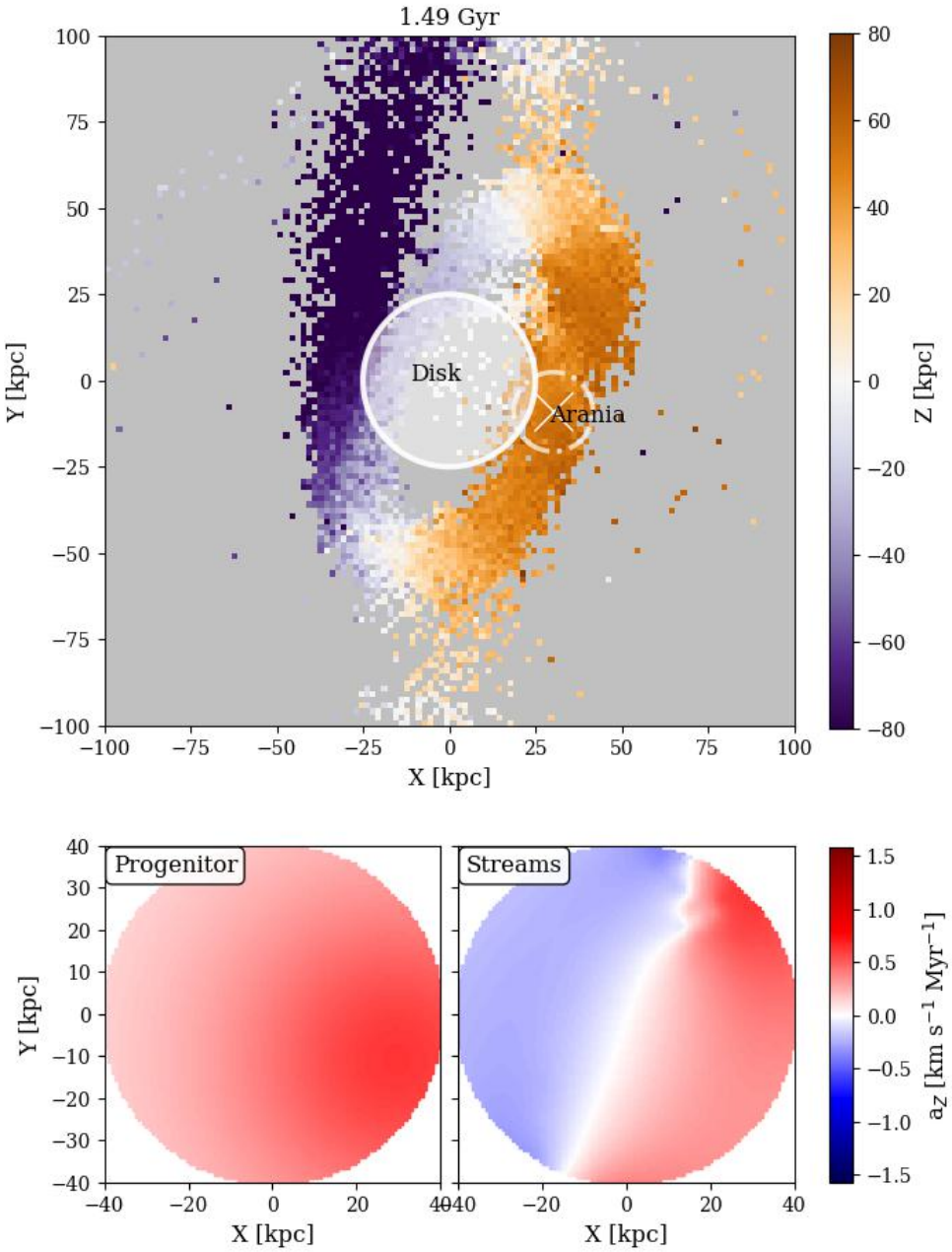


FIGURE G.1: **Top panel**: Vertical position of the streams at lookback time of 1.49 Gyr, where the satellite is situated at a galactocentric distance of 63.5 kpc (∼0.5 Gyr after its pericenter at a distance of ∼38 kpc). **Bottom left panel**: Vertical acceleration by the particles inside $5 \times R_{tidal}$ which we consider to belong to the progenitor. **Bottom left panel**: Vertical acceleration by the particles outside of $5 \times R_{tidal}$, which we consider to belong to the streams.

APPENDIX H

# Complete Fourierograms

In this Appendix, we take the same approach as in Chapter 4 and compute the complete Fourier decomposition of the different components of the phase space of the disk until Fourier mode $m = 4$ for the sake of completeness. The alignment and radial binning is the same as in Chapter 4 and Appendix D.

Throughout this thesis we have discussed the vertical behavior of the disk. We have calculated the bending modes via $Z$ (Fig. H.2) and $V_Z$ (Fig. H.3). We can observe that, generally, the first Fourier mode dominates over higher modes.

We also have established a relation with the main density structures (Fig. H.1), which are further discussed in Appendix D. We observe that higher modes are more notable in the external parts of the disk.

We also show $V_R$ (Fig. H.5) and $V_\phi$ (Fig. H.4) with similar diagrams. We observe that $V_{phi}$ is highly similar to the Fig. H.1, and thus, that it reflects the behavior of the density structures present on the disk. We observe that mode $m = 1$ of $V_R$ to follow the one armed density spiral, and the inner $m = 2$ mode corresponds to the cuadrupole made by the inner oval at the center of the disk. Thus, the planar dimension seems to be highly bound to the structures of the disks, as expected.

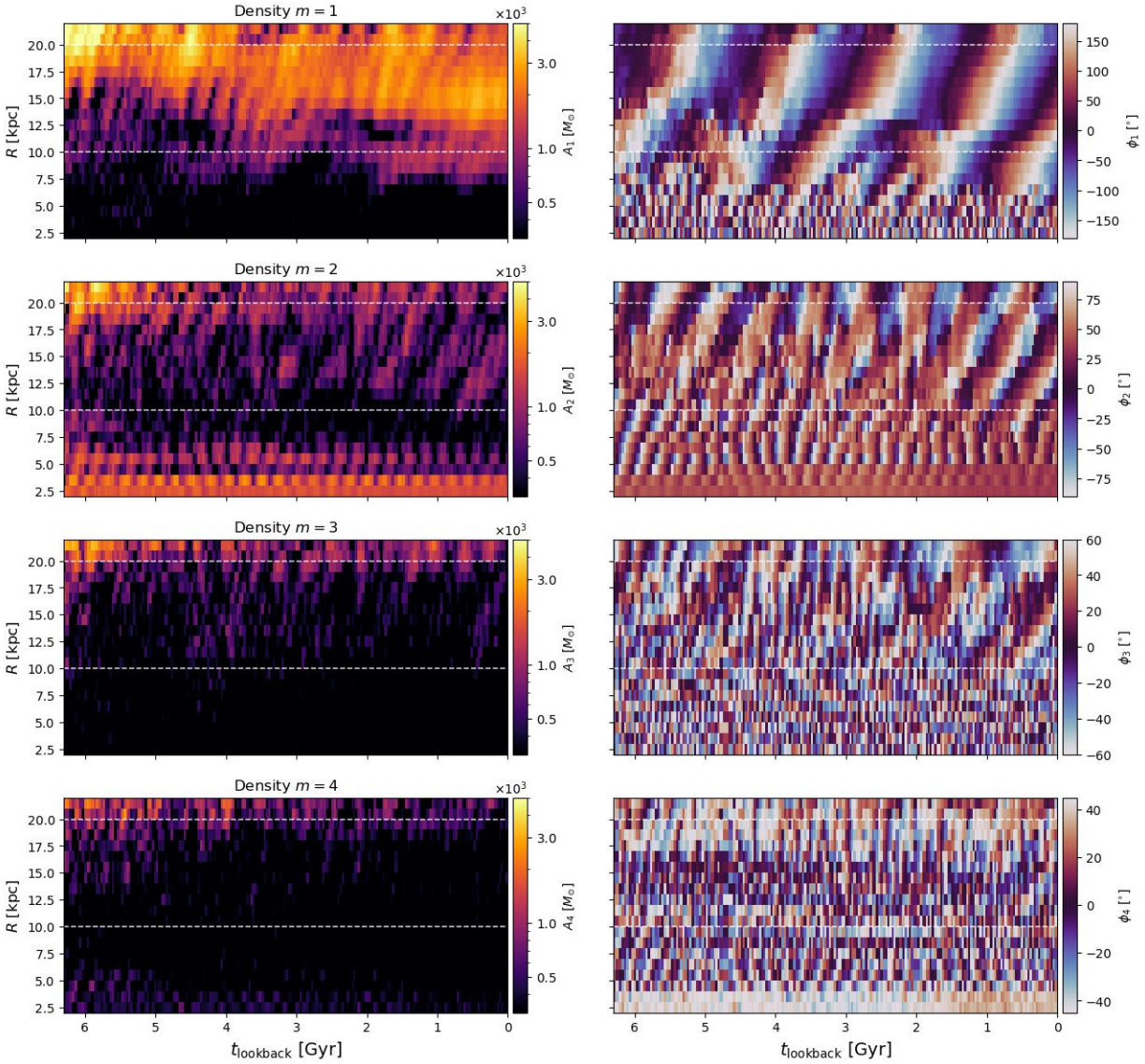


FIGURE H.1: Fourier modes of density from mode $m = 1$ (top) to $m = 4$ (bottom) with the corresponding amplitude (left panels) and phase (right panels), similar to Fig. D.1, with radial bins of 1 kpc.

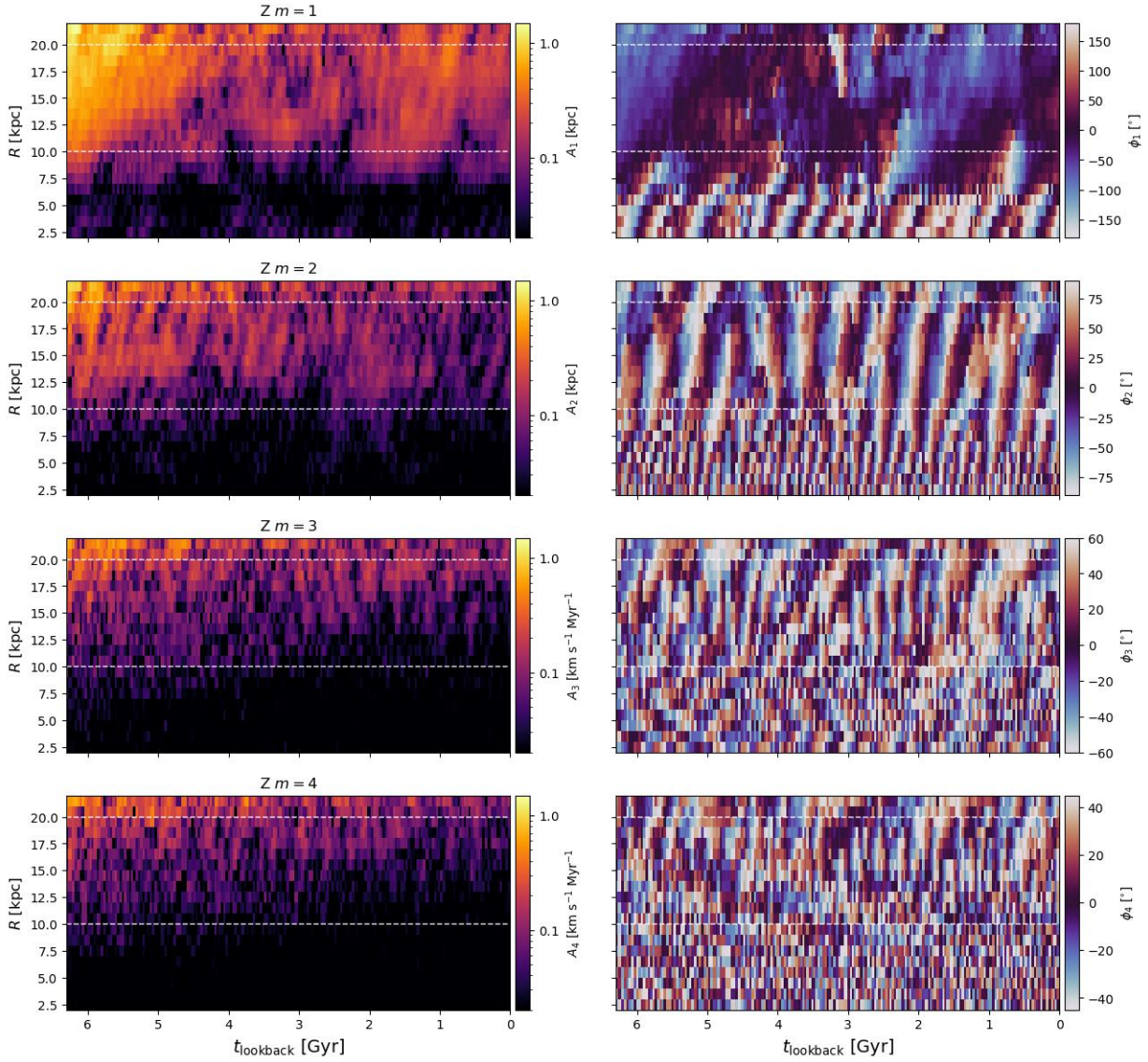


FIGURE H.2: Fourier modes of $Z$ from mode $m = 1$ (top) to $m = 4$ (bottom) with the corresponding amplitude (left panels) and phase (right panels).

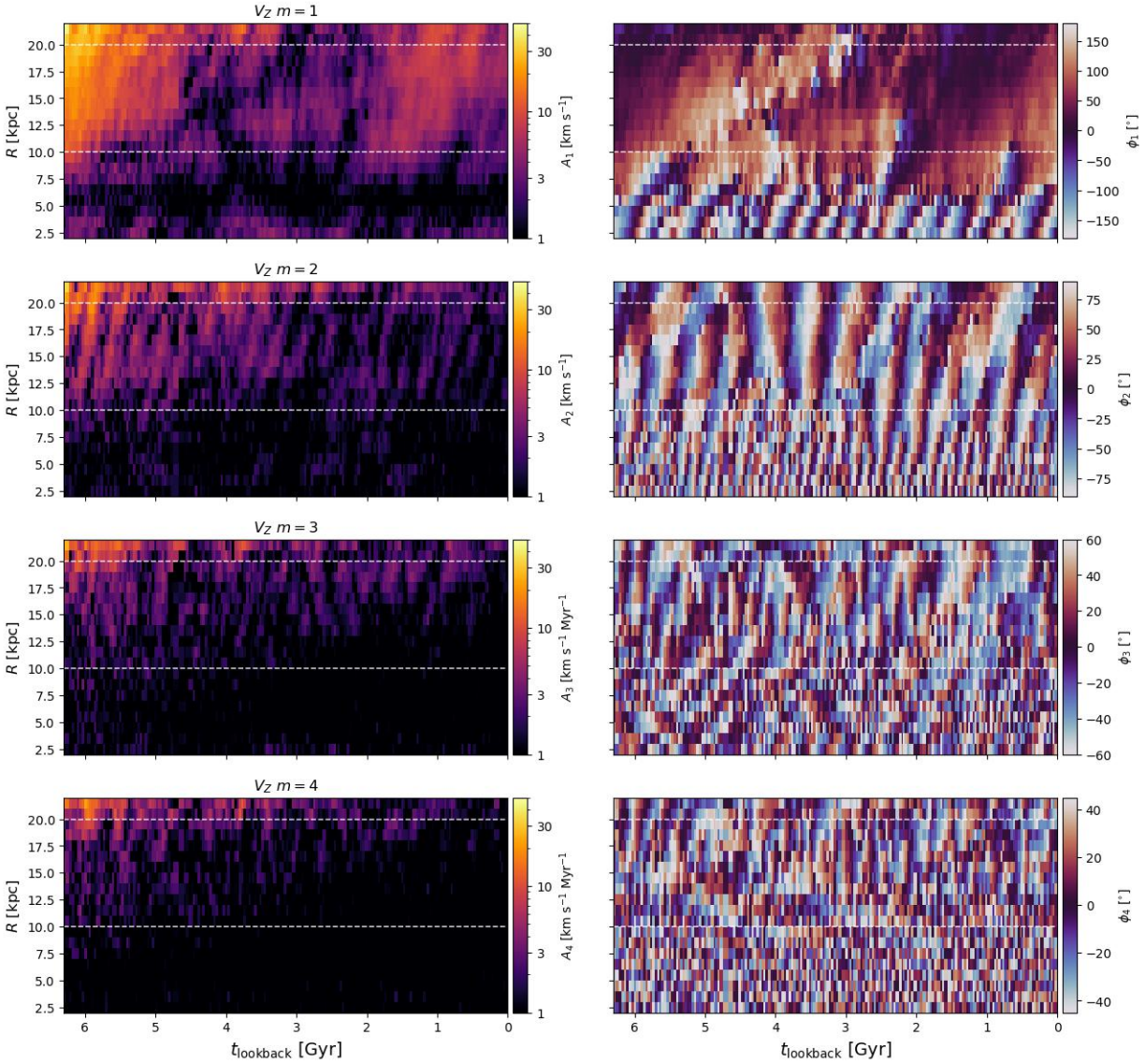


FIGURE H.3: Fourier modes of $V_Z$ from mode $m = 1$ (top) to $m = 4$ (bottom) with the corresponding amplitude (left panels) and phase (right panels).

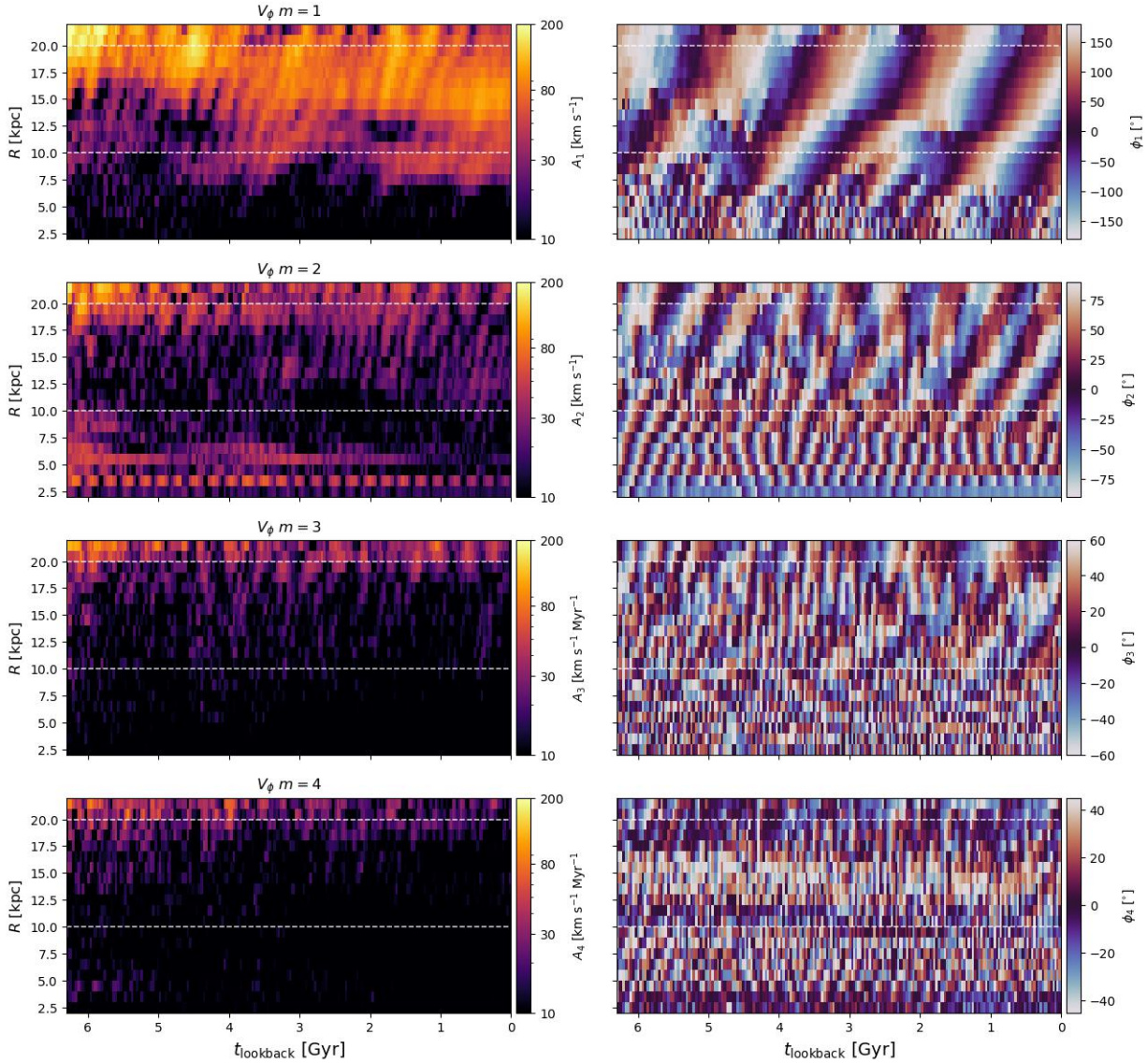


FIGURE H.4: Fourier modes of $V_\phi$ from mode $m = 1$ (top) to $m = 4$ (bottom) with the corresponding amplitude (left panels) and phase (right panels).

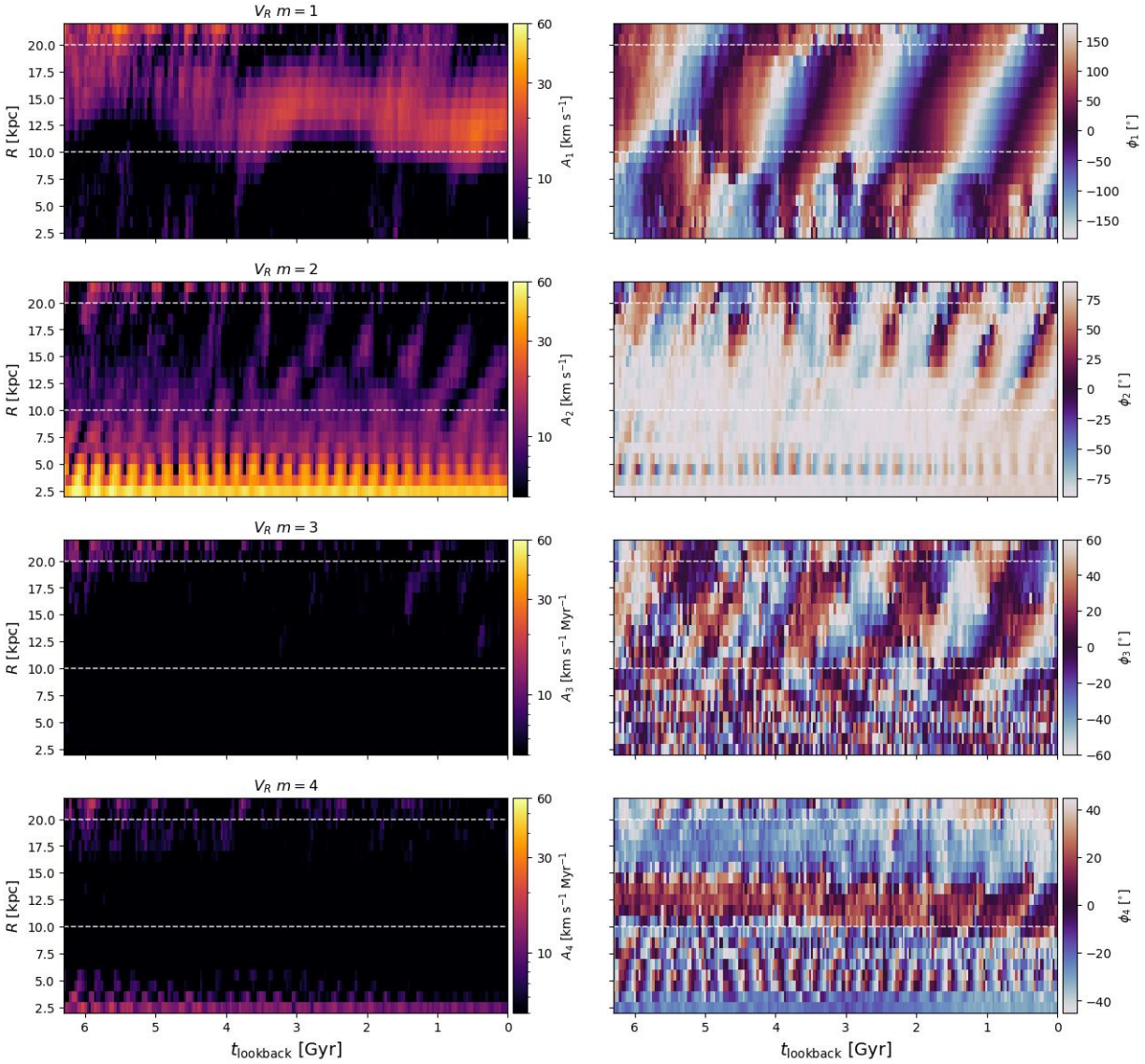


FIGURE H.5: Fourier modes of $V_R$ from mode $m = 1$ (top) to $m = 4$ (bottom) with the corresponding amplitude (left panels) and phase (right panels).

APPENDIX

# List of publications

## I.1 Articles in refereed journals (First author)

"Phase spirals in cosmological simulations of Milky Way-sized galaxies."

García-Conde, B., Roca-Fàbrega, S., Antoja, T., Ramos, P. and Valenzuela, O. (2022). *Monthly Notices of the Royal Astronomical Society, 510(1), 154-160.*

"Galactoseismology in cosmological simulations: Vertical perturbations by dark matter, satellite galaxies and gas."

García-Conde,B., Antoja, T., Roca-Fàbrega,S., Gómez, F., Ramos, P., Garavito-Camargo, N., and Gómez-Flechoso, MA. submitted to *Astronomy & Astrophysics*

## I.2 Articles in refereed journals (Co-author)

"The phase spiral in Gaia DR3"

Antoja, T., Ramos, P., García-Conde, B., Bernet, M., Laporte, C. F. P., and Katz, D. (2023). *Astronomy & Astrophysics, 673, A115.*

## I.3 Non-Refereed conferences contributions (First author only)

"Phase spirals in cosmological simulations"

García-Conde, B., Roca-Fàbrega, S., Antoja, T., Ramos, P. and Valenzuela, O.(2020) *XIV.0 Scientific Meeting (virtual) of the Spanish Astronomical Society, 138.*

"Phase spirals in cosmological simulations of Milky Way-sized galaxies"

García-Conde, B., Roca-Fàbrega, S., Antoja, T., Ramos, P. and Valenzuela, O.(2021) *Poster contribution at EAS Annual Meeting 2021.*

"Phase spirals in cosmological simulations of Milky Way-sized galaxies"

García-Conde, B., Roca-Fàbrega, S., Antoja, T., Ramos, P. and Valenzuela, O.(2022) *Poster contribution at EAS Annual Meeting 2022.*

"Phase spirals in cosmological simulations of Milky Way-sized galaxies"

García-Conde, B., Roca-Fàbrega, S., Antoja, T., Ramos, P. and Valenzuela, O.(2022) *Highlights of Spanish Astrophysics XI, Proceedings of the XV Scientific Meeting of the Spanish Astronomical Society held on September 4–9, 2022.*

"Phase spirals in cosmological simulations of Milky Way-sized galaxies"

García-Conde, B., Roca-Fàbrega, S., Antoja, T., Ramos, P. and Valenzuela, O.(2022) *Poster and Poster Session Presentation at EAS Annual Meeting 2023*

"Galactoseismology in cosmological simulations: vertical perturbations by dark matter, satellite galaxies and gas "

García-Conde,B., Antoja, T., Roca-Fàbrega,S., Gómez, F., Ramos, P., Garavito-Camargo, N., and Gómez-Flechoso, MA. *Poster contribution at EAS Annual Meeting 2023*

# Bibliography


Abadi, Mario G et al. (2003). "Simulations of galaxy formation in a $\Lambda$ cold dark matter universe. I. Dynamical and photometric properties of a simulated disk galaxy". In: *The Astrophysical Journal* 591.2, p. 499.

Agertz, Oscar et al. (2021). "VINTERGATAN–I. The origins of chemically, kinematically, and structurally distinct discs in a simulated Milky Way-mass galaxy". In: *Monthly Notices of the Royal Astronomical Society* 503.4, pp. 5826–5845.

Aghanim, Nabila et al. (2020). "Planck 2018 results-VI. Cosmological parameters". In: *Astronomy & Astrophysics* 641, A6.

Alinder, S., P. J. McMillan, and T. Bensby (Oct. 2023). "Investigating the amplitude and rotation of the phase spiral in the Milky Way outer disc". In: *Astronomy & Astrophysics* 678, A46, A46. DOI: 10.1051/0004-6361/202346560.

Alves, João et al. (Jan. 2020). "A Galactic-scale gas wave in the solar neighbourhood". In: *Nature* 578.7794, pp. 237–239. DOI: 10.1038/s41586-019-1874-z. arXiv: 2001.08748 [astro-ph.GA].

Anders, F. et al. (Feb. 2022). "Photo-astrometric distances, extinctions, and astrophysical parameters for Gaia EDR3 stars brighter than G = 18.5". In: *Astronomy & Astrophysics* 658, A91, A91. DOI: 10.1051/0004-6361/202142369. arXiv: 2111.01860 [astro-ph.GA].

Ann, HB and J-C Park (2006). "Warped disks in spiral galaxies". In: *New Astronomy* 11.4, pp. 293–305.

Antoja, T. et al. (Oct. 2015). "Detection of satellite remnants in the Galactic halo with Gaia- III. Detection limits for ultrafaint dwarf galaxies". In: *Monthly Notices of the Royal Astronomical Society* 453.1, pp. 541–560. DOI: 10.1093/mnras/stv1622. arXiv: 1507.04353 [astro-ph.GA].

Antoja, T. et al. (Sept. 2018). "A dynamically young and perturbed Milky Way disk". In: *Nature* 561.7723, pp. 360–362. DOI: 10.1038/s41586-018-0510-7. arXiv: 1804.10196 [astro-ph.GA].

Antoja, T. et al. (Dec. 2022). "Tidally induced spiral arm wraps encoded in phase space". In: *Astronomy & Astrophysics* 668, A61, A61. DOI: 10.1051/0004-6361/202244064. arXiv: 2206.03495 [astro-ph.GA].

Antoja, T. et al. (May 2023). "The phase spiral in Gaia DR3". In: *Astronomy & Astrophysics* 673, A115, A115. DOI: 10.1051/0004-6361/202245518.

Atek, Hakim et al. (2023). "Revealing galaxy candidates out to z  16 with JWST observations of the lensing cluster SMACS0723". In: *Monthly Notices of the Royal Astronomical Society* 519.1, pp. 1201–1220.

Athanassoula, E (2013). "Bars and secular evolution in disk galaxies: Theoretical input". In: *Secular Evolution of Galaxies* 305.

Athanassoula, E et al. (2016). "Forming disk galaxies in wet major mergers. I. Three fiducial examples". In: *The Astrophysical Journal* 821.2, p. 90.

Bailer-Jones, C. A. L. et al. (Mar. 2021). "Estimating Distances from Parallaxes. V. Geometric and Photogeometric Distances to 1.47 Billion Stars in Gaia Early Data Release 3". In: *The Astronomical Journal* 161.3, 147, p. 147. DOI: 10.3847/1538-3881/abd806. arXiv: 2012.05220 [astro-ph.SR].

Banik, Uddipan, Martin D. Weinberg, and Frank C. van den Bosch (Aug. 2022). "A Comprehensive Perturbative Formalism for Phase Mixing in Perturbed Disks. I. Phase Spirals in an Infinite, Isothermal Slab". In: *The Astrophysical Journal* 935.2, 135, p. 135. DOI: 10.3847/1538-4357/ac7ff9. arXiv: 2208.05038 [astro-ph.GA].

Barnes, Joshua E and Lars Hernquist (1992). "Dynamics of interacting galaxies". In: *Annual review of astronomy and astrophysics* 30.1, pp. 705–742.

Beane, Angus et al. (2019). "The Implications of Local Fluctuations in the Galactic Midplane for Dynamical Analysis in the Gaia Era". In: *The Astrophysical Journal* 883.1, p. 103.

Behroozi, Peter S., Charlie Conroy, and Risa H. Wechsler (July 2010). "A Comprehensive Analysis of Uncertainties Affecting the Stellar Mass-Halo Mass Relation for $0 < z < 4$". In: *The Astrophysical Journal* 717.1, pp. 379–403. DOI: 10.1088/0004-637X/717/1/379. arXiv: 1001.0015 [astro-ph.CO].

Behroozi, Peter S, Risa H Wechsler, and Hao-Yi Wu (2012). "The rockstar phase-space temporal halo finder and the velocity offsets of cluster cores". In: *The Astrophysical Journal* 762.2, p. 109.

Belokurov, V et al. (2018). "Co-formation of the disc and the stellar halo". In: *Monthly Notices of the Royal Astronomical Society* 478.1, pp. 611–619.

Bennett, Morgan and Jo Bovy (Jan. 2019). "Vertical waves in the solar neighbourhood in Gaia DR2". In: *Monthly Notices of the Royal Astronomical Society* 482.1, pp. 1417–1425. DOI: 10.1093/mnras/sty2813. arXiv: 1809.03507 [astro-ph.GA].

Bennett, Morgan and Jo Bovy (2021). "Did Sgr cause the vertical waves in the solar neighbourhood?" In: *Monthly Notices of the Royal Astronomical Society* 503.1, pp. 376–393.

Bennett, Morgan, Jo Bovy, and Jason A. S. Hunt (Mar. 2022). "Exploring the Sgr-Milky Way-disk Interaction Using High-resolution N-body Simulations". In: *The Astrophysical Journal* 927.1, 131, p. 131. DOI: 10.3847/1538-4357/ac5021. arXiv: 2107.08055 [astro-ph.GA].

Bensby, Thomas, Sofia Feltzing, and MS Oey (2014). "Exploring the Milky Way stellar disk-A detailed elemental abundance study of 714 F and G dwarf stars in the solar neighbourhood". In: *Astronomy & Astrophysics* 562, A71.

Benson, AJ et al. (2004). "Heating of galactic discs by infalling satellites". In: *Monthly Notices of the Royal Astronomical Society* 351.4, pp. 1215–1236.

Berger, Marsha J and Joseph Oliger (1984). "Adaptive mesh refinement for hyperbolic partial differential equations". In: *Journal of computational Physics* 53.3, pp. 484–512.

Binney, J and S Tremaine (2008). *Galactic Dynamics 2nd ed. ed J*.

Binney, James (1992). "Warps". In: *Annual review of astronomy and astrophysics* 30.1, pp. 51–74.

Binney, James and Ralph Schönrich (Dec. 2018). "The origin of the Gaia phase-plane spiral". In: *Monthly Notices of the Royal Astronomical Society* 481.2, pp. 1501–1506. DOI: 10.1093/mnras/sty2378. arXiv: 1807.09819 [astro-ph.GA].

Binney, James and Scott Tremaine (2008). *Galactic Dynamics: Second Edition*.

Bland-Hawthorn, Joss and Ortwin Gerhard (2016). "The galaxy in context: structural, kinematic, and integrated properties". In: *Annual Review of Astronomy and Astrophysics* 54, pp. 529–596.

Bland-Hawthorn, Joss and Ortwin Gerhard (Sept. 2016). "The Galaxy in Context: Structural, Kinematic, and Integrated Properties". In: *Annual Review of Astronomy and Astrophysics* 54, pp. 529–596. DOI: 10.1146/annurev-astro-081915-023441. arXiv: 1602.07702 [astro-ph.GA].

Bland-Hawthorn, Joss and Thor Tepper-García (July 2021). "Galactic seismology: the evolving 'phase spiral' after the Sagittarius dwarf impact". In: *Monthly Notices of the Royal Astronomical Society* 504.3, pp. 3168–3186. DOI: 10.1093/mnras/stab704. arXiv: 2009.02434 [astro-ph.GA].

Bland-Hawthorn, Joss et al. (June 2019). "The GALAH survey and Gaia DR2: dissecting the stellar disc's phase space by age, action, chemistry, and location". In: *Monthly Notices of the Royal Astronomical Society* 486.1, pp. 1167–1191. DOI: 10.1093/mnras/stz217. arXiv: 1809.02658 [astro-ph.GA].

Bland-Hawthorn, Joss et al. (2019). "The GALAH survey and Gaia DR2: dissecting the stellar disc's phase space by age, action, chemistry, and location". In: *Monthly Notices of the Royal Astronomical Society* 486.1, pp. 1167–1191.

Blitz, Leo and David N Spergel (1991). "Direct evidence for a bar at the Galactic center". In: *The Astrophysical Journal* 379, pp. 631–638.

Blomme, R. et al. (June 2022). "Gaia Data Release 3: Hot-star radial velocities". In: *arXiv e-prints*, arXiv:2206.05486, arXiv:2206.05486. arXiv: 2206.05486 [astro-ph.SR].

Bosch, Frank C van den et al. (1999). "Substructure in dark halos: orbital eccentricities and dynamical friction". In: *The Astrophysical Journal* 515.1, p. 50.

Bosch, Frank C van den et al. (2018). "Disruption of dark matter substructure: fact or fiction?" In: *Monthly Notices of the Royal Astronomical Society* 474.3, pp. 3043–3066.

Bovy, Jo (Feb. 2015). "galpy: A python Library for Galactic Dynamics". In: *The Astrophysical Journals* 216.2, 29, p. 29. DOI: 10.1088/0067-0049/216/2/29. arXiv: 1412.3451 [astro-ph.GA].

Boylan-Kolchin, Michael, James S Bullock, and Manoj Kaplinghat (2011). "Too big to fail? The puzzling darkness of massive Milky Way subhaloes". In: *Monthly Notices of the Royal Astronomical Society: Letters* 415.1, pp. L40–L44.

— (2012). "The Milky Way's bright satellites as an apparent failure of ΛCDM". In: *Monthly Notices of the Royal Astronomical Society* 422.2, pp. 1203–1218.

Brook, CB et al. (2011). "Hierarchical formation of bulgeless galaxies: why outflows have low angular momentum". In: *Monthly Notices of the Royal Astronomical Society* 415.2, pp. 1051–1060.

Brook, CB et al. (2012). "Hierarchical formation of bulgeless galaxies–II. Redistribution of angular momentum via galactic fountains". In: *Monthly Notices of the Royal Astronomical Society* 419.1, pp. 771–779.

Bryan, Greg L. and Michael L. Norman (Mar. 1998). "Statistical Properties of X-Ray Clusters: Analytic and Numerical Comparisons". In: *The Astrophysical Journal* 495.1, pp. 80–99. DOI: 10.1086/305262. arXiv: astro-ph/9710107 [astro-ph].

Bullock, James S and Michael Boylan-Kolchin (2017). "Small-scale challenges to the Λ CDM paradigm". In: *Annual Review of Astronomy and Astrophysics* 55, pp. 343–387.

Canny, John (Dec. 1986). "A Computational Approach To Edge Detection". In: *Pattern Analysis and Machine Intelligence, IEEE Transactions on* PAMI-8, pp. 679 –698. DOI: 10.1109/TPAMI.1986.4767851.

Caplar, Neven and Sandro Tacchella (2019). "Stochastic modelling of star-formation histories I: the scatter of the star-forming main sequence". In: *Monthly Notices of the Royal Astronomical Society* 487.3, pp. 3845–3869.

Carrillo, Ivonne et al. (2018). "Is the Milky Way still breathing? RAVE–Gaia streaming motions". In: *Monthly Notices of the Royal Astronomical Society* 475.2, pp. 2679–2696.

Chequers, Matthew H., Lawrence M. Widrow, and Keir Darling (Nov. 2018). "Bending waves in the Milky Way's disc from halo substructure". In: *Monthly Notices of the Royal Astronomical Society* 480.3, pp. 4244–4258. DOI: 10.1093/mnras/sty2114. arXiv: 1805.12449 [astro-ph.GA].

Chrobáková, Ž. et al. (Oct. 2020). "Gaia-DR2 extended kinematical maps. III. Rotation curves analysis, dark matter, and MOND tests". In: *Astronomy & Astrophysics* 642, A95, A95. DOI: 10.1051/0004-6361/202038736. arXiv: 2007.14825 [astro-ph.GA].

Clarke, Jonathan P and Ortwin Gerhard (2022). "The pattern speed of the Milky Way bar/bulge from VIRAC and Gaia". In: *Monthly Notices of the Royal Astronomical Society* 512.2, pp. 2171–2188.

Colín, Pedro et al. (2010). "Low-mass Galaxy Formation in Cosmological Adaptive Mesh Refinement Simulations: The Effects of Varying the Sub-grid Physics Parameters". In: *The Astrophysical Journal* 713.1, p. 535.

Colombi, S. (Mar. 2021). "Phase-space structure of protohalos: Vlasov versus particle-mesh". In: *Astronomy & Astrophysics* 647, A66, A66. DOI: 10.1051/0004-6361/202039719. arXiv: 2012.04409 [astro-ph.CO].

Conroy, Charlie et al. (Jan. 2021). "All-sky dynamical response of the Galactic halo to the Large Magellanic Cloud". In: *Nature* 592.7855, pp. 534–536. DOI: 10.1038/s41586-021-03385-7. arXiv: 2104.09515 [astro-ph.GA].

Cooley, James W. and John W. Tukey (Feb. 1965). "An algorithm for the machine calculation of complex Fourier series". In: *Math. Comp.* 19.1, pp. 297–301. DOI: https://doi.org/10.1090/S0025-5718-1965-0178586-1.

Darling, Keir and Lawrence M Widrow (2019). "Eigenfunctions of Galactic phase space spirals from dynamic mode decomposition". In: *Monthly Notices of the Royal Astronomical Society* 490.1, pp. 114–123.

Darling, Keir and Lawrence M. Widrow (Mar. 2019). "Emergence of the Gaia phase space spirals from bending waves". In: *Monthly Notices of the Royal Astronomical Society* 484.1, pp. 1050–1056. DOI: 10.1093/mnras/sty3508. arXiv: 1807.11516 [astro-ph.GA].

Darragh-Ford, Elise et al. (Feb. 2023). "ESCARGOT: Mapping Vertical Phase Spiral Characteristics Throughout the Real and Simulated Milky Way". In: *arXiv e-prints*, arXiv:2302.09086, arXiv:2302.09086. arXiv: 2302.09086 [astro-ph.GA].

Debattista, Victor P (2014). "The vertical structure and kinematics of grand design spirals". In: *Monthly Notices of the Royal Astronomical Society: Letters* 443.1, pp. L1–L5.

Dehnen, Walter, Dean E McLaughlin, and Jalpesh Sachania (2006). "The velocity dispersion and mass profile of the Milky Way". In: *Monthly Notices of the Royal Astronomical Society* 369.4, pp. 1688–1692.

Dekel, Avishai and Yuval Birnboim (2006). "Galaxy bimodality due to cold flows and shock heating". In: *Monthly notices of the royal astronomical society* 368.1, pp. 2–20.

Delgado-Serrano, R et al. (2010). "How was the Hubble sequence 6 Gyr ago?" In: *Astronomy & Astrophysics* 509, A78.

Diemand, Jürg, Ben Moore, and Joachim Stadel (2004). "Velocity and spatial biases in cold dark matter subhalo distributions". In: *Monthly Notices of the Royal Astronomical Society* 352.2, pp. 535–546.

Dolag, Klaus et al. (2008). "Simulation techniques for cosmological simulations". In: *Space science reviews* 134, pp. 229–268.

Dunkley, J et al. (2009). "Five-year wilkinson microwave anisotropy probe* observations: likelihoods and parameters from the wmap data". In: *The Astrophysical Journal Supplement Series* 180.2, p. 306.

D'Onghia, E et al. (2016). "Excitation of coupled stellar motions in the Galactic Disk by orbiting satellites". In: *The Astrophysical Journal* 823.1, p. 4.

Faure, Carole, Arnaud Siebert, and Benoit Famaey (2014). "Radial and vertical flows induced by galactic spiral arms: likely contributors to our 'wobbly Galaxy'". In: *Monthly Notices of the Royal Astronomical Society* 440.3, pp. 2564–2575.

Feldmann, Robert and Douglas Spolyar (2015). "Detecting dark matter substructures around the Milky Way with Gaia". In: *Monthly Notices of the Royal Astronomical Society* 446.1, pp. 1000–1012.

Feldmann, Robert et al. (2023). "FIREbox: Simulating galaxies at high dynamic range in a cosmological volume". In: *Monthly Notices of the Royal Astronomical Society* 522.3, pp. 3831–3860.

Ferland, GJ et al. (1998). "CLOUDY 90: numerical simulation of plasmas and their spectra". In: *Publications of the Astronomical Society of the Pacific* 110.749, p. 761.

Frankel, Neige et al. (2023). "Vertical motion in the Galactic disc: unwinding the Snail". In: *Monthly Notices of the Royal Astronomical Society* 521.4, pp. 5917–5926.

Friske, Jennifer K. S. and Ralph Schönrich (Dec. 2019). "More than just a wrinkle: a wave-like pattern in $U_g$ versus $L_z$ from Gaia data". In: *Monthly Notices of the Royal Astronomical Society* 490.4, pp. 5414–5423. DOI: 10.1093/mnras/stz2951. arXiv: 1902.09569 [astro-ph.GA].

Fujii, Michiko, Yoko Funato, and Junichiro Makino (2006). "Dynamical friction on satellite galaxies". In: *Publications of the Astronomical Society of Japan* 58.4, pp. 743–752.

Gaia Collaboration et al. (Nov. 2016). "The Gaia mission". In: *Astronomy & Astrophysics* 595, A1, A1. DOI: 10.1051/0004-6361/201629272. arXiv: 1609.04153 [astro-ph.IM].

Gaia Collaboration et al. (Aug. 2018a). "Gaia Data Release 2. Summary of the contents and survey properties". In: *Astronomy & Astrophysics* 616, A1, A1. DOI: 10.1051/0004-6361/201833051. arXiv: 1804.09365 [astro-ph.GA].

Gaia Collaboration et al. (Aug. 2018b). "Gaia Data Release 2. Summary of the contents and survey properties". In: *Astronomy & Astrophysics* 616, A1, A1. DOI: 10.1051/0004-6361/201833051. arXiv: 1804.09365 [astro-ph.GA].

Gaia Collaboration et al. (June 2022a). "Gaia Data Release 3: Chemical cartography of the Milky Way". In: *arXiv e-prints*, arXiv:2206.05534, arXiv:2206.05534. arXiv: 2206.05534 [astro-ph.GA].

Gaia Collaboration et al. (June 2022b). "Gaia Data Release 3: Mapping the asymmetric disc of the Milky Way". In: *arXiv e-prints*, arXiv:2206.06207, arXiv:2206.06207. arXiv: 2206.06207 [astro-ph.GA].

Gaia Collaboration et al. (July 2022c). "Gaia Data Release 3: Summary of the content and survey properties". In: *arXiv e-prints*, arXiv:2208.00211, arXiv:2208.00211. arXiv: 2208.00211 [astro-ph.GA].

Gallart, Carme et al. (2019). "Uncovering the birth of the Milky Way through accurate stellar ages with Gaia". In: *Nature Astronomy* 3.10, pp. 932–939.

Gandhi, Suroor S et al. (2022). "Snails across Scales: Local and Global Phase-mixing Structures as Probes of the Past and Future Milky Way". In: *The Astrophysical Journal* 928.1, p. 80.

Garavito-Camargo, Nicolás et al. (2021). "Quantifying the impact of the Large Magellanic Cloud on the structure of the Milky Way's dark matter halo using basis function expansions". In: *The Astrophysical Journal* 919.2, p. 109.

García-Conde, Begoña et al. (2022). "Phase spirals in cosmological simulations of Milky Way-sized galaxies". In: *Monthly Notices of the Royal Astronomical Society* 510.1, pp. 154–160.

Garrison-Kimmel, Shea et al. (2014). "Too big to fail in the local group". In: *Monthly Notices of the Royal Astronomical Society* 444.1, pp. 222–236.

Geha, Marla et al. (2017). "The SAGA Survey. I. Satellite galaxy populations around eight Milky Way analogs". In: *The Astrophysical Journal* 847.1, p. 4.

Gibbons, SLJ, V Belokurov, and NW Evans (2014). "'Skinny Milky Way please', says Sagittarius". In: *Monthly Notices of the Royal Astronomical Society* 445.4, pp. 3788–3802.

Gilmore, Gerard and Neil Reid (1983). "New light on faint stars–III. Galactic structure towards the South Pole and the Galactic thick disc". In: *Monthly Notices of the Royal Astronomical Society* 202.4, pp. 1025–1047.

Gingold, Robert A and Joseph J Monaghan (1977). "Smoothed particle hydrodynamics: theory and application to non-spherical stars". In: *Monthly notices of the royal astronomical society* 181.3, pp. 375–389.

Gómez, Facundo A. et al. (Feb. 2013). "Vertical density waves in the Milky Way disc induced by the Sagittarius dwarf galaxy". In: *Monthly Notices of the Royal Astronomical Society* 429.1, pp. 159–164. DOI: 10.1093/mnras/sts327. arXiv: 1207.3083 [astro-ph.GA].

Gómez, Facundo A et al. (2016a). "A fully cosmological model of a Monoceros-like ring". In: *Monthly Notices of the Royal Astronomical Society* 456.3, pp. 2779–2793.

Gómez, Facundo A et al. (2016b). "Warps and waves in the stellar discs of the Auriga cosmological simulations". In: *Monthly Notices of the Royal Astronomical Society* 465.3, pp. 3446–3460.

Gómez, Facundo A. et al. (Mar. 2017). "Warps and waves in the stellar discs of the Auriga cosmological simulations". In: *Monthly Notices of the Royal Astronomical Society* 465.3, pp. 3446–3460. DOI: 10.1093/mnras/stw2957. arXiv: 1606.06295 [astro-ph.GA].

Gómez, Facundo A. et al. (Feb. 2021). "A Tidally Induced Global Corrugation Pattern in an External Disk Galaxy Similar to the Milky Way". In: *The Astrophysical Journal* 908.1, 27, p. 27. DOI: 10.3847/1538-4357/abcd97.

Governato, Fabio et al. (2004). "The formation of a realistic disk galaxy in Λ-dominated cosmologies". In: *The Astrophysical Journal* 607.2, p. 688.

Grand, Robert J. J. et al. (Sept. 2023). "An ever-present Gaia snail shell triggered by a dark matter wake". In: *Monthly Notices of the Royal Astronomical Society* 524.1, pp. 801–816. DOI: 10.1093/mnras/stad1969.

Gravity Collaboration et al. (Jan. 2022). "Mass distribution in the Galactic Center based on interferometric astrometry of multiple stellar orbits". In: *Astronomy & Astrophysics* 657, L12, p. L12. DOI: 10.1051/0004-6361/202142465.

Grion Filho, Douglas et al. (2021). "A holistic review of a galactic interaction". In: *Monthly Notices of the Royal Astronomical Society* 507.2, pp. 2825–2842.

Guo, Qi et al. (Jan. 2020). "Further evidence for a population of dark-matter-deficient dwarf galaxies". In: *Nature Astronomy* 4, pp. 246–251. DOI: 10.1038/s41550-019-0930-9. arXiv: 1908.00046 [astro-ph.GA].

Haardt, Francesco and Piero Madau (1996). "Radiative transfer in a clumpy universe: Ii. the utraviolet extragalactic background". In: *The Astrophysical Journal*.

Haines, Tim et al. (July 2019). "Implications of a Time-varying Galactic Potential for Determinations of the Dynamical Surface Density". In: *The Astrophysical Journal Letters* 879.1, L15, p. L15. DOI: 10.3847/2041-8213/ab25f3. arXiv: 1903.00607 [astro-ph.GA].

Harikane, Yuichi et al. (2023). "A Comprehensive Study of Galaxies at z  9–16 Found in the Early JWST Data: Ultraviolet Luminosity Functions and Cosmic Star Formation History at the Pre-reionization Epoch". In: *The Astrophysical Journal Supplement Series* 265.1, p. 5.

Hawkins, Keith et al. (2015). "Using chemical tagging to redefine the interface of the Galactic disc and halo". In: *Monthly Notices of the Royal Astronomical Society* 453.1, pp. 758–774.

Helmi, Amina (2008). "The stellar halo of the Galaxy". In: *The Astronomy and Astrophysics Review* 15, pp. 145–188.

Helmi, Amina (Aug. 2020). "Streams, Substructures, and the Early History of the Milky Way". In: *Annual Review of Astronomy and Astrophysics* 58, pp. 205–256. DOI: 10.1146/annurev-astro-032620-021917. arXiv: 2002.04340 [astro-ph.GA].

Helmi, Amina et al. (2018). "The merger that led to the formation of the Milky Way's inner stellar halo and thick disk". In: *Nature* 563.7729, pp. 85–88.

Hernquist, Lars and Neal Katz (1989). "TREESPH-A unification of SPH with the hierarchical tree method". In: *Astrophysical Journal Supplement Series (ISSN 0067-0049), vol. 70, June 1989, p. 419-446. Research supported by the San Diego Supercomputer Center, Pittsburgh Supercomputer Center, and New Jersey High Technology Grant.* 70, pp. 419–446.

Hinshaw, Gary et al. (2013). "Nine-year Wilkinson Microwave Anisotropy Probe (WMAP) observations: cosmological parameter results". In: *The Astrophysical Journal Supplement Series* 208.2, p. 19.

Hunt, Jason A. S. et al. (Nov. 2021). "Resolving local and global kinematic signatures of satellite mergers with billion particle simulations". In: *Monthly Notices of the Royal Astronomical Society* 508.1, pp. 1459–1472. DOI: 10.1093/mnras/stab2580. arXiv: 2107.06294 [astro-ph.GA].

Hunt, Jason AS et al. (2022). "Multiple phase spirals suggest multiple origins in Gaia DR3". In: *Monthly Notices of the Royal Astronomical Society: Letters* 516.1, pp. L7–L11.

Ibata, Rodrigo et al. (1996). "The kinematics, orbit, and survival of the Sagittarius dwarf spheroidal galaxy". In: *arXiv preprint astro-ph/9612025*.

Ibata, Rodrigo A, Gerry Gilmore, and MJ Irwin (1994). "A dwarf satellite galaxy in Sagittarius". In: *Nature* 370.6486, pp. 194–196.

Jackson, R. A. et al. (Apr. 2021). "Dark matter-deficient dwarf galaxies form via tidal stripping of dark matter in interactions with massive companions". In: *Monthly Notices of the Royal Astronomical Society* 502.2, pp. 1785–1796. DOI: 10.1093/mnras/stab093. arXiv: 2010.02219 [astro-ph.GA].

Jiang, Ing-Guey and James Binney (1999). "Warps and cosmic infall". In: *Monthly Notices of the Royal Astronomical Society* 303.1, pp. L7–L10.

— (2000). "The orbit and mass of the Sagittarius dwarf galaxy". In: *Monthly Notices of the Royal Astronomical Society* 314.3, pp. 468–474.

Johnson, Alexander et al. (2023). "Dynamical Data Mining Captures Disc-Halo Couplings that Structure Galaxies". In: *arXiv preprint arXiv:2301.02256*.

Johnston, Kathryn V, Lars Hernquist, and Michael Bolte (1996). "Fossil signatures of ancient accretion events in the halo". In: *arXiv preprint astro-ph/9602060*.

Johnston, Kathryn V, David N Spergel, and Lars Hernquist (1995). "The disruption of the Sagittarius dwarf galaxy." In: *arXiv preprint astro-ph/9502005*.

Kafle, Prajwal R et al. (2012). "Kinematics of the stellar halo and the mass distribution of the Milky Way using blue horizontal branch stars". In: *The Astrophysical Journal* 761.2, p. 98.

Katz, D. et al. (June 2022). "Gaia Data Release 3 Properties and validation of the radial velocities". In: *arXiv e-prints*, arXiv:2206.05902, arXiv:2206.05902. arXiv: 2206.05902 [astro-ph.GA].

Kauffmann, G, Simon DM White, and B Guiderdoni (1993). "The formation and evolution of galaxies within merging dark matter haloes". In: *Monthly Notices of the Royal Astronomical Society* 264.1, pp. 201–218.

Kaviraj, S et al. (2017). "The Horizon-AGN simulation: evolution of galaxy properties over cosmic time". In: *Monthly Notices of the Royal Astronomical Society* 467.4, pp. 4739–4752.

Kazantzidis, Stelios et al. (2009). "Cold dark matter substructure and galactic disks. II. Dynamical effects of hierarchical satellite accretion". In: *The Astrophysical Journal* 700.2, p. 1896.

Khachaturyants, Tigran et al. (2022). "Bending waves excited by irregular gas inflow along warps". In: *Monthly Notices of the Royal Astronomical Society* 512.3, pp. 3500–3519.

Khoperskov, Sergey et al. (Feb. 2019). "The echo of the bar buckling: Phase-space spirals in Gaia Data Release 2". In: *Astronomy & Astrophysics* 622, L6, p. L6. DOI: 10.1051/0004-6361/201834707.

Khoperskov, Sergey et al. (2019). "The echo of the bar buckling: Phase-space spirals in Gaia Data Release 2". In: *Astronomy & Astrophysics* 622, p. L6.

Kim, Stacy Y, Annika HG Peter, and Jonathan R Hargis (2018). "Missing satellites problem: completeness corrections to the number of satellite galaxies in the milky way are consistent with cold dark matter predictions". In: *Physical review letters* 121.21, p. 211302.

Klypin, Anatoly et al. (1999a). "Galaxies in N-body simulations: overcoming the overmerging problem". In: *The Astrophysical Journal* 516.2, p. 530.

Klypin, Anatoly et al. (1999b). "Where are the missing galactic satellites?" In: *The Astrophysical Journal* 522.1, p. 82.

Klypin, Anatoly et al. (2001). "Resolving the structure of cold dark matter halos". In: *The Astrophysical Journal* 554.2, p. 903.

Klypin, Anatoly et al. (2015). "Abundance of field galaxies". In: *Monthly Notices of the Royal Astronomical Society* 454.2, pp. 1798–1810.

Kravtsov, Andrey V (2003). "On the origin of the global Schmidt law of star formation". In: *The Astrophysical Journal* 590.1, p. L1.

Kravtsov, Andrey V., Anatoly A. Klypin, and Alexei M. Khokhlov (July 1997). "Adaptive Refinement Tree: A New High-Resolution N-Body Code for Cosmological Simulations". In: *The Astrophysical Journal* 111.1, pp. 73–94. DOI: 10.1086/313015. arXiv: astro-ph/9701195 [astro-ph].

Kroupa, Pavel (2001). "On the variation of the initial mass function". In: *Monthly Notices of the Royal Astronomical Society* 322.2, pp. 231–246.

Kumar, Ankit et al. (2022). "Excitation of vertical breathing motion in disc galaxies by tidally-induced spirals in fly-by interactions". In: *Monthly Notices of the Royal Astronomical Society* 516.1, pp. 1114–1126.

Labbé, Ivo et al. (2023). "A population of red candidate massive galaxies˜ 600 Myr after the Big Bang". In: *Nature* 616.7956, pp. 266–269.

Lallement, R. et al. (May 2019). "Gaia-2MASS 3D maps of Galactic interstellar dust within 3 kpc". In: *Astronomy & Astrophysics* 625, A135, A135. DOI: 10.1051/0004-6361/201834695. arXiv: 1902.04116 [astro-ph.GA].

Laporte, Chervin F. P. et al. (May 2019). "Footprints of the Sagittarius dwarf galaxy in the Gaia data set". In: *Monthly Notices of the Royal Astronomical Society* 485.3, pp. 3134–3152. DOI: 10.1093/mnras/stz583. arXiv: 1808.00451 [astro-ph.GA].

Laporte, Chervin FP et al. (2018). "The influence of Sagittarius and the Large Magellanic Cloud on the stellar disc of the Milky Way Galaxy". In: *Monthly Notices of the Royal Astronomical Society* 481.1, pp. 286–306.

Law, David R. and Steven R. Majewski (May 2010). "The Sagittarius Dwarf Galaxy: A Model for Evolution in a Triaxial Milky Way Halo". In: *The Astrophysical Journal* 714.1, pp. 229–254. DOI: 10.1088/0004-637X/714/1/229. arXiv: 1003.1132 [astro-ph.GA].

Li, Zhao-Yu (Apr. 2021). "Vertical Phase Mixing across the Galactic Disk". In: *The Astrophysical Journal* 911.2, 107, p. 107. DOI: 10.3847/1538-4357/abea17. arXiv: 2011.11250 [astro-ph.GA].

Li, Zhao-Yu and Juntai Shen (Feb. 2020). "Dissecting the Phase Space Snail Shell". In: *The Astroghysical Journal* 890.1, 85, p. 85. DOI: 10.3847/1538-4357/ab6b21. arXiv: 1904.03314 [astro-ph.GA].

Licquia, Timothy C and Jeffrey A Newman (2015). "Improved estimates of the Milky Way's stellar mass and star formation rate from hierarchical Bayesian meta-analysis". In: *The Astrophysical Journal* 806.1, p. 96.

Łokas, Ewa L (2019). "Anatomy of a buckling galactic bar". In: *Astronomy & Astrophysics* 629, A52.

Lotz, Jennifer M et al. (2010). "The effect of mass ratio on the morphology and time-scales of disc galaxy mergers". In: *Monthly Notices of the Royal Astronomical Society* 404.2, pp. 575–589.

Lucy, Leon B (1977). "A numerical approach to the testing of the fission hypothesis". In: *Astronomical Journal, vol. 82, Dec. 1977, p. 1013-1024.* 82, pp. 1013–1024.

Madau, Piero and Mark Dickinson (2014). "Cosmic star-formation history". In: *Annual Review of Astronomy and Astrophysics* 52, pp. 415–486.

Martínez-Delgado, David et al. (2023). "Hidden depths in the local Universe: The Stellar Stream Legacy Survey". In: *Astronomy & Astrophysics* 671, A141.

Masseron, T and G Gilmore (2015). "Carbon, nitrogen and $\alpha$-element abundances determine the formation sequence of the Galactic thick and thin discs". In: *Monthly Notices of the Royal Astronomical Society* 453.2, pp. 1855–1866.

McMillan, Paul J (2011). "Mass models of the Milky Way". In: *Monthly Notices of the Royal Astronomical Society* 414.3, pp. 2446–2457.

McMillan, Paul J. (Feb. 2017). "The mass distribution and gravitational potential of the Milky Way". In: *Monthly Notices of the Royal Astronomical Society* 465.1, pp. 76–94. DOI: 10.1093/mnras/stw2759. arXiv: 1608.00971 [astro-ph.GA].

Mihos, J. Christopher and Lars Hernquist (Apr. 1994). "Triggering of Starbursts in Galaxies by Minor Mergers". In: *The Astrophysical Journal Letters* 425, p. L13. DOI: 10.1086/187299.

Miró-Carretero, Juan et al. (2023). "A search for stellar tidal streams around Milky Way analogues from the SAGA sample". In: *Astronomy & Astrophysics* 669, p. L13.

Mo, HJ, Shude Mao, and Simon DM White (1998). "The formation of galactic discs". In: *Monthly Notices of the Royal Astronomical Society* 295.2, pp. 319–336.

Monari, Giacomo, Benoit Famaey, and Arnaud Siebert (2015). "The vertical effects of disc non-axisymmetries from perturbation theory: the case of the Galactic bar". In: *Monthly Notices of the Royal Astronomical Society* 452.1, pp. 747–754.

Mor, R et al. (2019). "Gaia DR2 reveals a star formation burst in the disc 2–3 Gyr ago". In: *Astronomy & Astrophysics* 624, p. L1.

Naab, Thorsten et al. (2007). "Formation of early-type galaxies from cosmological initial conditions". In: *The Astrophysical Journal* 658.2, p. 710.

Nakada, Y et al. (1991). "Is the bulge of our Galaxy triaxial?" In: *Nature* 353.6340, pp. 140–141.

Nandakumar, Meera, Chaitra Narayan, and Prasun Dutta (2022). "Bending waves in velocity space: a first look at the THINGS sample". In: *Monthly Notices of the Royal Astronomical Society* 513.2, pp. 3065–3075.

Navarro, Julio F and Simon DM White (1994). "Simulations of dissipative galaxy formation in hierarchically clustering universes–II. Dynamics of the baryonic component in galactic haloes". In: *Monthly Notices of the Royal Astronomical Society* 267.2, pp. 401–412.

Neeleman, Marcel et al. (2020). "A cold, massive, rotating disk galaxy 1.5 billion years after the Big Bang". In: *Nature* 581.7808, pp. 269–272.

Nelson, Dylan et al. (2019). "First results from the TNG50 simulation: galactic outflows driven by supernovae and black hole feedback". In: *Monthly Notices of the Royal Astronomical Society* 490.3, pp. 3234–3261.

Niederste-Ostholt, M. et al. (Mar. 2010). "Re-Assembling the Sagittarius Dwarf Galaxy". In: *The Astrophysical Journal* 712.1, pp. 516–526. DOI: 10.1088/0004-637X/712/1/516. arXiv: 1002.0266 [astro-ph.GA].

Oh, KS, DNC Lin, and SJ Aarseth (1995). "On the tidal disruption of dwarf spheroidal galaxies around the galaxy". In: *The Astrophysical Journal* 442, pp. 142–158.

Okamoto, Takashi et al. (2003). "Momentum transfer across shear flows in smoothed particle hydrodynamic simulations of galaxy formation". In: *Monthly Notices of the Royal Astronomical Society* 345.2, pp. 429–446.

Ostriker, Jeremiah P et al. (2019). "Mind the gap: is the too big to fail problem resolved?" In: *The Astrophysical Journal* 885.1, p. 97.

Pawlowski, Marcel S and Pavel Kroupa (2013). "The rotationally stabilized VPOS and predicted proper motions of the Milky Way satellite galaxies". In: *Monthly Notices of the Royal Astronomical Society* 435.3, pp. 2116–2131.

Pérez-Villegas, Angeles, Christopher Wegg, and Ortwin Gerhard (2017). "Revisiting the tale of hercules: how stars orbiting the lagrange points visit the Sun". In: *The Astrophysical Journal Letters* 840.1, p. L2.

Pillepich, Annalisa et al. (2019). "First results from the TNG50 simulation: the evolution of stellar and gaseous discs across cosmic time". In: *Monthly Notices of the Royal Astronomical Society* 490.3, pp. 3196–3233.

Portail, Matthieu et al. (2016). "Dynamical modelling of the galactic bulge and bar: the Milky Way's pattern speed, stellar and dark matter mass distribution". In: *Monthly Notices of the Royal Astronomical Society*, stw2819.

Power, Chris et al. (2003). "The inner structure of ΛCDM haloes—I. A numerical convergence study". In: *Monthly Notices of the Royal Astronomical Society* 338.1, pp. 14–34.

Purcell, Chris W. et al. (Sept. 2011). "The Sagittarius impact as an architect of spirality and outer rings in the Milky Way". In: *Nature* 477.7364, pp. 301–303. DOI: 10.1038/nature10417. arXiv: 1109.2918 [astro-ph.GA].

Ramos, P., T. Antoja, and F. Figueras (Nov. 2018). "Riding the kinematic waves in the Milky Way disk with Gaia". In: *Astronomy & Astrophysics* 619, A72, A72. DOI: 10.1051/0004-6361/201833494. arXiv: 1805.09790 [astro-ph.GA].

Reid, M. J. and A. Brunthaler (Mar. 2020). "The Proper Motion of Sagittarius A*. III. The Case for a Supermassive Black Hole". In: *The Astrophysical Journal* 892.1, 39, p. 39. DOI: 10.3847/1538-4357/ab76cd. arXiv: 2001.04386 [astro-ph.GA].

Reshetnikov, Vladimir and Francoise Combes (1998). "Statistics of optical warps in spiral disks". In: *arXiv preprint astro-ph/9806114*.

Reshetnikov, Vladimir P et al. (2016). "Galaxies with conspicuous optical warps". In: *Monthly Notices of the Royal Astronomical Society* 461.4, pp. 4233–4245.

Robertson, Brant E et al. (2023). "Morpheus Reveals Distant Disk Galaxy Morphologies with JWST: The First AI/ML Analysis of JWST Images". In: *The Astrophysical Journal Letters* 942.2, p. L42.

Roca-Fàbrega, Santi et al. (June 2016). "GARROTXA Cosmological Simulations of Milky Way-sized Galaxies: General Properties, Hot-gas Distribution, and Missing Baryons". In: *The Astrophysical Journal* 824.2, 94, p. 94. DOI: 10.3847/0004-637X/824/2/94. arXiv: 1504.06261 [astro-ph.GA].

Rocha, Miguel, Annika HG Peter, and James Bullock (2012). "Infall times for Milky Way satellites from their present-day kinematics". In: *Monthly Notices of the Royal Astronomical Society* 425.1, pp. 231–244.

Rodríguez-Puebla, Aldo et al. (Sept. 2017). "Constraining the galaxy-halo connection over the last 13.3 Gyr: star formation histories, galaxy mergers and structural properties". In: *Monthly Notices of the Royal Astronomical Society* 470.1, pp. 651–687. DOI: 10.1093/mnras/stx1172. arXiv: 1703.04542 [astro-ph.GA].

Roškar, Rok et al. (2010). "Misaligned angular momentum in hydrodynamic cosmological simulations: warps, outer discs and thick discs". In: *Monthly Notices of the Royal Astronomical Society* 408.2, pp. 783–796.

Ruiz-Lara, Tomás et al. (May 2020). "The recurrent impact of the Sagittarius dwarf on the star formation history of the Milky Way". In: *Nature Astronomy* 4, pp. 965–973. DOI: 10.1038/s41550-020-1097-0. arXiv: 2003.12577 [astro-ph.GA].

Rybizki, Jan et al. (Feb. 2022). "A classifier for spurious astrometric solutions in Gaia eDR3". In: *Monthly Notices of the Royal Astronomical Society* 510.2, pp. 2597–2616. DOI: 10.1093/mnras/stab3588. arXiv: 2101.11641 [astro-ph.IM].

Santos-Santos, Isabel M, Rosa Dominguez-Tenreiro, and Marcel S Pawlowski (2020). "An updated detailed characterization of planes of satellites in the MW and M31". In: *Monthly Notices of the Royal Astronomical Society* 499.3, pp. 3755–3774.

Sawala, Till et al. (2023). "The Milky Way's plane of satellites is consistent with Λ CDM". In: *Nature Astronomy* 7.4, pp. 481–491.

Schaye, Joop et al. (2023). "The FLAMINGO project: cosmological hydrodynamical simulations for large-scale structure and galaxy cluster surveys". In: *arXiv preprint arXiv:2306.04024*.

Schönrich, Ralph and Walter Dehnen (2018). "Warp, waves, and wrinkles in the Milky Way". In: *Monthly Notices of the Royal Astronomical Society* 478.3, pp. 3809–3824.

Searle, Leonard and Robert Zinn (1978). "Compositions of halo clusters and the formation of the galactic halo". In: *Astrophysical Journal, Part 1, vol. 225, Oct. 15, 1978, p. 357-379.* 225, pp. 357–379.

Sellwood, J. A. (May 2012). "Spiral Instabilities in N-body Simulations. I. Emergence from Noise". In: *The Astrophysical Journal* 751.1, 44, p. 44. DOI: 10.1088/0004-637X/751/1/44. arXiv: 1203.0444 [astro-ph.GA].

Sellwood, JA (2010). "Dynamics of Disks and Warps". In: *arXiv preprint arXiv:1006.4855*.

Sellwood, JA and Victor P Debattista (2022). "Internally driven warps in disc galaxies". In: *Monthly Notices of the Royal Astronomical Society* 510.1, pp. 1375–1382.

Sellwood, Jerry A and Karen L Masters (2022). "Spirals in galaxies". In: *Annual Review of Astronomy and Astrophysics* 60, pp. 73–120.

Semczuk, Marcin et al. (2020). "Tidally induced warps of spiral galaxies in IllustrisTNG". In: *Monthly Notices of the Royal Astronomical Society* 498.3, pp. 3535–3548.

Serna, A, R Domínguez-Tenreiro, and A Sáiz (2003). "Conservation laws in smooth particle hydrodynamics: The deva code". In: *The Astrophysical Journal* 597.2, p. 878.

Shen, Juntai and J. A. Sellwood (July 2006). "Galactic warps induced by cosmic infall". In: *Monthly Notices of the Royal Astronomical Society* 370.1, pp. 2–14. DOI: 10.1111/j.1365-2966.2006.10477.x. arXiv: astro-ph/0604529 [astro-ph].

Smith, Britton D et al. (2017). "GRACKLE: a chemistry and cooling library for astrophysics". In: *Monthly Notices of the Royal Astronomical Society* 466.2, pp. 2217–2234.

Springel, Volker et al. (2005). "Simulations of the formation, evolution and clustering of galaxies and quasars". In: *nature* 435.7042, pp. 629–636.

Steinmetz, Matthias and Julio F Navarro (1999). "The cosmological origin of the tully-fisher relation". In: *The Astrophysical Journal* 513.2, p. 555.

Struck, Curtis, Clare L. Dobbs, and Jeong-Sun Hwang (July 2011). "Slowly breaking waves: the longevity of tidally induced spiral structure". In: *Monthly Notices of the Royal Astronomical Society* 414.3, pp. 2498–2510. DOI: 10.1111/j.1365-2966.2011.18568.x. arXiv: 1102.4817 [astro-ph.CO].

Teyssier, Romain (2002). "Cosmological hydrodynamics with adaptive mesh refinement-A new high resolution code called RAMSES". In: *Astronomy & Astrophysics* 385.1, pp. 337–364.

Teyssier, Romain, Damien Chapon, and Frédéric Bournaud (2010). "The driving mechanism of starbursts in galaxy mergers". In: *The Astrophysical Journal Letters* 720.2, p. L149.

Tian, Hai-Jun et al. (Oct. 2018). "Time Stamps of Vertical Phase Mixing in the Galactic Disk from LAMOST/Gaia Stars". In: *The Astrophysical Journal* 865.2, L19, p. L19. DOI: 10.3847/2041-8213/aae1f3. arXiv: 1809.06510 [astro-ph.GA].

Tomozeiu, Mihai, Lucio Mayer, and Thomas Quinn (2016). "Tidal stirring of satellites with shallow density profiles prevents them from being too big to fail". In: *The Astrophysical Journal Letters* 827.1, p. L15.

Toomre, Alar (1977). "Mergers and some consequences". In: *Evolution of Galaxies and Stellar Populations*, p. 401.

Toomre, Alar and Juri Toomre (Dec. 1972). "Galactic Bridges and Tails". In: *The Astrophysical Journal* 178, pp. 623–666. DOI: 10.1086/151823.

Trelles, A et al. (2022). "Concurrent infall of satellites-Collective effects changing the overall picture". In: *Astronomy & Astrophysics* 668, A20.

Tremaine, Scott, Neige Frankel, and Jo Bovy (2023). "The origin and fate of the Gaia phase-space snail". In: *Monthly Notices of the Royal Astronomical Society* 521.1, pp. 114–123.

Turk, M. J. et al. (Jan. 2011). "yt: A Multi-code Analysis Toolkit for Astrophysical Simulation Data". In: *The Astrophysical Journal Supplement Series* 192, 9, p. 9. DOI: 10.1088/0067-0049/192/1/9. arXiv: 1011.3514 [astro-ph.IM].

Urrejola-Mora, Catalina et al. (2022). "WiNDS: An H $\alpha$ Kinematics Survey of Nearby Spiral Galaxies—Vertical Perturbations in Nearby Disk-type Galaxies". In: *The Astrophysical Journal* 935.1, p. 20.

van der Walt, Stefan et al. (Jan. 2014). "scikit-image: Image processing in Python". In: *PeerJ* 2, e453, e453. DOI: 10.7717/peerj.453. arXiv: 1407.6245 [cs.MS].

Vasiliev, Eugene (Jan. 2019). "AGAMA: action-based galaxy modelling architecture". In: *Monthly Notices of the Royal Astronomical Society* 482.2, pp. 1525–1544. DOI: 10.1093/mnras/sty2672. arXiv: 1802.08239 [astro-ph.GA].

Vasiliev, Eugene and Vasily Belokurov (Oct. 2020). "The last breath of the Sagittarius dSph". In: *Monthly Notices of the Royal Astronomical Society* 497.4, pp. 4162–4182. DOI: 10.1093/mnras/staa2114. arXiv: 2006.02929 [astro-ph.GA].

Vega, Alexander de la et al. (2015). "Phase wrapping of epicyclic perturbations in the Wobbly Galaxy". In: *Monthly Notices of the Royal Astronomical Society* 454.1, pp. 933–945.

Virtanen, Pauli et al. (2020). "SciPy 1.0: Fundamental Algorithms for Scientific Computing in Python". In: *Nature Methods* 17, pp. 261–272. DOI: 10.1038/s41592-019-0686-2.

Vogelsberger, Mark et al. (2020). "Cosmological simulations of galaxy formation". In: *Nature Reviews Physics* 2.1, pp. 42–66.

Voort, Freeke van de et al. (2015). "The creation and persistence of a misaligned gas disc in a simulated early-type galaxy". In: *Monthly Notices of the Royal Astronomical Society* 451.3, pp. 3269–3277.

Wang, Yang et al. (2022). "A stochastic model to reproduce the star formation history of individual galaxies in hydrodynamic simulations". In: *Monthly Notices of the Royal Astronomical Society* 515.3, pp. 3249–3269.

Wang, Yougang, E Athanassoula, and Shude Mao (2020). "Basis function expansions for galactic dynamics: Spherical versus cylindrical coordinates". In: *Astronomy & Astrophysics* 639, A38.

Watkins, Laura L et al. (2019). "Evidence for an intermediate-mass Milky Way from Gaia DR2 halo globular cluster motions". In: *The Astrophysical Journal* 873.2, p. 118.

Weinberg, Martin D. (Aug. 1989). "Self-gravitating response of a spherical galaxy to sinking satellites". In: *Monthly Notices of the Royal Astronomical Society* 239, pp. 549–569. DOI: 10.1093/mnras/239.2.549.

Weinberg, Martin D (1998). "Dynamics of an interacting luminous disc, dark halo and satellite companion". In: *Monthly Notices of the Royal Astronomical Society* 299.2, pp. 499–514.

Weinberg, Martin D and Michael S Petersen (2021). "Using multichannel singular spectrum analysis to study galaxy dynamics". In: *Monthly Notices of the Royal Astronomical Society* 501.4, pp. 5408–5423.

Weinmann, Simone M et al. (2006). "Properties of galaxy groups in the Sloan Digital Sky Survey—I. The dependence of colour, star formation and morphology on halo mass". In: *Monthly Notices of the Royal Astronomical Society* 366.1, pp. 2–28.

White, Simon DM and Carlos S Frenk (1991). "Galaxy formation through hierarchical clustering". In: *Astrophysical Journal, Part 1 (ISSN 0004-637X), vol. 379, Sept. 20, 1991, p. 52-79. Research supported by NASA, NSF, and SERC.* 379, pp. 52–79.

Widmark, A., C. F. P. Laporte, and G. Monari (July 2022). "Weighing the Galactic disk using phase-space spirals. III. Probing distant regions of the disk using the Gaia EDR3 proper motion sample". In: *Astronomy & Astrophysics* 663, A15, A15. DOI: 10.1051/0004-6361/202142819. arXiv: 2111.13707 [astro-ph.GA].

Widmark, A., L. M. Widrow, and A. Naik (Dec. 2022). "Mapping Milky Way disk perturbations in stellar number density and vertical velocity using Gaia DR3". In: *Astronomy & Astrophysics* 668, A95, A95. DOI: 10.1051/0004-6361/202244453. arXiv: 2207.03492 [astro-ph.GA].

Widmark, A. et al. (Sept. 2021). "Weighing the Galactic disk using phase-space spirals. II. Most stringent constraints on a thin dark disk using Gaia EDR3". In: *Astronomy & Astrophysics* 653, A86, A86. DOI: 10.1051/0004-6361/202141466. arXiv: 2105.14030 [astro-ph.GA].

Widmark, A. et al. (July 2022). "Weighing the Galactic disk using phase-space spirals. IV. Tests on a three-dimensional galaxy simulation". In: *Astronomy & Astrophysics* 663, A16, A16. DOI: 10.1051/0004-6361/202243173. arXiv: 2201.04637 [astro-ph.GA].

Widmark, Axel, Chervin Laporte, and Pablo F. de Salas (Feb. 2021). "Weighing the Galactic disk using phase-space spirals I: Tests on one-dimensional simulations". In: *arXiv e-prints*, arXiv:2102.08955, arXiv:2102.08955. arXiv: 2102.08955 [astro-ph.GA].

Widrow, Lawrence M. et al. (May 2012). "Galactoseismology: Discovery of Vertical Waves in the Galactic Disk". In: *The Astrophysical Journal Letters* 750.2, L41, p. L41. DOI: 10.1088/2041-8205/750/2/L41. arXiv: 1203.6861 [astro-ph.GA].

Widrow, Lawrence M et al. (2012). "Galactoseismology: discovery of vertical waves in the Galactic Disk". In: *The Astrophysical Journal Letters* 750.2, p. L41.

Widrow, Lawrence M et al. (2014). "Bending and breathing modes of the Galactic disc". In: *Monthly Notices of the Royal Astronomical Society* 440.3, pp. 1971–1981.

Williams, Mary EK et al. (2013). "The wobbly Galaxy: kinematics north and south with RAVE red-clump giants". In: *Monthly Notices of the Royal Astronomical Society* 436.1, pp. 101–121.

Younger, Joshua D. et al. (Mar. 2008). "On the Origin of Dynamically Cold Rings around the Milky Way". In: *The Astrophysical Journal Letters* 676.1, p. L21. DOI: 10.1086/587099. arXiv: 0802.0872 [astro-ph].

# List of Figures

1.1 Different types of simulations, from large-scale structure to provide statistical samples of galaxies (bottom panels), to the zoom-in simulations to observe more details of certain gropus of galaxies (top panels). Simulations can be made with only dark matter with N-body algorithms (left panels) or they can include baryons, with a hidrodynamical component (right panels). From: (Vogelsberger et al., 2020). . . . . 6
1.2 Bending and breathing modes of the stellar disk. The dotted black line represents the galactic plane, and the displacement of the stars with respect to this plane are represented by the solid orange line. The bending mode of the disk is a systematic deviation from the plane, whereas the breathing mode follows an expansion or contraction behavior. . . . . 9
1.3 The Milky Way as seen by *Gaia*. From European Space Agency (ESA). . . . . 10
1.4 Local phase spiral of the Solar Neighbourhood as presented in Antoja et al., 2018 with data from *Gaia* DR2. The left panel shoes a 2D histogram of the local phase spiral, and central anf right panel shows this same phase spiral coloured by the cylindrical galactocentric velocities $V_R$ aand $V_\phi$, respectively. . . . . 11

2.1 GARROTXA's MW model G.323 components in the cosmological box (left) and the MW model (right). From top to bottom, stellar particles, dark matter particles and gas cells colored by their respective mass. . . . . 16
2.2 Mass distribution of the stellar particles inside the $R_{vir}$ at $z = 0$ for model G.323. . . . . 17
2.3 Density profile of the simulated galaxy at redshift $z = 0$. Horizontal lines represent each of the virial overdensities $\Delta_{vir} \times \rho_{crit}$, for $\Delta_{vir} = 97$ (red line),$\Delta_{vir} = 200$ (green line), and $\Delta_{vir}$ as in BN98 (blue line). . . . . 18
2.4 Reference system after centering and alignment of the galaxy. We use galactocentric cylindrical coordinates $(R, \phi, Z)$, and the system rotates in the clockwise direction. . . . . 19
2.5 Different stellar structures at present times $z = 0$. The left panel shows stars born 500 Myr after the last major merger (at 9.55 Gyr in lookback time). The panels in the central column show the older, hot disk. Lastly, in the right column, we show the old stellar ellipsoid. The top two rows show the surface density of the stellar particles in the X-Z and X-Y projections, respectively. The last row shows the face-on projection colored by age. . 21
2.6 Histogram of the $L_Z/L_{\rm circ}$ of the different stellar structures described in Fig.2.5: disk, with particles younger than 9.05 Gyr (blue), and particles older than 9.05 Gyr with $\cos\alpha > 0.7$ old disk (yellow), and $\cos\alpha < 0.7$ that conforms the ellipsoid (red). The grey zone indicates the ranges in which the stellar structure is rotationally supported, defined by $0.5 < L_Z/L_{\rm circ} < 1.5$. . . . . 22

2.7 Face-on projection of the stellar disk at $\sim 0$ Gyr. The top left panel shows an overdensity plot with a Gaussian filter of $\sigma = 6$. The next panels show 2D histograms weighted by $Z$, $V_Z$, $V_\phi$ and $V_R$, respectively. . . . . 23
2.8 Rotation curve of GARROTXA's MW model. The red curve is the spherical approximation and the black one is derived from radial accelerations. We also show the azimuthal velocity of cold gas (pink line), and disk stars and their dispersion (blue line, and blue shade) as well as the spherical tangential velocity (green line) which is defined as $V_t = \sqrt{V_\phi^2 + V_Z^2}$. . 24
2.9 Rotation periods of GARROTXA's MW model calculated from the $V_{\rm circ}$ with Eq. 2.3. The color code is the same as in Fig. 2.8. . . . . 25
2.10 Orbits of the main satellites in GARROTXA MW-sized model. **Top panel**: galactocentric distance to the main galactic system. **Bottom panel**: vertical distance $Z$ from the plane $Z = 0$. . . . . 27
2.11 Gas in Arania satellite at three different times before pericenters, at galactocentric distances of 60, 76 and 78 kpc respectively. The position of the satellite is marked as an "x" and the dotted line marks a circle of 5 kpc of radius in which we compute the mass of the gas with $T < 10^5 K$. . . . . 29
2.12 Same as in Fig. 2.11 but with Escarabajo satellite, when it has entered the virial radius of the galaxy (at a galactocentric distance of 76 kpc), and before its first pericenter. . . . . 30
2.13 Same as in Fig. 2.11 but with gas in the DM1119 satellite before its first pericenter at a galactocentric distance of 96 kpc. . . . . 30
2.14 Newly formed star mass (yellow histogram) and available gas (blue line) along the last 6 Gyr of evolution. . . . . 31
2.15 Comparison between the disk colored by $V_Z$ and reconstructed via Fourier decomposition from modes 0 to 4. . . . . 33
2.16 Fourier decomposition of $V_Z$ from modes 0 to 4. The sum of these modes leads to the reconstructed disk $V_Z$ shown in the right panel of Fig. 2.15. . . . . 33
2.17 Results of the phase of the maximum amplitude of the Fourier decomposition. The left panels show the decomposition for Fourier modes $m = 1$ and $m = 2$ (top and bottm panels respectively), with the same color scale as Fig. 2.15. The dots show the positions of the maximum amplitude for each ring. For mode $m = 2$, due to the duplicity of the signal, we show both maximums (black and green dots). The right panels show this angle as a function of galacticentric radius. . . . . 34

3.1 Phase space spirals ($Z - V_Z$) observed in the 0-5 Gyr stellar particles' age population of the GARROTXA simulation at 2.74 Gyr in lookback time, that is 1.1 Gyr after the pericenter of the most massive satellite (Arania). From left to right: a two-dimensional histogram with no weighting, $V_\phi$ weighted and $V_R$ weighted. . . . . 37
3.2 Phase spirals in the vertical phase space as scatter, (left columns), $V_\phi$ weighted (central panels) and $V_R$ weighted (right panels) at different azimuths and times between 5.3 - 3 Gyr in lookback time. . . . . 38
3.3 Phase spirals in the vertical phase space as scatter, (left columns), $V_\phi$ weighted (central panels) and $V_R$ weighted (right panels) at different azimuths and times between 3 - 1 Gyr in lookback time. . . . . 39

3.4 Vertical phase space distributions of stellar particles with age of $0-5$ Gyr at seven different radial bins (see top labels) and at a fixed azimuthal direction of 330° inside the disk, from the snapshot at 2.74 Gyr of lookback time. We show the phase space density (top), $V_\phi - <V_\phi>$ weighted (middle), and $V_R$ weighted (bottom). $<V_\phi>$ is the mean azimuthal velocity at each region. . . . . 40
3.5 Vertical phase space of seven age populations within a region with fixed azimuth (150°) and distance to the galactic center (10-12 kpc), at lookback time of 2.2 Gyr. From top to bottom we show: density of stars; $V_\phi - <V_\phi>$ weighted; $V_R$ weighted. Additionally, the first column shows the cold gas and the newborn stellar particles as black dots. . . . . 40
3.6 Amplitude of the phase spiral with time and relation with satellite orbits and star formation. **First three panels:** m=1 Fourier amplitude in the Z-$V_Z$ space, for the same regions and ages as in Fig. 3.2 and 3.3, computed for the density, $V_\phi$-weighted, and $V_R$-weighted, respectively. **Fourth panel:** acceleration onto the disk by the main satellites with darker colours indicating a lower vertical distance above/below the disk plane. Here the small discontinuities are artificially caused by our re-calculation of the virial radius. **Bottom panel:** star formation efficiency (histogram) and gas inflow histories (blue dots and line). Coloured vertical lines indicate the times of pericentres. . . . . 42

4.1 Overdensity plot of the disk particles with a Gaussian filter with $\sigma = 6$ (top panel), bending (middle), and breathing (bottom) maps at two different snapshots of the model of GARROTXA simulation in each column, 2.33 Gyr and 0.99 Gyr in lookback time. A strong bending mode can be seen at 0.99 Gyr (middle right panel). . . . . 50
4.2 Temporal evolution of the Fourier amplitude $A_m$ (top panels) and phase $\phi_m$ (bottom panels) of the $m = 1$ (left panels) and $m = 2$ (right panels) modes. The phase of mode $m = 2$ ranges between $-90°$ and $90°$ due to the duplicity of the structures. The white horizontal grey-dashed lines mark the division of the disk at a radius of 10 and 20 kpc. The bending $m = 1$ dominates over $m = 2$ and shows higher amplitudes at outer radii (R> 7 kpc) excited mainly at the beginning of the timespan studied and at later times from 2 Gyr on. The inner parts show faster retrograde bending waves with the highest amplitude happening around 4 Gyr of lookback time. . . . . 52
4.3 Vertical acceleration of dark matter (top panels) and gas (bottom panels). Black dot-dashed circles are situated at 20 kpc, illustrating the size of the stellar disk of the galaxy. The dark matter acceleration at the top three leftmost panels is dominated by the crossing of dark matter subhalos DM1119 and DM2595. The effect of gas at these times (bottom panels) is bimodal. The dark matter's $a_Z$ of the right block of panels is dominated by the satellite galaxy "Escarabajo", which applies positive $a_Z$ in the positive x - positive y region of the mesh. . . . . 53
4.4 Fourier decomposition of the vertical acceleration by dark matter particles onto the $Z = 0$ plane. We show $m = 1$ (left panels) and $m = 2$, from which we have the amplitude of the mode (top panels) and the phase where the maximum amplitude is located (bottom panels). These are similar to 4.2, but extended to 40 kpc of radius. The inner acceleration is dominated by the inner dark matter structure. . . . . 55

4.5 Total gravitational acceleration magnitude produced by each individual subhalo on the center of the galactic system (colored lines, right y-axis) and the sum of acceleration by the rest of (less massive) subhalos (black dashed line, right y-axis). Subhalos containing stellar particles are indicated as solid lines, and those with pure dark matter are shown as dashed lines. We also marked the moments and positions (cylindrical radius, left axis) when the satellites ("x") cross the galactic plane. The grey "x" symbols correspond to the crossings of less massive satellites. Background color and left axis are equivalent to the top-left panel in Fig. 4.4. Notice that, while the background color shows the vertical acceleration by all dark matter on the galactic plane $Z = 0$, lines show the total acceleration produced by subhalos at the galactic center, not at the $Z = 0$ plane. The latter gives proportionally lower values of acceleration due to the difference of the distance between the satellite and the closest point of the plane vs to the center of the galaxy. For the lines, we also use the data of $M_{\rm bound}$ for each satellite, re-evaluated at each apocenter. The masses indicated on the label are the first mass registered for each satellite, which corresponds to $M_{200}$. In this figure, we see that the vertical acceleration from the dark matter halo between 25-40 kpc is correlated with the pericentric passages of several satellites, dark or luminous. The ones exerting more vertical acceleration are DM1119 and Escarabajo, as well as DM479 and DM2113 at later times. . . . . 56

4.6 Fourier decomposition of the acceleration of the gas cells (similar to Fig. 4.4) onto the $Z = 0$ plane (galactic plane). We show $m = 1$ (left panels) and $m = 2$, from which we have the amplitude of the mode (top panels) and their corresponding phase of the maximum amplitude (bottom panels). . . . . 58

4.7 Distribution and temperature of the gas in GARROTXA. Left and central columns: Zoom-out face-on ($Y$-$X$ plane) and edge-on ($Y$-$Z$ plane) projection of the gas temperature at six different instances of the simulation colored by temperature. The crosses and dashed lines indicate the position and direction of the satellites Arania and Escarabajo. Right column: Edge-on projection of the gaseous disk, colored by temperature. The dotted horizontal line represents the plane of the stellar disk. The main inflow is reaching the galaxy from the negative Y direction. . . . . 60

4.8 Top left panel (**A**) mean value of the amplitude of Fourier mode $m = 1$ of $a_Z$ by the dark matter (blue lines) at external radii (20-40 kpc). The vertical lines show the moments of maximum approach to the disk by those satellites of higher mass, and the labels indicate their $M_{200}$ at infall. The left panels show the calculated properties at radii from 10 to 20 kpc, whereas the right panels show between 0 to 10 kpc. Panels **B** and **F** show the mean value of the amplitude of mode $m = 1$ of the vertical acceleration of dark matter (blue lines) and gas (orange lines). Panels **C** and **G** show the angle difference between the angular momentum of stars and the angular momentum of gas (dotted orange lines, leftmost axis) and the tilt of the central dark matter triaxial structure with respect to the disk (dotted blue lines rightmost axis), denoted by $\theta_{gas}$ and $\theta_{ellipsoid}$, respectively. Panels **D** and **H** show the angular momentum vector variation in relation to the previous snapshot divided by the timespan. Panels **E** and **I** show the mean amplitude of Fourier amplitudes for bending modes $m = 1$ (green lines) and $m = 2$ (purple lines). . . . . 62

4.9 Column density (left panels), temperature (central panels), and $a_Z$ by the gas at three different snapshots after the interaction with Escarabajo. The black dots represent newly formed stellar particles with ages smaller than 50 Myr. Apart from the initial misalignment of the gaseous disk in relation to the stellar disk, the star formation and subsequent SNe further displaces and perturbs the disk in this direction. . . . . 64

5.1 Phase spiral in the solar neighbourhood with *Gaia* DR3 data. **Left**: Two-dimensional histogram of the vertical projection of phase space ($Z$–$V_Z$) from the sample of stars with Galactocentric radii of $R_\odot \pm 0.1$ kpc and $\phi = 0 \pm 20$ deg. We used bins of $\Delta Z = 0.02$ kpc and $\Delta V_Z = 1\,\mathrm{km\,s^{-1}}$. **Middle**: Same projection but colour-coded by median radial velocity $V_R$. **Right**: Same projection but color-coded by median azimuthal velocity $V_\phi$, adjusting the colour bar limits so as to maximize the appearance of the spiral. . . . . 72

5.2 Phase spiral detected by the edge detection. **Top left**: Output of the algorithm applied to the same selection of stars as in Fig. 5.1, superposed to the counts from which it has been computed. We used $\sigma = 3$. **Bottom left**: Same but superposed to the projection coloured by $V_\phi$. **Top right**: Comparison with the Gaussian filter (colour, see text). **Bottom right**: Comparison with the Gaussian filter and the WT, with the respective values scaled to fit in the same plot, as indicated in the legend, in a one-dimensional case (see text). . . . . 73

5.3 Phase spiral at different Galactocentric radii with *Gaia* DR3 data. The panels show the vertical projection of phase space ($Z$–$V_Z$) colored by median $V_\phi$. We only use stars with $|\phi| < 20$ deg. Each region has a total radial width of 1 kpc and their centers are separated by the same amount. We used bins of $\Delta Z = 0.02$ kpc and $\Delta V_Z = 1\,\mathrm{km\,s^{-1}}$. The color-map ranges correspond to the percentiles 30 and 70 of the distribution of $V_\phi$ in each volume to maximize the appearance of the spiral. In the bottom part of the panels we indicate the number of stars. . . . . 75

5.4 Phase spiral for different angular momentum with *Gaia* DR3 data. We only use stars with $|\phi| < 20$ deg. The selections have a total angular momentum width of 200 $\mathrm{km\,s^{-1}kpc}$ and their centres are separated by the same amount. We used bins of $\Delta Z = 0.02$ kpc and $\Delta V_Z = 1\,\mathrm{km\,s^{-1}}$. **Top:** Counts projection after Gaussian masking (see text for details). The color bar is the same as in the top left panel of Fig. 5.2. We superpose our detected phase spiral via the edge detector method where we used $\sigma$=4.5 for $|L_Z| < 1600\,\mathrm{km\,s^{-1}kpc}$ and $\sigma$=3.5 for $|L_Z| \geq 1600\,\mathrm{km\,s^{-1}kpc}$. We indicate the number of stars in the bottom part of the panels. **Bottom**: Projection colored by $V_R$ with the same color scale as in the central panel of Fig. 5.1. . . . . 76

5.5 Superposed phase spiral for different angular momentum with *Gaia* DR3 data. We select only stars with $\phi \in [-20, 20]$ deg. We use bins of $\Delta L_Z = 200\,\mathrm{km\,s^{-1}kpc}$ and centres of bins separated by $100\,\mathrm{km\,s^{-1}kpc}$, from $L_Z = 1300\,\mathrm{km\,s^{-1}kpc}$ (bluer lines) to $L_Z = 2500\,\mathrm{km\,s^{-1}kpc}$ (redder lines) as indicted in the legend. In parenthesis, we give an indicative measure of guiding radius assuming a flat circular velocity curve. . . . . 77

5.6 Crossing positions of the phase spiral ($Z_c$). The blue circles and error bars mark the $Z$ coordinate for $V_Z = 0$ of the phase spiral determined from the edge detector for the SH sample. We mark the positions used for inferring the impact time with empty black circles. The dashed orange vertical line marks the angular momentum of the Sun. . . . . 78

5.7 Superposed phase spiral for different azimuths with *Gaia* DR3 data. We select only stars with $L_Z \in [-2100, -1800]$. We use bins of $\Delta\phi = 4$ deg and centers of bins separated by the same amount, from $\phi = -20$ deg (bluer lines) to $\phi = 20$ deg (redder lines) as indicated in the legend. In parenthesis, we give the average azimuth of the selection, which can differ by 1 deg compared to the center of the selection in some cases. For the edge detector, we used $\sigma = 3.5$. . . . . 80
5.8 Start time of the phase mixing as a function of angular momentum. The symbols indicate the time inferred from Eq. 5.5 for the different consecutive crossing points of the phase spiral and are coloured by height above the plane. The circles with error bars are the points that we consider valid while crosses are the rest of cases. An indicative guiding radius corresponding to the circular velocity curve of the McM17 potential is given in the upper horizontal axis. The dashed line marks a linear fit to the data points. . . . . 81
5.9 Time of start of phase mixing as a function of height above the plane. The symbols give the time inferred from Eq. 5.5 for the different consecutive crossing points of the phase spiral and are coloured by angular momentum. The circles with error bars are the points that we consider valid while crosses are the rest of cases. The dashed line marks a linear fit to the data points. . . . . 82
5.10 Time of start of phase mixing for different potentials. The figure is similar to Fig. 5.8 but we use frequencies of different potential models of the MW, as indicated in the legend. . . 84
5.11 Time of start of phase mixing for different kinetic temperatures. The figure is similar to Fig. 5.8 but we use orbits with different radial actions and methods, as indicated in the legend. . . . . 85
5.12 Time of start of phase mixing for different distances and data. The figure is similar to Fig. 5.8 but we use distances from BJ, from SH with distance biases of $\pm 10\%$ and for a selection of giant stars, as indicated in the legend. . . . . 86
5.13 Time of start of phase mixing for different parts of the phase spiral. The figure is similar to Fig. 5.8 but we use the fiducial case (blue dots) computed from $Z_c$ but also from $V_{Zc}$ (grey squares) to derive the times, as indicated in the legend. . . . . 89

A.1 3D example of a tilted stellar disk (tilted blue circle) in the cosmological box. The solid arrows represent the cosmological box original axis. The dotted blue arrow represents $L$ of the disk, and the new axis $z'$ after the change of basis. . . . . 104
A.2 **Left panel**: Definition of the $x'$ axis (dotted black arrow), which is a projection onto the galactic plane of the old $x$ axis (solid black arrow). **Right panel**: Definition of the $y'$ axis (dotted red arrow), defined as the cross product of $z'$ (dotted blue arrow) and $x'$ (dotted black arrow). . . . . 104
A.3 $L_Z$ misalignment of stars and gas in respect to the established $Z = 0$ plane where the second alignment has been done using stellar particles in the radial region of $R < 7$ kpc as a function of time (recomputed at each snapshot). From top to bottom, regions from 0 to 5 kpc, 5 to 10 kpc, 10 to 15 kpc and 15 to 20 kpc. . . . . 106
A.4 $L_Z$ misalignment of stars and gas in respect to the established $Z = 0$ plane, similar to A.3 where the second alignment has been done using stellar particles in the radial region of $R < 15$ kpc as a function of time (recomputed at each snapshot). From top to bottom, regions from 0 to 5 kpc, 5 to 10 kpc, 10 to 15 kpc and 15 to 20 kpc. . . . . 107

B.1 Distance of satellites to the center of the galaxy. The top panel shows dark satellites of $10^6$ $M_\odot$ < M <$10^7$ $M_\odot$. The second panel are satellites $10^7$ $M_\odot$ < M <$10^8$ $M_\odot$. Third one M > $10^8$ $M_\odot$. The bottom panel shows all subhalos containing stellar particles. . . . . 110

C.1 Phase spirals colored by $V_\phi$ of the model GARROTXA RAMSES along radius (from 6 kpc on the left to 12 kpc on the right) and azimuths (from 0° on the top panels to 330° on the bottom panels). . . . . 118
C.2 Similar to Fig C.1 but colored by $V_R$ . . . . . 119

D.1 Temporal evolution of the Fourier amplitude $A_m$ (top panels) and phase $\phi_m$ (bottom panels) of the $m = 1$ (left panels) and $m = 2$ (right panels) modes weighted by stellar mass. The phase of mode $m = 2$ ranges between $-90°$ and $90°$ due to the duplicity of the structures. The white horizontal grey-dashed lines mark the division of the disk at a radius of 10 and 20 kpc. . . . . 122
D.2 Similar to Fig. 4.2 but for the breathing. . . . . 123

E.1 Pearson's correlation coefficient in moving windows of 800 Myr of width for bending and breathing modes vs accelerations of gas and dark matter. We mark as circles the moments where Pearson's coefficient fulfils $|r| > 0.4$ and $p - value < 0.05$ . . . . . 127
E.2 Same as Fig E.1 but with variables of density vs gas and dark matter acceleration's $m = 1$. 128
E.3 Same as Fig E.1 but with variables of density vs bending and breathing modes. . . . . 129

F.1 Different age populations colored by $V_Z$ (bending modes), from younger particles (left) to older ones (right). . . . . 131

G.1 **Top panel**: Vertical position of the streams at lookback time of 1.49 Gyr, where the satellite is situated at a galactocentric distance of 63.5 kpc (∼0.5 Gyr after its pericenter at a distance of ∼38 kpc). **Bottom left panel**: Vertical acceleration by the particles inside $5 \times R_{tidal}$ which we consider to belong to the progenitor. **Bottom left panel**: Vertical acceleration by the particles outside of $5 \times R_{tidal}$, which we consider to belong to the streams. 134

H.1 Fourier modes of density from mode $m = 1$ (top) to $m = 4$ (bottom) with the corresponding amplitude (left panels) and phase (right panels), similar to Fig. D.1, with radial bins of 1 kpc. . . . . 136
H.2 Fourier modes of $Z$ from mode $m = 1$ (top) to $m = 4$ (bottom) with the corresponding amplitude (left panels) and phase (right panels). . . . . 137
H.3 Fourier modes of $V_Z$ from mode $m = 1$ (top) to $m = 4$ (bottom) with the corresponding amplitude (left panels) and phase (right panels). . . . . 138
H.4 Fourier modes of $V_\phi$ from mode $m = 1$ (top) to $m = 4$ (bottom) with the corresponding amplitude (left panels) and phase (right panels). . . . . 139
H.5 Fourier modes of $V_R$ from mode $m = 1$ (top) to $m = 4$ (bottom) with the corresponding amplitude (left panels) and phase (right panels). . . . . 140

# List of Tables

2.1 Main characteristics of the MW-sized model G.323 of GARROTXA simulation at z= 0 in comparison to the MW. From left to right, $R_{200}$ (on the left, calculated with our density profile analysis, on the right as calculated by Rockstar halo finder (Behroozi, Wechsler, and Wu, 2012)), virial radius, virial mass, the total stellar particles mass, the mass of the disk, the typical mass of the disk particles, and the number of disk particles. The estimations for the MWare from Dehnen, McLaughlin, and Sachania (2006), McMillan (2011), Gibbons, Belokurov, and Evans (2014), and Licquia and Newman (2015) . . . . . 20

2.2 Properties of the largest satellite galaxies in the simulation. From left to the right: total mass at first infall, denoted as $M_{inf}$ (we give two different values corresponding to the mass inside the virial radius and the one from abundance matching at $z \sim 2$, respectively); tidal radius ($R_t$), total mass inside the tidal radius ($M_t$). The next columns are computed with Rockstar halo finder, $R_{200}$, $M_{bound}$, and stellar mass. Values separated by "-" are values measured at the start and the end of the time studied (6.3 Gyr and 0 Gyr respectively). The last column is the orbit inclination with respect to the galactic plane with the two values being at 6 and 0 Gyr lookback time. Satellites indicated by "DM" are dark matter subhaloes in which we have not found stellar particles. The missing values of the first three columns indicate that the data were not calculated and the satellites were only computed with Rockstar halo finder. . . . . 26

5.1 Phase mixing times from the phase spirals. We show weighted and unweighted average (columns 2 and 3) with their standard errors, minimum and maximum values (columns 4 and 5), and ranges enclosing 80% of times (column 6). The last two columns (7 and 8) compare the times with the fiducial case (first row), showing the average differences and the ranges of differences. The different rows are for different cases as explained in the text. For the times derived from the $V_{Zc}$ (last row) we do not compute the differences with the fiducial case since there is not a point by point correspondence. . . . . 87

B.1 Complete satellite characteristics. R200, M200, stellar mass, minimum distance reached, and moment where they enter virial radius. . . . . 116